Washington University in St. Louis
Washington University Open Scholarship

Engineering and Applied Science Theses & Dissertations | McKelvey School of Engineering

Spring 5-15-2020

Chemistry of Nanoscale Solids and Organic Matter in Sustainable Water Management Systems

Xuanhao Wu
Washington University in St. Louis

Follow this and additional works at: https://openscholarship.wustl.edu/eng_etds

 Part of the Chemical Engineering Commons, Environmental Engineering Commons, and the Geochemistry Commons

Recommended Citation

Wu, Xuanhao, "Chemistry of Nanoscale Solids and Organic Matter in Sustainable Water Management Systems" (2020). *Engineering and Applied Science Theses & Dissertations*. 555.
https://openscholarship.wustl.edu/eng_etds/555

This Dissertation is brought to you for free and open access by the McKelvey School of Engineering at Washington University Open Scholarship. It has been accepted for inclusion in Engineering and Applied Science Theses & Dissertations by an authorized administrator of Washington University Open Scholarship. For more information, please contact digital@wumail.wustl.edu.

WASHINGTON UNIVERSITY IN ST. LOUIS

Department of Energy, Environmental and Chemical Engineering

Dissertation Examination Committee:

Young-Shin Jun, Chair
Zhen (Jason) He
Srikanth Singamaneni
Yinjie Tang
Patricia Weisensee

Chemistry of Nanoscale Solids and Organic Matter in Sustainable Water Management Systems

by
Xuanhao Wu

A dissertation presented to
The Graduate School
of Washington University in
partial fulfillment of the
requirements for the degree
of Doctor of Philosophy

May 2020
St. Louis, Missouri

© 2020, Xuanhao Wu

Table of Contents

List of Figures

List of Tables

Acknowledgments

First and foremost, I would like to express my deepest gratitude to my Ph.D. advisor, Dr. Young-Shin Jun, who has guided me patiently during this five year journey from a fresh graduate student to an independent researcher. Dr. Jun has taught me the important principles of being a good researcher, mentor, leader, and collaborator. Her valuable suggestions on how to conduct research, how to work with my mentees, how to schedule my time, and how to evaluate pros and cons in making decisions, will always be with me. As a life lesson, Dr. Jun has also taught me the way to become a mature man. Dr. Jun has kept pushing me to be a better person by telling me my strengths and weakness. Her care during my Ph.D. not only helped me to improve my research skills, but also led me try to learn from others and overcome my weaknesses. I also appreciate Dr. Jun's offering for many enriching opportunities during my Ph.D., including attending workshops and conferences, conducting experiments at Argonne, mentoring undergraduates, joining in the membrane group, and participating in faculty search. From all these precious experience, I have had the chance to broaden my horizon, meet with many people to advertise my research, and improve my presentation and communication skills. Without Dr. Jun's great mentorship, I could not have accomplished what I have achieved during my Ph.D..

Second, I would like to thank my thesis committee members, Dr. He (Jason) Zhen, Dr. Yinjie Tang, Dr. Srikanth Singamaneni, and Dr. Patricia Weisensee, for their serving and for providing valuable suggestions. Especially, I would like to thank Dr. Singamaneni, who has been my "second advisor" during my Ph.D. studies. During our collaboration, Dr. Singamaneni has inspired me a lot with his knowledge of materials chemistry, and he has provided many astute suggestions and new ideas for research, which have continuously pushed me.

I would also like to thank Dr. Byeongdu Lee, Dr. Xiaobing Zuo, and Dr. Sönke Seifert at Argonne National Laboratory for assisting me in using the beamline at the Advanced Photon Source. I am especially thankful for Dr. Byeongdu Lee's patient instructions that built my basic knowledge of X-ray synchrotron measurement and data analysis. For publishing research outcomes, I would like to thank Prof. James Ballard for his assistance in reviewing my manuscripts, and for being a great technical writing instructor.

Pursuing my Ph.D. in the Environmental Nanochemistry Laboratory has been a rewarding experience. For their collaboration and research discussions, and their friendship in life, I would like to thank my former group members, Dr. Jessica Ray, Dr. Chelsea Neil, Dr. Qingyun Li, Dr. Yujia Min, Dr. Haesung Jung, Dr. Doyoon Kim, Yue Hui, Dr. Yongfang Rao, and my current group members, Deoukchen Ghim, Yaguang Zhu, Zhenwei Gao, Albern Tan, Ping-I Chou, Eunyoung Jang, and Dandan Zhang. I also want to thank my promising undergraduate mentees, Samantha A Burnell, Daniel Delgado, Brandon Bowers, Adrian Martinez, and Junlong Huang, for their contributions to my research as companions in achieving scientific goals. I also thank my colleagues and friends in the Department of Energy, Environmental & Chemical Engineering for their help during my Ph.D..

The research conducted in this dissertation was supported by National Science Foundation Environmental Chemical Science program (CHE-1214090), National Science Foundation (EAR-1424927), and National Science Foundation Environmental Engineering Program (CBET-1604542). These funding sources are gratefully acknowledged.

Last but not least, I would like to express my gratitude to my family for their unconditional love and support. Particularly, I would like to thank my parents and my wife, for sharing my

happiness and sadness. With their encouragements, I finally reached the destination of my Ph.D. journey.

Xuanhao Wu

Washington University in St. Louis

May 2020

ABSTRACT OF THE DISSERTATION

Chemistry of Nanoscale Solids and Organic Matter in Sustainable Water Management Systems

by

Xuanhao Wu

Doctor of Philosophy in Energy, Environmental and Chemical Engineering

Washington University in St. Louis, 2020

Professor Young-Shin Jun, Chair

To alleviate global water scarcity and improve public health, engineered water treatment and management systems have been developed for purifying contaminated water and desalinating brackish or ocean water. These engineered systems provide substantial amounts of potable water and lessen environmental concerns about the release of contaminated water. Wastewater treatment plants (WWTPs), water desalination plants (WDPs), and managed aquifer recharge systems (MARs) are three representative sustainable water management (SWM) systems. But the operation of all three poses two fundamental questions: (1) What is the fate of nanoscale solids (e.g., engineered nanomaterials, naturally occurring nanoparticles) in SWM systems and how will their physicochemical properties be changed when they encounter other water constituents, including cations and anions, reactive radical species, and organic matter? (2) How can our current knowledge enable more stable, scalable, and sustainable nanomaterial-based technologies for next-generation water treatment? To seek answers to these two questions, this dissertation focuses on the interface of chemistry and environmental engineering in 3 Systems: advanced oxidation processes (AOPs), managed aquifer recharge (MAR), and membrane distillation (MD), to (i)

pursue in-depth and systematic investigations on solid-liquid interfacial interactions between nanoparticles and different water constituents (e.g., organic matter) in both water treatment and subsurface systems, and (ii) to utilize the knowledge obtained from fundamental mechanistic studies to develop nature-inspired nanomaterial-based membranes for sustainable water treatment.

First, **System 1** focused on investigating the surface chemistry of engineered nanomaterials (ENMs) in advanced oxidation processes (AOPs). The widespread industrial applications of ENMs, such as titanium oxide, cerium oxide, and graphene-based carbon materials, have increased the likelihood of their release into aquatic systems, including engineered water treatment systems, where they can undergo surface chemistry changes induced by water components. Using cerium oxide nanoparticles (CeO_2 NPs) as representative ENMs, I examined on the effects of both reactive oxygen species (ROS) generated during UV/H_2O_2 treatment and dissolved organic matter (DOM) on the NPs' colloidal stability and surface chemistry. During UV/H_2O_2 treatment, superoxide radicals ($O_2^{\cdot -}$) dominated in neutralizing the surface charge of CeO_2 NPs, leading to decreased electrostatic repulsive forces between nanoparticles and a higher extent of sedimentation. DOM was found to complex with the CeO_2 NPs' surface and to act as a protective layer, making direct reactions between ROS and CeO_2 and their impacts on colloidal stability insignificant in a short reaction period. These new findings have important implications for understanding the colloidal stability, sedimentation, and surface chemical properties of CeO_2 NPs in aqueous systems where DOM and ROS are present.

Second, **System 2** aimed at investigating sustainable water management by managed aquifer recharge (MAR). To alleviate groundwater over-drafting, MAR has widely applied the engineered injection of secondary water sources into aquifers. However, groundwater chemistry changes induced by recharged water can significantly affect arsenic mobility in subsurface

reservoir systems. Elevated arsenic mobility can result from increased oxidative dissolution of arsenic-bearing sulfide minerals, including arsenopyrite (FeAsS). In **System 2**, the effects of different water components, such as abundant oxyanions (i.e., phosphate, silicate, and bicarbonate) and DOM (natural and effluent organic matter), on the arsenic mobility from FeAsS were studied. Suwannee River DOM (SRDOM) was found to decrease arsenic mobility in the short term (< 6 hours) by inhibiting arsenopyrite oxidative dissolution, but it increased arsenic mobility over a longer experimental time (7 days) by inhibiting secondary iron(III) (hydr)oxide precipitation and decreasing arsenic adsorption onto iron(III) (hydr)oxide. *In situ* grazing incidence small-angle X-ray scattering (GISAXS) measurements suggested that SRDOM decreased iron(III) (hydr)oxide nucleus sizes and growth rates. A combined analysis of SRDOM and other proteinaceous or labile DOM (alginate, polyaspartate, and glutamate) revealed that DOM with higher molecular weights caused more increased arsenic mobility. In addition to DOM, phosphate showed a time-dependent reversed effect on arsenic mobility. In the short term (6 hours), phosphate promoted the dissolution of FeAsS through monodentate mononuclear surface complexation, while over a longer experimental time (7 days), the enhanced formation of secondary minerals, such as iron(III) (hydr)oxide (maghemite, γ-Fe_2O_3) and iron(III) phosphate (phosphosiderite, $FePO_4 \cdot 2H_2O$), helped to decrease arsenic mobility through re-adsorption. Over the entire 7-day reaction, silicate increased arsenic mobility, and bicarbonate decreased arsenic mobility in our batch experiments. The phosphate system showed the highest amount and largest sizes of secondary precipitates among the three oxyanions (phosphate, silicate, and bicarbonate). These new observations advance our understanding of the impacts of DOM and oxyanions in injected water on arsenic mobility and on secondary precipitate formation during the geochemical transformation of arsenic-containing sulfide minerals in MAR.

In many natural and engineered aquatic systems, including MAR, acid mine drainage, and hydraulic fracturing systems, poorly crystalline iron(III) (hydr)oxide nanoparticles with sizes on the order of 1–10 nm form ubiquitously. In particular, newly formed iron(III) (hydr)oxide nanoparticles can precipitate heterogeneously on substrates, altering the substrate's surface reactivity and serving as powerful sorbents for heavy metals (Cu, Zn, Pb, or Cd), anionic contaminants (As, Cr), and organic pollutants. Yet the thermodynamic and kinetic parameters, i.e., the effective interfacial (α') and apparent activation (E_a) energies of iron(III) (hydr)oxide nucleation on earth-abundant mineral surfaces, have not been determined, which hinders accurate prediction and control of iron(III) (hydr)oxide formation and its interactions with other water constituents. Using a flow-through, time-resolved, and *in situ* grazing incidence small-angle X-ray scattering (GISAXS) method, the work experimentally obtained the interfacial and activation energies of iron(III) (hydr)oxide heterogeneous nucleation on quartz. GISAXS measurements successfully enabled the detection of the nucleation rates of iron(III) (hydr)oxides under different supersaturations (σ, by varying pH between 3.3−3.6) and temperatures (12 ºC−35 ºC). Quantifying these rates led to the quantification of α' and E_a, respectively, which were not previously available. The thermodynamic and kinetic parameters obtained benefit predictions using reactive transport models and controlling iron(III) (hydr)oxide's formation, as well as understanding its effects on pollutant's fate and transport in natural and engineered water systems.

Third, **System 3** was developed to apply mechanistic knowledge gained from studies of solid–water interfaces to the development of nature-inspired nanomaterial-based membranes for sustainable desalination. In remote or underdeveloped areas, it is challenging to produce clean water because centralized water treatment techniques require high energy input and management cost. To support resilient community development, water treatment techniques for these areas

should be sustainable in terms of material design and energy consumption. To address these needs, a new water treatment system based on membrane distillation (MD) has been developed. In this novel MD system, called photothermal membrane distillation (PMD), the membrane is embedded with light-absorbing photothermal materials that harvest solar energy and generate localized heat at the water-membrane interface to drive the MD process. To develop several PMD membranes with high solar conversion efficiency, polydopamine (PDA), which possesses the advantages of easy synthesis, good biocompatibility, and excellent light-to-heat conversion, was used as the photothermal material. First, a simple, stable, and scalable PDA-coated polyvinylidene fluoride (PVDF) membrane was synthesized for PMD. In a direct contact membrane distillation (DCMD) system under 0.75 kW/m^2 solar irradiation, the membrane showed a high solar energy conversion efficiency (45%) and a high water flux (0.49 $kg/m^2 \cdot h$) This performance was facilitated by the PDA coating, whose broad light absorption and outstanding photothermal conversion properties enabled a higher transmembrane temperature difference and increased the driving force for vapor transport. In addition, the excellent hydrophobicity achieved by fluoro-silanization gave the membrane great wetting resistance and high salt rejection. More importantly, the robustness of the membrane, stemming from the excellent underwater adhesion of the PDA, made it an outstanding candidate for real-world applications. Further, to increase the solar energy conversion efficiency, bacterial nanocellulose (BNC) was utilized to replace commercial PVDF membranes to decrease heat conductive loss from the photothermal layer to the cold distillate. A new photothermal membrane was thermally-engineered to incorporate a bilayered structure composed of two environmentally sustainable materials, PDA particles and BNC. The size-optimized PDA particles on the top layer maximized sunlight absorption and sunlight-to-heat conversion, and the bottom BNC aerogel insulating layer achieved high vapor permeability and low conductive heat loss. This

thermally engineered design enabled a permeate flux of 1.0 kg/m^2·h under 1 sun irradiation, and a record high solar energy-to-collected water efficiency of 68%, without ancillary heat or heat recovery systems. Moreover, the membrane showed effective bactericidal activity and was easily cleaned, increasing its lifespan. This study provides a new paradigm for using photothermal material incorporated in an aerogel to sustainably purify water. Using renewable solar energy, the PMD system can also provide decentralized desalination for remote or underdeveloped areas and can support resilient community development.

In summary, the work described in this dissertation offers an in-depth and mechanistic understanding of the fate of nanoscale solids (e.g., engineered nanomaterials and naturally occurring nanoparticles) in SWM systems in the presence of different water constituents (e.g., anions, reactive radical species, and organic matter). It also provides insights for designing more stable, scalable, and sustainable nanomaterial-based membranes for water treatment and desalination. Ultimately, this research will better define the chemistry of nanoscale solids and organic matter in water management systems, benefiting the design of next-generation water treatment systems that are environmentally safer and more sustainable.

Chapter 1. Introduction

1.1 Sustainable water management (SWM) systems

Water, "the bloodstream of the biosphere",[1] is crucial for the sustainability of both ecological systems and human societies. Although 70% of the Earth's surface is covered by water, only 3% is fresh water that can be used for human consumption.[2] In natural systems, the water cycle is well balanced, and fluctuations of environmental water stocks are reversible. However, when human water consumption and anthropogenic alteration of the cycle are plugged into the natural water cycle, this balance can be jeopardized. Groundwater depletion, chemical pollution of surface waters and ground waters, and eutrophication can lead the water cycle to be unbalanced, which in turn can affect human societies.[3-5] To solve these problems, the idea of sustainable water management (SWM) has been put into practice in the past twenty years.[6]

SWM implies matching the natural water cycle and engineered water use cycle with minimal damage and maximum mutual support. To achieve this goal, many SWM systems have been designed and built in recent years for water conservation and purification, such as wastewater treatment plants (WWTPs), managed aquifer recharge systems (MAR), and water desalination plants (WDPs). WWTPs are built to convert wastewater into effluents that can be returned to the water cycle with minimal environmental issues.[7-8] Traditional WWTP processes include preliminary treatment (screening), primary treatment (flocculation), and secondary treatment (activated sludge).[9] Tertiary treatment processes, including advanced oxidation processes (AOPs) and membrane filtration, have also been applied in recent years to further improve the quality of the effluent before it is discharged to the receiving environment.[10]

MAR is widely applied to address problems caused by over-drafting of groundwater.[11] MAR involves purposely injecting water into aquifers and permeable geological strata for subsequent recovery.[12] Examples of MAR sites in the United States include the Groundwater Replenishment System (GWRS) of Orange County Water District (OCWD) in California using reverse osmosis treated tertiary water,[13] the Sustainable Water Initiative for Tomorrow (SWIFT) project established by the Hampton Roads Sanitation District (HRSD) in eastern Virginia using activated carbon treated tertiary water,[14] and the Peace River Manasota Regional Water Supply Authority in Florida using activated carbon treated river water.[15] Established MAR sites have utilized different water resources, including storm water, surface water from other aquifers, and reclaimed water, which will lead to varied water chemistry in aquifers once recharged.[16-17] Among all these water resources, reclaimed water, such as the effluents from municipal WWTPs, has now been more widely used due to a lack of conventional fresh water resources.[18] Water desalination plants are another important surface water facilities that convert high saline water, abundant in the ocean and in brackish aquifers, to potable water.[19] More than 18,000 water desalination plants have been built around the world, producing 8.68×10^7 m^3 of water per day to serve 300 million people.[20-21] Current water desalination techniques include conventional thermal distillation such as boiling, reverse osmosis (RO), and membrane distillation (MD).[22] The MD process is gaining increasing attention due to its ability to operate at temperatures below boiling and pressures lower than needed for RO.[23-24]

1.2 Nanoscale solids and organic matter in SWM systems

1.2.1 Nanoscale solids and organic matter

Water sources, such as seawater, groundwater, river water, and wastewater, vary in the types and concentrations of their components. Water usually contains naturally formed

nanoparticles, organic matter (OM), and inorganic ions dissolved from minerals.[25] It also can contain anthropogenic substances, such as pesticides, organic solvents, pharmaceuticals, and inorganic engineered nanomaterials (ENMs).[26] In addition, the formation of natural nanoparticles can be altered by anthropogenic activities. The ENMs in SWM systems can be separated into two types: those released into the water source unintentionally during industrial processes, and those intentionally added to the SWM systems to increase the water production or treatment efficiency.

ENMs are increasingly prevalent in SWM systems due to their wide range of applications in consumer products and engineering applications. Common ENMs include silica (SiO_2), titania (TiO_2), iron (Fe_2O_3), zinc (ZnO), aluminum (Al_2O_3), cerium (CeO_2) oxides, nano-silver particles (AgNPs), and carbon nanotubes (CNTs).[27] Based on Limbach *et al*., up to 6 wt % of CeO_2 NPs was found in the secondary effluent of a model wastewater treatment plant, largely due to the influence of surface charge and stabilizing surfactants added in the preparation of nanoparticle products.[28] Gottschalk et al. predicted the concentrations of several ENMs in sewage treatment effluents to be in the range of 4 ng/L (fullerenes) to 4 μg/L (nano-TiO_2).[29] The fate and transport of ENMs in advanced water treatment systems (i.e., tertiary treatment) after their release in secondary effluents are still unclear. Furthermore, ENMs have also been widely used in SWM systems to increase the efficiency of water treatment processes.[30-32] Efforts are continuing to synthesize better nanomaterials or modify current ones to improve their performance in SWM systems. ***A better understanding of the solid-liquid interfacial chemistry of natural and engineered nanoscale solids in SWM systems is needed, which includes two aspects: We need to know their fate and transport, and we need to achieve better applications of nanomaterials in the presence of organic matter in SWM systems.***

Organic matter, or dissolved organic matter (DOM), is a highly complex and polydisperse mixture of different organic constituents, containing carboxylic groups, phenolic groups, and aromatic structures.[33] Natural organic matter (NOM) is composed of organic compounds from the remains of organisms such as plants and animals, and from their waste products in the environment.[34] NOM includes both humic and non-humic fractions. The humic fraction includes high molecular weight organic molecules such as humic acids (HA) and fulvic acids (FA).[35] These substances, plus tannic acid, are the major fraction of DOM in water.[36] After going through WWTPs, NOM plus soluble microbial products (SMPs, e.g., polysaccharides, proteins) derived from biological processes of wastewater treatment are the major fraction of the effluent organic matter (EfOM).[37] The concentration of DOM in wastewater secondary effluents can be high (~5 mg C/L), indicating the possibility of DOM entering into subsequent water management systems.[38]

Organic matter can affect the fate and transport of nanoparticles during SWM systems. DOM has been shown to adsorb onto the surface of nanoparticles, affecting their surface properties, sedimentation, and dissolution.[39] Electrostatic interaction, hydrophobic interaction, ligand exchange-surface complexation, and hydrogen bonding have all been proposed as major mechanisms by which DOM adsorbs onto nanoparticle surfaces.[40] DOM adsorption onto nanoparticles can neutralize or even reverse the surface charge of colloids,[41] and can also change the hydrophobicity/hydrophilicity properties of nanoparticles.[42] The charge reversal effects of DOM on the stabilization of nanoparticles, including silver nanoparticles, gold nanoparticles, and carbon nanotubes, have been reported previously.[43-45] For example, Delay et al. found that in the presence of DOM, the colloidal stability of silver nanoparticles increased due to the adsorption process, resulting in steric stabilization effects.[43] Keller et al. reported the stabilization effects of NOM on TiO_2, ZnO, and CeO_2 NPs.[46] However, the interactions between DOM and natural and

engineered nanoparticles under SWM-relevant conditions have been rarely studied. ***More information is needed to elucidate the effects of DOM on the surface chemistry and precipitation of nanoscale solids in SWM systems.***

1.2.2 Nanoscale solids and organic matter in advanced oxidation processes (AOPs)

In addition to traditional wastewater treatment methods, advanced oxidation processes (AOPs) have been utilized in the last few decades to achieve tertiary treatment of contaminants such as trace organic pollutants.[47] The nanoscale solids and organic matter that remain in the secondary effluents could enter AOPs.[28-29, 38] AOPs involve O_3, H_2O_2, UV light, and chlorine.[48] AOPs usually consist of two stages: (1) the formation of strong oxidants (e.g., hydroxyl radicals, ·OH) and (2) the reaction of these oxidants with organic or inorganic contaminants in water. For example, during treatment with UV/H_2O_2, ultraviolet radiation can cleave the O–O bond in H_2O_2 and generate ·OH.[49] The following chain reactions produce other powerful reactive oxygen species (ROS), including superoxide radicals ($O_2^{\cdot-}$).[50-52] The strong radicals produced in AOPs, including ·OH, Cl·, ClO·, $^1O_2$ and $O_2^{\cdot-}$, can potentially react with the nanoscale solids and organic matter passing through. During the reactions, the colloidal stability, aggregation, and surface properties of these nanoparticles can be changed. For example, fullerene nanoparticles (nC_{60}) and fullerol ($C_{60}(OH)_x$) have been shown to be capable of reacting with different reactive radicals under UV irradiation.[53-56] Wu et al. reported enhanced oxidation, altered aggregation and altered surface hydrophilicity of nC_{60} by free chlorine under UVA light irradiation.[56] However, the fate and transport of many widely used ENMs during AOPs-relevant conditions are still unclear. CeO_2 NPs are of particular interest because they have been widely used in industry[57] and can easily enter

AOPs.[28] ***More studies are needed to elucidate how AOPs, and especially the reactive species they generate, affect the colloidal stability, aggregation, and surface properties of CeO_2 NPs.***

On the other hand, AOPs can also change the nature and properties of organic matter, which can subsequently affect the interactions between the organic matter and nanoparticles. During AOPs, DOM can be partially oxidized, leading to reduced aromaticity, smaller molecular size, and decreased hydrophobicity.[58-60] In WWTPs, CeO_2 NPs can encounter DOM before entering into AOPs, where DOM might play a significant role in controlling their fate by changing the surface charge and hydrophilicity. After entering into AOPs, CeO_2 NPs and DOM can both react with reactive species such as ROS. The adsorption of DOM on nanoparticle surfaces can be altered by ROS, and the surface chemical properties of nanoparticles can be affected subsequently. ***To obtain a better understanding of the fate and transport of CeO_2 NPs during AOPs, the roles of ROS in changing DOM adsorption on CeO_2 NPs should be investigated.***

1.2.3 Nanoscale solids and organic matter in managed aquifer recharge (MAR)

MAR is an engineering solution to mitigate the problems caused by over-drafting of groundwater. Because MAR is being utilized on a large scale, the environmental sustainability of these operations has to be fully considered. After the source water is injected into underground aquifers, the aquifer sediments can act as a natural filter to remove contaminants such as pathogens, disinfection by-products, and trace organic chemicals, in a process which is called soil aquifer treatment (SAT).[61] However, recharge of reclaimed water can also lead to unfavorable soil−water interactions, causing the local minerals to release toxic metalloids, such as arsenic.[62] Dissolution of arsenic-bearing minerals, such as arsenian pyrite ($FeAs_xS_{2-x}$) and arsenopyrite (FeAsS), is a dominant mechanism for arsenic mobilization during MAR.[63] During the dissolution, secondary

mineral precipitates such as iron(III) (hydr)oxides can form. Iron(III) (hydr)oxides play a crucial role in the biogeochemical cycling of both natural and anthropogenic contaminants in MAR systems.[64] Iron(III) (hydr)oxide nanoparticles can precipitate on other rocks' surfaces via heterogeneous nucleation and can change the reactivity of the pre-existing rocks.[65] For example, iron(III) (hydr)oxide-coated quartz has a much higher reactive surface area and adsorption capability for pollutants than pure quartz.[66] Therefore, this heterogeneous nucleation can influence the fate and transport of pollutants. During heterogeneous iron(III) (hydr)oxide precipitation, heavy metals (e.g., Cu, Zn, Pb, Cd) and toxic anions (e.g., As, Cr) can be immobilized on mineral surfaces through adsorption and co-precipitation.[67] Due to the toxicity of arsenic and the capability of iron(III) (hydr)oxide nucleation to mitigate arsenic mobilization, it is important to obtain a better understanding of how the chemical composition of MAR water affect arsenic mobility and iron(III) (hydr)oxide precipitation from dissolved arsenic-bearing minerals. Previous efforts have been put to investigate the effects of abundant anions (e.g., chloride and nitrate) and cations (e.g., Fe^{3+}) on arsenic mobilization and secondary mineral precipitation from arsenopyrite dissolution.[62, 68] In addition to these water components, oxyanions, including phosphate, silicate, and bicarbonate, are also abundant in the injected reclaimed water. ***More information is needed to elucidate the geochemical effects of these different oxyanions in recharged water on arsenic release from arsenic-bearing sulfide minerals and the secondary mineral precipitation under conditions relevant to MAR.***

Because reclaimed water is often used as a MAR water source, the organic matter in treated wastewater can also enter into MAR. DOM has been shown to play important roles in changing the fate and transport of other organic chemicals or inorganic solids in MAR. For example, DOM can enhance the decay of trace organic chemicals by promoting soil biomass growth and serving

as a co-substrate in a co-metabolic transformation of these contaminants.[69] In addition, DOM can also influence the dissolution and precipitation of nanoscale solids during MAR. For example, the presence of adsorbed DOM can strongly inhibit the dissolution of corundum (Al_2O_3) under acidic (pH < 5) conditions.[70] The adsorption of DOM can also alter the surface charge and hydrophobicity of a mineral's surface, subsequently influencing the adsorption of other chemicals onto the mineral.[71-72] For secondary mineral formation, DOM can induce unique fractal aggregation of iron(III) (hydr)oxide nanoparticles. Moreover, the coexistence of arsenic and DOM can lead to the formation of two distinct particle size ranges of iron(III) (hydr)oxide: larger particles dominated by arsenic effects, and smaller particles dominated by DOM effects.[73] However, few studies have been done to show the effects of different moieties of DOM molecules, such as humic acid, fulvic acid, and SMPs, on arsenic mobilization and iron(III) (hydr)oxide formation from arsenic bearing minerals. ***Overall, because the mobilization of toxic ions can be a concern during MAR, better information is needed concerning the impact of the chemical components of the water source, such as different kinds of oxyanions and DOM, on the interactions between arsenic-bearing minerals and the water injected. This information will offer useful insight into water chemistry factors during pretreatment for MAR source water to minimize arsenic mobilization.***

1.2.4 Nanoscale solids and organic matter in membrane distillation (MD)

Membrane distillation (MD) is a promising membrane based thermally-driven desalination technique.[24] MD can be operated under lower temperatures than boiling, and at lower hydrostatic pressure than is required for pressure-driven membrane processes including reverse osmosis (RO).[23] Common MD configurations include direct contact membrane distillation (DCMD), air gap membrane distillation (AGMD), sweeping gas membrane distillation (SGMD), and vacuum

membrane distillation (VMD).[23] In DCMD, a hot solution (feed) contacts the feed side of the membrane, where evaporation takes place. The hot feed water and cold distillate on the two sides of a hydrophobic MD membrane provide a transmembrane temperature difference, which offers a vapor pressure difference and a driving force for vapor transport through the membrane while bulk feed water cannot pass through it.[74]

Many efforts have been made to create efficient membranes for MD. Among these membranes, a hydrophobic polymer, polyvinylidene difluoride (PVDF), has been widely used.[75] Modifications of PVDF membranes using different chemicals, including nanoparticles and organic chemicals, have been intensively studied in recent years. For example, Leitch et al. used trichlorosilane vapor to increase the hydrophobicity of PVDF.[76] Silver nanoparticles, TiO_2, SiO_2, $CaCO_3$, and clays have all been used to form nanocomposites on PVDF to make the membrane surface superhydrophobic (contact angle > 150°).[77-80] Graphene oxide and carbon nanotubes for MD membranes are also emerging subjects of lab scale investigations.[81] However, MD systems using these membranes can suffer from several inherent limitations, mainly the energy needed to heat the feed solution.[82] Conventional ways to heat the feed solutions include integrating MD into industrial processes that generate heat or using a solar absorber plate above the feed channel.[83-84] Localized heating using renewable sunlight at the surface of the feed membrane interface has been a new and interesting recent direction.[21, 85-86] In this case, the membrane generates heat photothermally at the feed water-membrane interface and provides driving force for vapor transport. A few quite recent studies have created solar-enabled photothermal membranes by utilizing advanced nanomaterials, such as black carbon and Ag nanoparticles.[21, 85] However, there is still ample of room for the development of solar-enabled photothermal membranes that achieve higher distillation efficiency while the environmental sustainability can be achieved. ***Effective and***

environmentally sustainable syntheses and modifications of solar-enabled photothermal MD membranes using advanced nanomaterials and organics are needed.

1.3 Knowledge gaps and significance

Based on the discussion above, there are three major knowledge gaps in the chemistry of nanoscale solids and organic matter in SWM systems. First, we need to know more about the effects of SWM system-relevant conditions on the fate and transport of nanoscale solids. Examples of such solids are iron(III) (hydr)oxide nanoparticles in MAR, and ENMs, including the commonly used CeO_2 NPs in AOPs. Second, we need more studies to elucidate the interactions between DOM and nanoscale solids in SWM systems. For AOPs particularly, elucidation of the effects of UV irradiation and ROS on the surface chemistry of ENMs and DOM adsorption on ENMs is needed. For MAR, more information is required regarding the impacts of the chemical composition of the water injected, such as abundant oxyanions and different moieties of DOM, on secondary iron(III) (hydr)oxide formation. Finally, the application of sustainable nanomaterials in SWM systems should be further developed. For instance, membranes that have long term stability, commercial scalability, and environmental sustainability, are needed for advancing emerging solar-enabled photothermal MD process.

The results of this work can help better understand solid-liquid interfacial interactions, including nanoparticle–ROS, nanoparticle–DOM, and nanoparticle–mineral surface. The results can also assist us evaluate both the fate and applications of nanomaterials in SWM systems. For example, for nanoparticles that might be toxic to ecological systems, such as CeO_2 NPs, systematic studies of their colloidal stability, aggregation, and surface property changes in SWM systems will provide information about whether further processes are needed to remove them from water. For

nanoparticles naturally formed in SWM systems, such as iron(III) (hydr)oxides nucleated during MAR, studies about the effects of water chemistry on their nucleation behavior can help us to predict and interpret their formation and further impacts on contaminant transport. Studying the applications of nanomaterials in solar-enabled photothermal MD can promote to build more energy efficient MD systems, save energy, and produce portable water for households. Overall, the information obtained from these studies will benefit the design of safer and more sustainable water management systems.

1.4 Research objectives and tasks

System 1: Fate and transport of cerium oxide nanoparticles (CeO_2 NPs) in advanced oxidation process (AOPs).

Objective 1 Elucidate the co-effects of natural organic matter and UV/H_2O_2 on the colloidal stability, sedimentation, and surface properties of CeO_2 NPs

Task 1.1 Investigate the effects of UV/H_2O_2 and NOM on the colloidal stability, sedimentation, and surface properties of suspended CeO_2 NPs in aqueous systems.

Hypothesis 1.1 NOM can enhance the stability of CeO_2 NPs by surface complexation and increasing the electrostatic force between nanoparticles; UV/H_2O_2 treatment process can decrease the colloidal stability of CeO_2 NPs by decreasing the electrostatic force between nanoparticles. $O_2^{\cdot-}$ will be a dominant ROS which can affect the colloidal stability of CeO_2 NPs than ·OH because it can be negatively charged at the pH value selected in this study,[87] thus it can alter the surface charge of CeO_2.

Significance 1.1 In WWTPs, CeO_2 NPs can encounter NOM before entering into AOPs, where NOM might play a significant role in controlling the colloidal stability of CeO_2 NPs. After entering into AOPs, UV/H_2O_2 process might change the stability and surface properties of CeO_2 NPs equilibrated with NOM. There are few studies on co-effects of UV/H_2O_2 and NOM on the stability of ENMs, including CeO_2 NPs. The results from this study will provide insights into the significant roles of UV/H_2O_2 and NOM in changing the fate and transport of selected ENMs simultaneously.

System 2: Arsenopyrite mineral dissolution and iron(III) (hydr)oxide nucleation during managed aquifer recharge (MAR).

Objective 2 Investigate the effects of different oxyanions (phosphate, silicate, and bicarbonate) and dissolved organic matter (humic acid, fulvic acid, alginate, polyaspartate, and glutamate) on arsenopyrite dissolution and secondary mineral precipitation.

Task 2.1 Investigate the effects of different oxyanions (phosphate, silicate, and bicarbonate) on arsenopyrite dissolution and secondary mineral precipitation and their mechanisms under MAR-relevant conditions.

Hypothesis 2.1 Complexation between phosphate and dissolved iron from arsenopyrite can decrease the local saturation ratio of FeAsS, thus enhancing its dissolution. Phosphate, silicate, and bicarbonate can increase arsenic mobilization compared with a control system, due to their adsorption competition with arsenic species on iron(III) (hydr)oxides. Phosphate will have the highest amount of secondary mineral precipitation among the three oxyanions, owing to the co-precipitation of iron phosphate and iron(III) (hydr)oxides.

Significance 2.1 The oxidative dissolution of arsenic-bearing minerals, such as arsenopyrite (FeAsS), has been proved to be a dominant mechanism for arsenic mobilization during MAR. Phosphate, bicarbonate, or silicate may compete with arsenic from adsorption sites on iron(III) (hydr)oxides mineral surfaces, and might subsequently impact arsenic mobilization during MAR. An improved understanding on the effects of oxyanions in the source water of MAR on arsenopyrite dissolution and secondary mineral precipitation can help improve the management of MAR and provide useful guideline for pretreatments of water source for the MAR.

Task 2.2 Examine the behavior of different components of DOM, humic acid, fulvic acid, alginate, polyaspartate, and glutamate on arsenopyrite dissolution and secondary mineral precipitation.

Hypothesis 2.2 Different components of DOM have varied molecular weight distributions and complexation capacities. Fulvic acid (FA) has higher negative charge than humic acid (HA), and a higher number of total binding groups, including carboxylic and phenolic sites.[88-90] Therefore, it will have a larger electrostatic attraction for positively charged iron ions and iron(III) (hydr)oxide nuclei, thus decreasing iron(III) (hydr)oxides precipitation. Arsenic mobility in HA will be higher than FA due to its larger molecular weight and a higher extent of adsorption competition with arsenic on iron(III) (hydr)oxides.

Significance 2.2 DOM can be present in the water injected for aquifer recharge. The effects of different fractions of DOM on arsenic mobility are still unknown. Thus, it is important to investigate which fraction of DOM will play a more significant role in changing the arsenic mobilization and secondary mineral precipitation of arsenopyrite.

Objective 3 Elucidate the kinetic and thermodynamic parameters for heterogeneous nucleation of iron(III) (hydr)oxides on an earth-abundant mineral surface (quartz).

Task 3.1 Investigate the effective interfacial energy and apparent activation energy for heterogeneous nucleation of iron(III) (hydr)oxides on quartz.

Hypothesis 3.1 The interfacial and activation energies for heterogeneous nucleation of iron(III) (hydr)oxides on quartz will be obtained by *in situ* GISAXS.

Significance 3.1 The quantification of interfacial and activation energies of iron(III) (hydr)oxides will result in a better prediction of iron(III) (hydr)oxide heterogeneous formation in natural and engineered water systems using reactive transport models.

System 3: Developing photothermal membrane distillation (PMD) using renewable solar energy and nature-inspired nanomaterials.

Objective 4 Develop novel nature-inspired photothermal membranes for solar-enabled photothermal membrane distillation.

Task 4.1 Modify commercial poly(vinylidene fluoride) (PVDF) membranes using polydopamine **(**PDA) and (tridecafluoro-1,1,2,2-tetrahydrooctyl) trichlorosilane (FTCS), and examine the performance of the synthesized membranes in solar-enabled photothermal membrane distillation.

Hypothesis 4.1 A photothermally-active PDA coating on PVDF will increase the light absorption capability of the membrane. FTCS will make the surface hydrophobic, based on silanization interactions, and make the membrane permeable only for vapor not liquid water.

Significance 4.1 Localized heating using sunlight at the surface of the feed membrane interface has been a new direction for recent MD developments. Modification of commercially available

membranes, such as PVDF, can save the cost and time of synthesizing new membranes for MD system. Use of biocompatible and bio-inspired photothermal materials, including PDA, will make the membrane environmental friendly and viable for sustainable desalination applications.

Task 4.2 Design a new bilayered photothermal membrane by using bacterial nanocellulose (BNC) as a supporting layer and PDA particles as the photothermal material, and examine the performance of the modified membrane in solar-enabled photothermal membrane distillation.

Hypothesis 4.2 BNC will work as a good platform for membrane distillation owing to its favorable mechanical strength, high vapor permeability, and low heat conductivity. A modified hydrophobic PDA particles loaded BNC bilayer aerogel membrane will have better light absorption, higher photothermal conversion, and more efficient vapor transport through the membrane than other PMD membranes.

Significance 4.2 Environmentally-friendly membranes for solar-enabled photothermal MD processes with high photothermal conversion efficiency can have promising applications in real systems. Current MD techniques require a large amount of electrical energy, which usually comes from conventional power infrastructures. Compared with the conventional MD process, localized photothermal PDA-BNC aerogel membrane can minimize the substantial power requirements to heat the feed water by external energy sources and increase the sustainability of the MD system. More importantly, its highly scalable and cost-effective materials are biodegradable materials, which are environmentally friendly and will not pose a threat to ecosystems.

1.5 Dissertation overview

To realize the objectives in the three systems described above, six tasks were completed, with each task corresponding to a chapter in later sections. **Task 1.1** addresses **System 1**. **Tasks 2.1**, **2.2**, and **3.1** investigate **System 2**. **Tasks 4.1** and **4.2** develop **System 3**. **Task 1.1** determined the fate and transport of cerium oxide nanoparticles (CeO_2 NPs) in AOPs. **Task 2.1** investigated the effects of abundant oxyanions on arsenopyrite dissolution and secondary precipitation. **Task 2.2** elucidated the effects of dissolved organic matter on arsenopyrite dissolution and secondary precipitation. **Task 3.1** quantified thermodynamic and kinetic parameters for heterogeneous nucleation of iron(III) (hydr)oxides on quartz. **Task 4.1** focused on the development of a photothermal polydopamine-coated PVDF membrane to achieve localized heating for a novel membrane distillation process. **Task 4.2** focused on the synthesis of a thermally-engineered polydopamine-bacterial nanocellulose bilayered membrane for more environmentally sustainable photothermal membrane distillation. **Figure 1.1** shows an overview of the dissertation, the three systems, and the tasks related for each system.

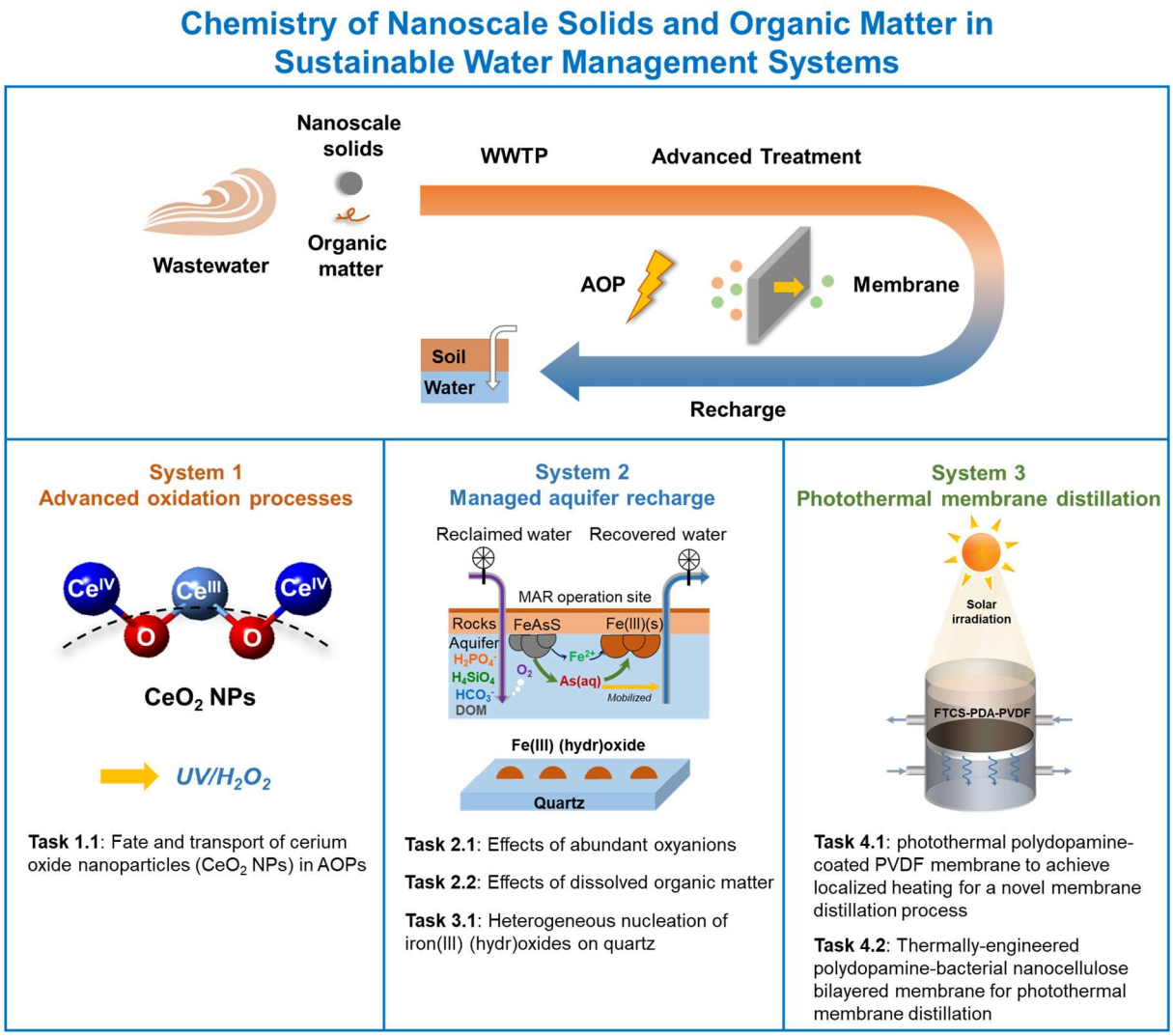

Figure 1.1 Overview of the dissertation. Three Systems include **System 1**: advanced oxidation processes (AOPs). Inset figure: reproduced from Ref.91 with permission.[91] Copyright 2018 Royal Society of Chemistry. **System 2**: managed aquifer recharge (MAR). Inset figure: reproduced from Ref.92 with permission.[92] Copyright 2019 American Chemical Society. **System 3**: photothermal membrane distillation (PMD). Inset figure: reproduced from Ref.93 with permission.[93] Copyright 2018 Royal Society of Chemistry. **Task 1.1 addresses System 1. Tasks 2.1, 2.2, and 3.1 investigate System 2. Tasks 4.1 and 4.2 aim on** System 3.

Chapter 2. Fate and transport of cerium oxide nanoparticles (CeO_2 NPs) during advanced oxidation process (AOPs)

Reproduced from Ref. 91 with permission from The Royal Society of Chemistry:[91] Wu, X., Neil, C. W., Kim, D., Jung, H., Jun, Y. S.* Co-effects of UV/H_2O_2 and Natural Organic Matter on the Surface Chemistry of Cerium Oxide Nanoparticles, *Environmental Science: Nano*, **2018**, 5, 2382-2393. DOI: 10.1039/c8en00435h. Copyright 2018 Royal Society of Chemistry.

Abstract

In **Chapter 2,** we focus on **System 1**, which concerns the fate and transport of cerium oxide nanoparticles in AOPs. The widespread industrial applications of cerium oxide (CeO_2) nanoparticles (NPs) have increased their likelihood of entering into natural and engineered aqueous environments. This study investigates the surface chemistry changes of CeO_2 NPs at pH 5.4 in the presence of both UV/H_2O_2 and natural organic matter (NOM). This condition can be relevant to advanced oxidation processes (AOPs). The results indicated that NOM stabilized CeO_2 NPs in solution through surface complexation between the COO^- functional groups of NOM and CeO_2 surfaces, reversing the zeta potential of CeO_2 from 39.5 ± 2.7 mV to -38.3 ± 1.8 mV. Exposure to the UV/H_2O_2 treatment reduced the colloidal stability of CeO_2 NPs, increased the percentage of Ce^{3+} on the surface from 17.8% to 28.3%, and lowered the zeta potential to close to neutral (3.8 ± 3.4 mV). With UV/H_2O_2 and NOM together, NOM coated on CeO_2 NPs acted as a protective layer, making the direct reactions between reactive oxygen species (ROS) and CeO_2 and their impacts on the colloidal stability to be insignificant in a short reaction period. During the UV/H_2O_2 treatment, the adsorption of superoxide radicals ($O_2^{\cdot-}$) dominated in neutralizing the surface charge of CeO_2, leading to decreased electrostatic repulsive forces between nanoparticles and a higher extent of sedimentation. These new findings provide important implications for understanding the colloidal stability, sedimentation, and surface chemical properties of CeO_2 NPs in aqueous systems where NOM and ROS are present.

2.1 Introduction

Cerium oxide (CeO_2) nanoparticles (NPs) have been widely utilized as an engineered nanomaterial (ENM) in industrial applications, such as chemical mechanical polishing (CMP) processes and catalytic processes.[57] The wide applications of CeO_2 NPs have led to a higher possibility of their existence in natural and engineered water systems. An estimated 10,000 metric tons of CeO_2 NPs were produced and used in 2010 globally, of which 1,100 metric tons went through wastewater treatment plants (WWTPs).[26] In WWTPs, the majority of CeO_2 NPs can be removed by activated sludge through adsorption or aggregation.[94-97] However, a significant fraction of the total CeO_2 NPs introduced to wastewater (up to 6–11 wt%) can still remain in the secondary effluents due to the influence of surface charge and stabilizing surfactants.[28, 94-97] The remaining CeO_2 NPs in the secondary effluents will then be released into subsequent engineered or natural water systems, in which they might form aggregates or remain colloidally stable, affecting the water quality and resulting toxicity to the biosphere.[98-100] Therefore, it is vital to improve our understanding of the fate and transport of CeO_2 NPs after their release in secondary effluents.

In addition to traditional wastewater treatment methods, advanced oxidation processes (AOPs) have been developed and utilized in last few decades to achieve tertiary treatment of contaminants.[47-48] Thus, the CeO_2 NPs remaining in secondary effluents could enter AOPs. UV-driven AOPs, such as the UV/H_2O_2 process, are widely used due to their high removal rate of contaminants and lower cost compared with ozone (O_3) treatment.[48, 101] During UV/H_2O_2, ultraviolet radiation cleaves the O–O bond in H_2O_2 and generates hydroxyl radicals (·OH).[49] Subsequent chain reactions produce other powerful reactive oxygen species (ROS), including superoxide radicals ($O_2^{\cdot-}$).[50-52] CeO_2 NPs have been shown to be able to react with ROS, and the

scavenging effect of CeO_2 on ROS has been reported in biological systems.[102] The redox cycles between the Ce^{3+} and Ce^{4+} oxidation states allow CeO_2 NPs to react catalytically with $O_2^{\cdot-}$/·OH, mimicking the behavior of two key antioxidant enzymes, superoxide dismutase and catalase.[103-106] Interestingly, no studies have examined the chemical reactions of CeO_2 NPs under combined UV/H_2O_2 conditions, which generates $O_2^{\cdot-}$ or ·OH from H_2O_2. The effects of these two ROS in affecting the surface chemistry, colloidal stability, and aggregation of CeO_2 NPs are thus still unknown. Furthermore, a better mechanistic understanding of the relationship between the surface chemistry change and the aggregation of CeO_2 NPs is needed.

Natural organic matter (NOM), one of the major components in wastewater,[37, 107-108] also reacts with CeO_2 NPs. Derived from the degradation of plants and microorganisms in natural systems, NOM enters into engineered water treatment processes, causing problems including unwanted disinfection byproducts and bacterial regrowth in water distribution systems.[109-110] The humic-substances of NOM can also be produced from biological processes in WWTPs, and constitute an important fraction of the total soluble microbial products (SMPs).[111-114] NOM is a complex mixture of different organic constituents, containing carboxylic groups, phenolic groups, and aromatic structures.[25] NOM can adsorb onto nanoparticles' surfaces through various mechanisms,[39-40, 115] altering the surface charge,[41] colloidal stability,[43-45, 116-117] and hydrophobicity/hydrophilicity of NPs.[42] Previous studies have reported the stabilization of CeO_2 NPs by NOM.[46, 118-119] The influence of NOM on the toxicity and bioaccumulation of CeO_2 NPs has also been examined recently.[120] In WWTPs, besides associating with microbial products,[94, 121] CeO_2 NPs can also form complexes with NOM. Due to NOM's notable presence in wastewater and its ability to stabilize CeO_2 NPs in an early stage of treatment processes, NOM can play an important role in controlling the fate and transport of CeO_2 NPs before their entrance into AOPs.

However, the detailed mechanism of NOM adsorption onto CeO_2 NPs surfaces and the influence of AOPs on the adsorption process have not been fully investigated.

As a major constituent of effluent organic matter (EfOM) in secondary effluents, NOM (~ 5 mg C/L) can also enter into tertiary treatment processes, including AOPs.[38, 122] During AOPs, NOM can be partially oxidized quickly,[123] leading to a decrease in its aromaticity,[60] molecular size,[59] and hydrophobicity.[58] After CeO_2 NPs-NOM complexes enter AOPs, the ROS generated could react with both CeO_2 NPs and NOM, possibly changing the NOM coating and the surface chemical properties CeO_2 NPs. The main goal of this study was to evaluate the co-effects of ROS and NOM on the colloidal stability, surface charge, and Ce^{3+}/Ce^{4+} oxidation state change of CeO_2 NPs during the UV/H_2O_2 process. Using a combination of qualitative and quantitative methods, the roles of two different ROS ($O_2^{\cdot-}$/·OH) were also elucidated. Our findings are crucial for understanding the impacts of NOM and ROS on the fate and transport of CeO_2 NPs in AOPs.

2.2 Experimental section

2.2.1 Chemicals and materials

Reaction solutions were prepared using sodium chloride (NaCl, ACS grade, BDH, PA), hydrogen peroxide (H_2O_2, 30%, ACS grade, BDH, PA), 2-methyl-2-propanol (tertbutyl alcohol, t-ButOH, purity > 99.5%, Sigma Aldrich, MO), superoxide dismutase (SOD, Cu/Zn-SOD, ≥ 90%, Sigma Aldrich, MO), and ultrapure deionized (DI) water (resistivity > 18.2 MΩ-cm). To prepare CeO_2 NPs suspended solutions, purchased CeO_2 NPs (Sigma Aldrich, MO) were used to better represent commercially available engineered NP−environmental systems. CeO_2 NPs were characterized using high resolution transmission electron microscopy (HRTEM, JEOL 2100F) (**Figure 2-S1A** and **2-S1B** in Supporting Information of Chapter 2) and wide angle X-ray

diffraction (WAXRD) in sector 11-ID-B at the Advanced Photon Source (APS) at Argonne National Laboratory (IL, USA) (**Figure 2-S1C**). Suwannee River NOM (SRNOM, 2R101N, RO isolation), purchased from the International Humic Substances Society, was the NOM source. Details on the preparation of SRNOM stock solutions and the characterization of SRNOM are in the 2-SI (**Table 2-S1**).[124] For all experiments, 10 mM of NaCl solution was added to ensure consistent ionic strength (IS). The initial pH of all solutions, 5.4 ± 0.2, was chosen for two reasons. First, this was the pH of the system after adding NaCl, thus reducing the effects of pH adjustment on the ionic strength. Second, acidic conditions (pH 3–6) are preferred in most established UV/H_2O_2 systems due to their higher efficiency in producing ROS.[125] A high intensity UVA lamp (Ultra-Violet Products Ltd., Black ray B-100A, Upland, CA) was the UV source. The irradiance spectrum of the UVA light source is provided in the SI (**Figure 2-S2**).

2.2.2 Colloidal CeO_2 NPs and aqueous chemistry measurements

To quantify changes in the colloidal stability and the sedimentation of CeO_2 NPs, UV−Vis spectroscopy (Thermo Fisher Scientific Inc., Evolution 60S, Waltham, MA) was utilized to measure the absorbance of CeO_2 at a wavelength of 305 nm, where the absorbance is proportional to CeO_2 concentration.[126] Six different systems were tested for both light and dark conditions: CeO_2 NPs-only system (light/dark); CeO_2 NPs with 3 and 30 mM H_2O_2 (light/dark); CeO_2 NPs with NOM (light/dark); and CeO_2 NPs with 3 and 30 mM H_2O_2 with NOM (light/dark) (**Table 2-S2**). Triplicate experiments were conducted for each condition. The CeO_2 NPs-only system in the dark was called as the control system. For each reaction condition, 50 mg/L CeO_2 NP dispersions were created in 50 mL test tubes and ultrasonicated for 1 hr before reaction, using an ultrasonic bath (model no. FS6, Fisher Scientific). The H_2O_2 concentrations chosen in this study have been

commonly used, both in industrial UV/H_2O_2 systems and in previous studies.[127-128] The concentration of NOM was 3.3 ± 0.2 mg C/L, confirmed by a non-purgeable organic carbon measurement (NPOC, Shimadzu TOC Analyzer). This concentration of NOM is in the range of NOM concentrations commonly found in wastewater effluents.[38, 122] Aliquots of CeO_2 NPs dispersions were taken from the supernatant at 0, 20, 40, 60, 80, 100, and 120 minutes during particle sedimentation experiments. Percentages of suspended CeO_2 NPs were obtained by normalization using the initial concentrations. The detailed experimental design for the UV-Vis study is available in the 2-SI (**Figure 2-S2**).

Zeta potential (ζ) values of CeO_2 NPs were measured using a Zetasizer (Malvern Instruments Inc., Nano ZS, Westborough, MA) with capillary Zeta cells (DTS1070) at reaction time points of 1 hr and 2 hrs. The isoelectric point of CeO_2 NPs was measured to be around pH 6.9 (**Figure 2-S1D** and **Table 2-S3**). At our pH conditions, the unreacted CeO_2 NPs should be positively charged. To measure the hydrodynamic particle diameter of CeO_2 NPs, the Zetasizer was also used with dynamic light scattering (DLS) cells (DTS0012, Malvern Instrument Inc., MA). HRTEM was used to compare the morphology of CeO_2 NPs reacted under different conditions. The pH change during the reaction period was also monitored (**Table 2-S4**). To test CeO_2 NPs dissolution during the reactions, inductively coupled plasma optical emission spectrometry (ICP-OES) was applied. Reactions were prepared as described for sedimentation experiments. At 1 hr and 2 hrs, samples were ultracentrifuged, filtered, and acidified to be measured by ICP-OES. Detailed experimental information about the dissolution test is provide in the ESI (**Table 2-S5**). Ion chromatography (IC) was incorporated to test the decomposition of NOM during the reaction with CeO_2 and UV/H_2O_2 (**Figure 2-S5**).

2.2.3 Oxidation state determination using X-ray photoelectron spectroscopy (XPS)

X-ray photoelectron spectroscopy (XPS, PHI 5000 VersaProbe II, Ulvac-PHI with monochromatic Al Kα radiation (1486.6 eV)) was utilized to quantify the oxidation states of cerium (Ce 3d) before and after reaction with UV/H_2O_2 and NOM, and to observe the adsorption of NOM as represented by carbon (C 1s) peaks. While accurate quantitative comparison of C 1s peaks is not possible, the relative quantitative change can be determined. To prepare the samples, after 2 hrs reaction, CeO_2 NP solutions were centrifuged at 5000 rpm for 15 minutes (Centrifuge 5804, Eppendorf Inc.), and the supernatants were removed, leaving only the CeO_2 NP sediment in the test tube. The sediment was left to dry in an anaerobic chamber to prevent any further oxidation by oxygen in the air. The detailed sample preparation for XPS is available in the ESI (**Figure 2-S2**). For XPS data analysis, the binding energies were referenced to the C 1s line at 284.8 eV. The reference binding energy peaks for Ce^{3+} are at 885.0 (v′) and 903.5 (u′) eV, and the reference peaks for Ce^{4+} are at 907.2 (u′′), 900.6 (u), 897.9 (v′′′), 888.3 (v′′), and 889.1 (v) eV.[129-130] The XPS reference binding energies, absolute values of areas for each peak, and calculated percentages for oxidation states/bonds for Ce 3d and C 1s under different reaction conditions are provided in **Tables 2-S6** and **2-S7**. **Equation 2.1** was used to calculate the Ce^{3+} percentage on the surface, which was the sum of the Ce^{3+} peak areas over the total area.[131-132]

$$Ce^{3+}\% = \frac{A_{u'}+A_{v'}}{A_{u''}+A_{u'}+A_{u}+A_{v'''}+A_{v''}+A_{v'}+A_{v}} \quad . \qquad \textbf{(eq 2.1)}$$

2.2.4 NOM adsorption measurements using attenuated total reflection Fourier transform infrared (ATR-FTIR) spectroscopy and contact angle measurements

Attenuated total reflection Fourier transform infrared (ATR-FTIR; Thermo Scientific Nicolet Nexus 470 spectrometer equipped with a diamond crystal) spectroscopy was used to analyze the adsorption of NOM on the CeO_2 NPs surfaces. The sample preparation process for the ATR-FTIR was the same as that for XPS analysis (**Figure 2-S2**). An average of 400 scans with a resolution of 4 cm^{-1} was used. To determine the change in the extent of hydrophilicity/hydrophobicity of CeO_2 NPs before and after reaction with NOM and UV/H_2O_2, we conducted replicate contact angle measurements using CeO_2 NP-sputtered Si wafers. CeO_2 NP-sputtered Si wafers were prepared using a method introduced in our previous study.[56] Reaction solutions were prepared in the same way as for the sedimentation experiment, except that CeO_2 NP-sputtered Si wafers (5 mm × 5 mm) were put into the solutions instead of CeO_2 powders. After reaction, deionized water was dropped onto the dried wafer surface, and a contact angle analyzer (Phoenix 300, Surface Electro Optics Co. Ltd) was used to measure contact angles.

2.2.5 ROS scavenging experiments using UV-Vis spectroscopy and X-ray photoelectron spectroscopy (XPS)

To better understand the roles of two different ROS, the hydroxyl radical (·OH) and superoxide radical ($O_2^{\cdot-}$), in affecting the sedimentation and surface properties of CeO_2, experiments using ROS scavengers were conducted. CeO_2 NPs dispersions were prepared as described in the sedimentation experiments. Tertbutyl alcohol (t-ButOH, 0.1 M) and superoxide dismutase (SOD, 0.5 μM) were used as scavengers of ·OH and $O_2^{\cdot-}$, respectively, based on **equations 2.2–2.4**.[133-134]

$$(CH_3)_3COH + \cdot OH \rightarrow \cdot CH_2(CH_3)_2COH + H_2O \quad \textbf{(eq 2.2)}$$

$$Cu^{2+} - SOD + O_2^{\cdot -} \rightarrow Cu^{+} - SOD + O_2 \quad \textbf{(eq 2.3)}$$

$$Cu^{+} - SOD + O_2^{\cdot -} + 2H^{+} \rightarrow Cu^{2+} - SOD + H_2O_2 \quad \textbf{(eq 2.4)}$$

Once the samples were reacted in the presence of the scavengers, UV−Vis spectroscopy was utilized to measure the absorbance of CeO_2 NPs at 305 nm. Then, X-ray photoelectron spectroscopy (XPS) was used for characterizing surface oxygen species on the CeO_2 NPs surface in the presence of different ROS.

2.3 Results and discussion

2.3.1 Effects of UV/H_2O_2 and NOM on the colloidal stability of CeO_2 NPs

The colloidal stability of CeO_2 NPs in the presence of UV/H_2O_2 decreased significantly (**Figure 2.1A**). Specifically, UV-Vis spectrometer results showed that, after 2 hrs, the concentration of CeO_2 NPs in the supernatant was much lower with UV and H_2O_2, than the control group, which contained only CeO_2 NPs. This indicates that UV/H_2O_2 exposure decreased the colloidal stability of CeO_2 NPs. For example, 76% of the initial CeO_2 NPs remained in the supernatant in the control group after 2 hrs, while only 24% of the initial CeO_2 NPs remained colloidally stable in the presence of UV and 30 mM H_2O_2. In the presence of NOM, almost all the CeO_2 NPs remained colloidally stable in the supernatant, indicating that NOM stabilizes CeO_2 NPs. The difference in NP sedimentation due to the presence of UV/H_2O_2 and NOM could also be observed visually (**Figure 2-S3**). Moreover, as shown in Fig. 1A, when UV/H_2O_2 was added together with NOM, the CeO_2 NPs remained colloidally stable during the first 40 minutes, and after that, they started to settle, with 53% of the initial CeO_2 NPs remaining colloidally stable after 2 hrs. The settlement velocity was close to that of CeO_2 NPs with UV/H_2O_2, while faster than the

settlement velocity of the CeO_2 NPs only system. These observations suggest that there was reaction between CeO_2 NPs and UV/H_2O_2 after 40 minutes, but before 40 minutes, this reaction was not significant. IC results (**Figure 2-S5**) show that NOM itself also participated in redox reactions with UV/H_2O_2 and decomposed rapidly into smaller molecules (i.e., acetate) during the first 40 minutes. Considering the results from both the UV-Vis and IC measurements, in the first 40 minutes, ROS generated from UV/H_2O_2 reacted mainly with NOM, and after that, ROS reacted with CeO_2 NPs to promote their aggregation. Thus, we infer that NOM on CeO_2 NPs acted as a protective layer, which made the reactions between CeO_2 NPs and ROS insignificant in a shorter reaction period.

To understand the effects of UV/H_2O_2 and NOM on the particle aggregate sizes and surface charges of CeO_2 NPs in the supernatant, the zeta potentials (ζ) and hydrodynamic particle sizes were measured (**Figure 2.1B and 2.1C**). The zeta potential for stable dispersions of unreacted CeO_2 in DI water with 10 mM NaCl at pH 5.4 was 39.2 ± 3.4 mV. For the CeO_2-only system, the zeta potential was 38.6 ± 5.1 mV after 2 hr settlement. The presence of UV and 30 mM H_2O_2 decreased the absolute value of the zeta potential to 3.8 ± 3.4 mV after 2 hrs, while NOM reversed the zeta potential to -38.3 ± 1.8 mV. The lowered absolute value of the zeta potential in the presence of UV/H_2O_2 resulted in weaker electrostatic repulsive forces between CeO_2 NPs, making it easier for them to aggregate and then settle, which can explain the decreased colloidal stability of CeO_2 NPs from the UV-Vis results. However, in the presence of NOM, the absolute value of the zeta potential was close to that of unreacted CeO_2 NPs, thus maintaining the strong electrostatic repulsive forces and resisting their aggregation. When both NOM and UV/H_2O_2 were present in a system, the zeta potential was altered to -12.9 ± 2.1 mV after 2 hrs (not -38.3 ± 1.8 mV), suggesting that the effect of the NOM on the CeO_2 NPs had been changed by UV/H_2O_2.

Hydrodynamic size also provided a useful clue. The hydrodynamic particle size was 140.7 ± 53.0 nm for stable dispersions of unreacted CeO_2 in DI water at pH 5.4. After 2 hrs, for the CeO_2 NPs control system, the hydrodynamic size was 460 ± 60 nm. UV/H_2O_2 treatment increased the size to 5,574 ± 253 nm, while NOM kept the size at 175 ± 39 nm. When NOM and UV/H_2O_2 were present together, the size still increased to 3,276 ± 122 nm after 2 hr reaction. The results from the zeta potential and particle size analyses all indicated that NOM stabilized CeO_2 NPs at first, and then the reaction between NOM and UV/H_2O_2 eventually destabilized CeO_2 NPs to form larger aggregates and settle. The zeta potential and hydrodynamic particle size values for all the conditions are also in the 2-SI (**Table 2-S3**).

CeO_2 NPs morphology change was monitored by HRTEM (**Figure 2.2**). Compared with the CeO_2 control system (**Figure 2.2A**), UV/H_2O_2 treatment resulted in forming large aggregates, helping the particles to settle (**Figure 2.2B**). In the presence of NOM (**Figure 2.2C**), however, CeO_2 NPs were observed to be coated with NOM, which helped to keep particles separate from each other and inhibited aggregation. Similar coatings of NOM on other nanoparticles, such as zero-valent iron, mercuric sulfide, and carbon nanotubes, have been reported before.[135-137] With UV/H_2O_2 and NOM together, after 2 hrs, the adsorbed NOM was decomposed into smaller molecules (**Figure 2.2D**), and CeO_2 NPs were bonded closely to each other to form aggregates.

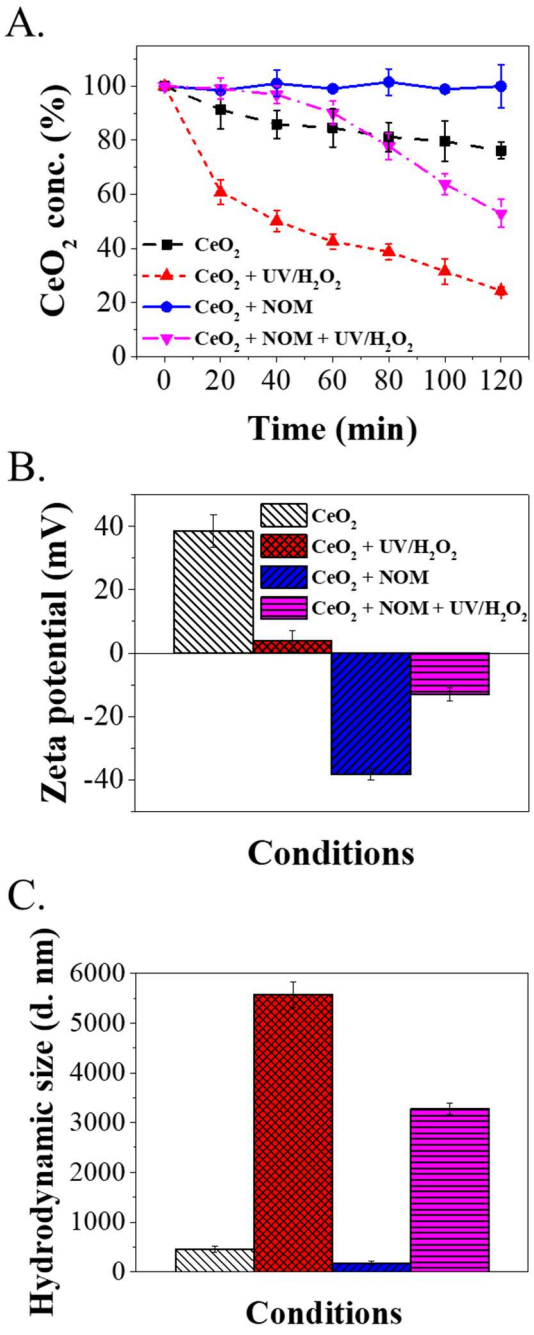

Figure 2.1 (**A**) UV-Vis data showing the sedimentation of CeO_2 NPs at 10 mM NaCl and pH 5.4 in the presence and absence of UV/H_2O_2 (30 mM) and NOM (3.3 ± 0.2 mg C/L). The percentages were obtained by normalizing the suspended nanoparticle concentration by the initial concentration. (**B**) Zeta potential results for CeO_2 NPs in the presence and absence of UV/H_2O_2 (30 mM) and NOM. The zeta potential for stable dispersions of unreacted CeO_2 in DI water with 10 mM NaCl at pH 5.4 was 39.2 ± 3.4 mV. (**C**) Hydrodynamic particle size values for CeO_2 NPs in the presence and absence of UV/H_2O_2 (30 mM) and NOM. The error bars represent the standard deviation from triplicate experiments. Only representative

conditions are presented here, and other detailed results are provided in the 2-SI (**Figure 2-S4** and **Table 2-S2**).

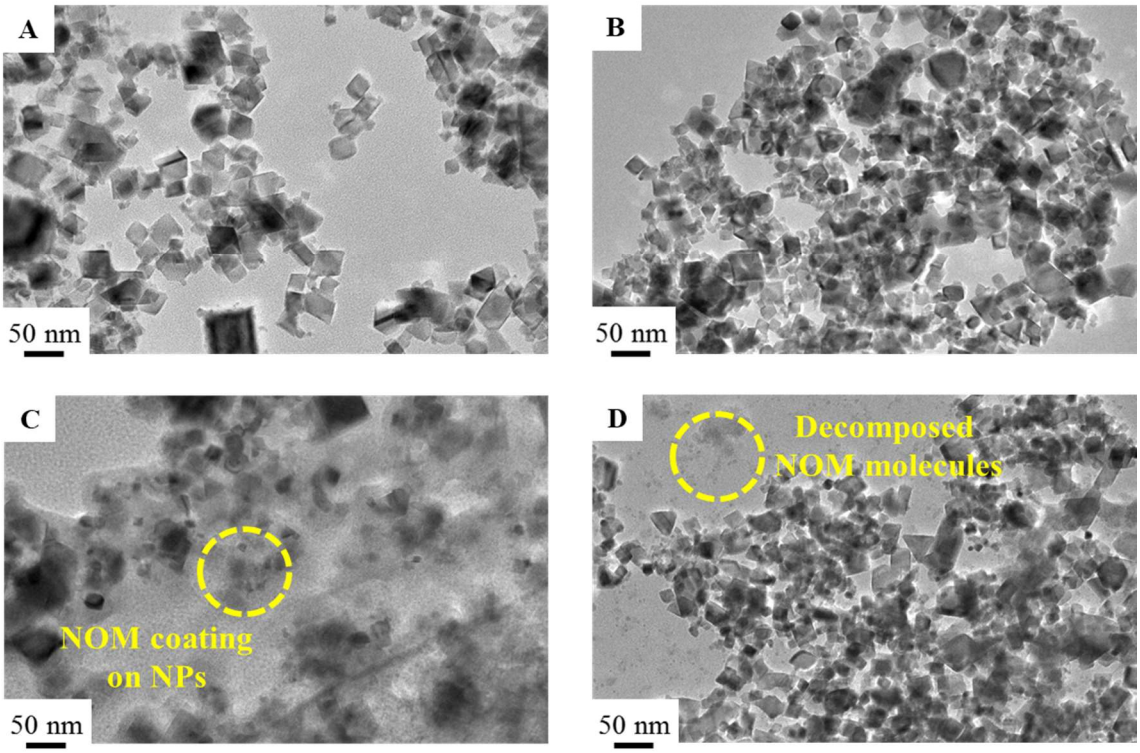

Figure 2.2 Representative TEM images for CeO_2 NPs with 10 mM NaCl at pH 5.4 after 2 hrs. (**A**) CeO_2 control, (**B**) CeO_2 with UV/H_2O_2, (**C**) CeO_2 with NOM, and (**D**) CeO_2 with NOM and UV/H_2O_2.

2.3.2 Oxidation state change of CeO_2 NPs

We hypothesized that the promoted sedimentation of suspended CeO_2 NPs exposed to UV/H_2O_2 was due to redox reactions between CeO_2 and ROS generated from UV/H_2O_2. Thus, to observe changes in the Ce oxidation states on the nanoparticle surface after 2 hrs, XPS was conducted (**Figure 2.3A**). The Gaussian−Lorentzian curve-fitting of XPS spectra shows that CeO_2 NPs in this study had both Ce^{3+} and Ce^{4+} on the surface, while Ce^{4+} was the dominant oxidation state. Surface Ce for unreacted CeO_2 consisted of 82.2% Ce^{4+} and 17.8% Ce^{3+}. After reaction with UV/H_2O_2 for 2 hrs, surface Ce contained 71.7% Ce^{4+} and 28.3% Ce^{3+}, indicating that UV/H_2O_2 process reduced Ce^{4+} on the CeO_2 surface partially to Ce^{3+} and increased the Ce^{3+}/Ce^{4+} ratio. Based

on ICP-OES data, the dissolved Ce concentration did not increase within an experimental error range in the presence of UV/H_2O_2, which indicates that the newly produced Ce^{3+} stayed on the surface of the CeO_2 NPs, rather than dissolving into solution (**Table 2-S5**). NOM itself did not change the percentage of Ce^{3+} much, but the presence of both NOM and UV/H_2O_2 still increased the percentage of Ce^{3+} to 21.8%. As shown from XPS, in the presence of UV/H_2O_2, the redox reactions between CeO_2 and ROS resulted in an increased Ce^{3+}/Ce^{4+} ratio on the CeO_2 NPs' surfaces. This observation can partially explain the decreased surface charge of CeO_2 NPs that we observed, which can also result from other factors, such as the adsorption of negatively charged anions, discussed in section 3.4. Recent studies have shown that the redox state ratio of Ce^{3+}/Ce^{4+} on a CeO_2 surface can change the direction of the redox reaction between CeO_2 and ROS, but the fundamental mechanism behind the redox state ratio-dependent properties of CeO_2 in the presence of ROS is still elusive.[105-106, 138-141] With a high Ce^{3+}/Ce^{4+} ratio, Ce^{3+} on the CeO_2 surface can be oxidized by $O_2^{\cdot-}$ to form Ce^{4+}, which is the SOD mimetic activity of CeO_2.[105, 139-141] On the other hand, with a low Ce^{3+}/Ce^{4+} ratio, H_2O_2 can reduce Ce^{4+} to Ce^{3+} with the oxidation of H_2O_2 to molecular O_2 and the production of protons, which is the catalase mimetic activity of CeO_2.[106, 138, 141] Similarly, here we report that Ce^{4+} can also be reduced to Ce^{3+} with a low Ce^{3+}/Ce^{4+} ratio under the UV/H_2O_2 condition, in which a pH decrease was also observed (**Table 2-S4**). This decrease reflects protons being produced from the oxidation of H_2O_2 or ·OH (**eq 2.5–2.7**).[106, 138]

$$2Ce^{4+} + H_2O_2 \rightarrow 2Ce^{3+} + O_2 + 2H^+ \quad \textbf{(eq 2.5)}$$

$$H_2O_2 \xrightarrow{UV} 2 \cdot OH \quad \textbf{(eq 2.6)}$$

$$2Ce^{4+} + 2 \cdot OH \rightarrow 2Ce^{3+} + O_2 + 2H^+ \quad \textbf{(eq 2.7)}$$

A systematic study of the effect of the Ce^{3+}/Ce^{4+} ratio on redox chemistry between CeO_2 NPs and ROS is an interesting future direction.

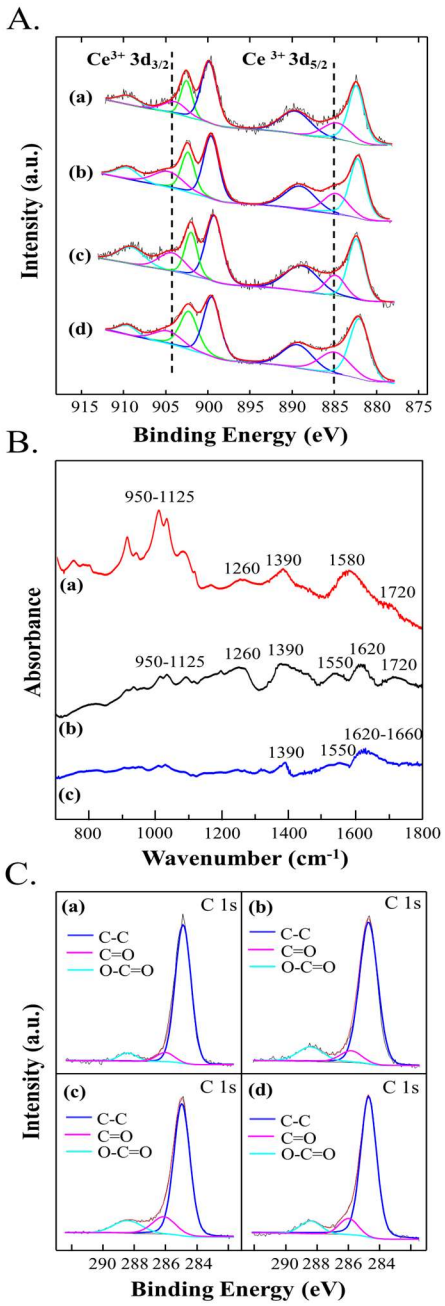

Figure 2.3 (**A**) XPS spectra of Ce 3d obtained from CeO_2 sedimentation with 10 mM NaCl at pH 5.4 after 2 hrs reaction. (**a**) CeO_2 control, (**b**) CeO_2 with UV/H_2O_2, (**c**) CeO_2 with NOM, and (**d**) CeO_2 with NOM and UV/H_2O_2. Dotted lines show the position of two different Ce^{3+} peaks: Ce^{3+} $3d_{5/2}$ and Ce^{3+} $3d_{3/2}$. The red curves are the Gaussian−Lorentzian curve-fitting of XPS spectra. The variation of calculated Ce^{3+} and Ce^{4+} percentages from the fitting of at least triplicate samples was within ±1%. (**B**) FTIR spectra of CeO_2 sedimentation with 10 mM NaCl at pH 5.4 after 2 hrs reaction. (**a**) NOM, (**b**) NOM reacted with CeO_2, (**c**) NOM reacted with CeO_2 and UV/H_2O_2. The spectra of NOM with CeO_2 and NOM with CeO_2/UV/H_2O_2 (**b** and **c**) were obtained by subtracting the spectrum of pure CeO_2 from their measured spectra. (**C**) XPS spectra of C 1s obtained from CeO_2 sedimentation with 10 mM NaCl at pH 5.4 after 2 hrs reaction. (**a**) CeO_2 control, (**b**) CeO_2 with UV/H_2O_2, (**c**) CeO_2 with NOM, and (**d**) CeO_2 with NOM and UV/H_2O_2.

2.3.3 NOM adsorption on CeO_2 NPs surface

ATR-FTIR provides valuable information on the structural and functional properties of NOM molecules and their adsorption onto the CeO_2 NPs surface.[40] ATR-FTIR spectrum of unreacted CeO_2 NPs showed peaks around 585, 720, 1350, 1570, 1630, and 3400 cm^{-1}. These peaks were assigned as hydroxyl residues and bridged, bidentate, and monodentate carbonates adsorbed on the surface (**Figure 2-S6**).[142-144] **Figure 2.3B** shows the ATR-FTIR spectra of (**a**) NOM, (**b**) NOM adsorbed on CeO_2, and (**c**) NOM adsorbed on CeO_2 in the presence of UV/H_2O_2. The spectra **b** and **c** were obtained by subtracting the spectrum of pure CeO_2 from the spectrum of CeO_2 with NOM or NOM/UV/H_2O_2. Several peaks in the spectrum a can be identified as specific functional groups of NOM, including 1720 cm^{-1} (C–O stretching of COO^-), 1580 cm^{-1} (asymmetric stretching of COO^-), 1390 cm^{-1} (symmetrical stretching of COO^-), 1260 cm^{-1} (phenolic O–H), and 950–1125 cm^{-1} (C–O stretching) (**Figure 2.3B**, **a**).[40, 145-147] For the NOM used, the pK_{a1} for carboxylic groups was 4.16, and the pK_{a2} for phenolic groups was 9.99,[124] thus the carboxylic portion of NOM would be partly deprotonated at pH 5.4, existing as COO^-, and the phenolic groups would mainly exist as O–H. The spectrum of the sample containing CeO_2 and NOM showed peaks at 1720, 1620, 1550, 1390, 1260, and 950–1125 cm^{-1}, confirming the adsorption of NOM on the CeO_2 surfaces (**Figure 2.3B**, **b**). Peaks at 1720 and 1390 cm^{-1} indicated the adsorption of COO^- functional groups of NOM on the CeO_2 surface. In spectrum **b**, peak 1550 cm^{-1} could be identified as the asymmetric stretching of COO^- complexed with the CeO_2 surfaces (CeO_2≡) (**eq 2.8**), while it shifted a bit towards lower wavenumbers compared with the carboxylate asymmetric vibrational frequencies for other metal–carboxylate complexes.[146, 148] The peak at 1620 cm^{-1} represents the adsorption of aromatic C=C or conjugated carbonyl C=O.[33, 40, 147] The peak around 1260 cm^{-1} in

the spectrum **b** indicates the complexation between phenolic O–H functional groups of NOM and CeO_2 surfaces (CeO_2≡) (**eq 2.9**).

$$CeO_2 \equiv OH_2^+ + \ ^-OOC-NOM-COO^- \rightarrow CeO_2 \equiv OOC-NOM-COO^- + H_2O \qquad \textbf{(eq 2.8)}$$

$$CeO_2 \equiv OH \ + \ HO-NOM-OH \ \rightarrow \ CeO_2 \equiv O-NOM-OH \ + \ H_2O \qquad \textbf{(eq 2.9)}$$

From eq. 8, after the adsorption of NOM, the COO^- functional groups of NOM reversed the surface charge of CeO_2 NPs from positive to negative, which was observed through zeta potential measurements. When adding UV/H_2O_2 together with NOM, the peaks around 1720, 1550, 1390, 1260, and 950–1125 cm^{-1} all decreased, indicating that UV/H_2O_2 decomposed NOM adsorbed on the CeO_2 surface by breaking the COO complexation between NOM and the CeO_2 surface (**Figure 2.3B**, **c**). The remaining small intensity of these peaks could be the adsorption of NOM decomposition products such as aldehydes and carboxylic acids on the CeO_2 surface,[59-60] while the peak expansion around 1620–1660 cm^{-1} could result from the adsorption of hydroxyl-like groups produced after reaction with UV/H_2O_2.[142] XPS data for C 1s gives further evidence of NOM adsorption on CeO_2 (**Figure 2.3C**). Three peaks were used to fit the C 1s spectra: C–C (284.8 eV), C=O (285.6 eV), and O–C=O (288.8 eV).[147] Compared with unreacted CeO_2 (**Figure 2.3C**, **a**), the presence of NOM increased the total percentage of C=O and O–C=O on the CeO_2 surface from 14.0% to 36.3%, while the addition of UV/H_2O_2 into the NOM system decreased the percentages of C=O and O–C=O back to 23.0%. Detailed XPS reference binding energies for C 1s are available in the ESI (**Table 2-S6**).

To investigate the effects of NOM adsorption on the hydrophobicity/hydrophilicity of the CeO_2 NPs surface, the contact angles of a DI water drop on CeO_2-sputtered Si wafer surfaces were measured (**Figure 2-S7A**). For an unreacted CeO_2-sputtered Si wafer, the contact angle was 82.2º ± 2.2º (**Figure 2-S7A**, **i**), and after 2 hrs wetting using a 10 mM NaCl solution, the contact angle

decreased to 78.2º ± 3.6º (**Figure 2-S7A**, **ii**). After reaction with NOM, the contact angle decreased to 57.0º ± 2.5º (**Figure 2-S7A**, **iii**). NOM has been shown to contain both hydrophobic fractions, including humic species, and hydrophilic fractions, including carboxylic acids, carbohydrates, and amino acids.[149-150] This decreased contact angle indicates that NOM adsorption on CeO_2 NPs makes their surfaces more hydrophilic. With the addition of UV/H_2O_2, together with NOM, the contact angle became even smaller (36.6º ± 4.2º), suggesting that the presence of both NOM and UV/H_2O_2 could make the CeO_2 surface more hydrophilic (**Figure 2-S7A**, **iv**). Regardless of this increased hydrophilicity, however, CeO_2 NPs tended to aggregate more. This observation indicates that factors other than hydrophilicity, such as steric interactions and electrostatic repulsive forces, are dominant in affecting CeO_2 colloidal stability.

2.3.4 Dominant reaction mechanisms

To provide a more detailed mechanism explaining the decreased colloidal stability of CeO_2 NPs during treatment with UV/H_2O_2, ROS scavenging experiments were conducted using UV-Vis and XPS to elucidate the role of two radicals, $O_2^{\cdot-}$ and ·OH, in changing the surface chemistry of CeO_2 NPs (**Figure 2.4**). **Figure 2.4A** shows the UV-Vis absorbance of CeO_2 at elapsed times under different reaction conditions. Here, SOD was utilized to quench $O_2^{\cdot-}$ ($k = 1.79 \times 10^9$ M^{-1} s^{-1})[50], and t-ButOH was used to quench ·OH ($k = 6 \times 10^8$ M^{-1} s^{-1})[133]. In the presence of SOD, the sedimentation of CeO_2 NPs slowed significantly, indicating that $O_2^{\cdot-}$ played an important role in destabilizing CeO_2. After the addition of t-ButOH, the sedimentation of CeO_2 NPs was further promoted compared to the system with only UV/H_2O_2. This finding suggests that ·OH and $O_2^{\cdot-}$ affect the colloidal stability of CeO_2 differently: $O_2^{\cdot-}$ promotes the sedimentation of CeO_2, while ·OH inhibits the sedimentation of CeO_2.

To better understand the surface oxygen species on CeO_2 surfaces after the reaction, the O 1s spectra from XPS were fitted with four peak contributions, referred to as O_I, O_{II}, O_{III}, and O_{IV} peaks (**Figure 2.4B**). The major peak O_I (BE ≈ 528.6–529.0 eV) is characteristic of lattice oxygen in CeO_2.[151-152] Peak O_{III} (BE ≈ 531.3–532.0 eV) belongs most likely to hydroxyl-like groups,[153-155] and peak O_{IV} (BE ≈ 533.5–534.3 eV) is characteristic of residual adsorbed H_2O.[156] In the presence of UV/H_2O_2 (**Figure 2.4B**, **b**), the area ratio of peak O_{II} (BE ≈ 530.1–530.7 eV) was 36.8%, much higher than that of unreacted CeO_2 (11.5%, **Table 2-S5**). The presence of t-ButOH further increased the ratio of peak O_{II} to 48.0% (**Figure 2.4B**, B). In contrast, the presence of SOD decreased the ratio of peak O_{II} back to 18.2% (**Figure 2.4B**, **d**). These results indicate that the increase of peak O_{II} may involve the bonding of $O_2^{\cdot-}$ with the CeO_2 surface. In earlier reports, peak O_{II} (530–531 eV) has been assigned to provide evidence for chemisorbed molecular oxygen species such as peroxo-like species[156-158] or superoxo-like species[159], although most of them are dealing with other nanoparticles than CeO_2. Peak O_{II} has also been reported to result from carbonates.[160] However, with the pH conditions in this study, the dissolved CO_2 in the solution for different systems would be similar, thus the contribution of carbonates to the peak O_{II} should be similar.[156] Based on UV-Vis results, $O_2^{\cdot-}$ played the main role in promoting the sedimentation of CeO_2, and its negative charge was capable of neutralizing the positive surface charge of CeO_2. Thus, we deduce that the bonding of $O_2^{\cdot-}$ with the CeO_2 surface contributes dominantly to the increase of peak O_{II}. The ability of $O_2^{\cdot-}$ to bond with the CeO_2 surface has also been reported by other studies.[161] It should be noted that XPS results could not directly show the adsorption of $O_2^{\cdot-}$ radicals onto CeO_2 surface, because $O_2^{\cdot-}$ would change into oxygen bonding after the adsorption. However, this consequent oxygen bonding shown by XPS still suggests the adsorption of metastable molecular oxygen species onto the CeO_2 surface during the reaction.

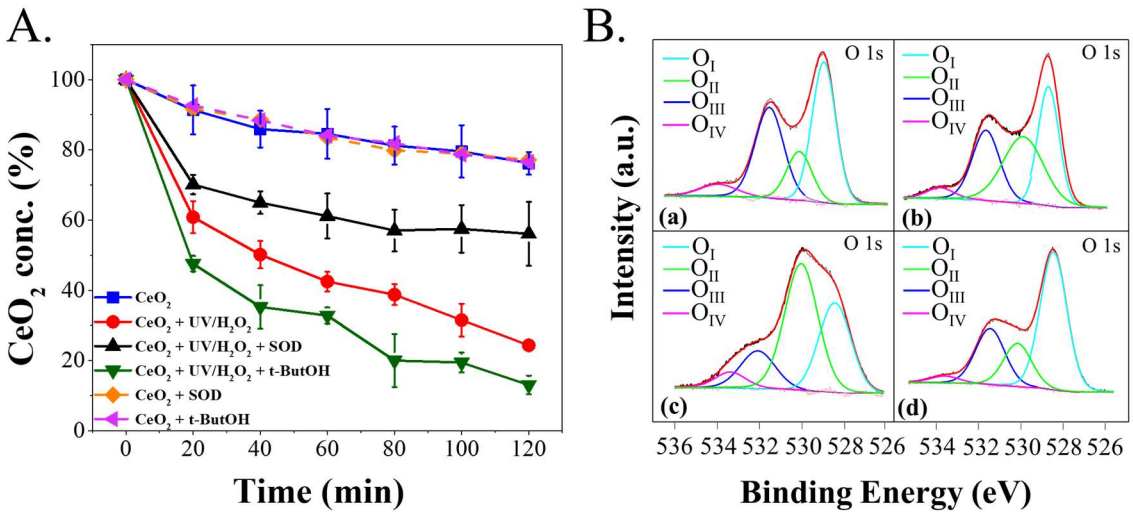

Figure 2.4 (**A**) CeO_2 NP concentration measured by UV-Vis with 10 mM NaCl at pH 5.4 with SOD and t-ButOH. Dotted lines are control experiments with only SOD and t-ButOH. The percentages were obtained from the suspended nanoparticle concentrations normalized by the initial suspended concentration. The error bars represent the standard deviation of CeO_2 NP concentrations from triplicate experiments. (**B**) XPS spectra of O 1s obtained from CeO_2 sedimentation with 10 mM NaCl at pH 5.4 after 2 hrs reaction. (**a**) CeO_2 control, (**b**) CeO_2 with UV/H_2O_2, (**c**) CeO_2 with UV/H_2O_2 and t-ButOH, and (**d**) CeO_2 with with UV/H_2O_2 and SOD.

Summarizing the results of the UV-Vis and XPS experiments, a mechanism regarding the reaction between CeO_2 NPs and ROS was proposed, shown in **Figure 2.5**. Before reaction with ROS, CeO_2 NPs contained relatively a lower ratio of Ce^{3+}/Ce^{4+} (**stage I**). During UV/H_2O_2 process, the ROS generated, such as ·OH and $O_2^{\cdot-}$, reacted with CeO_2, reducing part of the Ce^{4+} to Ce^{3+} on the CeO_2 surface and increasing the ratio of Ce^{3+}/Ce^{4+}. During this process, protons were released, which contributed to the decreased pH values observed. Oxygen molecules were also generated from the oxidation of H_2O_2 or ·OH by CeO_2.[106, 138] At **stage I**, the CeO_2 surface was positively charged due to surface adsorbed hydroxyl functional groups such as $–OH_2^+$.[40, 162-163] From **stage I** to **stage II**, $O_2^{\cdot-}$ radicals adsorbed onto the CeO_2 surface by exchanging with $–OH_2^+$ functional groups and neutralized the surface charge of CeO_2, as observed from zeta potential measurements. A lowered surface charge resulted in smaller electrostatic repulsive forces between nanoparticles,

making them aggregate and settle. The electron from each adsorbed $O_2^{\cdot-}$ could be transferred to or shared with one Ce^{4+} ion on the CeO_2 surface, making it form Ce^{3+}. This formation might be the reason for the observed higher ratio of Ce^{3+} on the CeO_2 surface in our systems, but we still will need a separate future study to confirm this interesting point.

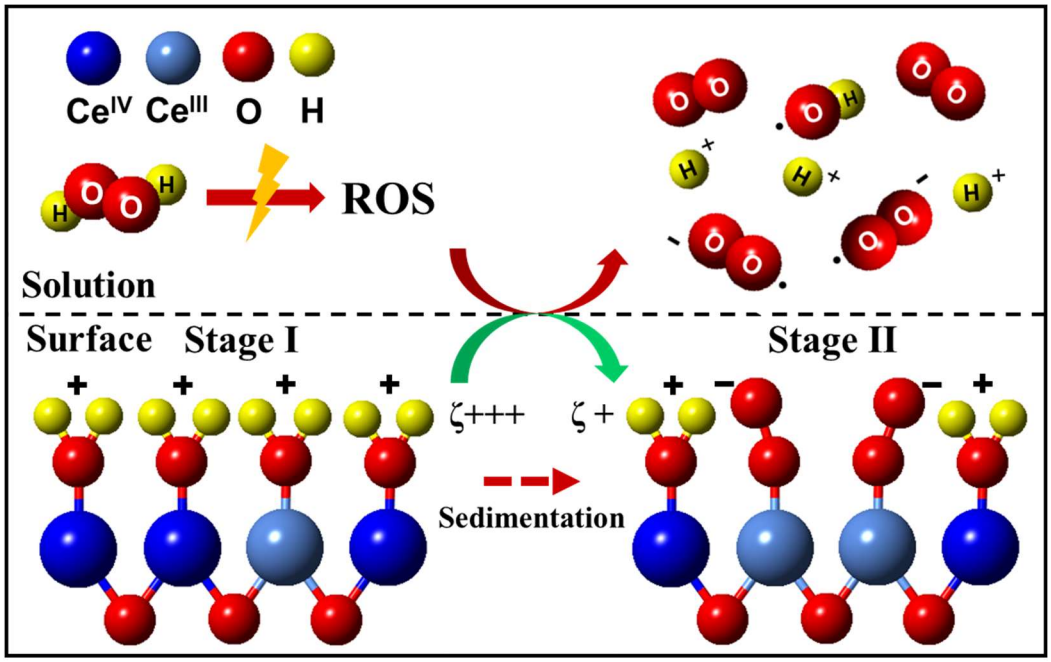

Figure 2.5 Schematic diagram for the proposed mechanism of the reaction between CeO_2 and ROS generated during UV/H_2O_2 exposure.

2.4 Conclusions and environmental implications

The wide applications of engineered nanomaterials in industry have increased their chances of entering into engineered water treatment processes, including AOPs. Our work, for the first time, systematically evaluated the co-effects of NOM and ROS on the surface properties, colloidal stability, and aggregation of CeO_2 NPs in simulated AOPs. It was found that UV/H_2O_2 promoted CeO_2 NPs sedimentation by neutralizing the surface charge of NPs, while NOM helped to stabilize CeO_2 NPs by reversing the surface charge of NPs and maintaining the electrostatic repulsive forces. In the presence of NOM and UV/H_2O_2 together, however, NOM on CeO_2 NPs acted as a protective

layer, which made the reactions between CeO_2 NPs and ROS insignificant in a shorter reaction period. The roles of different types of ROS in changing the surface chemistry and colloidal stability of CeO_2 NPs were also evaluated. In the experimental system, the adsorption of superoxide radicals ($O_2^{\cdot-}$) dominated in neutralizing the surface charge of CeO_2 NPs compared with other ROS, such as hydroxyl radicals (·OH). Previously the redox reactions between ROS and CeO_2 NPs (in particular, the change of the Ce^{3+}/ Ce^{4+} ratio on the surface) were mainly considered, but in this study, we showed that ROS could have surface complexation with CeO_2 NPs and change their surface charge, which leads to the aggregation and sedimentation of NPs.

The results have significant implications for better understanding the fate and transport of CeO_2 NPs in WWTPs (in particular, AOPs). Organic matter, such as NOM, can help to stabilize CeO_2 NPs through surface complexation and by changing the steric interactions between NPs. Therefore, it is likely that CeO_2 NPs associated with NOM will be transported in wastewater without much sedimentation and removal, increasing their transport distances and potentially increasing their concentration in the secondary effluents. The complexation mechanism of NOM on CeO_2 NPs, its effect on CeO_2 NPs' surface charge and hydrophilicity, and the alleviation of the CeO_2 NPs-ROS reaction by NOM coating can all contribute to a mechanistic understanding of the effects of organic matter on the fate and transport of CeO_2 NPs in WWTPs.

CeO_2 NPs in WWTPs can also form complexes with other types of organic matter, including SMPs which contain higher fractions of hydrophilic constituents (i.e., polysaccharides and proteins) than NOM.[111-114] Considering that NOM is an organic macromolecule that contains many of the same functional groups that occur in cellular debris, it is a useful probe molecule to provide insights into the role of organic matter in changing the fundamental chemistry of CeO_2 NPs in the UV/H_2O_2 system. However, the effects of different types of organic matter in WWTPs

(i.e., NOM, SMPs, and EfOM) on the aggregation of CeO_2 NPs in AOPs should all be carefully studied and compared in the future. After the CeO_2 NPs and organic matter complexes enter AOPs, the ROS can decompose the organic matter coated on CeO_2 NPs surface and also reduce the colloidal stability of CeO_2 NPs through the neutralization of their surface charge, which can lead to the sedimentation of NPs. Thus, AOPs could possibly provide another mechanism to remove and recover CeO_2 NPs from secondary effluents. In the future, besides different organic matter types, more efforts should also be devoted to evaluate the effects of water chemistry (i.e., pH values, ionic strength) and water constituents (i.e., cations, anions) on the fate of CeO_2 NPs or other engineered nanomaterials in AOPs.

Our findings also have intriguing implications for other research areas. For example, in natural water systems, it is also possible for CeO_2 NPs to meet NOM and ROS together. Our results will help to predict CeO_2 NPs' fate under such circumstances. Furthermore, because of the free-radical-scavenging property of CeO_2 NPs, there have been many studies discussing using them as antioxidants for cells to resist the ROS-induced cell injury.[164-166] Our study also suggests that in such biomedical applications, CeO_2 NPs might aggregate after their reaction with ROS, especially $O_2^{\cdot-}$. The toxicity of aggregated CeO_2 NPs to normal cells, the influence of CeO_2 NPs aggregation on their therapeutic behavior, and their transport in the body should be carefully elucidated.

Acknowledgments

We are grateful for support received from the Environmental Chemical Science program of the National Science Foundation (CHE-1214090). We wish to thank the Institute of Materials Science and Engineering (IMSE) in Washington University in St. Louis for the use of a clean room, XPS, and HRTEM. We also thank the Nano Research Facility (NRF) at Washington University in

St. Louis for use of ICP-OES and ultracentrifuge. Thank Prof. James Ballard for carefully reviewing our manuscript. Lastly, we also thank the Environmental NanoChemistry Group members for providing valuable discussions and suggestions for this paper.

Supporting information for Chapter 2

2-S1. Characterization of CeO_2 nanoparticles

TEM Sample Preparation: Approximately 50 µL of the CeO_2 solution was placed onto 200-mesh Cu grids with Formvar-carbon films. After drying, the morphology and lattice spacing were determined using high resolution transmission electron microscopy (HRTEM, JEOL 2100F) with a 200 kV accelerating voltage. The lattice spacings closely matched those of CeO_2 nanoparticles.[167-168]

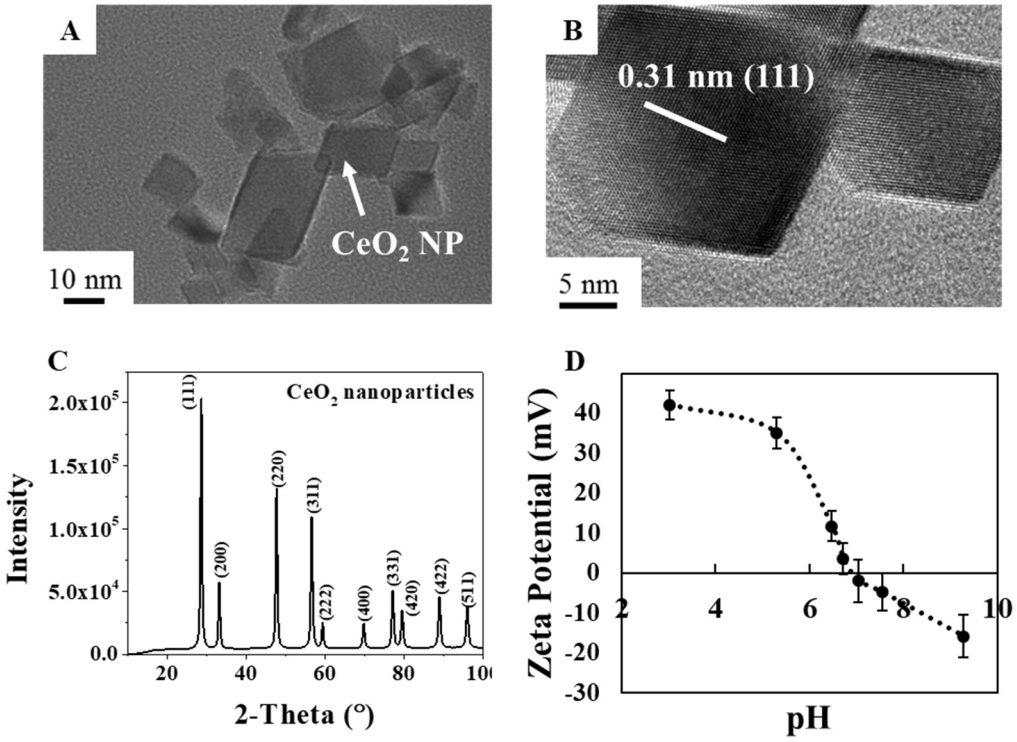

Figure 2-S1 (A) and (B): Representative TEM images and lattice spacing for unreacted CeO_2 NPs with 10 mM NaCl at pH 5.4. (C): Wide angle X-ray diffraction patterns of CeO_2 NPs taken at sector 11-ID-B of the Advanced Photon Source at Argonne National Laboratory. (D) Zeta potential of CeO_2 NPs in 10 mM NaCl at different pH values to determine the isoelectric point (i.e., ~ pH 6.9).

2-S2. NOM stock solution preparation.

Preparation of NOM Stock Solution: To create SRNOM stock solutions, 100 mg of NOM was added to 200 mL of DI water and stirred overnight in dark conditions (the bottle was wrapped in aluminum foil). The pH of the solution was then adjusted to 8.5 to increase the solubility before vacuum-filtering. This SRNOM stock solution was refrigerated prior to experimentation. Non-purgeable organic carbon (NPOC) concentrations in the stock solution were measured using a Shimadzu total organic carbon (TOC) Analyzer.

Table 2-S1. Characterization of Suwannee River NOM provided by the International Humic Substances Society (IHSS).[169]

Carboxyl (meq/g C)	Phenolic (meq/g C)	Q_1	$LogK_1$	n_1	Q_2	$LogK_2$	n_2	N	RMSE
11.21	2.47	11.20	4.16	3.44	1.60	9.99	1.03	1705	0.1360
Source: Department of Chemistry, Environmental Sciences Ph.D. Program, Ball State University, Muncie, IN, U.S.A.									
Q_1 and **Q_2** are the maximum charge densities of the two classes of binding sites **Log K_1** and **Log K_2** are the mean log K values for proton binding by the two classes of sites **n_1** and **n_2** are empirical parameters that control the width (in log K) of a class of proton binding sites									

2-S3. CeO_2 sedimentation experimental design.

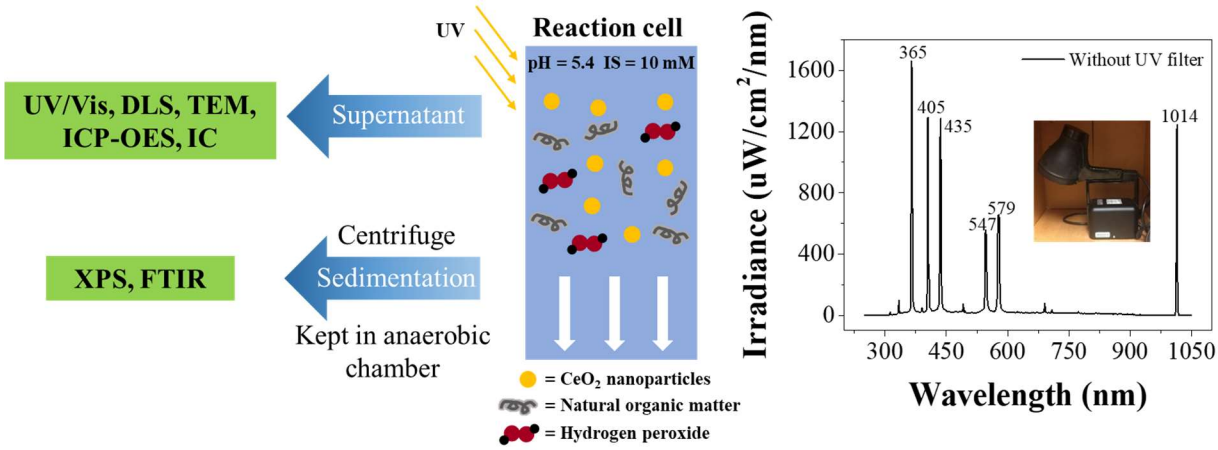

Figure 2-S2 Experimental procedures for UV-Vis, DLS, ICP-OES, TEM, XPS, and FTIR, and the irradiance spectrum of the UVA light source measured using a SpectrlLight 3. Suspended CeO_2 solutions at pH 5.4 were put into 50 mL test tubes and reacted for 2 hours. The ionic strength of the solutions was controlled at 10 mM using NaCl. At certain reaction times, 1 mL of supernatant was taken out to be measured using UV-Vis and DLS. After 2h reaction, the solutions were centrifuged for 15 minutes. The supernatant was taken out, leaving the sediment in the test tubes. The sediment was left to dry in an anaerobic chamber to prevent any further oxidation from air. XPS and FTIR were measured using the sedimentation as soon as it was dried.

Table 2-S2. Detailed experimental conditions for UV-Vis experiments.

Conditions		CeO_2 (mg/L)	H_2O_2 (mM)	NOM (mg C/L)	UV	pH	NaCl (mM)
Light	H_2O_2	50	0/3/30	-	Yes	5.4 ± 0.1	10
	NOM	50	-	3.3 ± 0.2	Yes	5.4 ± 0.1	10
	H_2O_2 + NOM	50	3/30	3.3 ± 0.2	Yes	5.4 ± 0.1	10
Dark	H_2O_2	50	0/3/30	-	No	5.4 ± 0.1	10
	NOM	50	-	3.3 ± 0.2	No	5.4 ± 0.1	10
	H_2O_2 + NOM	50	3/30	3.3 ± 0.2	No	5.4 ± 0.1	10

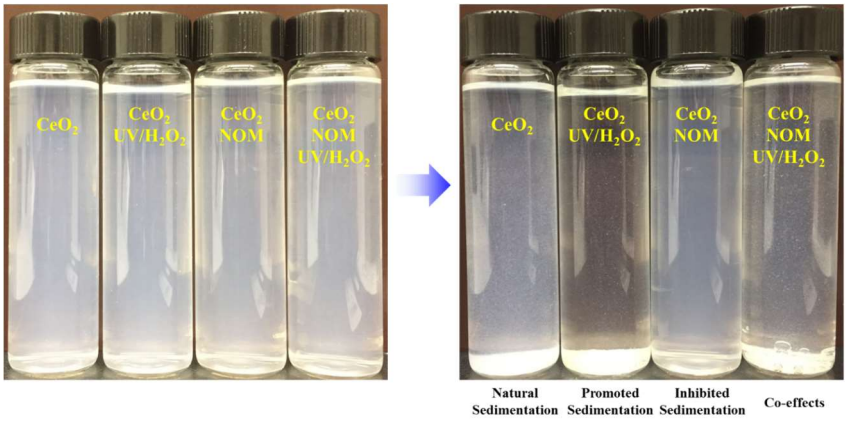

Figure 2-S3 Observed differences in the sedimentation of CeO_2 NPs in the presence of UV/H_2O_2 and/or NOM compared with the control experiment with 10 mM NaCl at pH 5.4 after 2 hrs reaction.

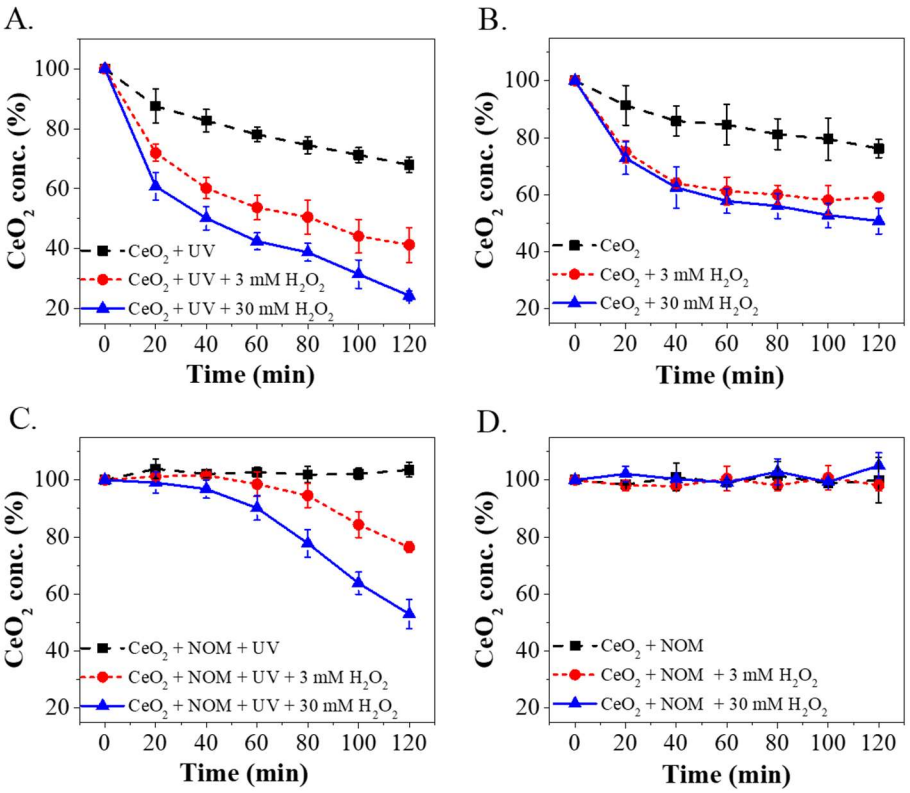

Figure 2-S4 UV-Vis data showing sedimentation of CeO_2 NPs with 10 mM NaCl at pH 5.4 in the presence and absence of UV/H_2O_2 and NOM: (A) CeO_2 with UV and H_2O_2. A higher concentration of H_2O_2 increased the extent of sedimentation; (B) CeO_2 with H_2O_2. H_2O_2 alone showed destabilizing effects on CeO_2; (C) CeO_2 with NOM, UV, and H_2O_2. With a higher concentration of H_2O_2, CeO_2 started to settle in a shorter time range; and (D) CeO_2 with NOM and H_2O_2. NOM concentration was quantified as 3.3 ± 0.2 mg C/L by NPOC. The percentages were obtained by normalizing the suspended nanoparticle concentration by the initial suspended concentration measured using UV-Vis. The error bars represent the standard deviation of CeO_2 NP concentrations from triplicate experiments.

Table 2-S3. Zeta potential and hydrodynamic particle size values for CeO_2 NPs with 10 mM NaCl at pH 5.4 in the presence and absence of UV/H_2O_2 and NOM. The initial CeO_2 NPs concentration was 50 mg/L, and the NOM concentration was 3.3 ± 0.2 mg C/L. The zeta potential for stable dispersions of unreacted CeO_2 in DI water at pH 5.4 was 39.2 ± 3.4 mV. The hydrodynamic particle size was 140.7 ± 53.0 nm for stable dispersions of unreacted CeO_2 in DI water at pH 5.4.

Conditions	Zeta potential (mV)		Z-Ave (d. nm)	
	1 hr	2 hrs	1 hr	2 hrs
CeO_2	39.5 ± 2.6	38.6 ± 5.1	256.0 ± 49.0	460.0 ± 60.1
CeO_2 + UV	38.8 ± 4.2	35.0 ± 4.6	275.0 ± 59.9	513.0 ± 74.0
CeO_2 + 30 mM H_2O_2	32.0 ± 4.5	30.9 ± 3.3	1983.0 ± 132.1	2706.0 ± 145.4
CeO_2 + UV + 30 mM H_2O_2	5.4 ± 3.8	3.8 ± 3.4	3954.0 ± 171.8	5574.0 ± 252.8
CeO_2 + NOM	-43.9 ± 6.9	-38.3 ± 1.8	153.0 ± 35.5	174.7 ± 38.5
CeO_2 + NOM + UV	-40.8 ± 4.6	-36.4 ± 1.7	172.3 ± 34.5	182.0 ± 39.2
CeO_2 + NOM + 30 mM H_2O_2	-39.5 ± 5.2	-36.2 ± 1.1	173.9 ± 30.9	183.9 ± 39.3
CeO_2 + NOM + UV + 30 mM H_2O_2	-38.9 ± 5.6	-12.9 ± 2.1	250.6 ± 41.4	3276.0 ± 122.3

Table 2-S4. pH measurements of the reaction and control systems for CeO_2 NPs at 10 mM NaCl and an initial pH of 5.4.

Conditions	Starting pH values	Final pH values (2h)
CeO_2	5.4 ± 0.1	5.7 ± 0.1
CeO_2 + UV	5.4 ± 0.1	5.6 ± 0.1
CeO_2 + 3 mM H_2O_2	5.4 ± 0.1	5.3 ± 0.1
CeO_2 + 30 mM H_2O_2	5.4 ± 0.1	5.3 ± 0.1
CeO_2 + UV + 3 mM H_2O_2	5.4 ± 0.1	5.3 ± 0.1
CeO_2 + UV + 30 mM H_2O_2	5.4 ± 0.1	5.1 ± 0.1
CeO_2 + NOM	5.4 ± 0.1	5.1 ± 0.1
CeO_2 + NOM + UV	5.4 ± 0.1	4.9 ± 0.1
CeO_2 + NOM + 3 mM H_2O_2	5.4 ± 0.1	4.9 ± 0.1
CeO_2 + NOM + 30 mM H_2O_2	5.4 ± 0.1	4.9 ± 0.1
CeO_2 + NOM + UV + 3 mM H_2O_2	5.4 ± 0.1	4.7 ± 0.1
CeO_2 + NOM + UV + 30 mM H_2O_2	5.4 ± 0.1	4.6 ± 0.1

CeO_2 nanoparticle dissolution tests using inductively coupled plasma optical emission spectrometry (ICP-OES): Due to the low solubility of CeO_2, 250 mg/L CeO_2 suspensions and 150 mM H_2O_2 were used in order to achieve aqueous Ce concentrations higher than the detection limit of ICP-OES (25 μg/L). Because the concentrations of CeO_2 and H_2O_2 were scaled up by the same multiples, this elevated concentration system is relevant to lower concentration systems. Reactions were prepared as described for sedimentation experiments. At 1 hr and 2 hrs, triplicate samples were placed in ultracentrifuge tubes (PC Oak Ridge Tubes, Fisher Scientific) and ultracentrifuged using a Thermo Scientific Sorvall WX Ultra Series Centrifuge with a T865 Fixed Angle Rotor at 40,000 rpm (or 115,861g) for 30 min. After ultracentrifuging, samples were filtered

using a 0.2 μm polypropylene filter (Millipore syringe filter) to ensure the removal of all bulk CeO_2 NPs and aggregates. The filtrate was collected and acidified to 1% v/v nitric acid for ICP-OES measurements. This method was also used in our previous studies and other CeO_2 NP dissolution studies.[126, 170] From the results (Table S2), UV/H_2O_2 exposure did not promote CeO_2 NP dissolution compared with the control system.

Table 2-S5. Dissolved Ce concentrations (μg/L) in NaCl systems in the presence of UV and H_2O_2 at pH 5.4, measured by ICP-OES. Std. Dev., standard deviation with 95% confidence level.

System	1 hr	Std. Dev.	2 hrs	Std. Dev.
CeO_2 + NaCl + UV + H_2O_2	11.9	2.3	6.4	3.2
CeO_2 + NaCl + UV	17.7	4.7	20.6	21.6
CeO_2 + NaCl + H_2O_2	26.6	4.4	23.9	6.1
CeO_2 + NaCl	18.6	5.2	39.7	14.8

NOM decomposition measurement using ion chromatography (IC): Reactions were prepared as described for sedimentation experiments. At 0, 20, 40, 60, 80, 100, and 120 minutes, triplicate samples were filtered using a 0.2 μm polypropylene filter (Millipore syringe filter). Both formate and acetate were measured, but only acetate was detected during the reaction.

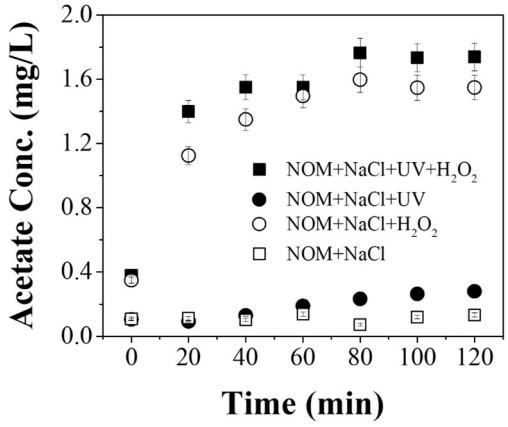

Figure 2-S5 Measurement of acetate produced from the decomposition of NOM during the reaction with CeO_2 and UV/H_2O_2 exposure using ion chromatography (IC).

2-S4. XPS reference

Table 2-S6. XPS reference binding **energies**, absolute values of areas for each peak, and calculated percentages of Ce^{3+} at different conditions for Ce 3d.

	U''	U'	U	V'''	V''	V'	V	
BE (eV)	907.20	903.50	900.60	897.90	888.30	885.0	881.90	Ce^{3+}%
	Ce^{4+}	Ce^{3+}	Ce^{4+}	Ce^{4+}	Ce^{4+}	Ce^{3+}	Ce^{4+}	
CeO_2 control	1708	1614	2762	6150	4992	2797	4730	17.8%
CeO_2 + UV/H_2O_2	8524	15094	11555	22697	16731	16128	19459	28.3%
CeO_2 + NOM	2907	3234	3498	7190	5238	2361	6671	18.0%
CeO_2 + NOM + UV/H_2O_2	3139	5960	11753	16325	11326	11179	18904	21.8%

Table 2-S7. XPS reference binding energies, absolute values of areas for each peak, and calculated percentages of each corresponding bond at different conditions for C 1s.

Area and percentages	C 1s			
	C-C (284.8 eV)	C=O (285.6 eV)	O-C=O (288.8 eV)	Total of C=O and O-C=O
CeO_2 control	6427	653	396	1049
	86.0%	8.7%	5.3%	14.0%
CeO_2 + UV/H_2O_2	14828	1985	2140	4125
	78.2%	10.5%	11.3%	21.8%
CeO_2 + NOM	10786	4203	1951	6154
	63.7%	24.8%	11.5%	36.3%
CeO_2 + NOM + UV/H_2O_2	15586	3027	1642	4669
	77.0%	14.9%	8.1%	23.0%

Table 2-S8. XPS reference binding energies, absolute values of areas for each peak, and calculated percentages of each corresponding bond at different conditions for O 1s.

Area and percentages	O 1s			
	O_I	O_{II}	O_{III}	O_{IV}
	Lattice oxygen (528.9 eV)	Superposition of CO_3^{2-} and $O_2^{\cdot-}$ (530.1 eV)	Hydroxyl-like groups (531.8 eV)	Residual adsorbed H_2O (534.1 eV)
CeO_2 control	8942 51.6%	1988 11.5%	5188 29.9%	1221 7.0%
CeO_2 + UV/H_2O_2	5799 32.6%	6545 36.8%	4662 26.2%	765 4.3%
CeO_2 + UV/H_2O_2 + t-ButOH	5628 31.1%	8675 48.0%	2709 15.0%	1058 5.9%
CeO_2 + UV/H_2O_2 + SOD	8176 53.9%	2759 18.2%	3738 24.6%	506 3.3%

2-S5. FTIR spectrum of unreacted CeO_2 NPs

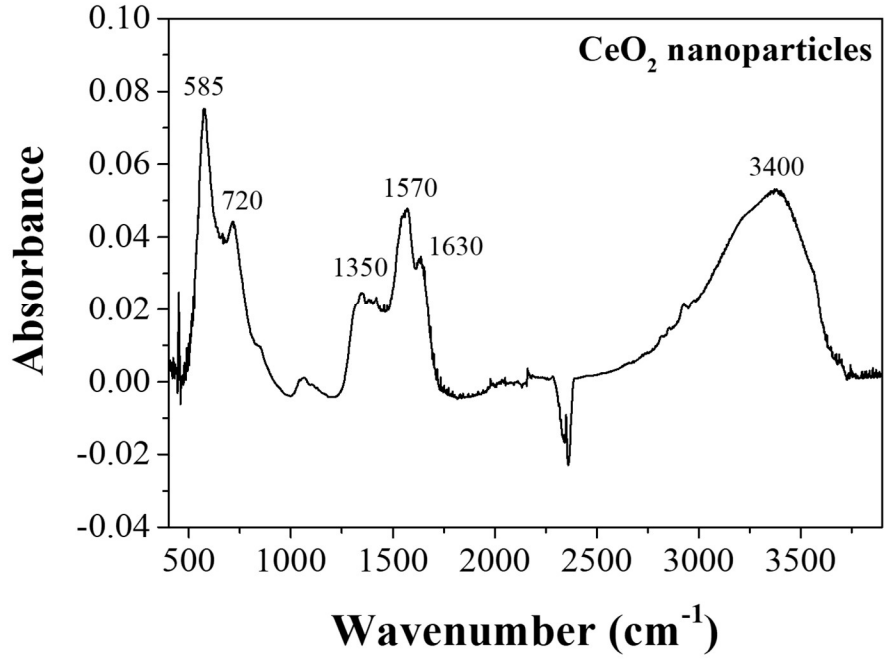

Figure 2-S6 FTIR spectrum of unreacted CeO_2 NPs.

2-S6. Contact angles of DI water on CeO_2-sputtered Si wafers under different conditions

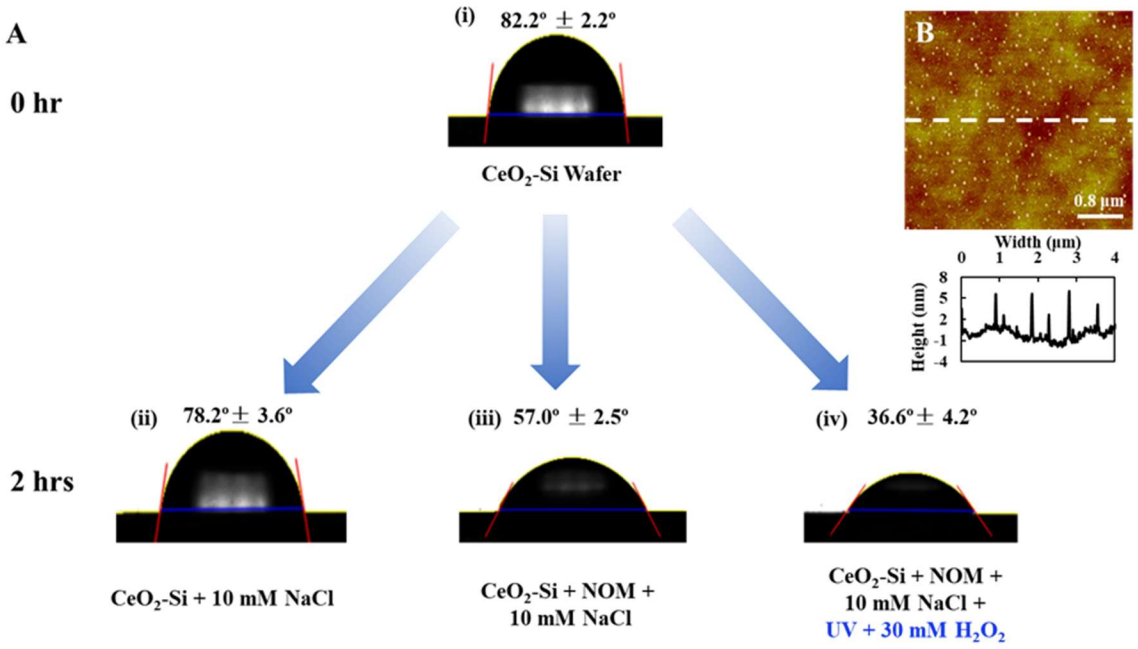

Figure 2-S7 Measurements of contact angles for CeO_2-sputtered Si wafers at 10 mM IS and pH 5.4. **A**: contact angles of (i) unreacted CeO_2-Si wafer at 0 hr, (ii) CeO_2-sputtered Si wafer with NaCl solution at 2 hrs, (iii) CeO_2-sputtered Si wafer with 10 mM NaCl and 3.3 mg C/L NOM at 2 hrs, (iv) CeO_2-sputtered Si wafer with 10 mM NaCl, 3.3 ± 0.2 mg C/L NOM, UV, and 30 mM H_2O_2 at 2 hrs. **B**: Atomic force microscopy (AFM) image (4 µm × 4 µm) of an unreacted CeO_2-sputtered Si wafer surface. For each experimental condition, a 5 mm × 5 mm CeO_2-sputtered Si wafer piece was cut from a larger CeO_2-sputtered Si wafer to be used.

Chapter 3. Arsenic mobilization during managed aquifer recharge: effects of abundant oxyanions on arsenopyrite dissolution and secondary precipitation

Reproduced from Ref. 171 with permission from American Chemical Society:[171] Wu, X., Burnell, S., Neil, C., Kim, D., Zhang, L., Jung, H., Jun, Y. S.* Effects of Phosphate, Silicate, and Bicarbonate on Arsenopyrite Dissolution and Secondary Mineral Precipitation, *ACS Earth & Space Chemistry*, **2020**. DOI: 10.1021/acsearthspacechem.9b00273. Copyright 2020 American Chemical Society.

Abstract

In **Chapter 3** we focus on **System 2**, which is about sustainable water management by managed aquifer recharge (MAR). Here we first discuss the effects of oxyanions (phosphate, silicate, bicarbonate) on arsenic mobilization from arsenopyrite and secondary mineral precipitation. Managed aquifer recharge (MAR) has been applied to meet quickly growing water demands. However, during MAR operations, the injected water can induce dissolution of local minerals and result in the release of toxic metalloids, such as arsenic. To alleviate this concern, it is pivotal to understand the effects of injected water chemistry on arsenic mobilization during MAR. In this bench-scale study with geochemical conditions relevant to MAR operations, we investigated the impacts of three environmentally abundant oxyanions (i.e., phosphate, silicate, and bicarbonate) on arsenic mobilization from arsenopyrite (FeAsS) and secondary mineral precipitation. Phosphate showed time-dependent reversed effect on arsenic mobility. In short term (6 hours), phosphate promoted the dissolution of FeAsS through monodentate mononuclear surface complexation. However, over a longer experimental time (7 days), the enhanced formation of secondary minerals, such as iron(III) (hydr)oxide (maghemite, γ-Fe_2O_3) and iron(III) phosphate (phosphosiderite, $FePO_4 \cdot 2H_2O$), helped to decrease arsenic mobility through re-adsorption. Silicate increased the arsenic mobility and bicarbonate decreased the arsenic mobility during the entire 7-day reaction. Phosphate system showed the highest amount and largest sizes of secondary precipitates among the three oxyanions. These new observations provide useful mechanistic understanding of the impacts of different oxyanions on arsenic mobilization and secondary mineral formation during the geochemical transformation of arsenic-containing sulfide minerals in MAR, and also offer useful insight into water chemistry factors during pretreatment for MAR source water.

3.1 Introduction

Owing to increased agricultural irrigation and unprecedented socioeconomic development, groundwater usage has been rapidly growing.[172] For example, by 2014, the average annual use of groundwater reached 40% of the total water demand in California.[173] In India, about 90 million rural households directly rely on groundwater for irrigation.[174] Intensive water demands have led to over-extraction of groundwater resources, as occurred in regions in California's Central Valley and the North China Plain.[175-176] This causes severe environmental problems, including land subsidence, flood inundation, and saltwater intrusion.[173, 177-178] Currently, to alleviate these impacts caused by groundwater over-drafting, managed aquifer recharge (MAR), an engineered process of injecting secondary water sources into aquifers, has been widely applied.[12] Among all secondary water sources, reclaimed water, such as treated municipal wastewater effluents, has been more used for MAR in recent years.[16, 18]

Lately, however, the release of arsenic was noted as a serious concern during MAR.[17, 62, 67, 179] Arsenic concentrations in recovered water from MAR sites, such as southwest central Florida (10–130 μg/L) and South Australia (14–25 μg/L), were much higher than the injected water (3 μg/L for both sites), also surpassing the 10 μg/L arsenic maximum level set by the U.S. EPA.[17, 67, 179] First, the oxidative dissolution of arsenic-bearing minerals, such as arsenian pyrite ($FeAs_xS_{2-x}$, < 0.5−10 wt% As) and arsenopyrite (FeAsS), is a dominant mechanism for arsenic mobilization during MAR.[17, 63, 67, 180-181] In addition, non-redox-related arsenic mobilization mechanisms can exist. For instance, competitive ligand interactions[17] and pH changes[182] of groundwater induced by recharged water injection can increase arsenic mobility.

During the oxidative dissolution of arsenopyrite induced by dissolved oxygen (O_2) or nitrate (**eq 3.1a−b**),[183] arsenic and iron are released and oxidized from arsenic(-I) to arsenic(III)

and arsenic(IV), and from iron(II) to iron(III).[184] Iron(III) further forms secondary mineral phases, such as iron(III) (hydr)oxides, which can in turn adsorb aqueous arsenic species and decrease their mobility.[67, 184-185]

$$FeAsS(s) + 1.5H_2O + 2.75O_2(aq) \rightarrow Fe^{2+}(aq) + H_3AsO_3(aq) + SO_4{}^{2-}(aq) \quad \textbf{(eq 3.1a)}$$

$$10Fe(As,S)_2(s) + 26NO_3{}^{-}(aq) + 2H_2O + 6H^{+}(aq) \rightarrow 10Fe^{2+}(aq) + 10HAsO_4{}^{2-}(aq) + 10SO_4{}^{2-}(aq) + 13N_2(g) \quad \textbf{(eq 3.1b)}$$

Changes in local water chemistry induced by MAR can impact the oxidative dissolution of arsenopyrite, secondary iron(III) (hydr)oxides formation and their physicochemical properties, and the adsorption of arsenic onto iron(III) (hydr)oxides.[64] In particular, different water components in the recharged water may have varied impacts on arsenopyrite dissolution and secondary iron(III) (hydr)oxide precipitation. For example, chloride, unlike nitrate, was found to promote the phase transformation of iron(III) (hydr)oxides through Ostwald ripening.[62] Fe^{3+} addition enhances arsenopyrite dissolution and iron(III) (hydr)oxide formation.[186] Dissolved organic matter inhibits iron(III) (hydr)oxide precipitation and increases arsenic mobilization.[187] In addition to these water components, oxyanions, including phosphate, silicate, and bicarbonate, are also abundant in the injected reclaimed water.[188-190] These oxyanions possess similar structures with arsenic species, and can compete with arsenic during adsorption onto iron(III) (hydr)oxide's surface,[189, 191-192] hence they can significantly impact arsenic mobility during MAR. Phosphate and arsenate have nearly identical pKa values,[193] and close thermochemical radii that differ by only 4%.[194] Previously, phosphate was reported to significantly reduce arsenic adsorption onto iron(III) (hydr)oxides.[192, 195-197] In recharged water at MAR sites, phosphate can come from diverse sources, including phosphate fertilizers,[198] and the desorption of phosphate originally adsorbed or precipitated on soil surfaces.[199] Phosphate concentrations in recharged water could be as high as 10 mg/L (0.3 mM),

which is much higher compared with phosphate concentrations in typical groundwater (~0.04 mg/L).[188]

Silicate in ground water is usually derived from the weathering of soil minerals.[200] Silicate concentrations in natural waters varies from 0.45 to 14 mg/L (0.01–0.5 mM).[189-190] It was reported that silicate can significantly decrease the adsorption capacity of iron(III) (hydr)oxides for both arsenic(V) and arsenic(III).[189, 201-202] In addition, silicate can interact with iron(III) to form soluble polymers and highly dispersed colloids, affecting the extent of iron(III) (hydr)oxide precipitation.[189, 201] Bicarbonate, which has a typical concentration range of 30.5–488 mg/L (0.5–8 mM) in the U.S. groundwater,[203] can influence the adsorption of arsenic onto iron(III) (hydr)oxides, but the effects are more intricate than those of phosphate and silicate.[204-207] In the presence of bicarbonate, both enhanced and inhibited adsorption of arsenic onto iron(III) (hydr)oxides were reported, depending on the pH and the bicarbonate concentrations.[189, 191, 207-208] Bicarbonate can also affect iron release from dissolution of iron-containing mineral surfaces,[209] suggesting that bicarbonate in recharged water can change the dissolution behavior of arsenopyrite, and may subsequently influence arsenic mobilization and secondary mineral precipitation.

Still, insufficient attention has been given to the geochemical effects of these different oxyanions in recharged water on arsenic release from arsenic-bearing sulfide minerals and the secondary mineral precipitation under conditions relevant to MAR. Therefore, this study aims to systematically investigate arsenic mobilization, as well as the extent, morphology, and phases of secondary mineral precipitates from arsenopyrite in the presence of three oxyanions: phosphate, silicate, and bicarbonate. The new observations in this study will advance our understanding of the impacts of oxyanions on arsenic mobility and secondary precipitate formation, which provide mechanistic insight for arsenic control during MAR. Moreover, the findings will offer useful

information about key water chemistry parameters for minimizing the mobilization of toxic elements, such as arsenic, and the secondary pollution of recovered water from MAR sites by mineral dissolution.

3.2 Experimental section

3.2.1 Chemicals and materials

Reaction solutions were prepared using sodium nitrate ($NaNO_3$, ACS grade, Baker), sodium phosphate (Na_2HPO_4, dibasic, anhydrous, HPLC grade, EMD), sodium silicate solution ($Na_2O(SiO_2)_x \bullet xH_2O$, reagent grade, Sigma Aldrich), sodium bicarbonate ($NaHCO_3$, ACS grade, BDH) and ultrapure deionized (DI) water (resistivity > 18.2 MΩ-cm). Arsenopyrite ore samples from Gold Hill, Tooele County, UT, were purchased from the Mineralogical Research Company (San Jose, CA). Arsenopyrite ore samples were ground using a mortar and pestle, and sieved to collect powders in the size range of 300–500 μm for dissolution experiments. Our previous characterization of FeAsS powders showed that the raw sample contained a mixture of quartz and arsenopyrite.[62, 186] To remove any pre-oxidized part of the samples, powders were cleaned using an acid-washing procedure and stored in an anaerobic chamber prior to batch experiments.[210] For surface morphology characterization, flat and polished arsenopyrite coupons were used to observe the morphological changes of arsenopyrite mineral surface and heterogeneous secondary precipitates. Arsenopyrite coupons were prepared by Burnham Petrographics, LLC (Rathdrum, Idaho, USA) using the same arsenopyrite ore as the powder samples.[62] Coupons were stored in the anaerobic chamber and cleaned before reaction using acetone, ethanol, and isopropanol to remove any surface organic compounds and rinsed with DI water.

3.2.2 Batch reactor experiments

To observe the extents of arsenopyrite dissolution with different oxyanions, a series of batch reactor experiments were conducted. Sodium nitrate (10 mM $NaNO_3$) was added in each reactor to control the ionic strength. To start the reaction, 0.05 g of arsenopyrite powder was added to 250 mL sodium nitrate solution. Immediately after the powder was added, the oxyanion stock solutions were added to their respective batch reactors to achieve a concentration of 0.1 mM for each oxyanion. This concentration was in the range of different oxyanion concentrations observed in potential water sources utilized for MAR systems, and particularly in reclaimed water.[188-190] A batch reactor which contained only sodium nitrate solution and arsenopyrite powders without any oxyanions was used as the control system. The pH of these solutions was adjusted to 7.0 ± 0.2 before reaction using diluted nitric acid (HNO_3, ACS grade, VWR) and sodium hydroxide (NaOH, ACS grade, VWR). The pH value and ionic strength were chosen to mimic the conditions of wastewater secondary effluents.[62] At this pH, based on thermodynamic calculations using MINEQL+ (version 5.0), $H_2PO_4^-$ and HPO_4^{2-} were main phosphate species (61.2% and 38.8%, respectively). The speciation of silicate was calculated to be 99.9% $Si(OH)_4$. The speciation of bicarbonate was calculated to be 81.6% HCO_3^- and 18.4% H_2CO_3 (aq). The conditions for each oxyanion system are summarized in **Table 3-S1**. After the reaction started, samples were taken at each hour during the first 6 hours, and each day for 7 days. For each sampling, aliquots of 2 mL of solution were taken from the reactors, filtered using 0.2 μm poly-tetrafluoroethylene (PTFE) membrane syringe filters, and acidified to 2% v/v acid with nitric acid. Arsenic and iron concentrations for these samples were measured using inductively coupled plasma mass spectrometry (ICP-MS) (7500ce, Agilent Technologies, CA). Sulfate concentration was quantified using Ion Chromatography (IC, Thermo Scientific, Dionex ICS-1600). Over the 7-day reaction

period, at each sampling time, pH and oxidation reduction potentials (ORP) for each system were also monitored using a pH electrode (VWR 89231-604 with an Ag/AgCl internal reference) and an ORP electrode (VWR 89231-642 with an Ag/AgCl internal reference), respectively. The ORP value of each batch reactor is helpful for representing the relative ratio of oxidants and reductants, which is controlled by different water components, including dissolved O_2 from atmosphere, temperature, pH, cations and anions, and different rates of arsenopyrite dissolution and secondary precipitation. The measured ORP values were converted to E_h values by adding the potential (E_{ref} = 207 mV at 25 °C) developed by the reference electrode portion relative to the Standard Hydrogen Electrode (SHE). All reactors were at room temperature (25 °C) and open to the atmosphere (P_{O2} = 0.21 atm). Because of the aerobic conditions of batch reactors, sulfide fouling would not be anticipated to affect ORP measurement. For all conditions, triplicate batch experiments were conducted. The detailed experimental method for aqueous phase analyses is also available in the Supporting Information (**Figure 3-S1A**). The isoelectric point of arsenopyrite powders in 10 mM $NaNO_3$ solution (pH_{iep}) was measured to be ~3.6 by quantifying the zeta potentials at different pH using a Zetasizer (Malvern Instruments Inc., Nano ZS, Westborough, MA) with capillary Zeta cells (DTS1070) (**Figure 3-S1B**).

3.2.3 Characterization of secondary mineral precipitates

Arsenopyrite coupons were utilized to observe the effects of different oxyanions on the extents, phases, and morphology of heterogeneous secondary mineral precipitation (**Figure 3-S2**). Before reaction, tapping mode atomic force microscopy (AFM, Veeco Inc., Nanoscope V multimode) was used to confirm the flat surface of unreacted arsenopyrite coupons (**Figure 3-S2B**). For reactions, four coupons (2 mm × 2 mm) were put into each reactor together with 250 mL sodium nitrate solution and 0.05 g arsenopyrite powder. At 6 hours, 1 day, 4 days, and 7 days,

coupons were taken out, rinsed with DI water, and dried with high purity nitrogen gas. To mitigate the effects of further oxidation by oxygen in the atmosphere, reacted coupons were stored in the anaerobic chamber prior to surface analyses. The heights of secondary mineral precipitates on coupons were measured using AFM and analyzed by Nanoscope 7.20 software (Veeco Inc.). Each coupon was measured at five different locations on the substrate surface. At least 50 particles were analyzed to obtain the average sizes of precipitates. The surface root-mean-square (RMS) roughness of coupons was obtained from AFM images using the Nanoscope 7.20.[93] X-ray photoelectron spectroscopy (XPS, PHI 5000 VersaProbe II, Ulvac-PHI with monochromatic Al Kα radiation (1486.6 eV)) characterized the oxidation states of iron (Fe 2p), and provided information about the adsorption of elements such as phosphorus (P 2p), silicon (Si 2p) and carbon (C 1s) on arsenopyrite coupons. For XPS data analysis, the binding energies were referenced to the C 1s line at 284.8 eV. For all conditions, triplicate batch experiments with coupons were conducted. Scanning electron microscopy (SEM, OVA NanoSEM 230, FEI) and energy dispersive X-ray analysis (EDX) was utilized to show the morphology of arsenopyrite coupons and measure the atomic ratio of iron, sulfur, and arsenic on arsenopyrite coupon surfaces after 7 days in different oxyanion systems.

To identify the phases of heterogeneously formed secondary mineral precipitates on coupons, Raman measurements (InVia Raman Microscope, Renishaw, UK) were carried out with a 514 nm laser (~4 mW) and a grating of 1800 lines/mm. A 20× objective and decreased power of 50% were utilized, which did not affect coupon aging.[62, 187] At least three spots on each coupon were measured to obtain their Raman spectra. To provide references at their characteristic peaks for comparison with reacted samples, iron (hydr)oxide standards and unreacted arsenopyrite coupons were measured using Raman. In addition, wide angle X-ray diffraction (WAXD) was

used to provide complementary phase information of secondary minerals formed on the powder surface or in the solution. After 7 days, solutions together with powders were filtered using filter paper (VWR, Grade 410, 1 μm). Residues on filter paper were collected, washed using DI water and dried in the anaerobic chamber. WAXD for these filtered particles was collected at sector 11-ID-B at the Advanced Photon Source at Argonne National Laboratory (Argonne, IL, USA) using a 58.66 keV X-ray beam. A Fourier transform infrared (FTIR) spectrometer (Thermo Scientific, Nicolet Nexus 470) equipped with a diamond crystal was utilized to measure the chemical bond between different oxyanions and arsenopyrite powder surfaces. To obtain discernible chemical bond information, for FTIR analyses, higher concentrations of arsenopyrite powders (2 g/L) and oxyanions (0.1 M) were reacted at pH 7.0 ± 0.2 for 6 hours. These higher concentrations of arsenopyrite powders and oxyanions may not represent concentrations in environmental conditions, but it could successfully indicate the binding information between arsenopyrite and oxyanions. The powders were then filtered, cleaned with DI water and dried before FTIR measurement. An average of 400 scans with a resolution of 4 cm^{-1} was used for each FTIR measurement.

3.3 Results and discussion

3.3.1 Arsenic mobility from arsenopyrite

Figure 3.1 shows the aqueous arsenic concentration changes in the presence of 10 mM sodium nitrate and 0.1 mM oxyanions within 6 hours (**Figure 3.1A**) and 7 days (**Figure 3.1B**). The arsenic concentrations measured by ICP-MS are net concentrations, reflecting the intrinsic arsenic dissolution from arsenopyrite minus the arsenic adsorbed by or incorporated into secondary precipitates. We hypothesized that the effects of secondary precipitates (adsorption/incorporation) on arsenic mobility within 6 hours would be minor compared with the longer period, and shorter

experimental time would show the effects of oxyanions on arsenic intrinsic dissolution better. The AFM results in the next section confirmed our hypothesis that the extent of secondary precipitation after 6 hours was significantly less than that in longer time, especially in the control system. Therefore, both short time (6 hours) and long time (7 days) periods were tested to differentiate the impacts of the intrinsic dissolution of arsenopyrite that would be dominant in the shorter time period, from the impacts of arsenic adsorption on the secondary precipitates that would be more significant in the longer time. At 6 hours, compared with the control system which contained only sodium nitrate, phosphate and silicate increased arsenic concentrations by 16% and 45%, respectively, while bicarbonate decreased arsenic concentration by 13% (**Figure 3.1A**). Over 7 days (**Figure 3.1B**), although phosphate increased arsenic concentration during the first 0–1 day, it contrarily reduced arsenic concentration in the longer reaction periods (43% lower than the control system on day 7). Silicate kept increasing arsenic concentration relative to the control system over the 7 days by 9%–47%, with the largest difference happening on day 1. In the presence of bicarbonate, arsenic concentration was reduced over the 7-day reaction time by 1%–26%, with the largest difference happening on day 7. Dissolved iron concentrations were also monitored during the 7-day reaction period (**Figure 3-S3A**). The highest iron concentration was observed in the phosphate system (up to 181.2 μg/L on day 2). After 2 days, the iron concentration in the phosphate system started to decrease. Note that ICP-MS measurements quantify the net iron concentrations, which are the amount dissolved from arsenopyrite minus the amount precipitated. Therefore, the decreasing iron concentration suggested that the formation rate of secondary iron-bearing minerals surpassed the iron dissolution rate from arsenopyrite. Sulfate concentrations were much higher (2–3.5 mg/L) compared with arsenic and iron concentrations for all four systems (0.2–1 mg/L for arsenic, and 0.05–0.2 mg/L for iron) (**Figure 3-S3B**), which may stem from the

incongruent dissolution of arsenic, iron, and sulfur from arsenopyrite, or more precipitation/adsorption removing iron and arsenic from the aqueous solutions. The incongruent dissolution of arsenic, iron, and sulfur from arsenopyrite has also been reported by previous studies on arsenopyrite dissolution.[183, 185, 187, 211] Characterization of reacted arsenopyrite by SEM-EDX (**Figure 3-S6F**) also indicated a lower atomic ratio of sulfur compared to arsenic and iron at surface after arsenopyrite dissolution, which will be discussed in next section.

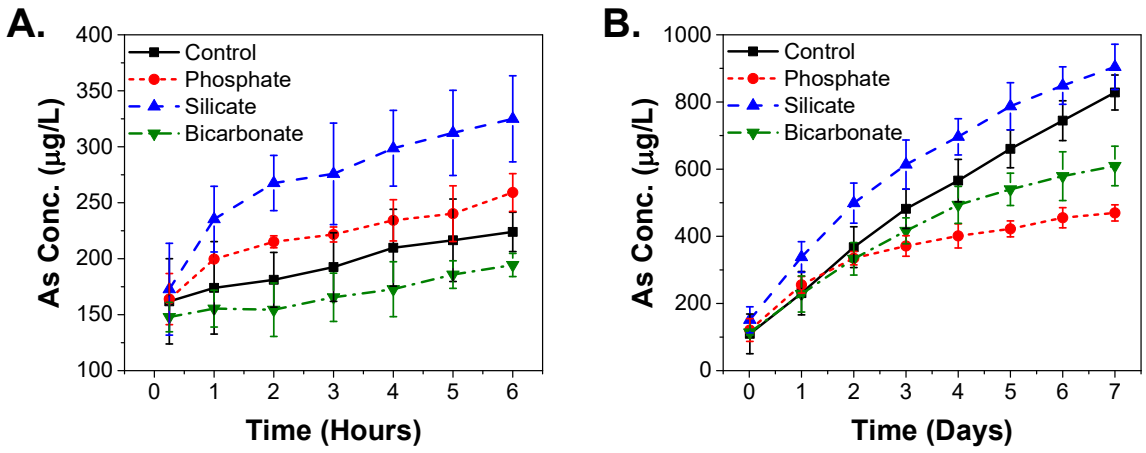

Figure 3.1 ICP-MS data showing aqueous arsenic concentrations at 10 mM IS and pH 7.0 in the presence of different oxyanions within 6 hours (**A**) and 7 days (**B**). The error bars represent the standard deviation of arsenic concentrations from triplicate batch experiments. The first samples for different systems were sampled after adjusting the pH of the mixed solutions to 7 (time = 20 minutes).

3.3.2 Secondary mineral precipitation

A better understanding of the differences in the extent, morphology, and surface properties of secondary minerals among the three oxyanions systems yields further insights into the observed trends in arsenic mobilization. **Figure 3.2** shows the AFM height mode images after 6 hours, 1 day, 4 days and 7 days in the presence of different oxyanions. These four systems exhibited differences in the extent and morphology of secondary mineral precipitation. To quantitatively understand the precipitation extents in these four systems, AFM height profile analysis of

secondary precipitates on arsenopyrite coupons after reactions for (i) 1 day and (ii) 7 days were conducted using Nanoscope 7.20 (**Figure 3-S4**). At least 50 particles per condition were analyzed. For the control system (**Figure 3.2A**), there was little precipitation after 6 hours, and the size of precipitates gradually increased from 18.3 ± 4.7 nm after 1 day to 39.5 ± 8.2 nm after 7 days. In the phosphate system, a significant amount of small precipitates covered the entire surface after 6 hours of reaction (**Figure 3.2B** (**i**)). During the entire reaction period, the vertical height of secondary precipitates was larger than the control system, and grew gradually from 20.7 ± 6.5 nm after 1 day to 61.0 ± 9.8 nm after 7 days. After 7 days (**Figure 3.2B** (**iv**)), the precipitates on the coupon formed aggregates, which also possessed bigger lateral dimensions than precipitates in other systems. The size of secondary precipitates in the silicate system grew from 15.2 ± 5.5 nm after 1 day to 29.1 ± 6.7 nm after 7 days, and the precipitates in the bicarbonate system grew from 17.5 ± 4.0 nm after 1 day to 25.5 ± 7.8 nm after 7 days. After 7 days, the precipitates in the phosphate system showed wider size distribution than those in the silicate and bicarbonate systems. The root-mean-square (RMS) roughness analyses of arsenopyrite coupons reacted for 1 day and 7 days were obtained from AFM images (**Figure 3-S5**). After 7 days, the RMS of the coupons reacted in the phosphate system was the highest among four systems (10.2 ± 2.0 nm), followed by silicate (9.2 ± 0.9 nm), bicarbonate (8.6 ± 0.2 nm), and the control (7.8 ± 1.0 nm). SEM images additionally showed the morphology change of coupon surfaces after 7 days (**Figure 3-S6A-E**). SEM-EDX showed that the relative atomic ratios of iron and arsenic normalized by sulfur on coupon surface increased in all the four systems compared with the unreacted arsenopyrite coupon (**Figure 3-S6F**). This increased ratios of Fe/S and As/S after dissolution can be resulted from incongruent dissolution among sulfur, arsenic, and iron, or larger incorporation extents of arsenic and iron into secondary precipitates than sulfur. The increased ratios of Fe/S and As/S on

arsenopyrite surface and the higher aqueous sulfur concentration than arsenic and iron indicate that the dissolved sulfur stayed more in the bulk solution rather than incorporating into/adsorbing on the mineral surfaces.

XPS experiments provided complementary evidence about the surface chemical property changes of arsenopyrite coupons after batch reactions (**Figure 3-S7**). The binding energy peaks of Fe 2P were separated into Fe $2p_{3/2}$, Fe $2p_{3/2}$ satellites, Fe $2p_{1/2}$, and Fe $2p_{1/2}$ satellites,[212-214] with peaks for Fe^{2+} (710.43 eV, 713.61 eV, 723.45 eV, and 728.54 eV), and peaks for Fe^{3+} (711.70 eV, 719.05 eV, and 725.89 eV).[212-216] A Gaussian−Lorentzian curve-fitting method was utilized to obtain the absolute areas for different peaks, and the areas were then used to calculate the percentages of Fe^{2+} and Fe^{3+} and the ratio of Fe^{2+}/Fe^{3+}.[217] A summary of XPS Fe2p reference binding energies, absolute values of areas for each peak, and calculated percentages for oxidation states are provided in **Table 3-S2**. The unreacted arsenopyrite coupons contained small amount of Fe^{3+} on the surface (78% Fe^{2+} and 22% Fe^{3+}), and the Fe^{2+}/Fe^{3+} ratio was calculated to be 3.54. In comparison with the unreacted arsenopyrite, all the four systems exhibited a decreased Fe^{2+}/Fe^{3+} ratio on the coupon surface after 7 days. The increase of Fe^{3+} percentage on coupon surface can be attributed to iron(III) secondary mineral precipitation and Fe^{3+} adsorption. Although XPS result cannot show quantitatively the amount of iron(III) phases formed (including precipitation and adsorbed ions), it can be used to semi-quantitatively compare the extent of iron(III) solid phases formation on coupons in each system. For the control, the Fe^{2+}/Fe^{3+} ratio decreased to 1.17 after 7 days. All the three oxyanions showed smaller Fe^{2+}/Fe^{3+} ratio than the control, among which the phosphate system exhibited the lowest Fe^{2+}/Fe^{3+} ratio ($Fe^{2+}/Fe^{3+} = 0.69$) after 7 days, indicating a highest extent of iron(III) phases formation on the coupons. In addition, the O 1s, C 1s, P 2p, and

Si 2p peaks were measured for different oxyanion systems to confirm the presence of phosphate, silicate, and bicarbonate on arsenopyrite coupons (**Figure 3-S8**).

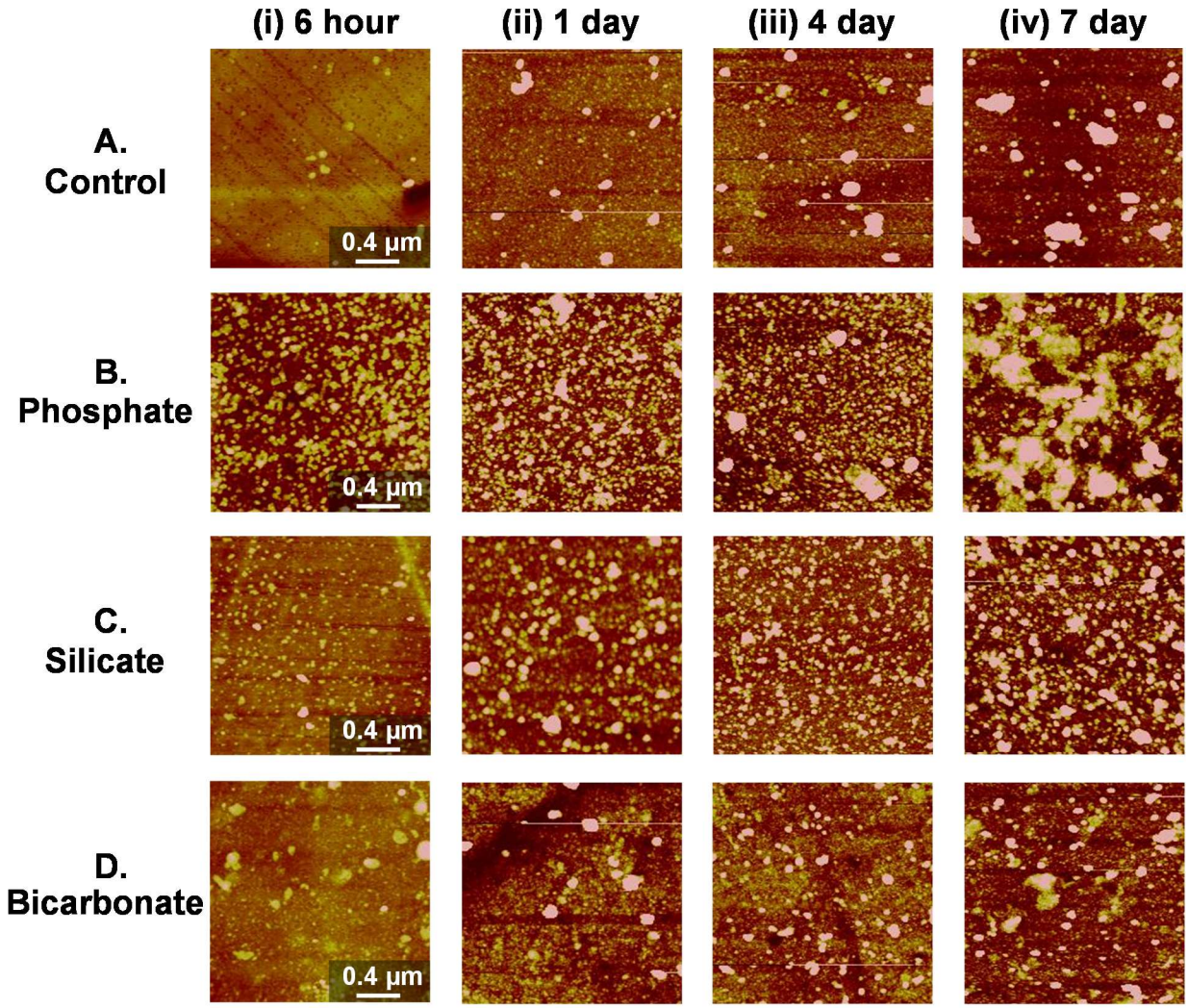

Figure 3.2 Tapping mode AFM images (2 µm × 2 µm) showing secondary mineral precipitations on arsenopyrite coupons at 10 mM IS and pH 7.0 after 6 hours (**i**), 1 day (**ii**), 4 days (**iii**), and 7 days (**iv**) in the (**A**) control, (**B**) phosphate, (**C**) silicate, and (**D**) bicarbonate systems. Height scale: 20 nm.

3.3.3 Secondary mineral phase identification

Secondary mineral phase on coupons was identified using Raman spectroscopy by comparing their spectra with iron oxide references (**Figure 3.3**). The Raman spectrum of unreacted arsenopyrite showed three characteristic peaks at 333, 827, and 1368 cm^{-1}, corresponding to the

vibrations of As−S bonds, the arsenate anionic groups (As−O), and Fe−O bonds, respectively.[218-220] For the control system which contained only sodium nitrate (**Figure 3.3A**), there was no detectable secondary mineral precipitation on the surface in the early reaction period (< 1 day). After 7 days, two additional peaks appeared at 1330 cm^{-1} and 1600 cm^{-1}. The 1330 cm^{-1} and 1600 cm^{-1} peaks were also observed from the Raman spectra of an iron(III) (hydr)oxide mineral, maghemite (γ-Fe_2O_3).[221-223] Previously, Mazzetti and Thistlethwaite used these two bands to identify maghemite during the transformation of ferrihydrite to hematite.[223] The yellow coating of iron(III) (hydr)oxides on the arsenopyrite surface could also be observed in the optical images for 7 days. The Raman spectra of the phosphate system (**Figure 3.3B**) showed the appearance of 1330 cm^{-1} and 1600 cm^{-1} peaks in the early reaction period (< 1 day), and showed the highest intensity of these two peaks after 7 days, suggesting that the presence of phosphate ions accelerated the formation of secondary iron(III) (hydr)oxide on coupon surface. In the silicate and bicarbonate systems, the formation of maghemite on the coupons was also observed after 7 days **Figure 3.3C** and **3.3D**). The relative intensities of representative peaks of observed maghemite on reacted coupons were different compared with maghemite reference sample, which might be due to the orientation or particle size difference of maghemite formed in our samples.[224-225] Formation of maghemite from the oxidation of arsenopyrite or pyrite has also been reported by previous studies.[226-227] Other types of iron-containing minerals, such as iron oxides including six-line ferrihydrite (~370, 510 and 710 cm^{-1}),[222] magnetite (~670 cm^{-1}),[222] goethite (~385 cm^{-1}),[222] and hematite (~1300 cm^{-1}),[222] iron carbonate minerals including siderite (287, 731 and 1090 cm^{-1}),[222] iron arsenates including scorodite (~800 cm^{-1}),[228] quartz (~460 cm^{-1}),[229] and iron phosphates including phosphosiderite (~990 cm^{-1})[230] were also considered, but their spectra did not match with those found on coupons reacted for 1 day and 7 days. Maghemite was identified here as the

main secondary mineral precipitate, however, whether maghemite precipitates directly or is transformed from less crystalline iron (hydr)oxide phases during arsenopyrite dissolution is still in contention. Future *in situ* study can investigate the phase transformation of secondary mineral precipitates from arsenopyrite dissolution.

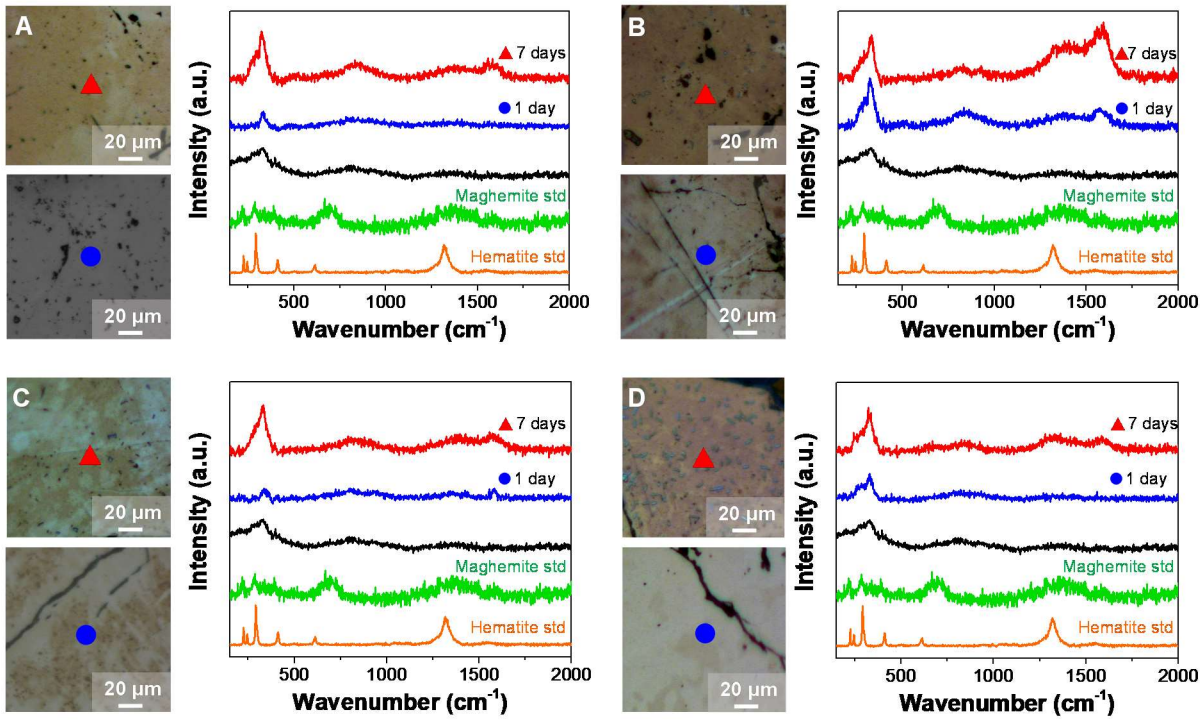

Figure 3.3 Optical microscope images and Raman spectra for unreacted arsenopyrite (black) and arsenopyrite coupons reacted in the (**A**) control, (**B**) phosphate, (**C**) silicate, and (**D**) bicarbonate systems for 1 day (●, blue) and 7 days (▲, red). Two iron oxide references were used: maghemite standard (green) and hematite standard (orange). For each coupon, at least three spots were measured, and the results were consistent.

WAXD measurements provided complementary information of secondary mineral phases formed on powder surfaces or in the solution (**Figure 3.4A**). The WAXD pattern of unreacted arsenopyrite powders showed characteristic peaks of arsenopyrite at 26.1, 40.8, and 45.8 nm^{-1} (yellow triangles), and peaks of quartz at 18.8 and 34.6 nm^{-1} (purple triangles), which were consistent with arsenopyrite and quartz XRD patterns.[62] After reaction for 7 days, the phosphate

system showed clear increase of peaks indicating maghemite (green triangles in **Figure 3.4A**, see **Figure 3-S9** for detailed reference peak information).[231] In comparison, the maghemite peaks were indiscernible in the control, silicate and bicarbonate systems, which can be explained by the fact that the amount of secondary precipitates in phosphate system was significantly higher than other systems as shown from AFM and Raman results. Additionally, in the phosphate system, new peaks at 13.1, 17.2, 24.6, 35.0 nm^{-1} were observed (orange triangles in **Figure 3.4A**), which matched with the patterns of an iron(III) phosphate mineral, phosphosiderite ($FePO_4 \cdot 2H_2O$, see **Figure 3-S9** for detailed reference peaks of different iron phosphates).[230] The existence of iron(III) phosphate as a secondary mineral phase was not observed in the Raman spectra of phosphate system, which can be affected by the large quantities of iron(III) (hydr)oxide precipitates on the coupon surface. It is also possible that secondary minerals phases formed on millimeter sized coupons may differ from those formed on micrometer-sized powder surfaces or in the solution. In addition, Raman measurement provides the representative phase information in spots that have been measured, while WAXD provides averaged phase information of the entire solid product after reaction. By using Visual MINTEQ (ver. 3.1), the saturation indices of potential secondary mineral phases in different systems after reaction for 1 day and 7 days were calculated as shown in **Table 3-S3**. The saturation index (SI, $\log(IAP/K_{sp})$) of maghemite (SI = 6.87) was much higher than that of iron(III) phosphate (SI = 2.63). Thus, in the phosphate system, while iron(III) phosphate may be present, the majority of secondary mineral phases should be maghemite.

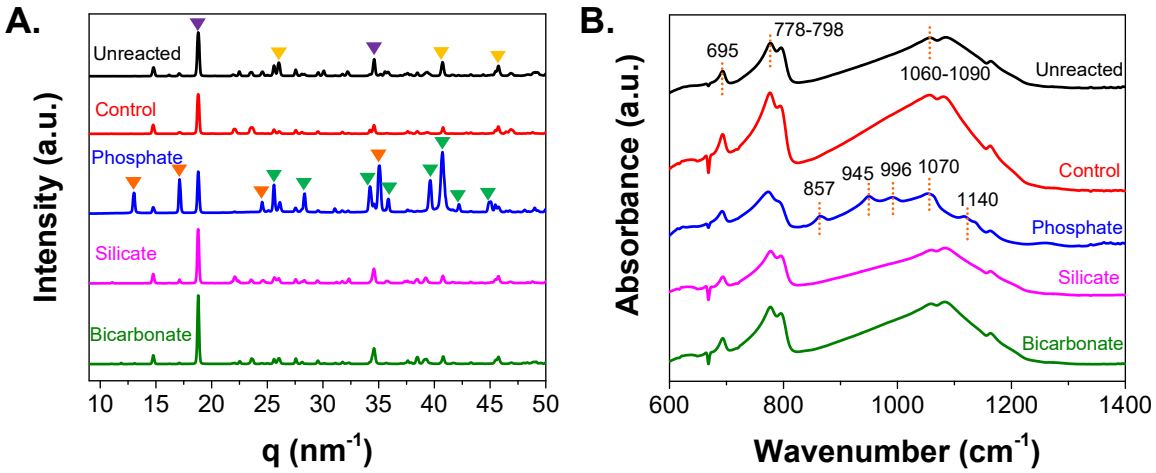

Figure 3.4 (**A**) WAXD patterns for unreacted arsenopyrite and arsenopyrite powders reacted at 10 mM IS and pH 7.0 for 7 days in the presence of different oxyanions. ▼: arsenopyrite; ▼: quartz; ▼: maghemite; ▼: phosphosiderite. (**B**) FTIR spectra of unreacted arsenopyrite powders, and arsenopyrite powders reacted with different oxyanions.

3.3.4 Mechanisms of arsenic mobilization and secondary mineral precipitation in different oxyanion systems

To provide information about the chemical bonds between different oxyanions and the arsenopyrite powder surfaces, FTIR measurements were conducted (**Figure 3.4B**). Detailed FTIR reference peak positions for phosphate, silicate, and bicarbonate interactions with solid surfaces are provided in the supporting information (**Table 3-S4**). Arsenopyrite powders can interact with water and oxygen in the atmosphere during the preparation process, forming sulfates and oxides on the surface. Therefore, even unreacted arsenopyrite showed characteristic peaks of SO_4^{2-} adsorption on solid surfaces at 695 and 778–798 cm^{-1}, and S–O/S=O vibrations at 1060–1090 cm^{-1},[232] which are consistent with a previous pyrite study.[233] The spectrum of the phosphate system showed the additional characteristic peaks of phosphate adsorption, including ν_s(P–OH) vibration at 857 cm^{-1}, and ν_3(P–O) asymmetric vibration split at 945, 1070, 1140 cm^{-1}.[234] The peak at 996

cm^{-1} is attributed to Fe–PO_4 surface monodentate mononuclear complexation.[235-236] These peaks suggested binding interactions between phosphate and arsenopyrite surfaces, which can explain the promoted arsenopyrite dissolution by phosphate discussed earlier. For the arsenopyrite powders reacted with silicate and bicarbonate, there was no obvious peak showing the binding interactions between the oxyanion and arsenopyrite powder surface.

From the aqueous and solid phase analysis using arsenopyrite powders and coupons under conditions relevant to MAR operations, distinct arsenopyrite dissolution and secondary mineral precipitation behaviors were observed for the three oxyanion systems (table adjoining **Figure 3.5**). As shown in aqueous phase analysis (**Figure 3.1**), phosphate showed time-dependent reversed effect on arsenic mobility, with increased arsenic mobility over a short reaction period (< 1 day), and decreased arsenic mobility in the long term (> 1 day). The increased arsenic mobility over short term (< 1 day) can result from the promoted dissolution of arsenopyrite by surface complexation and competitive adsorption. As shown from FTIR (**Figure 3.4B**), the complexation between phosphate anions and the arsenopyrite powder surfaces, such as the monodentate mononuclear surface complexation between iron and phosphate, can promote the release of iron, and further enhance the dissolution of arsenic.[235-236] The dissolved iron(II) in the solution can be further oxidized to form iron(III), which can in turn promote dissolution and secondary mineral formation by triggering electron transfer between iron(III) and iron(II) in arsenopyrite.[186] The faster formation of secondary minerals, such as iron(III) (hydr)oxide and iron(III) phosphate, could lower the iron concentration near arsenopyrite powder surface and facilitate arsenopyrite dissolution. Furthermore, competitive adsorption between phosphate and arsenate anions onto iron(III) (hydr)oxide adsorption sites can lead to less adsorption of arsenate and consequently increase its mobility.[192, 195-197]

In the long term (> 1 day), large quantities of secondary precipitates could adsorb a significant amount of arsenic from the solution, compensating the effects from promoted dissolution and competitive adsorption. The E_h measurements provide additional insight into dissolution and precipitation trends. E_h measurements for the four systems during 7 days indicated that the phosphate system had the highest redox potential over the entire reaction period (**Figure 3.5A**), which could be the result of higher concentrations of dissolved iron (**Figure 3-S3A**). The high positive redox potential in the phosphate system indicates that the condition is an oxidizing environment for arsenopyrite dissolution. This could promote the oxidative dissolution of arsenopyrite, the oxidation of dissolved iron(II) to iron(III), and the precipitation of iron(III) minerals, a process consistent with our AFM, Raman, and WAXD experimental observations. Our previous study using grazing incidence small-angle X-ray scattering (GISAXS) showed that the nucleation and growth of iron(III) (hydr)oxide precipitates were promoted in the presence of phosphate,[64] which was partly owing to the negatively charged phosphate anions incorporation into the positively charged iron(III) (hydr)oxides, decreasing the surface charge and thus decreasing the repulsive forces between nuclei. Bridging effects of phosphate and higher saturation indices with respect to iron(III) (hydr)oxide resulting from higher iron concentrations can also contribute to the observed significantly increased secondary mineral precipitation in the phosphate system.[64, 237]

In the silicate system, the arsenic mobility was increased over the entire reaction period. Previous studies about silicate effects on iron sulfides dissolution showed that silicate can passivate the mineral surface and decrease dissolution rate.[238-239] Thus, the increased arsenic mobility in silicate system should be attributed to other potential mechanisms instead of promoted dissolution. First, silicate was found to significantly decrease arsenic removal by iron(III) (hydr)oxide

precipitates via the competitive adsorption between arsenic species and silicate.[189, 202, 240] Second, silicate can also complex with dissolved iron(III) or newly formed iron(III) (hydr)oxide precursors, hindering the precipitation and aggregation of iron(III) (hydr)oxide.[241-244] The inhibited formation of iron(III) (hydr)oxide consequently decreases the adsorption sites for arsenic. Our AFM images also confirmed that silicate decreased the average secondary precipitate sizes compared with the control system (**Figure 3.2** and **Figure 3-S4**).

In the bicarbonate system, the arsenic mobility was decreased both in 6 hours and 7 days compared with the control system. The pH measurements in 6 hours (**Figure 3-S10B**) and 7 days (**Figure 3.5B**) can provide more insights. In both 6 hours and 7 days, the trend of pH values in four systems was: bicarbonate > phosphate > control > silicate. The addition of bicarbonate decreased the pH drop both in 6 hours and in 7 days due to its buffering effect, and the higher pH could slow down the dissolution of arsenopyrite based on Eq. 1b, resulting the lowered arsenic mobility in 6 hours compared with the control system. Over 7 days, because of higher pH values in the bicarbonate system than in the control system, the extent of iron(III) (hydr)oxide precipitation can be enhanced. While electrostatic interaction could decrease arsenic adsorption at higher pH, the enhanced iron(III) (hydr)oxide precipitation may compensate for this effect by creating more reactive sites for adsorption or by incorporating more arsenic into iron(III) (hydr)oxide than in the control system, further decreasing arsenic mobility. It should also be noted that the effects of bicarbonate on arsenic adsorption onto iron(III) (hydr)oxide surfaces is highly pH and concentration dependent.[191, 208] Our results indicate that ~0.1 mM bicarbonate can decrease arsenic mobility from arsenopyrite at pH 7. Some other studies suggested that with higher pH values and increased bicarbonate concentrations (> 20 mM), carbonate species can decrease arsenic adsorption on mineral surfaces and form aqueous complexes with arsenic, leading to higher

arsenic mobility.[205, 245-248] In the broad context, because the bicarbonate concentration in the injected water of MAR sites (< 0.25 mM) is often lower than that in the original underground water system (0.5–8 mM in the U.S. groundwater),[249] the MAR operation may actually dilute the bicarbonate concentration in the underground water system and help to decrease arsenic mobility from arsenopyrite in the short term. In the long term, the bicarbonate concentrations will ultimately depend on field-specific interactions. For example, at calcite- or carbonate-rich MAR sites, the pH of the aquifer water can be mainly controlled by the aqueous carbonate chemistry of the specific sites after the initial impacts from recharged water.[17]

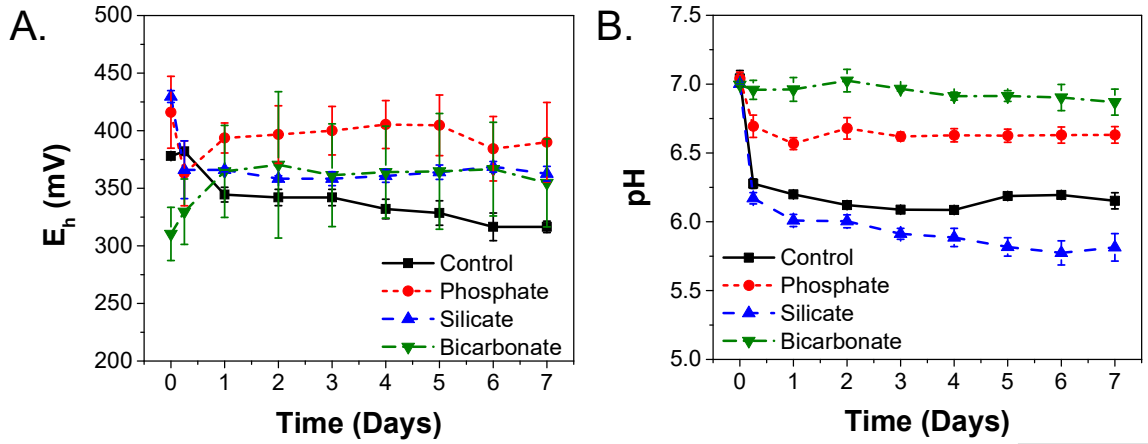

Systems	As mobility (6 hours)	As mobility (7 days)	Size of precipitates (day 7)	Phases of precipitates	Surface Fe^{2+}/Fe^{3+} ratio	Chemical binding
Phosphate	↑↑	↓↓↓	↑↑↑	γ-Fe_2O_3 $FePO_4 \cdot 2H_2O$	↓↓↓	monodentate mononuclear
Silicate	↑↑↑	↑↑↑	↓↓	γ-Fe_2O_3	↓↓	-
Bicarbonate	↓↓	↓↓	↓	γ-Fe_2O_3	↓	-

Figure 3.5 (**A**) E_h (mV) values of different oxyanion systems during the 7-day reaction period. All reactors were at room temperature (25 °C) and open to the atmosphere (P_{O_2} = 0.21 atm); (**B**) pH measurement of different oxyanion systems during the 7-day reaction period. The table adjoining **Figure 3.5** contains a summary of different oxyanions effects on arsenic mobility and secondary precipitation from arsenopyrite.

3.4 Conclusions and environmental implications

In this work, we evaluated the effects of three oxyanions, phosphate, silicate and bicarbonate, on arsenic mobilization from arsenopyrite and secondary mineral precipitation by conducting bench-scale experiments simulating MAR systems, and obtained a more comprehensive understanding of water chemistry effect on arsenic mobilization in MAR. Phosphate showed time-dependent reversed effect on arsenic mobility, which can result from the compensating effects between promoted dissolution and enhanced adsorption on secondary mineral phases. Initially, phosphate promoted the dissolution of arsenopyrite through monodentate mononuclear surface complexation, thus increasing arsenic mobility. However, in the long term, the enhanced formation of secondary minerals, such as iron(III) (hydr)oxides (i.e., maghemite) and iron(III) phosphate (i.e., phosphosiderite), could adsorb a significant amount of arsenic from the solution. Therefore, the elevated phosphate concentration after injecting reclaimed water into MAR sites may actually reduce arsenic mobility in the long term. The results also showed that silicate can increase the arsenic mobility, therefore its concentration should be decreased before injection and carefully monitored during MAR operation. The oxyanions that we added had varied buffering capacity themselves as shown from the pH measurements. In some MAR sites, sediments can provide some pH buffering capacity, such as carbonate species from calcite-rich sediments.[17] In this case, stronger pH buffering capacity of sediments may counter the pH drop caused by secondary iron(III) hydrolysis from arsenopyrite dissolution, thus causing a higher extent of secondary iron(III) (hydr)oxide formation.

The arsenic concentrations observed in our batch experiments (~100–900 μg/L) were higher than those in recovered water from MAR field sites (~10–100 μg/L),[17, 179] which may lead to an increased iron(III) (hydr)oxide particle size by the bridging effect.[64] Even so, our laboratory

batch experiments on the effects of oxyanions on arsenopyrite dissolution and secondary mineral precipitation can provide useful information on arsenic mobilization trends in highly redox complex systems, and offer important implications for field-scale MAR projects. Together with other water components, including abundant anions (Cl^- and NO_3^-),[62] cation (Fe^{3+}),[186] and dissolved organic matter[187], the effects of different oxyanions examined in this study provide a comprehensive and systematic understanding of unintentional geochemical reactions and mineral–injected water interactions that lead to arsenic mobilization from arsenic bearing minerals in underground solid–aqueous systems. As reclaimed water will be utilized as a main water resource for MAR systems, a specific chemical composition control of recharged water, for example, the concentrations of oxyanions, should be considered as an important parameter to monitor during MAR operation. New observations from this study also offer insight into preventing unnecessary secondary pollution when building new sustainable water management systems.

Acknowledgments

We are grateful for support received from the National Science Foundation (EAR-1424927). We wish to thank the Institute of Material Science & Engineering Recharge Center (IMSE) and the Nano Research Facility (NRF) at Washington University in St. Louis for offering the opportunity to use instruments. Use of the Advanced Photon Source (Sector 11-ID-B for WAXD) at Argonne National Laboratory was supported by the U.S. Department of Energy, Office of Science, Office of Basic Energy Sciences, under Contract No. DE-AC02-06CH11357. Lastly, we thank the Environmental NanoChemistry Lab members for providing valuable discussions and suggestions and thank to Prof. James Ballard for his careful review of the manuscript.

Supporting information for Chapter 3

3-S1. Experimental design for aqueous and solid phase analysis

Table 3-S1. Experimental conditions for batch reaction systems.

Oxyanions	Concentration of Oxyanions (mM)	pH	IS (mM)	FeAsS (g)
Control	0	7.0 ± 0.1	10	0.050 ± 0.001
Phosphate	0.1	7.0 ± 0.1	10	0.050 ± 0.001
Bicarbonate	0.1	7.0 ± 0.1	10	0.050 ± 0.001
Silicate	0.1	7.0 ± 0.1	10	0.050 ± 0.001

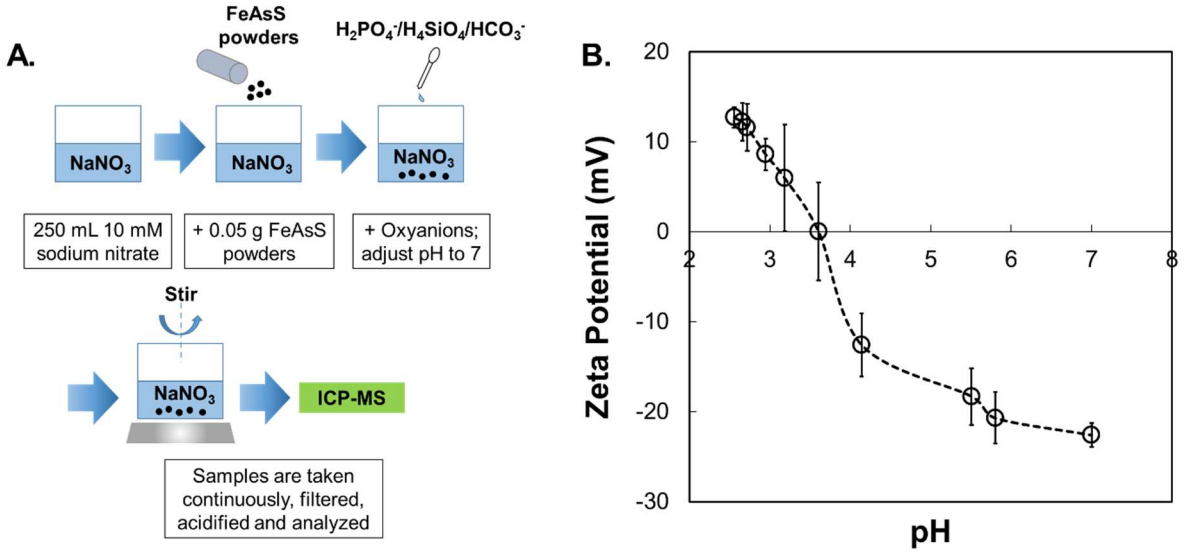

Figure 3-S1. (A) Experimental protocol for aqueous phase analyses. Sieved arsenopyrite (FeAsS) powders were sonicated and washed to remove fine arsenopyrite from the surface. The samples were then stirred in a 10% HCl bath for two hours to remove any oxidation from the surface. Finally, samples were filtered and washed with ethanol before drying in the anaerobic chamber. Samples were stored in the anaerobic chamber prior to use to prevent re-oxidation. 250 mL of 10 mM sodium nitrate solution was prepared in each batch system. 0.05 g of arsenopyrite powders were added to each solution. 2.5 mL of 10 mM oxyanion stock solution was added to their batch reactor to achieve a concentration of 0.1 mM for the oxyanions. The pH of these solutions was adjusted to 7.0 ± 0.2 before reaction using nitric acid and sodium hydroxide. The reactors were stirred continuously during the entire reaction time. At each sampling time, aliquots of 2 mL solution were taken out, filtered, and acidified to 2% v/v acid with nitric acid, and capped before

measurement using ICP-MS. (B) Zeta potentials of arsenopyrite powders with various pH values. The isoelectric point of arsenopyrite powders (pH_{iep}~3.6) was determined. The pH values were changed by adding sodium hydroxide and nitric acid.

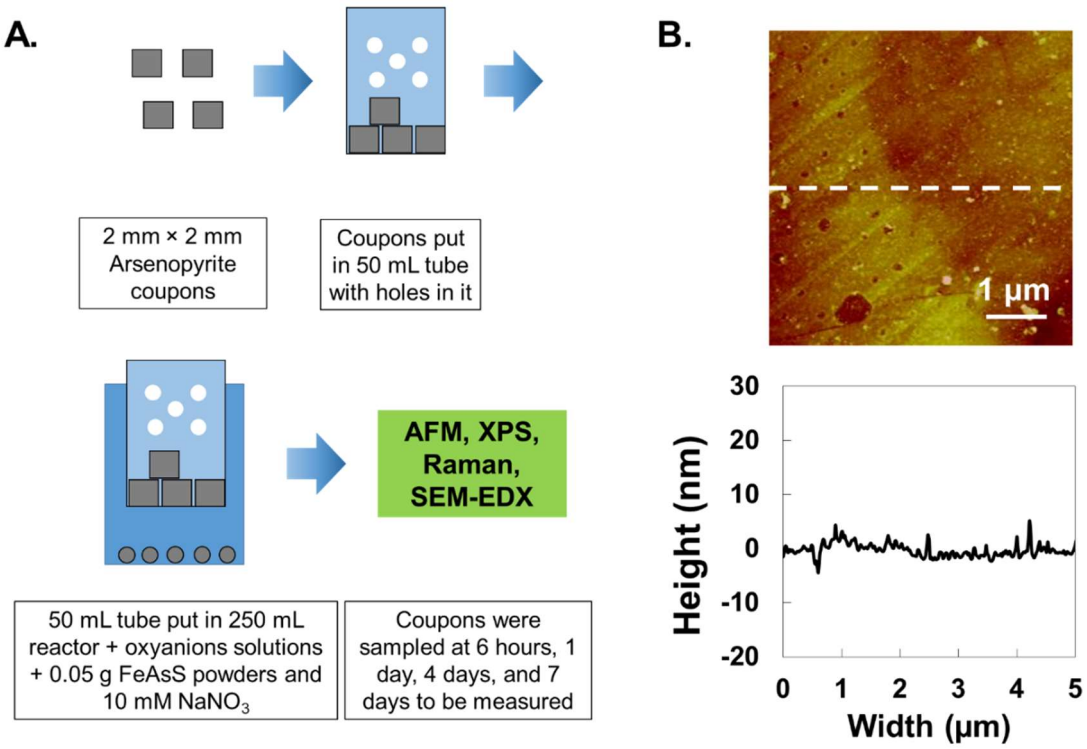

Figure 3-S2. (A) Experimental protocol for solid phase analyses. 2 mm × 2 mm arsenopyrite coupons were prepared and added into a 50 mL tube with several holes on it. This 50 mL tube with coupons was then submerged into 250 mL of 10 mM sodium nitrate solution. This setup allowed the solution condition in the 50 mL tube to be the same as the outside solution, while stirring the outside solution did not physically move the coupons, eliminating the effects of solution movement on secondary mineral precipitations on coupons. 0.050 ± 0.001 g of arsenopyrite powder were added to each solution. 2.5 mL of 10 mM oxyanion stock solution was added to their batch reactors to achieve a concentration of 0.1 mM for the oxyanion (TOTP, TOTSi, and TOTC). The pH of these solutions was adjusted to 7.0 ± 0.2 before reaction using nitric acid and sodium hydroxide. The reactors were stirred continuously during the entire reaction time. At 6 h, 1 day, 4 days, and 7 days, coupons were taken out, rinsed with deionized water, and dried with high purity nitrogen gas (Airgas Inc.). Reacted coupons were stored in the anaerobic chamber prior to analysis using AFM, XPS, Raman, and SEM-EDX. (B) Tapping mode AFM image (5 μm × 5 μm) of unreacted arsenopyrite coupon. Height scale: 20 nm. Flat arsenopyrite coupons were cleaned using acetone, ethanol, and isopropanol prior to use.

3-S2. Quantification of iron and sulfate concentrations.

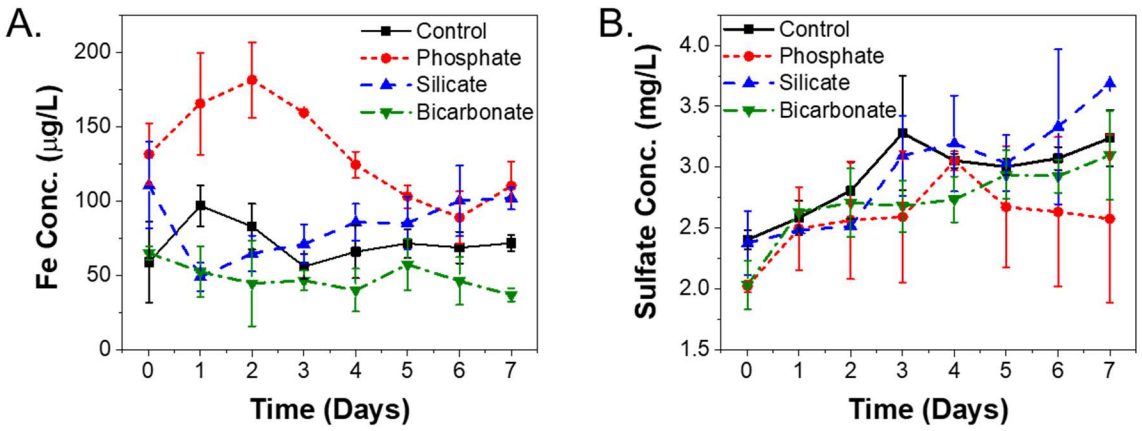

Figure 3-S3. (A) ICP-MS data showing aqueous iron concentrations at 10 mM IS and pH 7.0 in the presence of different oxyanions during 7 days. (B) IC results showing the sulfate concentrations at 10 mM IS and pH 7.0 in the presence of different oxyanions during 7 days. The error bars represent the standard deviation of iron and sulfate concentrations from triplicate batch experiments. The first samples for different systems were sampled after adjusting the pH of the mixed solutions to 7 (time = 20 minutes).

3-S3. AFM information.

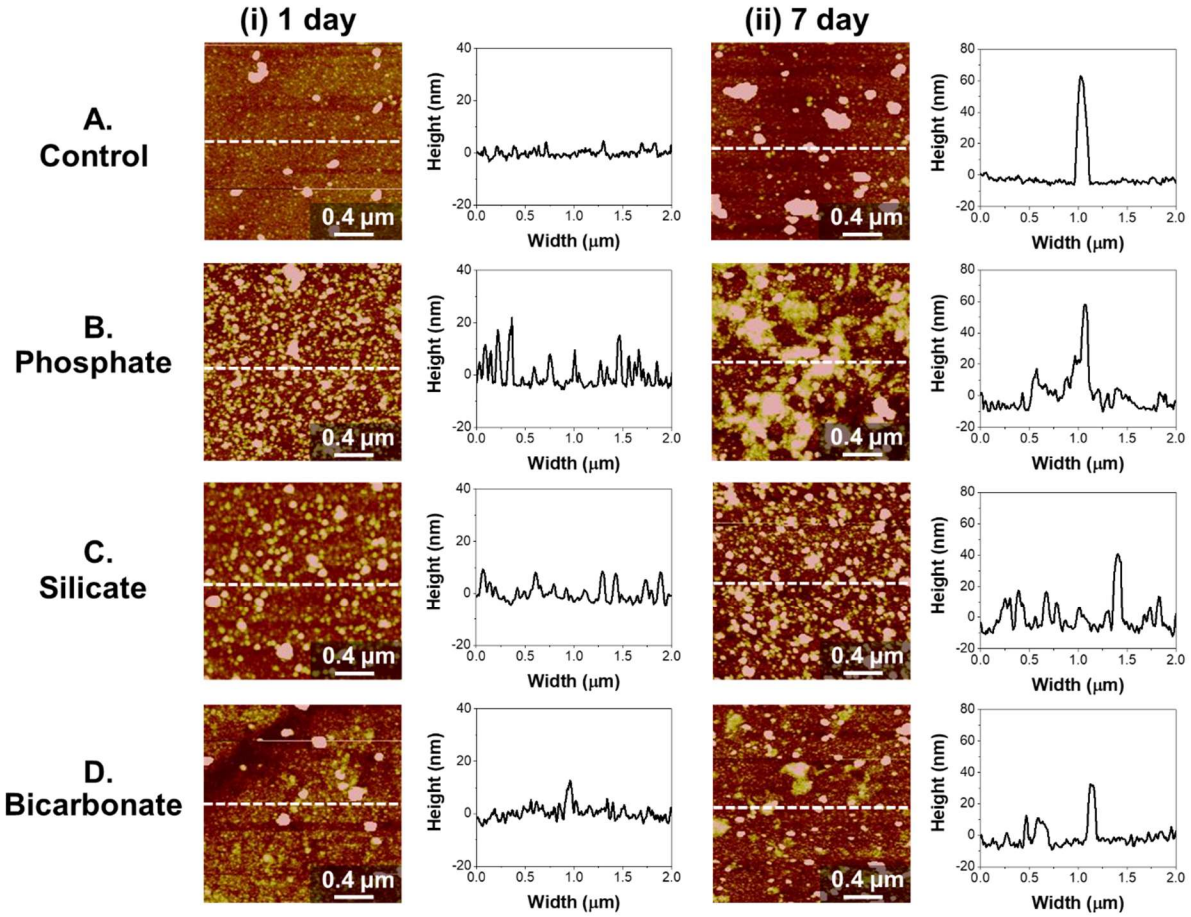

Figure 3-S4. Height information of secondary precipitates on arsenopyrite coupons after reactions for (i) 1 day and (ii) 7 days in the presence of (A) control, (B) phosphate, (C) silicate, and (D) bicarbonate. AFM images were cut using Nanoscope 7.20, shown using dotted lines, to provide the height profile graphs next to each image.

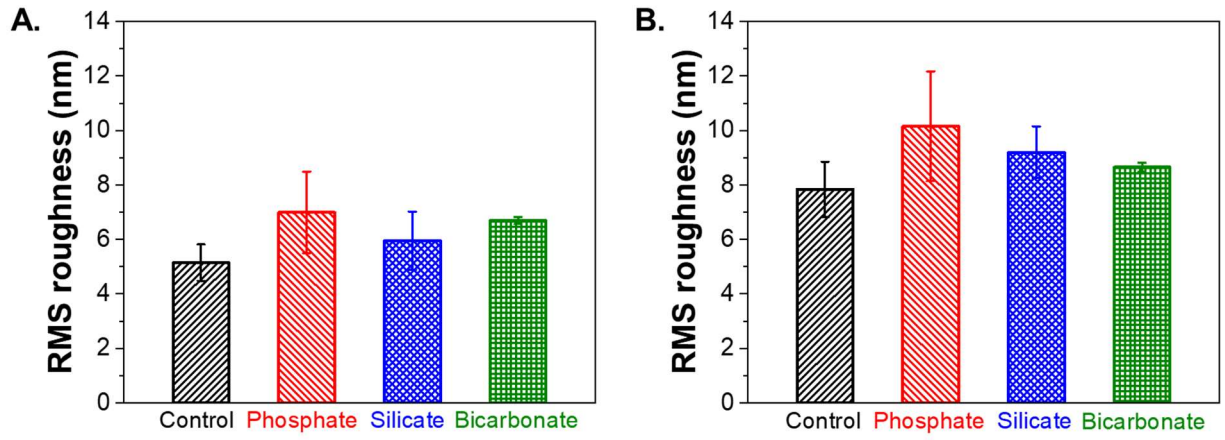

Figure 3-S5. The root-mean-square (RMS) roughness of FeAsS coupons after reaction for 1 day (A) and 7 days (B) obtained from AFM images.

3-S4. SEM images of reacted arsenopyrite coupons.

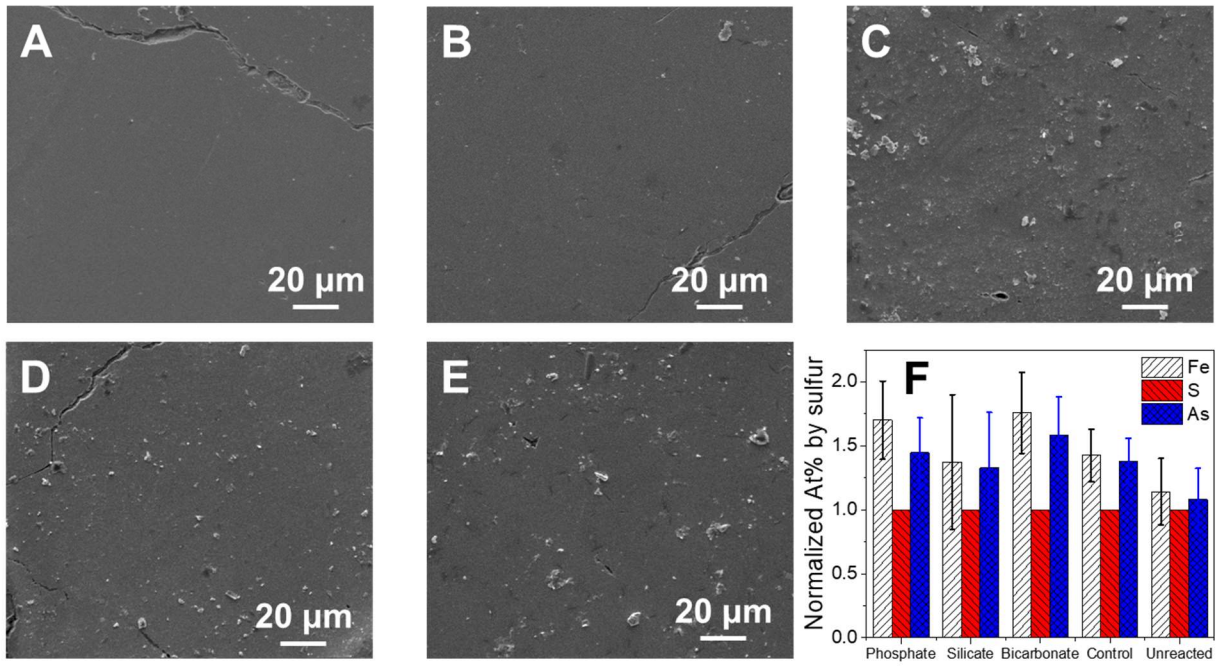

Figure 3-S6. SEM images (× 2000 magnification, 10 kV acceleration voltage) of arsenopyrite coupons after 7 days for (A) unreacted, (B) control, (C) phosphate, (D) silicate, and (E) bicarbonate systems. (F) Normalized atomic ratio of iron and arsenic by sulfur from energy dispersive X-ray analysis (EDX) imaging of arsenopyrite coupons.

3-S5. XPS information.

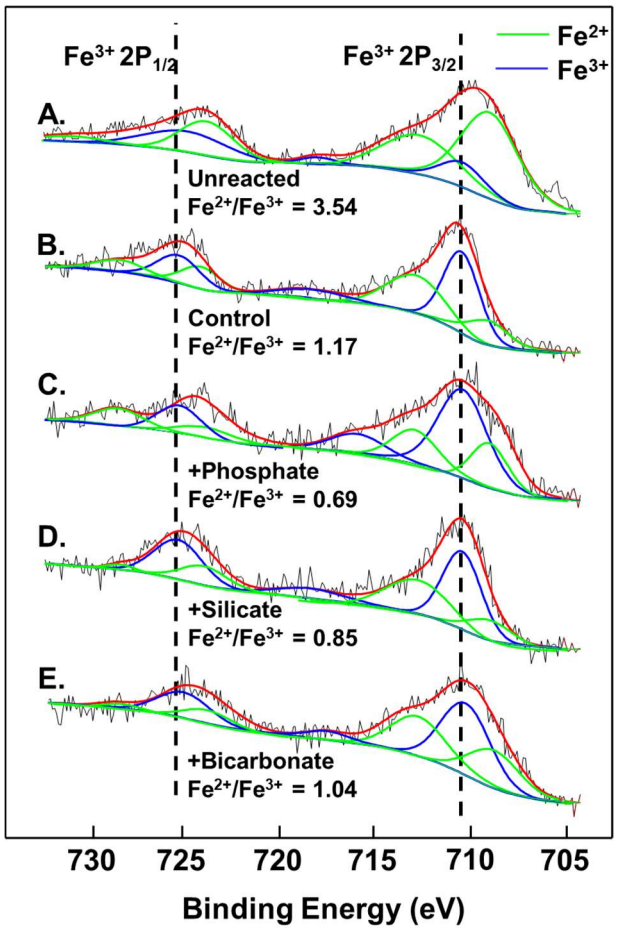

Figure 3-S7. XPS spectra of Fe 2p obtained from arsenopyrite coupons at 10 mM IS and pH 7.0 after 7 days reaction in the presence of different oxyanions: (A) unreacted FeAsS; (B) control; (C) phosphate; (D) silicate; and (E) bicarbonate. Dotted lines are the position of two different Fe 2p peaks: $Fe2p_{3/2}$ and $Fe2p_{1/2}$. Blue and green peaks represent Fe^{3+} and Fe^{2+}, respectively. The red curves were the fitting results from the Gaussian−Lorentzian curve-fitting method. Triplicate samples were measured for calculating the Fe^{2+}/Fe^{3+} ratios of each system (error ≈ ± 0.1).

Table 3-S2. XPS reference binding energies, absolute values of areas for each peak, and calculated ratios of Fe^{2+}/Fe^{3+} with different oxyanions for Fe 2p.[212-214]

Peaks		Fe $2p_{3/2}$		Fe $2P_{3/2}$ satellites		Fe $2P_{1/2}$		Fe $2P_{1/2}$ satellites	Fe^{2+}/Fe^{3+} ratio
		Fe^{2+}	Fe^{3+}	Fe^{2+}	Fe^{3+}	Fe^{2+}	Fe^{3+}	Fe^{2+}	
BE (eV)		710.4	711.7	713.6	719.1	723.5	725. 9	728.5	
Unreacted	Area	1744	350	978	73	591	549	128	78%/22% =3.54
	%Area	39.5	7.9	22.2	1.6	13.4	12.5	2.9	
Control	Area	213	601	535	124	201	227	130	54%/46% =1.17
	%Area	11.3	29.3	26.1	6.1	9.8	11.1	6.4	
Phosphate	Area	270	674	219	154	115	220	121	41%/59% =0.69
	%Area	15.2	38.0	12.4	8.7	6.5	12.4	6.8	
Silicate	Area	163	526	462	121	171	323	24	46%/54% =0.85
	%Area	9.1	29.4	25.8	6.8	9.6	18.0	1.33	
Bicarbonate	Area	199	330	203	32	80	125	18	51%/49% =1.04
	%Area	20.2	33.4	20.5	3.3	8.1	12.7	1.8	

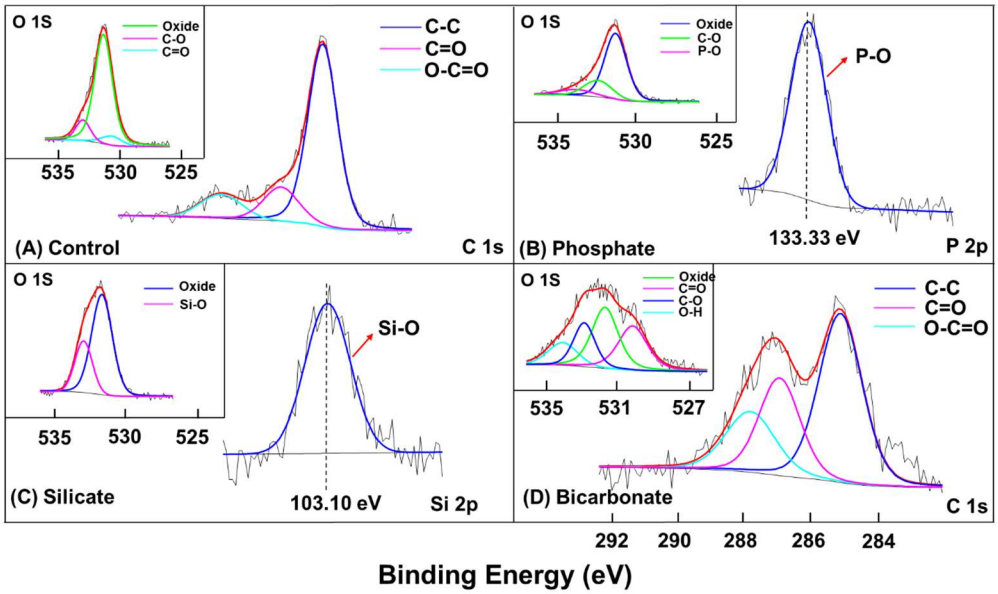

Figure 3-S8. O 1s, C 1s, P 2p, and Si 2p peaks for different oxyanions. (A) O 1s and C 1s for control system;[250] (B) O 1s and P 2p for phosphate system;[251-252] (C) O 1s and Si 2p for silicate system;[253] (D) O 1s and C 1s for bicarbonate system.[250]

3-S6. WAXD information.

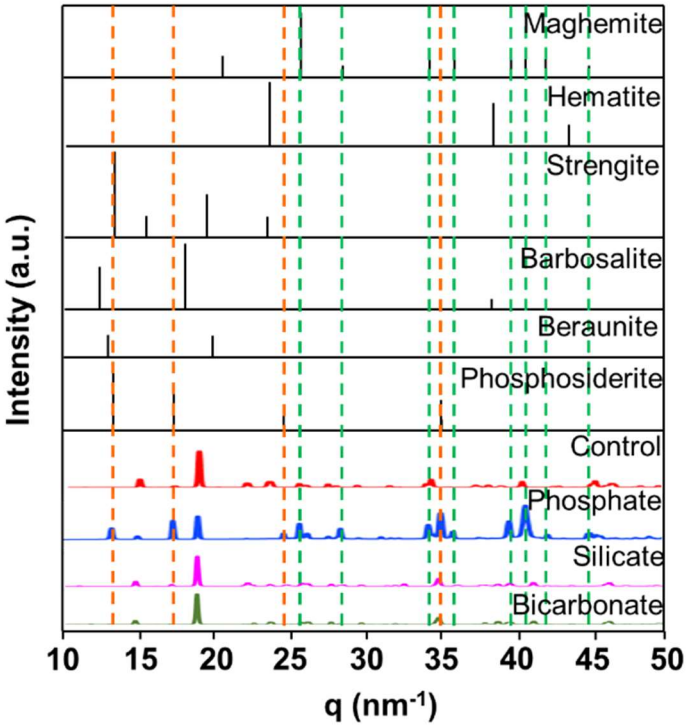

Figure 3-S9. WAXD patterns of arsenopyrite powders reacted for 7 days and representative iron (hydr)oxide and iron phosphate references. The orange lines indicate the characteristic peaks of phosphosiderite.[230] The green lines indicate the characteristic peaks of maghemite.[231]

3-S6. Saturation index (SI) calculation.

Table 3-S3. Saturation indices (SI) of potential secondary mineral phases in different systems after reaction for 1 day and 7 days calculated using Visual MINTEQ (ver. 3.1).

Saturation index (=logIAP - $logK_{sp}$)*	Day 1	Day 7
Control	Maghemite SI = 5.90	Maghemite SI = 5.53
Phosphate	Maghemite SI = 7.10 Strengite§ SI = 2.82	Maghemite SI = 6.87 Strengite SI = 2.63
Silicate	Maghemite SI = 6.92 Quartz SI = 0.001 SiO_2(am) = undersaturated	Maghemite SI = 5.15 Quartz SI = 0.001 SiO_2(am) = undersaturated
Bicarbonate	Maghemite SI = 6.88 Siderite = undersaturated	Maghemite SI = 6.39 Siderite = undersaturated

* The input conditions for saturation indices, e.g., pH, ionic strength, concentrations of arsenic, iron, and oxyanions were based on measured concentrations after day 1 and day 7 experiments using ICP-MS. The arsenic and iron in the systems were assumed to be 100% As(V) and Fe(III) in calculation. Therefore, there is a caveat that *in situ* iron and arsenic concentrations can be underestimated if there is significant precipitation in systems.

§ Strengite ($FePO_4 \cdot 2H_2O$) was used a model compound for iron phosphate minerals in the software.

3-S7. FTIR measurements.

Table 3-S4. FTIR reference peak positions for phosphate, silicate and bicarbonate interactions with solid surfaces.

Species	Bond (cm^{-1})	Attribution	Reference
Phosphate	545	O=P–O	Arai and Sparks, 2001[254]
	1140, 1070, 945	ν_3 asymmetric vibration split (related to ν_{as}(P–O), ν_s(P–O) and ν_{as}(P–OH) vibration bands)	Borgnino et al., 2010[234]
	857	ν_1 vibration band (ν_s(P–OH) vibration band)	Borgnino et al., 2010[234]
	996	Fe–PO_4 monodentate mononuclear complexation	Zhang et al., 2017[236]
Silicate	640–680	Si–O–Si and O–Si–O bending modes	Abdelghany et al., 2014[255]
	1050–1120	Antisymmetric stretching of Si–O–Si linkages	Abdelghany et al., 2014[255]
	1630–1645	Molecular water	Abdelghany et al., 2014[255]
Bicarbonate	1280 and 1620	Bidentate carbonate	Liao et al., 2002[256]
	1450	Monodentate carbonate or free carbonate	Liao et al., 2002[256]
	834	Sodium bicarbonate deformation band	Criado et al., 2005[257]

3-S9. E_h and pH measurements.

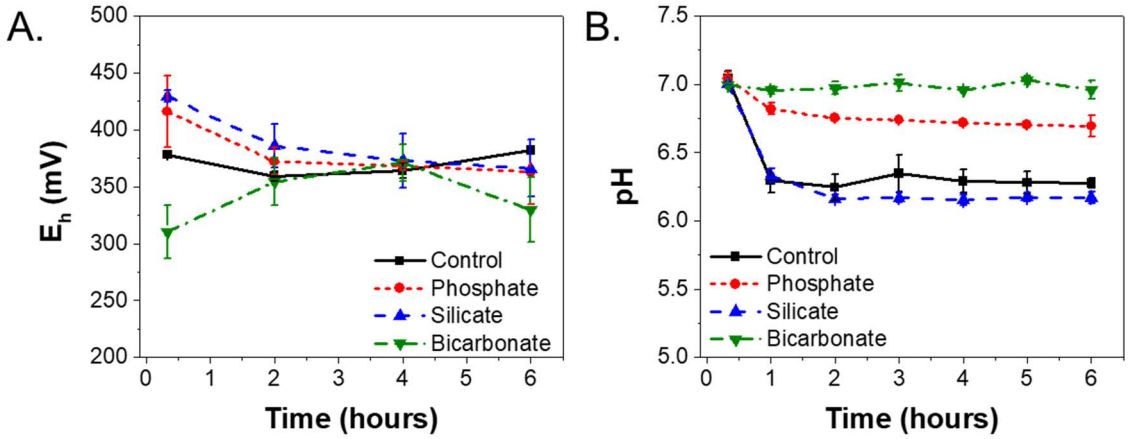

Figure 3-S10. (A) E_h (mV) values of four systems during 6-hour reaction period. All reactors were at room temperature (25 °C) and open to the atmosphere (P_{O_2} = 0.21 atm); (B) pH measurement of four systems during 6-hour reaction period.

Chapter 4. Arsenic mobilization during managed aquifer recharge: effects of dissolved organic matter on arsenopyrite dissolution and secondary precipitation

Reproduced from Ref. 92 with permission from American Chemical Society:[92] Wu, X., Bowers, B., Kim, D., Jun, Y. S.* Dissolved Organic Matter Affects Arsenic Mobility and Iron(III) (hydr)oxides Formation: Implications for Managed Aquifer Recharge, *Environmental Science & Technology*, **2019**, 53, 24, 14357-14367. DOI: 10.1021/acs.est.9b04873. Copyright 2019 American Chemical Society.

Abstract

In **Chapter 4** we continue to focus on **System 2**, delving further into sustainable water management by managed aquifer recharge (MAR). In addition to the oxyanions' effects discussed in **Chapter 3**, here we discuss the effects of dissolved organic matter (natural and effluent organic matter) on arsenic mobilization from arsenopyrite and secondary mineral precipitation. During managed aquifer recharge (MAR), injected water significantly alters water chemistry in an aquifer, affecting arsenic mobility. To elucidate the effects of dissolved organic matter (DOM) on arsenic mobilization during MAR, this bench-scale study examined arsenic mobilization from arsenopyrite (FeAsS, an arsenic-containing sulfide) in the presence of Suwannee River natural organic matter, humic acid, and fulvic acid (SRNOM, SRHA, and SRFA), alginate (Alg), polyaspartate (PA), and glutamate (Glu). Suwannee River DOM (SRDOM) decreased arsenic mobility in the short term (< 6 hours) *via* inhibiting arsenopyrite oxidative dissolution, but increased arsenic mobility over a longer experimental time (~7 days) *via* inhibiting secondary iron(III) (hydr)oxide precipitation and decreasing arsenic adsorption onto iron(III) (hydr)oxide. *In situ* grazing incidence small angle X-ray scattering (GISAXS) measurements indicated that SRDOM decreased iron(III) (hydr)oxide nucleus sizes and growth rates. A combined analysis of SRDOM and other proteinaceous or labile DOM (Alg, PA, and Glu) revealed that DOM with higher molecular weights would cause increased arsenic mobility. These new observations advance our understanding of the impacts of DOM in injected water on arsenic mobility and secondary precipitate formation during MAR, and in other systems where interactions between DOM, arsenic, and iron(III) (hydr)oxides take place.

4.1 Introduction

Groundwater usage, which accounts for one third of the global water withdrawals, serves more than 2 billion people as their primary water source.[258] Over-extraction of groundwater for irrigation and insufficient aquifer management have led to groundwater depletion, one of the highest threats to global water security.[259] Areas such as California's Central Valley,[260] the North China Plain,[261] and Northwestern India[262] suffer from irreversible environmental problems caused by groundwater depletion, including land subsidence and saltwater intrusion.[263] In the past few decades, managed aquifer recharge (MAR), an engineered process of intentionally injecting secondary water sources (e.g., reclaimed water, rain water, or run-off) into ground aquifers, has been applied globally to better manage groundwater and alleviate the severe consequences of groundwater over-drafting.[264]

However, in MAR operations, the water chemistry change induced by recharged water can significantly affect the mobility of a toxic metalloid, arsenic, from subsurface reservoir systems.[62, 67] For example, the arsenic concentrations in recovered water from MAR sites in South Central Florida (10–130 μg/L) and South Australia (14–25 μg/L) were higher than those prior to injection (~3 μg/L for both sites), and all surpassed the Environmental Protection Agency's maximum concentration level for arsenic (10 μg/L).[17, 179] Elevated arsenic mobility has been shown to result from the increased oxidative dissolution of arsenic-bearing sulfide minerals, frequently iron sulfides, such as arsenopyrite (FeAsS) and arsenian pyrite [$Fe(As, S)_2$, 0.5−10 wt% As], through the following reactions with dissolved oxygen (O_2) and nitrate (**eq 4.1a−b**) in the injected water:[17, 63, 183]

$$FeAsS(s) + 1.5H_2O + 2.75O_2(aq) \rightarrow Fe^{2+}(aq) + H_3AsO_3(aq) + SO_4{}^{2-}(aq) \quad \textbf{(eq 4.1a)}$$

$$10Fe(As, S)_2(s) + 26NO_3{}^{-}(aq) + 2H_2O + 6H^{+}(aq)$$

$$\rightarrow 10Fe^{2+}(aq) + 10HAsO_4{}^{2-}(aq) + 10SO_4{}^{2-}(aq) + 13N_2(g) \quad \textbf{(eq 4.1b)}$$

During the oxidation of arsenic-containing pyrites, the mobilized Fe(II) can be further oxidized and hydrolyzed to form secondary mineral precipitates,[184, 265] including iron(III) (hydr)oxides, which can attenuate arsenic mobility through adsorption and incorporation.[17]

Furthermore, dissolved organic matter (DOM), which is composed of organic compounds from the remains of organisms, notably exists in water sources for MAR (3–30 mg/L as dissolved organic carbon, DOC[266-267]), including reclaimed water from wastewater treatment plants (WWTPs) and rain water. After being injected into groundwater systems, DOM in the reclaimed water can significantly elevate DOC levels above those in the original groundwater (typically 0–2 mg/L as DOC).[268] In addition, although DOM can be attenuated through soil filtration, sorption, and biodegradation,[269] it can still travel long distances at MAR sites, with residence times up to 8 years.[61, 270] However, insufficient attention has been given to the effects of DOM on the mobility of arsenic from arsenic-bearing sulfide minerals and the subsequent secondary iron(III) (hydr)oxide precipitation under conditions relevant to MAR operations.

During interactions with arsenic and iron(III) (hydr)oxides, DOM can influence arsenic speciation[271-272] and increase arsenic mobility via aqueous complexation[273-274] or by decreasing arsenic adsorption on iron(III) (hydr)oxides (e.g., goethite, hematite, and ferrihydrite).[275-276] Using reclaimed water obtained from a WWTP in Cincinnati, our previous study observed that secondary iron(III) (hydr)oxide precipitation was inhibited during arsenopyrite dissolution, in comparison to systems containing only either sodium nitrate or sodium chloride.[62] We postulated that this difference could be attributed to the presence of DOM in the reclaimed water, as DOM might form aqueous complexation with iron[274] and prevent iron(III) (hydr)oxide formation. Moreover, the electron shuttling capacity of DOM can locally facilitate the reductive dissolution of precipitated

iron(III) (hydr)oxides,[277-278] potentially leading to a reduced amount of precipitation and fewer adsorption sites for arsenic. Therefore, when DOM interacts with arsenic-bearing sulfide minerals, including arsenopyrite, under MAR relevant conditions, arsenic mobility should be carefully studied.

In addition, DOM in reclaimed water is a mixture of natural organic matter (NOM), derived from the degradation of organisms in natural systems, and effluent organic matter (EfOM), originating from WWTPs.[279-280] Both NOM and EfOM consist of humic substances, such as humic acids (HAs) and fulvic acids (FAs), which contain aromatic and aliphatic hydrocarbon structures with carboxyl and hydroxyl functional groups.[281] EfOM also contains other types of compounds, such as soluble microbial products (SMPs) (e.g., polysaccharides, proteins) generated during biological treatments in WWTPs.[282-283] Various components of DOM may have different impacts on arsenic mobility, based on their extents of complexation or reducing capacities. However, there has been little research on the effects of different components of DOM on the arsenic dissolution from arsenic-bearing sulfide minerals and the secondary iron(III) (hydr)oxide precipitation.

Therefore, this bench-scale study aims to systematically examine the kinetics of arsenic mobilization and secondary mineral precipitation from arsenopyrite in the presence of six model DOM types: Suwannee River natural organic matter (SRNOM), Suwannee River humic acid (SRHA), Suwannee River fulvic acid (SRFA), alginate (Alg, a representative of polysaccharide), polyaspartate (PA, a representative of protein), and glutamate (Glu, a representative of amino acid). These model DOM types were chosen because of their confirmed presence in reclaimed water and groundwater, and their known characteristics and chemical compositions.[35] This study provides the extent, morphology, and phases of secondary iron (hydr)oxides precipitation, which affects arsenic mobility through adsorption or incorporation. The new observations in this study will

advance our understanding of the impacts of DOM on arsenic mobility and secondary precipitate formation during MAR, and have important environmental implications for other systems in which the interactions between DOM, arsenic, and iron(III) (hydr)oxides might also exist, including acid mine drainage (AMD), acid sulfate soils (ASS), and uranium mine tailing operations.[284-285]

4.2 Experimental section

4.2.1 Preparation of arsenopyrite powders and coupons

Arsenopyrite was chosen as the model arsenic-containing mineral because it vastly exists and is more energetically favorable to form than arsenian pyrite in natural systems.[180] Natural arsenopyrite ore samples from Gold Hill, Tooele County, UT, were purchased from the Mineralogical Research Company (San Jose, CA). Our previous characterization of these arsenopyrite ore samples showed that they contained a mixture of quartz and arsenopyrite.[62] Arsenopyrite powders for dissolution tests were prepared by grinding ore samples using a mortar and pestle, and sieving to collect grains in the size range of 300–500 μm. To remove any pre-oxidized part of arsenopyrite samples, their powders were washed using a hydrochloric acid-washing procedure suggested by McGuire et al.[286]. Then, to mitigate oxidation by atmospheric oxygen, they were stored in an anaerobic chamber prior to batch experiments. For easier characterization of surface morphology changes, flat, polished arsenopyrite coupons prepared by Burnham Petrographics, LLC (Rathdrum, Idaho, USA) from the same arsenopyrite ore as the powder samples were used to observe heterogeneous iron(III) (hydr)oxide precipitates on arsenopyrite surfaces. Coupons were stored in the anaerobic chamber and were cleaned before reaction using acetone, ethanol, and isopropanol to remove surface organic compounds and rinsed with deionized (DI) water (resistivity > 18.2 MΩ-cm).

4.2.2 Batch Experiments

To mimic the ionic strength of reclaimed water,[62] reaction solutions were prepared using DI water and 10 mM sodium nitrate (0.85 g/L $NaNO_3$, ACS reagent, Baker). Our previous study suggested that sodium chloride, unlike sodium nitrate, can promote the phase transformation of iron(III) (hydr)oxides through Ostwald ripening,[62] thus sodium nitrate was used here to minimize the effects of salts. The Suwannee River organic matter—SRNOM (2R101N), SRHA (2S101H), and SRFA (2S101F)—were purchased from the International Humic Substances Society (IHSS). Sodium alginate (ACS reagent, Spectrum), polyaspartic acid (ACS reagent, LanXess), and glutamic acid (ACS reagent, Baker) were used as representative proteinaceous or labile DOM types. The preparation method of organic matter stock solutions and their composition information are in the Supporting Information (**Table 4-S1**).[35] The SRNOM, SRHA, and SRFA from the IHSS were isolated using the XAD-8 resin adsorption method, thus polysaccharides, simple sugars, and low-molecular-weight organic acids are not isolated with the humic substances.[287] The organic matter stock solutions were added into batch reactors (polypropylene, VWR) containing 250 mL $NaNO_3$ solutions to obtain a carbon concentration of 10 mg/L, confirmed by a non-purgeable organic carbon measurement (NPOC, Shimadzu TOC Analyzer, TOC-L CPH). The pH was adjusted to 7.0 ± 0.2 before reaction using nitric acid and sodium hydroxide to simulate the average pH of wastewater effluents.[62] To eliminate potential influences of buffer on arsenopyrite dissolution, no buffer was used for pH maintenance in this study, but we closely monitored the pH changes throughout the experiments. To start the reaction, 0.05 g of arsenopyrite powder was added to each solution to achieve a 0.2 g/L solid-to-liquid (S/L) ratio, which can facilitate arsenopyrite oxidative dissolution.[62, 68, 288] In MAR sites, the injected waters are commonly equilibrated with the atmosphere and thus contain high dissolved oxygen concentrations (~8–15

mg/L), exceeding those of native groundwater (<1 mg/L).[67] Therefore, to mimic the early stage of arsenopyrite minerals contacting with oxygenated injected water, the solutions were reacted under aerobic condition. Aqueous samples were taken at each hour during the first 6 hours, and at 1 day, 3 days, 5 days, and 7 days. For each sampling, 2 mL of solution was taken from the reactors, filtered using 0.2-μm PTFE membrane syringe filters, and acidified to 2% v/v acid with nitric acid. Inductively coupled plasma mass spectrometry (ICP-MS) (Perkin Elmer ELAN DRC II) was used to quantify the arsenic and iron concentrations. Additional tests were conducted to quantify the arsenic amount adsorbed on solid phases (both arsenopyrite powders and secondary precipitates), using the same conditions as in the batch dissolution experiments. NaOH (0.5 M) was used to extract reacted solutions for 1 hour, which recovered >95% of the adsorbed arsenic,[289-290] and then the total arsenic concentration (aqueous + adsorbed) was measured by ICP-MS. The concentration of arsenic (adsorbed) was calculated from the difference between arsenic (aqueous + adsorbed) and arsenic (aqueous). Sulfate anion concentration was determined using ion chromatography (IC, Thermo Scientific, Dionex ICS-1600). Statistical tests (t-Test) were conducted to evaluate the significance of differences between the control and any of the DOM systems at the 0.05 significance level.[291]

The alterations of pH values and oxidation reduction potentials (ORP) were monitored during 7 days using a pH electrode (VWR 89231-604 with an Ag/AgCl internal reference) and an ORP electrode (VWR 89231-642 with an Ag/AgCl internal reference), respectively. The ORP values were converted to E_h values by adding the potential (E_{ref} = 207 mV at 25 °C) developed by the reference electrode portion relative to the Standard Hydrogen Electrode (SHE). The reactor without any organic matter was used as the control system. Triplicate batch experiments were conducted for each condition. The arsenic speciation, As(III) versus As(V), during 7 days was

measured using an anion-exchange column packed with resin in chloride form (Dowex, Sigma Aldrich).[62] The detailed anion-exchange column method is described in the Supporting Information. Ion chromatography (IC, Thermo Scientific, Dionex ICS-1600), specific ultraviolet (UV) light absorbance (Thermo Scientific, Evolution 60S), and NPOC measurements were used to test the chemical composition alteration of DOM during the batch experiments, confirming that there is no degradation of DOM within 7 days. A Fourier transform infrared (FTIR) spectroscope (Thermo Scientific, Nicolet Nexus 470) equipped with a diamond crystal was used to obtain chemical bonding information about the complexes between DOM and arsenopyrite powder surfaces. In this experimental system, the effects of any microorganisms on arsenopyrite reactions would be negligible for the following reasons: the DOM stock solutions were vacuum-filtered during their preparation; the DI water used in this study was filtered; the FeAsS powders were washed using acid before use; and batch reactors were rinsed using 2% nitric acid and DI water before the dissolution experiments.

4.2.3 Characterization of Secondary Mineral Precipitates

To observe the morphology of heterogeneous secondary mineral precipitation, arsenopyrite coupons were utilized. Three coupons (5 mm in length and width, 1 mm in thickness) were added to each of the four batch reactors, which contained 250 mL $NaNO_3$ solution, 10 mg/L organic matter as carbon, and 0.05 g arsenopyrite powders at pH 7.0 ± 0.2. At 6 hours, 3 days, and 7 days, coupons were removed, rinsed with deionized water, and dried with high purity nitrogen gas. Triplicate batch experiments with coupons were conducted. To measure the morphological change of secondary mineral precipitates on coupons, tapping mode atomic force microscopy (AFM, Veeco Inc., Nanoscope V multimode SPM) was used. Each sample was measured at five different

locations on the substrate surface. To obtain quantitative information about the average sizes of the precipitates, the heights of at least 50 particles in each image were analyzed using Nanoscope 7.20 software (Veeco Inc.). The surface root-mean-square (RMS) roughness of coupons was obtained from AFM images using the Nanoscope 7.20.[93] To identify the phases of heterogeneous secondary mineral precipitation on coupons, Raman measurements (InVia Raman Microscope, Renishaw, UK) were carried out with a 514 nm laser (~4 mW) and a grating of 1800 lines/mm. A 20× objective and decreased power of 50% were utilized to minimize aging induced by a strong laser intensity. At least three spots on each coupon were measured to obtain their Raman spectra.

4.2.4 In situ grazing incidence small-angle X-ray scattering (GISAXS) experiments

To provide mechanistic understanding of the effects of different model DOM on the secondary iron(III) (hydr)oxides nucleation on pre-existing mineral surfaces, GISAXS measurements were conducted at beamline 12-ID-B at the Advanced Photon Source in Argonne National Laboratory (Argonne, IL). A flat quartz substrate was chosen for heterogeneous nucleation because of its environmental abundance.[292] In this study, we simulated the case in which aqueous iron ions dissolved from arsenopyrite are forming iron (hydr)oxides on nearby surfaces. A quantitative understanding of this nucleation process of iron (hydr)oxides is important because it directly impacts net dissolved arsenic concentrations. The reaction solutions for GISAXS contained DI water, 10^{-4} M iron(III) from reagent grade iron nitrate ($Fe(NO_3)_3 \cdot 9H_2O$), 10^{-2} M sodium nitrate ($NaNO_3$), and 1.5 mg carbon/L DOM as measured by NPOC, which is in the range of DOM concentrations in groundwater.[268] The pH of all reaction solutions was 3.6 ± 0.2 after mixing the constituents, and it did not vary over the GISAXS measurement period (40 min). This

pH value was chosen for two reasons: First, the nucleation of iron(III) (hydr)oxides is slower than that at pH 7.0 owing to the lower saturation index; thus it provided a clearer understanding of the early nucleation processes of iron (hydr)oxides.[73, 293] By using MINEQL+ (version 5.0), the saturation index (SI, $\log(IAP/K_{sp})$) of iron(III) (hydr)oxides at pH 3.6 with 10^{-4} M iron(III) was calculated to be 0.97 in terms of ferrihydrite, and we expect that close to the mineral surface, the local iron(III) concentrations and local saturations can be even higher.[293] Second, pH 3.6 was the pH value of the solution after mixing, thus minimizing the nucleation induced by pH alteration. Triplicate GISAXS experiments were conducted for different model DOM and control systems. Using the GISAXSshop software in Igor 6.3, developed at APS beamline 12-ID-B, the GISAXS 2D images after background subtraction were cut along the Yoneda wing, where the scattering is enhanced by the grazing incidence effect, to produce 1D plots of scattering intensity (I) versus q. A MatLab macro developed by APS beamline 12-ID-B was used to fit the 1D data, which provides estimations for the radius of gyration (R_g) of the newly formed nanoparticles.[293] Detailed clean quartz substrate preparation, GISAXS experiment setup, and GISAXS data analysis are available in the Supporting Information.

4.3 Results and discussion

4.3.1 Effects of Suwannee River organic matter on arsenic mobility

Figure 4.1 shows the aqueous arsenic concentration changes in the SRNOM, SRHA, SRFA systems, and in the control system within 6 hours (**A**) and 7 days (**B**). These two different time periods were tested to differentiate the impacts on aqueous arsenic concentrations of the dissolution of arsenopyrite (in the shorter time period) from the impacts of arsenic adsorption on the secondary precipitates (in the longer time period). Note that the arsenic concentration measured

by ICP-MS is a net concentration, reflecting the intrinsic arsenic dissolution from arsenopyrite minus the arsenic adsorbed by secondary precipitates. After 6 hours, compared with the control system, which contained only sodium nitrate, the three model DOM decreased arsenic concentrations by 33% (SRNOM), 31% (SRHA), and 29% (SRFA). However, over the longer reaction time (7 days), the arsenic concentrations with different DOM showed varied trends. In the presence of SRHA, the arsenic concentration surpassed that in the control system after 3 days and increased by 22% after 7 days. The arsenic concentrations with SRNOM and SRFA were lower than the control after 7 days, but only by 3% and 4%, respectively.

The decreased arsenic concentrations in the presence of DOM at 6 hours could be due to (1) inhibited arsenic dissolution from arsenopyrite, or (2) enhanced arsenic adsorption onto secondary precipitates. To delineate these two possible mechanisms, additional dissolution tests were conducted to differentiate the amount of aqueous arsenic and arsenic adsorbed on secondary precipitates. As shown in **Figure 4-S1A**, at 6 hours, the total arsenic dissolved (aqueous + adsorbed) was decreased in the presence of DOM compared to the control system. In addition, the adsorbed arsenic amount was also decreased in DOM systems, which might be due to adsorption competition between arsenic and DOM, or inhibited secondary precipitate formation. These results indicate that the decreased arsenic mobility in DOM systems at 6 hours was mainly due to the inhibited arsenic dissolution from arsenopyrite. The pH and E_h values monitored in 7 days can further provide insights into the DOM effects. **Figure 4-S1B** shows the pH value change during 7 days with different types of DOM. After 6 hours, the pH drop in the control system was the highest, from pH 7.0 to pH 6.2, and it slowly decreased to pH 6.1 after 7 days. In contrast, the pH drops in the presence of DOM (from pH 7.0 to pH 6.4 after 7 days) were less significant than that in the control system. The smaller pH drop in DOM systems can be attributed to (i) decreased amount of

iron hydrolysis, or (ii) the buffering effect from DOM functional groups. The lower pH in the control system might in turn cause more proton promoted dissolution of arsenopyrite. **Figure 4-S1C** shows that before the reaction, the E_h value in the control system was the highest (440 ± 17 mV), compared with those of SRNOM (372 ± 21 mV), SRHA (416 ± 12 mV), and SRFA (402 ± 14 mV). The more reductive condition in the presence of DOM could inhibit the oxidative dissolution of arsenopyrite. After the reaction started, the E_h values in all four systems decreased, owing to the consumption of oxidants in the solution. The decrease of the E_h value was the largest in the control system, from 440 mV to 363 mV within 6 hours, while the E_h value decreases in the DOM systems were relatively small. This behavior suggests that a higher rate of oxidative dissolution and significant consumption of oxidants occurred in the control system.

The trends in arsenic concentration after 7 days, especially the higher arsenic concentration in the HA system, however, can be attributed to other aspects, that counteracted the inhibited initial dissolution by DOM. Aromatic DOM with carboxyl and hydroxyl functional groups can bind with dissolved arsenic and iron to form aqueous As-DOM, Fe-NOM, and As-Fe-DOM colloids/complexes, which can potentially increase arsenic mobility in aqueous systems.[273-274] In addition, after 7 days, the effect of secondary precipitates such as iron(III) (hydr)oxides on arsenic mobility became more significant through adsorption or co-precipitation than that in 6 hours. In the presence of aromatic DOM such as HA and FA, the sorption of arsenic onto iron(III) (hydr)oxides can be decreased due to the competition of arsenic and DOM for sorption sites.[275-276] Furthermore, the aqueous complexation between DOM and iron might lead to reduced formation of iron(III) (hydr)oxide secondary precipitates and thus fewer adsorption sites for arsenic. The effects of secondary iron (hydr)oxide precipitates on arsenic mobility will be further discussed in the next section to elucidate the different behaviors among the three model DOM.

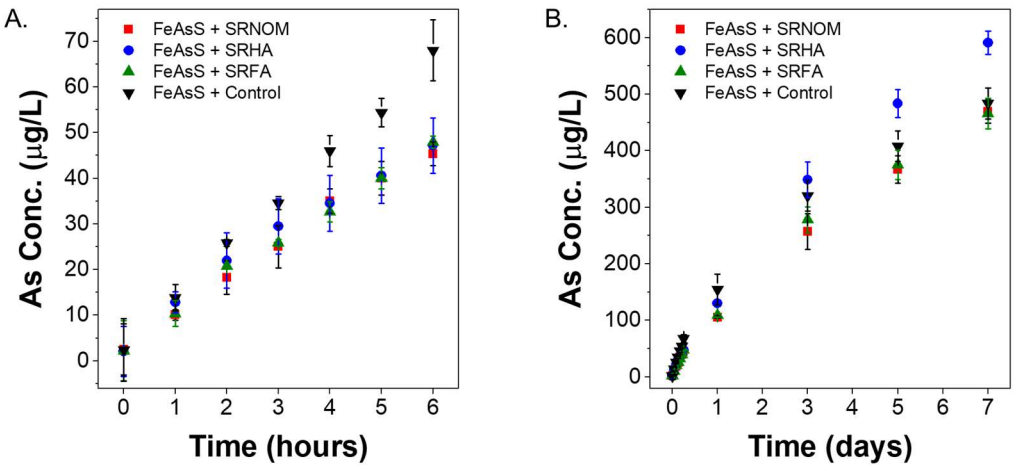

Figure 4.1 Aqueous arsenic concentrations in the presence of different model SRDOM and in the control system over 6 hours (**A**) and 7 days (**B**). Error bars represent the standard deviation from triplicate batch experiments. For 6 hours results, a t-Test showed that, at the 0.05 significance level, the p-values of the three SRDOM systems (SRNOM: 0.0119; SRHA: 0.00373; SRFA: 0.00686) were <0.05, indicating that the concentration differences between the SRDOM systems and the control system were statistically significant.

The dissolved iron concentration evolution was also monitored using ICP-MS (**Figure 4-S2A**). For the first 6 hours, iron was not detectable in the four systems, while after 1 day, DOM systems showed higher iron concentrations than the control system. The complexation between aqueous iron and carboxyl functional groups from aromatic DOM can induce higher dissolved iron concentration.[274] The arsenic speciation, determined by anion-exchange column tests, showed that more than 94% (1 day) and 98% (7 days) of arsenic in the four systems was arsenate species (**Figure 4-S2B**). Considering the high E_h in our batch experiments (> 332 mV), the dominant arsenic species in the system at pH 7 would be arsenate ($HAsO_4^{2-}$), based on an Eh-pH diagram.[294] The sulfate anion concentrations (**Figure 4-S2C**) determined by IC measurements indicated that DOM systems exhibited slightly lower sulfate concentrations than the control system after 1 day, while after 7 days, the sulfate concentration in DOM systems, especially in the SRFA system, surpassed that of the control system. The sulfate concentrations were one or two orders of

magnitude higher than dissolved arsenic and iron concentrations. This different dissolved ion concentrations may result from incongruent dissolution of these elements and the different reactivities for their subsequent incorporation into secondary mineral precipitates.

4.3.2 Morphology and identity of secondary precipitates

To evaluate the morphologies and sizes of secondary mineral precipitation in different systems, tapping mode AFM measurements were made on arsenopyrite coupons reacted in batch experiments. **Figure 4.2** shows AFM height mode images of coupons after 6 hours and after 7 days in the three DOM systems and the control. After 6 hours, small heterogeneous nanoparticles could be observed on the coupons in four systems **Figure 4.2A1–D1**). Analyses of more than 50 nanoparticles in each image revealed that the presence of DOM reduced the height of secondary precipitates (**Figure 4-S5B**). After 7 days, the precipitates in each system gradually grew in height to 18.9 ± 3.8 nm (SRNOM), 22.1 ± 4.3 nm (SRHA), 10.1 ± 2.3 nm (SRFA), and 30.7 ± 4.7 nm (control). In particular, in the presence of SRFA, the secondary precipitates formed monodisperse particles with the smallest size among the three DOM systems (**Figure 4.2C1** and **C2**), while the other systems contained a mixture of both large and small particles. The surface RMS roughness obtained from AFM images (**Figure 4-S5C**) showed that after 7 days, the coupon surface of the control system was much rougher (RMS = 10.7 ± 2.0 nm) than the surfaces of coupons in the DOM systems. The SRFA system showed the smallest roughness after 7 days (RMS = 5.5 ± 0.1 nm).

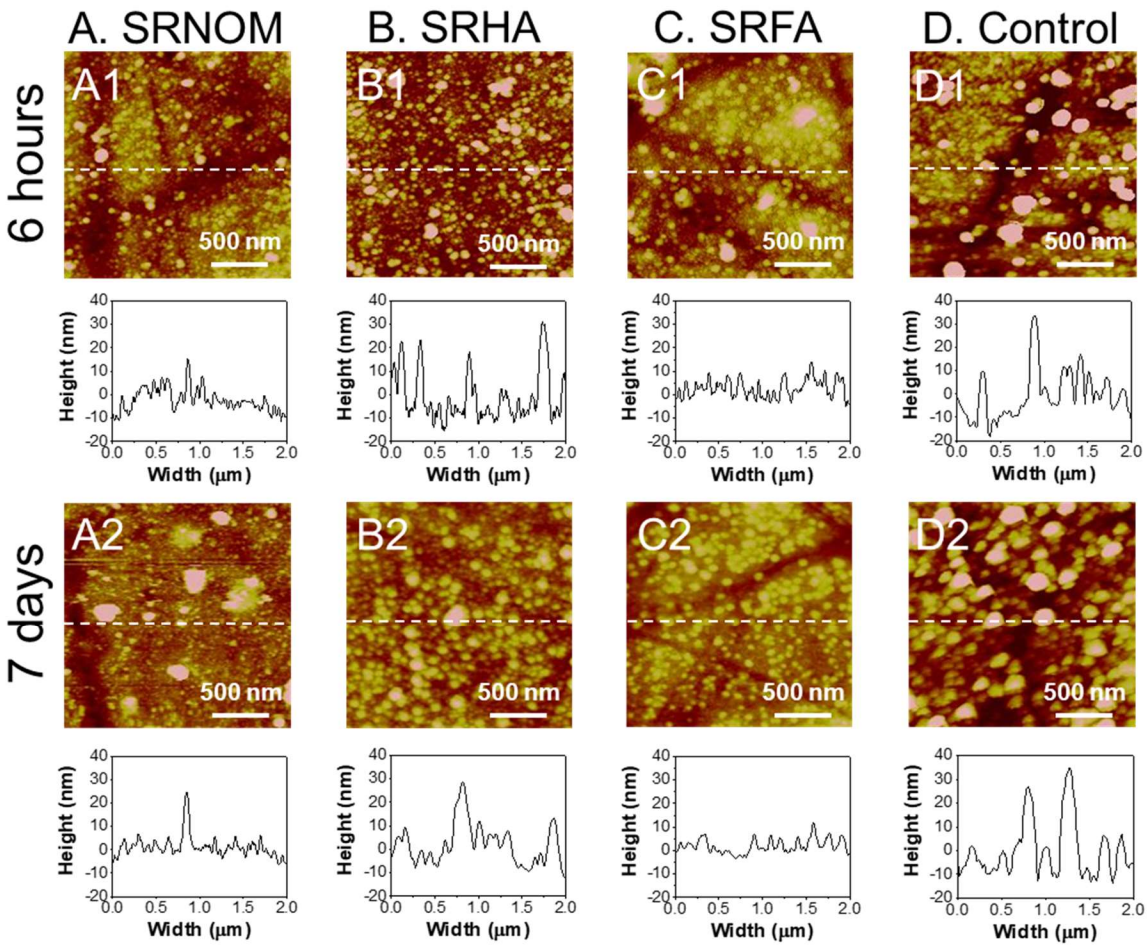

Figure 4.2 Representative AFM height mode images (2 μm × 2 μm) of arsenopyrite coupons after 6 hours (**A1–D1**) and 7 days (**A2–D2**). Color scale: 40 nm. At least three different spots on each coupon were measured. The precipitate height was averaged from more than 50 nanoparticles in each condition. Dotted lines indicate where the image was cut to produce the height profile graphs below each image. An AFM image of the unreacted coupon can be found in 4-SI **Figure 4-S5A**.

Raman spectroscopy identified the phases of secondary precipitates on coupons reacted for 3 days and 7 days (**Figure 4.3**). For unreacted arsenopyrite, the Raman spectrum contains three characteristic peaks at around 333, 827, and 1368 cm^{-1}, which can be attributed to the vibrations of As-S bonds, the arsenate anionic groups (As-O), and Fe-O bonds, respectively.[218-220] The Raman spectra of coupons reacted for 3 days in the DOM and the control systems had acquired two additional broad bands with maxima at ~1330 cm^{-1} and ~1600 cm^{-1} as compared with the unreacted

sample. These two broad bands matched with the characteristic Raman peaks of an iron(III) (hydr)oxide mineral, maghemite (γ-Fe_2O_3).[222, 295] After 7 days, the intensities of these two bands increased in four systems, indicating more maghemite precipitation on coupon surfaces. In the control system (**Figure 4.3D**), another characteristic peak of maghemite, ~720 cm^{-1},[222, 295] also appeared after 7 days. It should be noted that the carbons from organic matter adsorbed on coupons can also contribute to the peak at ~1600 cm^{-1},[222] which might lead to the relatively higher intensity from the band at ~1600 cm^{-1} than ~1330 cm^{-1} in DOM systems compared with the maghemite standard and the control system. The characteristic peaks of other iron(II-III) or iron(III) (hydr)oxide minerals, such as magnetite (~670 cm^{-1})[295], or hematite (~1300 cm^{-1})[295] were not observable for coupons reacted for 3 days, 7 days, and 14 days (**Figure 4-S6C**). The formation of maghemite as a heterogeneous precipitate on arsenopyrite surfaces during arsenopyrite oxidative dissolution has also been reported by previous studies.[62, 68].

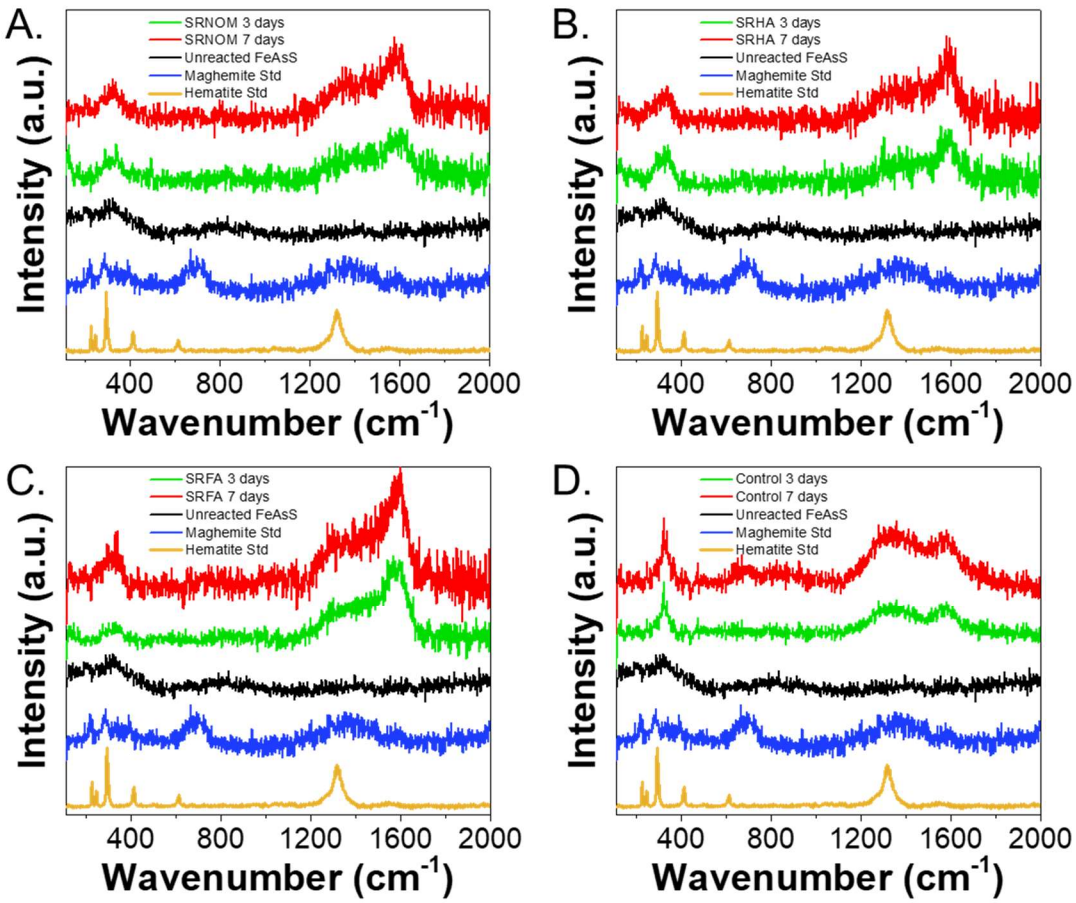

Figure 4.3 Secondary mineral identification using representative Raman spectra for arsenopyrite coupons reacted in the presence of different model SRDOM (**A-C**) and the control system (**D**) after 3 days and 7 days. The size of each coupon was 5 mm × 5 mm. At least three spots were measured on each coupon.

4.3.3 Comparison of Suwannee River DOM with proteinaceous or labile DOM

Three proteinaceous or labile DOM types, alginate (Alg), polyaspartate (PA), and glutamate (Glu), were further tested to compare their effects on arsenopyrite dissolution and secondary mineral precipitation with those from Suwannee River DOM that contain more complex and aromatic structures. The Alg system showed similar trends of arsenic release with Suwannee River DOM. The PA system increased arsenic mobility even more than those with three Suwannee River DOM types in both 6 hours and 7 days (**Figure 4.4A** and **B**). It has been reported that aspartic acid enhanced arsenic mobilization from mine tailings under neutral pH conditions through

forming aqueous organic complexes.[296] PA has also been shown to inhibit the formation of iron(III) (hydr)oxide precipitation,[297] thus it can increase arsenic mobility by decreasing adsorption sites. We found that the Glu system showed the lowest arsenic mobility after 7 days **(Figure 4.4B**). Such a low arsenic mobility can be resulted from inhibited oxidative dissolution of arsenopyrite, or enhanced adsorption of arsenic onto iron(III) (hydr)oxide precipitation by surface complexation. The E_h results indicated that the Glu system exhibited the lowest E_h value among these proteinaceous or labile DOM systems after 7 days (**Figure 4-S7B**), which can lead to the least amount of oxidative dissolution. The sizes of secondary mineral precipitates formed in Alg, PA, and Glu systems were 28.7 ± 4.5 nm, 20.6 ± 5.5 nm, and 15.6 ± 3.3 nm, respectively (**Figure 4.4C**). In particular, the secondary mineral precipitate in the Glu system also exhibited monodisperse sizes, similar with those found in the SRFA system.

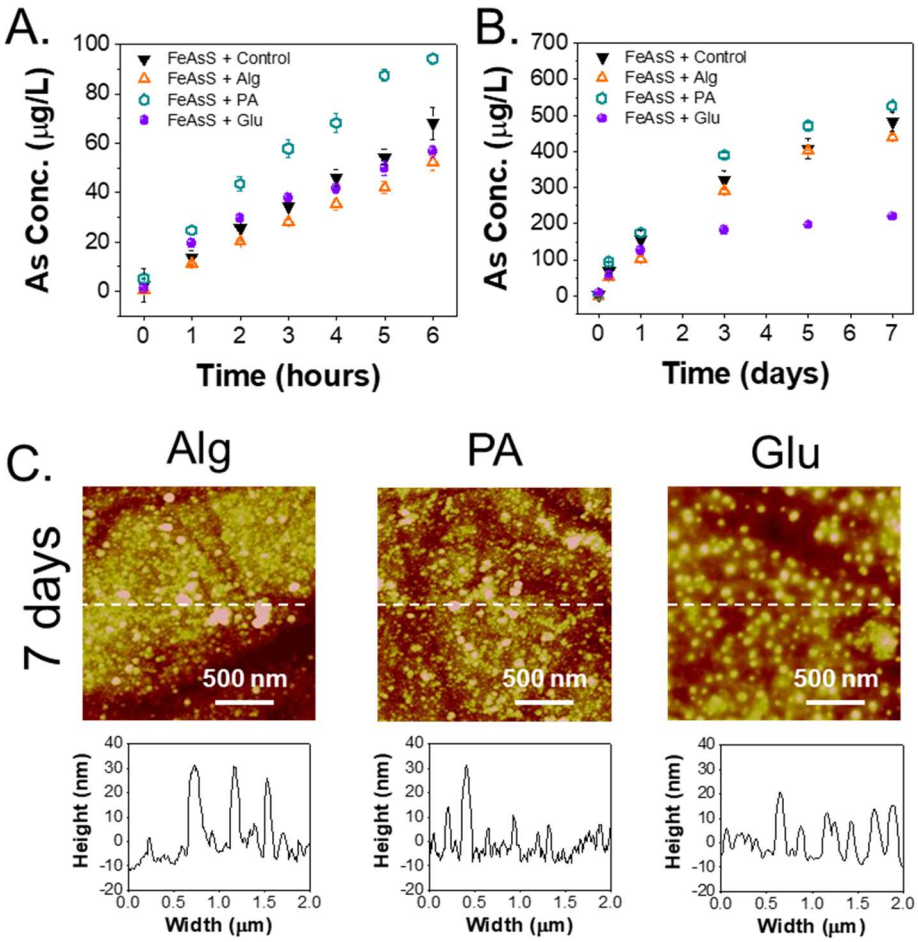

Figure 4.4 Aqueous arsenic concentrations in the presence of alginate (Alg), polyaspartate (PA), and glutamate (Glu) in 6 hours (**A**) and 7 days (**B**). Error bars represent the standard deviation from triplicate batch experiments. (**C**) Representative AFM height mode images (2 µm × 2 µm) of arsenopyrite coupons reacted in the Alg, PA, and Glu systems after 7 days. Color scale: 40 nm. At least three different spots on each coupon were measured. The precipitate height was averaged from more than 50 nanoparticles in each condition.

4.3.4 Effects of organic matter on iron(III) (hydr)oxides nucleation

During MAR operations, the consequential formation of secondary iron(III) (hydr)oxide precipitates from the arsenopyrite dissolution crucially affects the fate and transport of arsenic via co-precipitation or adsorption. The effect of aqueous constituents on the early heterogeneous nucleation behavior of iron(III) (hydr)oxides is therefore important to help us quantify the iron (III) (hydr)oxides' formation that attenuates arsenic. **Figure 4.5** presents the *in situ* GISAXS results for

the four systems in the q range of 0.01–0.30 $Å^{-1}$. In 40 minutes, the radius of gyration (R_g) of newly formed iron(III) (hydr)oxides in the control system grew from 1.9 nm to 2.5 nm. In contrast, SRNOM (R_g = 1.3–1.8 nm), SRHA (R_g = 1.5–2.3 nm), and SRFA (R_g = 1.1–1.4 nm) showed smaller nucleation sizes and slower particle size growth within the measurement time. In particular, SRFA decreased the initial nuclei size and growth rate of iron(III) (hydr)oxides as compared with SRNOM and SRHA, a finding which is consistent with AFM results. The decreased size and growth rate of nuclei by SRFA may result in the smaller particle sizes of later aggregates found in AFM images. The difference between the scattering of the control system and the DOM systems in the small q range, 0.01–0.03 $Å^{-1}$, could be attributed to fractal aggregation caused by DOM.[73] Both the smallest individual primary particles and the associated nanoparticles along DOM chains can scatter X-rays, and they therefore showed distinct scattering patterns compared with the control. The fractal dimension (d), which is equal to the negative power law exponent of the low q region, can be used to characterize the density of fractal aggregates and distinguish between surface fractals and mass fractals.[298] In the three DOM systems, small d values ($d_{SRNOM} \approx 1.53$, $d_{SRHA} \approx 1.55$, and $d_{SRFA} \approx 1.52$,) were observed, indicating mass fractal formation, and fast aggregate formation in the diffusion-limited cluster aggregation (DLCA) regime.[299] In previous *ex situ* grazing incidence wide-angle X-ray scattering (GIWAXS) experiments under the same experimental conditions, we found that particles on the quartz surface were amorphous phase iron(III) (hydr)oxides.[300] The early nucleation of iron (hydr)oxides formation was tested within only 1 hr, thus the mineral phase formed can be different from what we observed for iron (hydr)oxides formed in FeAsS dissolution systems over longer reaction time. Even so, the GISAXS experiments provide quantitative information about iron(III) (hydr)oxide nuclei sizes and their heterogeneous growth on surfaces in the presence of different DOM.

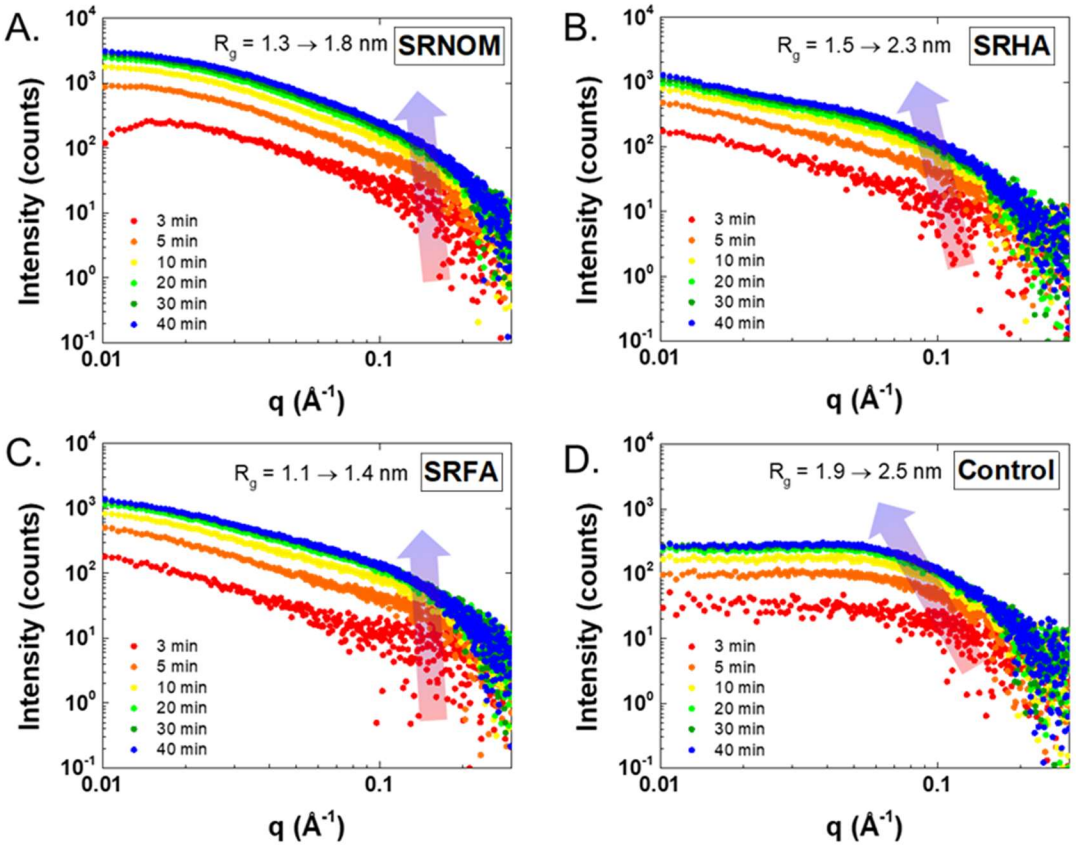

Figure 4.5 GISAXS 1D scattering intensity for iron(III) (hydr)oxides heterogeneous nucleation on quartz in the presence of different model SRDOM (**A-C**) and the control system (**D**). The radius of gyration (R_g) of nanoparticles is noted at the top of each plot. At least triplicate tests were conducted for each system.

4.3.5 Mechanism of organic matter effects on iron(III) (hydr)oxide formation and arsenic mobility

The *in situ* GISAXS and AFM results both showed that, in comparison with SRHA, SRFA decreased the sizes of initial nuclei, and the later growth and aggregation of iron(III) (hydr)oxides. Based on these observations, two possible mechanisms can be proposed. First, FA was found to exhibit higher negative charge (mean 8.0 equiv/kg, where 1 equiv is the extent of negative charge that can be neutralized by 1 mole of proton binding) than HA (mean 5.9 equiv/kg), and a higher number of total binding groups, including carboxylic and phenolic sites.[88-90] For example, based

on their characterizations (**Table 4-S1**), SRFA has higher carboxylic groups content (11.17 mM/g) compared with SRHA (9.13 mM/g).[35] Therefore, FA can bind with a higher amount of positively charged ions, including dissolved iron(III) through iron(III)−fulvate aqueous complexation,[88] which might contribute to the highest aqueous iron concentration found in the FA system as shown from ICP-MS result (**Figure 4-S2A**), and also inhibit the later formation of iron(III) (hydr)oxides. Second, the higher number of binding groups, i.e., carboxylic and phenolic sites, can also help FA to bind with highly positively charged iron(III) (hydr)oxide nuclei (both heterogeneous and homogeneous) and thus constrain their further growth (heterogeneous) or aggregation (homogeneous).[301] It should be noted that the arsenic anion itself could also have effects on the size of iron(III) (hydr)oxide precipitates. It was shown that arsenate can increase iron(III) (hydr)oxide nucleation size by the bridging effect.[64] Thus, the higher concentration of arsenic in the control system after 6 hours could partially lead to larger aggregates. However, after 7 days, the arsenic concentrations in DOM systems were similar or even higher than in the control system, indicating that other components, e.g., DOM, could play more significant roles in controlling the size of iron(III) (hydr)oxide precipitates in the long term.

In terms of arsenic mobility, the inhibited secondary precipitate formation in the SRFA system may result in higher arsenic mobility over longer reaction times due to fewer available adsorption sites. However, the SRHA system showed even higher arsenic mobility after 7 days than SRFA, although its inhibition of secondary iron(III) (hydr)oxide precipitates was weaker than SRFA. Therefore, we deduce that other mechanisms, such as stronger adsorption competition onto iron(III) (hydr)oxide between HA molecules and arsenic, may dominate in controlling arsenic mobility in the SRHA system. SRFA (500–1500 Da) and SRHA (1000–8000 Da) differ in their molecular weight distributions, with a larger fraction of higher molecular weight DOM in

SRHA.[287, 302] It has been reported that, compared to FA, much more HA adsorbs onto iron oxides,[90] and there is a preferred adsorption of higher molecular weight DOM onto mineral surfaces.[72, 303] Further, both HA and FA can decrease the adsorption of arsenic on iron oxides by adsorption competition.[275-276] The preferred adsorption of HA on iron(III) (hydr)oxide may lead to a lower extent of arsenic adsorption, and to higher arsenic concentrations in the solution. This molecular weight influence could also exist when considering Alg (5000–10000 Da), PA (10000–20000 Da), and Glu (147 Da) effects on arsenic mobility. The aqueous arsenic concentration trends in different DOM systems after 7 days (PA > SRHA > Alg > SRFA > Glu) follow closely with the order of their molecular weight sequence (PA > SRHA ≈ Alg > SRFA > Glu). Hence, we suggest that the molecular weight of DOM plays a significant role in determining DOM's interaction with arsenic. With a higher molecular weight, stronger adsorption competition between DOM and arsenic may occur, leading to elevated arsenic mobility.

4.4 Conclusions and environmental implications

Our study elucidated the effects of six different types of DOM on arsenic mobilization from arsenopyrite. The results from two timescale experiments, short (<6 hours) and long term (7 days), have different implications for MAR operations. DOM decreased arsenic mobility during the short time period by inhibiting oxidative dissolution, but increased arsenic mobility in the long term via inhibiting secondary iron(III) (hydr)oxides formation. These results are consistent with our previous study using a reclaimed water source (with 12.42 mg/L of DOC) from a WWTP in Cincinnati,[62] in which we found that secondary iron(III) (hydr)oxide precipitation was inhibited in the reclaimed water system. Here, as indicated from AFM and GISAXS observations, DOM inhibits both the nucleation and the later growth and aggregation of iron(III) (hydr)oxides. The

suppressed formation of iron(III) (hydr)oxides will lead to higher arsenic mobility due to less absorption sites. Therefore, DOM in recharged water can be a concern in mobilizing arsenic when the exposure time of DOM to arsenopyrite reaches several days or weeks. In developing transport models to predict the fate and transport of arsenic during MAR, the effects of DOM on arsenic mobility should be fully considered from the aspects of both oxidative dissolution and secondary mineral formation. While a clear delineation of the fate of each element (iron, arsenic, and sulfur) is challenging due to the extremely complex nature of the system, if possible, a quantitative description of the mass balance of each element during arsenopyrite dissolution will also benefit a comprehensive understanding of arsenic mobility in MAR. In addition, different phases of secondary Fe-containing mineral phases (e.g., ferrihydrite, magnetite, maghemite, and hematite) will have various adsorption affinities towards arsenic. For example, more crystalized forms of iron(III) (hydr)oxides have been shown to possess lower adsorption capacity towards arsenic.[304] Thus, the phase transformation pathway of secondary mineral precipitates from arsenopyrite dissolution should be carefully studied to provide a better understanding of arsenic mobility at different time stages.

Different components of DOM in recharged water, humic substances (HAs, FAs), polysaccharides, proteins, and amino acids, will have various effects on arsenic mobility. DOM with higher molecular weight tends to increase arsenic mobility more, potentially due to stronger adsorption competition between DOM and arsenic. Therefore, the DOM molecular weight distribution in recharge water should be carefully monitored before injecting into MAR systems. Our results can be applicable to MAR sites which use secondary effluents from WWTPs containing high DOM concentrations as their recharge water. However, if the recharge water source is from tertiary effluents after advanced treatment, like the case in Orange County in

California[249], the DOM concentration can be largely decreased. Even in such cases, the findings from this study can provide fundamental information about the reactions between diverse DOM moieties and arsenic-containing sulfide minerals. Our findings can also have implications in analyzing arsenic mobility in other systems in which DOM, arsenic, and iron(III) (hydr)oxides co-exist, including acid mine drainage systems and subsurface energy-related operations.

Acknowledgments

We are grateful for support received from the National Science Foundation (EAR-1424927). We thank the Nano Research Facility (NRF) at Washington University in St. Louis for use of ICP-MS. Use of the Advanced Photon Source (Sector 12 ID-B for GISAXS) at the Argonne National Laboratory was supported by the U.S. Department of Energy, Office of Science, Office of Basic Energy Sciences, under Contract no. DE-AC02-06CH11357. We thank Prof. James Ballard for carefully reviewing our manuscript, and also thank the Environmental NanoChemistry Group members for valuable discussions.

Supporting information for Chapter 4

4-S1. DOM stock solution preparation.

Preparation of DOM Stock Solution: To create Suwannee River DOM stock solutions, 100 mg of SRDOM was added to 200 mL of DI water and stirred overnight in dark conditions (the bottle was wrapped in aluminum foil). The pH of the solution was then adjusted to 8.5 to increase the solubility before vacuum-filtering. This DOM stock solution was refrigerated prior to experimentation. The alginate, polyaspartate, and glutamate stock solutions were prepared by dissolving correspond organic matter solids into DI water. Non-purgeable organic carbon (NPOC) concentrations in the stock solution were measured using a Shimadzu total organic carbon (TOC) Analyzer. The SRNOM, SRHA, and SRFA from the International Humic Substances Society (IHSS) were isolated from Suwannee River using the XAD-8 resin adsorption method, thus they contain only hydrophobic organic acids. Other classes of organic compounds such as polysaccharides, simple sugars, and low-molecular-weight organic acids are not isolated with the humic substances.[287]

Table 4-S1. Characterization of SRNOM (2R101N), SRHA (2S101H), and SRFA (2S101F) provided by the IHSS.[35]

DOM	Acidic functional groups (mM/g)		Elemental compositions % (w/w)					$LogK_1$	$LogK_2$
	Carboxyl	Phenolic	C	H	O	N	S		
SRNOM	11.21	2.47	50.7	4.0	41.5	1.3	1.8	4.16	9.99
SRHA	9.13	3.72	52.6	4.3	42.0	1.2	0.5	4.35	10.44
SRFA	11.17	2.84	52.3	4.4	43.0	0.7	0.5	3.76	9.84

4-S2. Batch experiments.

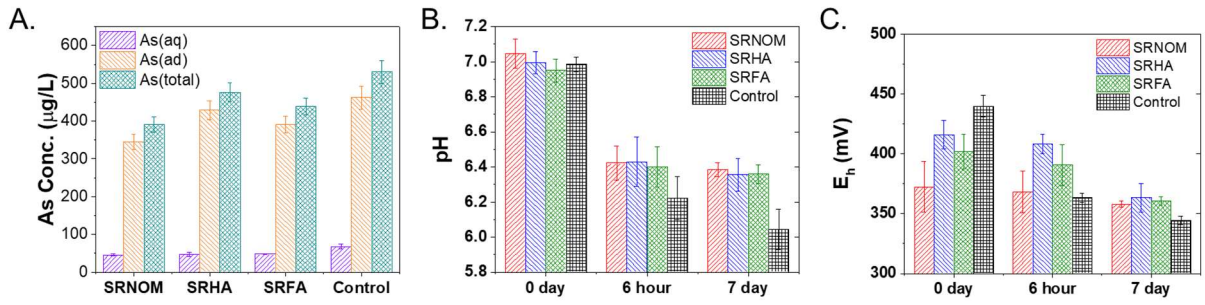

Figure 4-S1 (A) Arsenic concentrations, including aqueous, adsorbed, and total arsenic, in SRDOM systems and the control system after 6 hours dissolution. Error bars represent the standard deviation from triplicate batch experiments. Comparing the total arsenic concentrations in the SRDOM systems and the control system, a two-sample t-Test showed that, at the 0.05 significance level, the p-values of the three SRDOM systems (SRNOM: 0.0004; SRHA: 0.00928; SRFA: 0.00149) were <0.05, indicating that the differences between the SRDOM systems and the control system were significant. (B) pH values of four systems during the 7-day reaction period measured by a pH electrode (VWR 89231-604 with an Ag/AgCl internal reference). Comparing the pH values in the SRDOM systems and the control system at 6 hours, a two-sample t-Test showed that, at the 0.05 significance level, the p-values of the three SRDOM systems (SRNOM: 0.01224; SRHA: 0.01789; SRFA: 0.01757) were <0.05, indicating that the concentration differences between the SRDOM systems and the control system were statistically significant. (C) E_h values (mV) of four systems during the 7-day reaction period measured with an ORP electrode (VWR 89231-642 with an Ag/AgCl internal reference). The ORP values were converted to E_h values by adding the potential (E_{ref} = 207 mV at 25 °C) developed by the reference electrode portion relative to the Standard Hydrogen Electrode (SHE). Comparing the E_h values in the SRDOM systems and the control system at 0 day, a two-sample t-Test showed that, at the 0.05 significance level, the p-values of three SRDOM systems (SRNOM: 0.00301; SRHA: 0.04186; SRFA: 0.00309) were <0.05, indicating that the differences between the SRDOM systems and the control system were statistically significant. All reactors were at room temperature (25 °C) and open to the atmosphere (P_{O2} = 0.21 atm).

Anion-exchange column experiments for determining arsenic speciation: At 1 day and 7 days, 10 mL of filtered solution from each batch reactor's supernatant was adjusted to pH 3.5. The solution was then passed through a chloride anion-exchange column, then the first 5 mL was discarded and the next 5 mL was collected for ICP-MS analysis. Arsenate was retained in the column, while arsenite passed through. Comparison of ICP-MS measurements of arsenic concentration before and after column exchange revealed the percentage of arsenite in the solution.

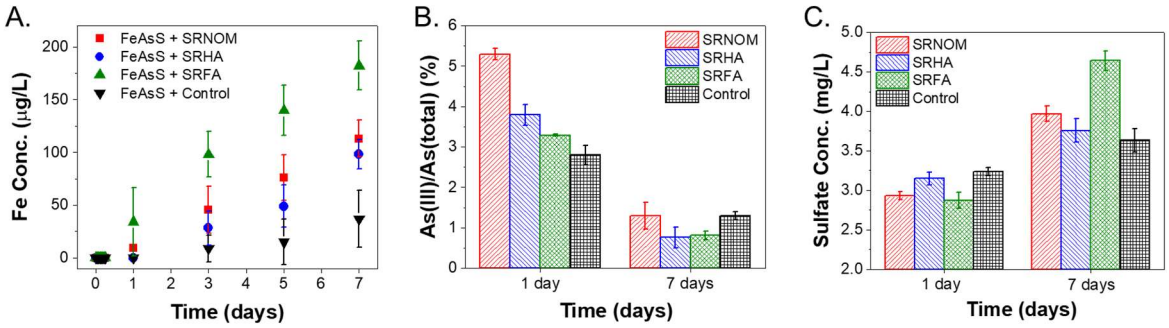

Figure 4-S2 (A) Aqueous iron concentrations in the presence of different model DOM and the control system within 7 days. Error bars represent the standard deviation from triplicate batch experiments. The dissolved iron concentrations in 6 hours were below the detection limit of ICP-MS, indicating that the NaOH extraction tests for 6 hours did not cause additional iron (hydr)oxide precipitation to adsorb/incorporate more arsenic. (B) Arsenite (As(III)) percentages from total arsenic concentration in solutions, determined by anion-exchange column tests from triplicate batch experiments. (C) Sulfate concentrations in the presence of different model DOM and the control system, measured by ion chromatography (IC).

DOM decomposition test: Ion chromatography (IC), specific ultraviolet (UV) light absorbance at 254 nm, and NPOC measurements were used to test the chemical composition alteration of DOM during the batch experiments. Before reaction and after 7 days reaction, aliquots of the solutions in each system were taken and measured using IC, UV254, and NPOC. The formation of acetate was not detectable in solutions reacted for 7 days. UV254 and NPOC showed no significant alteration after reaction, indicating that DOM remained stable over 7 days.

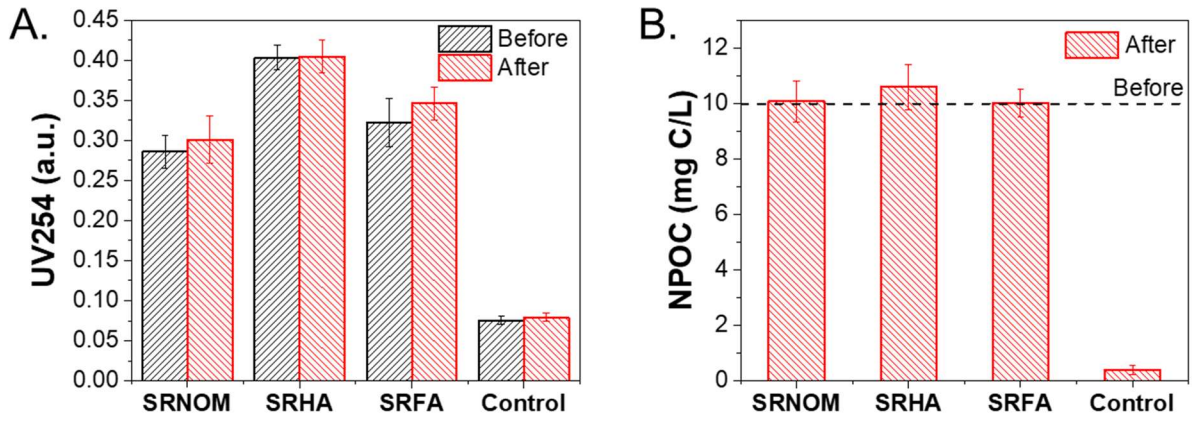

Figure 4-S3. NOM decomposition test using (A) specific ultraviolet (UV) light absorbance at 254 nm, and (B) NPOC measurements for solutions after 7 days. The dotted line indicates the NPOC level (10 mg/L) in the four systems before reaction.

4-S3. FTIR measurement.

FTIR measurement: A Fourier transform infrared (FTIR) spectroscope (Thermo Scientific, Nicolet Nexus 470) equipped with a diamond crystal provided information about the complexation between DOM and arsenopyrite powder surfaces. To obtain clearer bonding information, higher concentrations of arsenopyrite powders (2 g/L) and organic matter (100 mg/L as carbon) than in the batch experiments were reacted at pH 7.0 ± 0.2 for 6 hours. The powders were then filtered, cleaned with DI water, and dried before FTIR measurement.

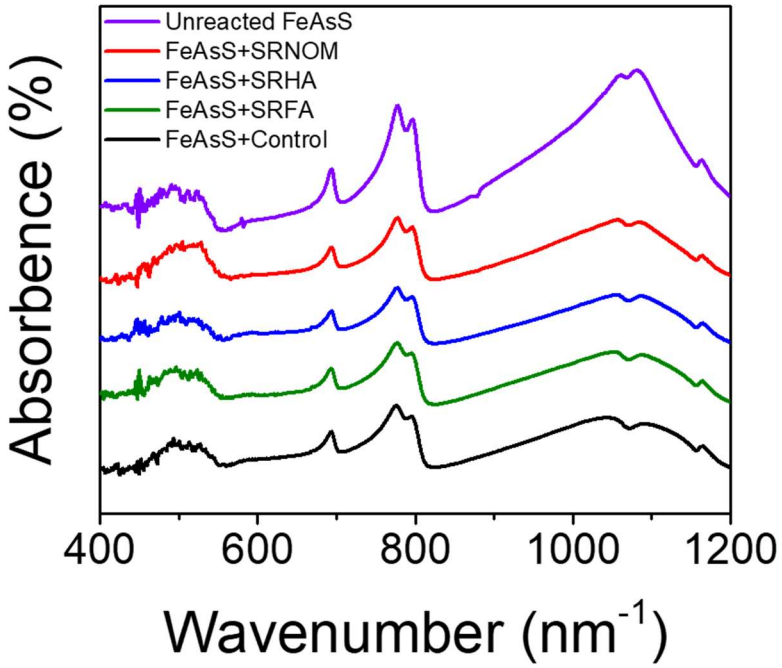

Figure 4-S4. FTIR spectra of unreacted arsenopyrite powders, and arsenopyrite powders reacted with different DOM.

4-S4. AFM measurement.

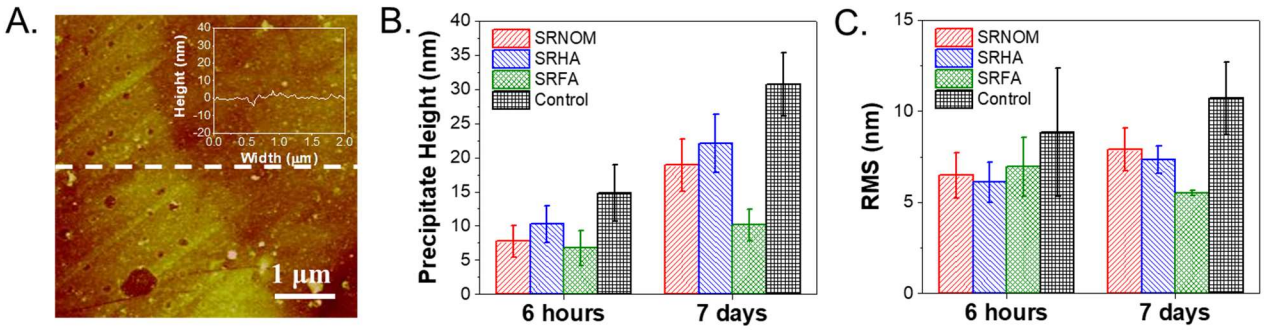

Figure 4-S5. (A) Tapping mode AFM image (5 μm × 5 μm) of unreacted arsenopyrite coupon surface (color scale: 20 nm). (B) The height of precipitates on coupons after 6 hours and 7 days. For each system, at least 50 nanoparticles were cut to get average height information and standard deviation, using Nanoscope 7.20 software (Veeco Inc.). (C) Surface root-mean-square (RMS) roughness obtained from AFM images of 6 hours and 7 days.

4-S5. Raman measurement.

Raman measurement: Raman measurements (InVia Raman Microscope, Renishaw, UK) were carried out with a 514 nm laser (~4 mW) and a grating of 1800 lines/mm. A 20× objective and decreased power of 50% were utilized to minimize aging. Tests showed that Raman measurement at this condition did not cause artificial phase transformation of secondary precipitates (Figure S6 A and B).

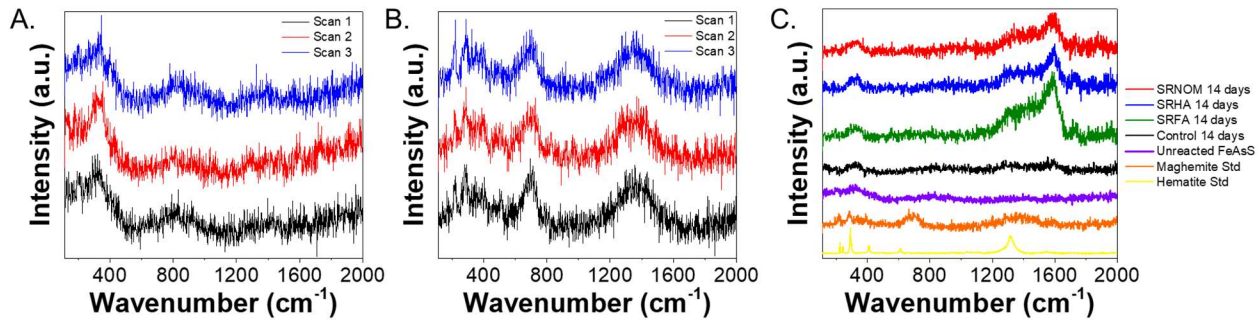

Figure 4-S6. (A) Raman spectroscopy of unreacted arsenopyrite coupon after multiple scans. (B) Raman spectroscopy of maghemite standard sample after multiple scans. (C) Raman spectroscopy of arsenopyrite coupons reacted in DOM systems and the control system after 14 days.

4-S6. Dissolution tests with proteinaceous or labile DOM.

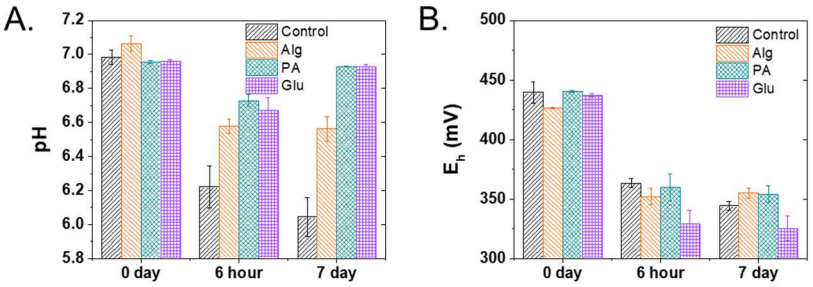

Figure 4-S7. (A) pH values of systems containing alginate (Alg), polyaspartate (PA), and glutamate (Glu) after 6 hours and 7 days. (B) E_h values (mV) of systems containing Alg, PA, and Glu after 6 hours and 7 days. Error bars represent the standard deviation from triplicate batch experiments.

4-S7. GISAXS measurement and analysis.

Preparation of clean quartz substrate: x-cut (110) quartz purchased from MTI Corporation was cut into 5 mm × 5 mm squares using a slow diamond saw (MTI Corporation, Richmond, CA). The quartz was then cleaned thoroughly using acetone, Nochromix®, sulfuric acid, and DI water prior to experiments. Tapping mode AFM was used to confirm the clean surface of the quartz after the cleaning processes.

GISAXS experiment setup: For each GISAXS experiment, a clean piece of (110) surface of quartz (5 mm × 5 mm, MTI Corporation, Richmond, CA) was placed in a specially designed GISAXS fluid cell.[65, 305] The quartz substrate from MTI has atomically flat surfaces with a surface roughness of less than 5 Å. Before each measurement, the quartz position was aligned with respect to the X-ray beam, and a background image was taken of the clean quartz surface in DI water. Then the DI water was removed and freshly made reaction solution was injected into the cell. After the reaction started, the first GISAXS image was taken at 3 minutes from the creation of the solution. The incidence angle was 0.11º to achieve 98% reflectivity with 14 keV beam energy on

the quartz substrates. Scans of multiple locations on the sample were taken to confirm that no beam interactions occurred. The scattering vector q range was 0.01–0.30 $Å^{-1}$.

GISAXS data analysis: The background subtraction of GISAXS 2D images were conducted using GISAXSshop software in Igor 6.3. After subtracting background intensities from DI water scattering, GISAXS 2D images were cut along the Yoneda wing and 1D plots of scattering intensity (I) versus q were made. Using the following relationship between $I(q)$ and q, $I(q) = N \cdot \Delta\rho^2 \cdot \int D(R)V^2(R)P(q,R)dR \cdot [I_{pow}q^{-p} + S(q)]$, the newly formed particle sizes were obtained.[306] In the equation, N is the total particle number, $\Delta\rho$ is the electron density difference between particles and background, $D(R)$ is the size distribution, $V(R)$ is the particle volume, $P(q,R)$ is the form factor, $I_{pow}q^{-p}$ is the power law (for aggregated particles), and $S(q)$ is the structure factor. A polydisperse sphere model with the Schultz size distribution was used to represent the observed size polydispersity of the particles.[293] Detailed information on data fitting can also be found in our previous publications.[73, 293, 297, 300]

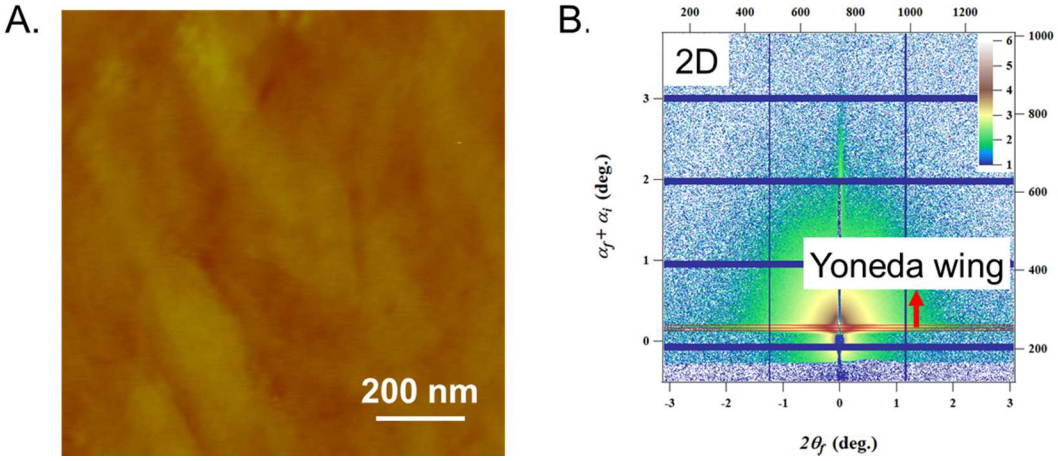

Figure 4-S8. (A) Tapping mode AFM image (1 μm × 1 μm) of unreacted quartz substrate surface (color scale: 10 nm). (B) GISAXS 2D image, showing the Yoneda wing.

Chapter 5. Elucidate thermodynamic and kinetic parameters for heterogeneous nucleation of iron(III) (hydr)oxides on earth-abundant mineral surfaces (quartz)

Abstract

In **Chapter 5** we continue to focus on **System 2**. In **Chapters 3 & 4**, we focused on the effects of different water constituents in injected water on arsenic mobilization from arsenopyrite and secondary mineral precipitation. Here in **Chapter 5**, we elucidate the thermodynamic and kinetic parameters of iron(III) (hydr)oxide nucleation on earth-abundant mineral surfaces, which will have implications for the prediction of iron(III) (hydr)oxide formation in MAR. Poorly crystalline iron(III) (hydr)oxide nanoparticles are often found in many environmental systems. Yet, the thermodynamic and kinetic parameters, e.g., the effective interfacial (α') and apparent activation (E_a) energies, of iron(III) (hydr)oxide nucleation on earth-abundant mineral surfaces have not been determined, which hinders an accurate prediction of iron(III) (hydr)oxide formation and its interactions with other toxic or reactive ions. Here, for the first time, we report experimentally obtained α' and E_a for iron(III) (hydr)oxide nucleation on quartz mineral surfaces, by employing a flow-through, time-resolved grazing incidence small angle X-ray scattering (GISAXS). GISAXS enabled the *in situ* detection of iron(III) (hydr)oxide nucleation rates under different supersaturations (σ, achieved by varying pH 3.3−3.6) and temperatures (12−35ºC). By quantitative analyses based on classical nucleation theory, α' was obtained to be 34.6 mJ/m^2 and E_a was quantified as 32.8 kJ/mol. The fundamental thermodynamic and kinetic parameters obtained here will improve the accuracy of reactive transport model predictions of iron(III) (hydr)oxide's formation, as well as its effects on the fate and transport of pollutants in natural and engineered water systems. The *in situ* flow-through GISAXS method can also be adapted for many important solid–liquid systems to quantify thermodynamic and kinetic parameters at interfaces.

5.1 Introduction

Poorly crystalline iron(III) (hydr)oxide nanoparticles, with particle sizes on the order of 1–10 nm, exist abundantly in natural and engineered aqueous environments,[307] such as acid mine drainage (AMD),[308] managed aquifer recharge (MAR),[62, 92] and hydraulic fracturing systems.[309] During their early formation, iron(III) (hydr)oxide nanoparticles nucleate from a supersaturated solution onto substrates (i.e., a heterogeneous nucleation process) and they further evolve by growth, ripening or aggregation, and phase transformation. Early-formed highly-hydrated iron(III) (hydr)oxide nanoparticles are of particular environmental importance because their small sizes result in their high specific surface area and high adsorption capacity towards contaminants (e.g., Pb, Cd, As, and Cr)[310-313] to minimize their excessive surface energy.[314] Such a heterogeneous nucleation also affects the substrate's surface charge, wettability, dissolution, and redox reactivity towards components in surrounding water.[307] Compared with homogeneously formed particles (particle formation in solution), heterogeneously formed iron(III) (hydr)oxides play a more significant role in immobilizing contaminants because they are in a static state, rather than being mobile like homogeneously nucleated particles, and possess a higher specific surface area due to smaller nucleus sizes. In engineered applications, iron(III) (hydr)oxide is also widely used as coagulants[315] or catalysts[316]. In particular, heterogeneous iron(III) (hydr)oxides on substrates are common catalysts to facilitate Fenton reactions.[317] Given iron(III) (hydr)oxide's high environmental relevance, a better understanding of its nucleation process in aqueous systems is crucial for predicting and controlling its fate and transformation in natural environments and engineered applications.

To quantitatively describe the nucleation of a solid, classical nucleation theory (CNT) proves useful. While non-classical nucleation theories provide more sophisticated descriptions of

the nucleation pathways, CNT offers a more quantitative platform, which has been successfully applied to describe the condensation of a vapor to a liquid,[318] and has also been extended to describe nucleation from solutions in liquid–solid systems, including the nucleation of metals (e.g., gold nanoparticles[319]), metal oxides (e.g., iron oxide[320-321]), or minerals (e.g., calcium carbonate,[322] calcium phosphate[323]). In CNT, the nucleation rate (J_n) and the critical nucleus size (r_c) are two key characteristic properties of the nucleation process.[293, 306, 320, 324] The nucleation rate (J_n) can be expressed as[324-325]

$$J_n = J_0 \cdot \exp\left(-\frac{\Delta g_n}{k_B T}\right) \quad , \qquad \textbf{(eq 5.1)}$$

where J_0 is a kinetic factor of the system, Δg_n is the free energy barrier that the system has to overcome to form a critical nucleus, k_B is the Boltzmann constant (1.38×10^{-23} J/K), and T is the temperature (K). The free energy barrier of a system can be calculated by[306, 324]

$$\Delta g_n = \frac{16\pi {v_m}^2 {\alpha'}^3}{3{k_B}^2 T^2 \sigma^2} \quad , \qquad \textbf{(eq 5.2)}$$

where α' is the effective interfacial energy (mJ/m^2), and v_m is the molecular volume of the nucleated phase (cm^3/molecule). σ is the supersaturation (= ln(IAP/K_{sp})), where IAP is the ion activity product of dissolved components and can be calculated from the water chemistry. From **eq 5.2**, α' and σ are the two main parameters that control the extent of the thermodynamic barrier for nucleation (Δg_n).[306, 324] Combining **eqs 5.1** and **5.2**, the nucleation rate is exponentially proportional to ${\alpha'}^3$, indicating that a slight change of α' will significantly affect the nucleation rate. In **eq 5.1**, J_0 can be further expressed with an Arrhenius equation[324, 326-327]

$$J_0 = A \cdot \exp\left(-\frac{E_a}{k_B T}\right) \quad , \qquad \textbf{(eq 5.3)}$$

where A is a pre-exponential kinetic factor related to ion diffusion and nuclei surface properties, and E_a is the apparent activation energy (J/mol), which is the kinetic barrier of the entire system.

Although α' and E_a are key thermodynamic and kinetic parameters for heterogeneous nucleation, yet they have not been experimentally determined for iron(III) (hydr)oxide nucleation on earth-abundant mineral surfaces. This lack hinders an accurate prediction and control of iron(III) (hydr)oxide formation and its interactions with other aqueous ions. A main challenge that conventional characterization techniques face is an accurate *in situ* quantification of nucleation rates in time-resolved measurements with constant water chemistry. In recent years, synchrotron-based X-ray techniques have been shown to be powerful in measuring the nucleation behaviors of nanoparticles, including iron oxide,[293, 320] calcium carbonate,[306, 328-329] and manganese (hydr)oxide,[65, 330] in solution (homogeneous nucleation) and on substrates (heterogeneous nucleation). Legg et al. used small-angle X-ray scattering (SAXS) to quantify the interfacial energy (70−160 mJ/m^2) of homogeneously nucleated iron oxyhydroxide, β-FeOOH (akaganeite), in aqueous $FeCl_3$ solutions.[331] In work by Hiemstra, the interfacial Gibbs free energy of ferrihydrite was estimated to be 186 mJ/m^2.[332] Hiemstra also suggested that the surface Gibbs free energies of metal (hydr)oxides follow the order of oxides > oxyhydroxides > hydroxides.[332] Indeed, for more crystalized iron oxides, the surface energies were significantly larger than those of more amorphous and hydrated phases, such as 380−1,920 mJ/m^2 for goethite[333-335] and 510−2,630 mJ/m^2 for hematite[333]. The previously reported surface energies of iron (oxy)(hydr)oxides were, however, either for homogeneously nucleated particles in solution or for bulk and more crystalized iron oxides, and these values could be significantly different from the interfacial energies of initially formed and extremely hydrous iron(III) (hydr)oxide heterogeneously nucleated on mineral surfaces. Furthermore, the quantification of the kinetic factor J_0 and activation energy barrier E_a are often overlooked, on the assumption that these kinetic parameters influence nucleation rates less than the free energy barrier Δg_n and interfacial energy α'.[336] Nevertheless, kinetic parameters

can significantly influence nucleation.[326, 337] For example, Wallace et al. observed that silica nucleation rates on substrates are sensitive to J_0, which can account for a more than 10-fold increase of nucleation rate on NH_3^+/COO^- coated substrates than that on COO^- coated surfaces.[337] Li et al. quantified the E_a of calcium carbonate nucleation on quartz by analyzing the nucleation rates as a function of temperature.[326] Further, Li and Jun suggested that J_0 becomes highly important for calcium carbonate nucleation on quartz, especially at high ionic strength (i.e., high salinity).[327]

Here, utilizing *in situ* grazing incidence small angle X-ray scattering (GISAXS), we determined α' and E_a of iron(III) (hydr)oxide heterogeneous nucleation on quartz, which was chosen as an example of an earth-abundant mineral surface.[292] GISAXS has been shown to be a powerful technique for measuring nucleation behaviors on surfaces.[293, 306, 320, 338] GISAXS signals are strengthened by the grazing incidence effect, which enhances SAXS signals from particles on substrate surfaces because no signal is absorbed by the substrates. The signals are also enhanced by the large sampling area and the X-ray standing wave effect.[339] Using a specially designed flow-through GISAXS cell to form iron(III) (hydr)oxide heterogeneous nucleation on the (110) surface of quartz under constant aqueous conditions, we successfully quantified nucleation rates *in situ* from the time-resolved measurements. The obtained α' and E_a values for iron(III) (hydr)oxide nucleation on the mineral surface can be applied to reactive transport models to simulate iron(III) (hydr)oxide's formation in natural environments and engineered applications, such as we recently successfully utilized for quantifying calcium carbonate nucleation in cement systems.[340] Such an *in situ* GISAXS experimental design can be adapted widely to quantify fundamental thermodynamic and kinetic parameters of other environmental nanoparticle nucleation on substrates.

5.2 Experimental section

5.2.1 Substrate preparation

Quartz (SiO_2) was chosen as the model substrate because it is one of the most abundant minerals in the Earth's continental crust[292] and iron(III) (hydr)oxide often forms on quartz in engineered applications.[341] In our work, high quality single crystal quartz wafers were purchased from MTI Corporation (Richmond, CA), which had atomically flat surfaces with a surface roughness of less than 5 Å (Supporting Information, **Figure 5-S1**).[92] The quartz was exposing the (110) surface, which is as abundant in natural systems as other quartz surfaces with close surface energies (e.g., (101)).[64, 337] Detailed preparation and washing procedures of quartz substrates is available in the Supporting Information (5-S1).

5.2.2 Solution chemistry

To initiate iron(III) (hydr)oxide nucleation on quartz, two reaction solutions were created from reagent grade $Fe(NO_3)_3 \cdot 9H_2O$ and $NaNO_3$, respectively. Nitrate was used instead of chloride because chloride can promote the phase transformation of iron(III) (hydr)oxides through Ostwald ripening.[300] The reagent concentrations, pH values, and the supersaturations with respect to ferrihydrite after 1:1 volumetric mixing of $Fe(NO_3)_3$ and $NaNO_3$ solutions, are listed in **Table 5.1**. The supersaturations, defined as $\sigma = \ln(IAP/K_{sp})$, were calculated by Visual MINTEQ (Ver. 3.1) using the thermo.vdb database file. Visual MINTEQ calculates σ in $\log_{10}(IAP/K_{sp})$, which was converted to $\ln(IAP/K_{sp})$ in this work, for further theoretical calculations. Our previous GISAXS batch experiments on iron(III) (hydr)oxide nucleation in stagnant systems used pH 3.6 and an 0.1 mM iron(III) concentration.[64, 293, 297, 300] In this study, to measure iron(III) (hydr)oxide heterogeneous nucleation rates in a flow-through system, pH 3.6 and an 0.1 mM iron(III)

concentration at room temperature (25ºC) were also chosen as starting conditions (σ = 3.77, **C2** in **Table 5.1**). Then, to obtain α', two other pH conditions, pH 3.3 (σ = 2.54, 25ºC, **C1** in **Table 5.1**) and pH 3.9 (σ = 4.87, 25ºC, **C3** in **Table 5.1**), were employed to provide decreased and increased supersaturations, respectively. The pH values (3.3−3.9) were also within the pH values in acid mine drainage systems where iron(III) (hydr)oxide exists.[342] The solubility product (K_{sp}) of ferrihydrite in the Visual MINTEQ database is $10^{3.2}$ at 25ºC.[343] In theoretical analysis, ferrihydrite was used as the representative iron(III) (hydr)oxide phase for calculating supersaturations for two reasons: First, it was previously identified as the main *ex situ* measured phase of homogeneously nucleated iron(III) (hydr)oxide in a mixed solution of 0.1 mM $Fe(NO_3)_3$ and 10 mM $NaNO_3$ at pH 3.6 in a batch system.[64, 338] Second, ferrihydrite was known to be the initial phase of iron(III) (hydr)oxide nanoparticles while our phase can be poorly crystalline structure of ferrihydrite.[344] Further, to obtain E_a, two other temperature conditions, 12ºC and 35ºC (**C4** and **C5** in **Table 5.1**), were imposed the experimental systems at pH 3.3. The concentrations of $Fe(NO_3)_3$ solution at the lower and higher temperatures were tuned slightly to obtain the same supersaturation (σ = 2.54) of the mixed solution as that at 25ºC. The K_{sp} values of ferrihydrite in the Visual MINTEQ database are $10^{4.0}$ at 12ºC and $10^{2.6}$ at 35ºC.[343] Detailed information on solution chemistry can be found in the Supporting Information (5-S1).

Table 5.1 Chemical composition, pH value, supersaturation, and temperature of different mixed solutions for nucleation experiments.

System	$Fe(NO_3)_3$ (mM)	$NaNO_3$ (mM)	pH	σ^a	Temperature (ºC)
C1	0.1	10	3.3 ± 0.1	2.54	25
C2	0.1	10	3.6 ± 0.1	3.77	25
C3	0.1	10	3.9 ± 0.1	4.87	25

C4	0.4	10	3.3 ± 0.1	2.54	12
C5	0.038	10	3.3 ± 0.1	2.54	35

[a]Supersaturation (σ) is defined as $\ln(IAP/K_{sp})$, where IAP is the ion activity product with respect to ferrihydrite, and K_{sp} is the solubility product of ferrihydrite. K_{sp} in the database for ferrihydrite is $10^{3.2}$.[343] All five systems were oversaturated with respect to ferrihydrite ($\sigma>0$). Values of σ were calculated by Visual MINTEQ (ver. 3.1) using the thermo.vdb database file.
[b]The temperature of mixed solutions were monitored before and after the reaction, using a benchtop controller thermocouple probe (OMEGA CSI32K-C24, US) with a response time of 5 s and resolution of ± 0.5°C.

5.2.3 *In situ* GISAXS measurements

GISAXS experiments were conducted at the beamline 12-ID-B of the Advanced Photon Source (Argonne National Laboratory, USA). Clean quartz substrates were put into a flow-through cell specially designed for *in situ* GISAXS experiments (**Figure 5.1A** and **5.1B**). To initiate nucleation, $Fe(NO_3)_3$ and $NaNO_3$ solutions were pumped into the GISAXS cell in a 1:1 v/v ratio. Timekeeping started when the mixed solution entered into the GISAXS cell and contacted the quartz. The actual experimental setup at the beamline can be seen in **Figure 5-S2**. The flow-through setup provided a constant supersaturation condition in the cell. For temperature experiments, the batch solutions of $Fe(NO_3)_3$ and $NaNO_3$ were either pre-heated in the tubing using a heating plate or pre-cooled with a water/ice mixture. GISAXS 2D patterns were taken after the well-mixed solution entered into the cell, using a brief X-ray exposure (10 seconds at each measurement time point) to minimize beam effects. At least triplicate GISAXS experiments were conducted for each condition. After each GISAXS experiment, grazing incidence wide angle X-ray scattering (GIWAXS) was used to identify the phases of newly formed iron(III) (hydr)oxide heterogeneous nanoparticles on the quartz substrate. Detailed information on GISAXS measurements can be found in the Supporting Information (5-S1).

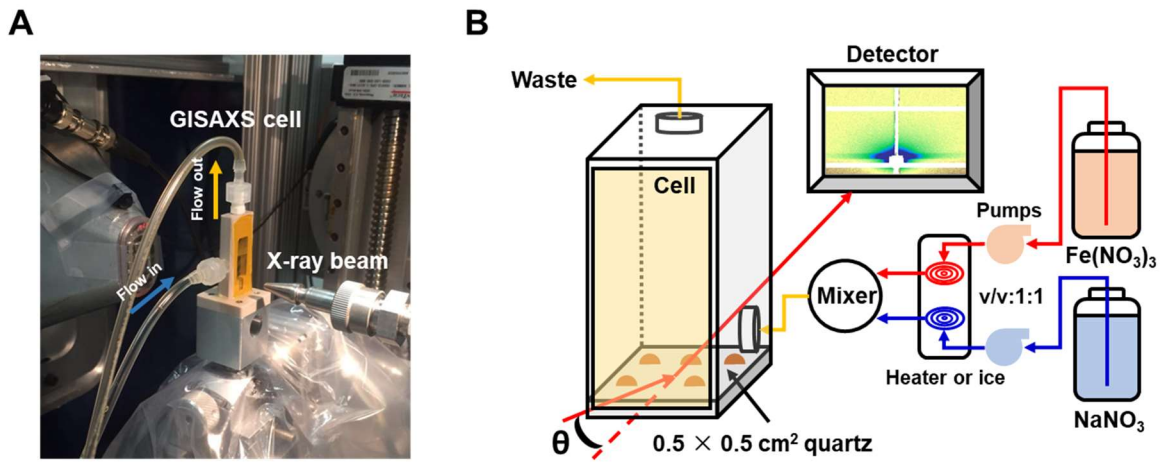

Figure 5.1 (**A**) *In situ* GISAXS experiment setup at beamline 12-ID-B in APS. (**B**) Schematic of a flow-through GISAXS system for iron(III) (hydr)oxide heterogeneous nucleation. Two identical peristaltic pumps were used to pump reservoir solutions into a micromixer in a 1:1 v/v ratio. For effective interfacial energy measurements, the pH of the mixed solutions was in the range of 3.3−3.9. For apparent activation energy measurements, the solutions of $Fe(NO_3)_3$ (0.038−0.4 mM) and $NaNO_3$ (10 mM) were either heated in the tubing using a heating plate to reach 35ºC, or cooled with a water/ice mixture to reach 12ºC.

5.2.4 GISAXS data analysis to obtain effective interfacial and apparent activation energies of iron(III) (hydr)oxides nucleation on quartz

To generate 1D plots, the obtained GISAXS 2D patterns were further analyzed using GISAXSshop software in Igor 6.3 (**Figures 5-S3**). After the background intensities from DI water scattering were subtracted, the GISAXS 2D images were cut along the Yoneda wing and 1D plots of scattering intensity *I(q)* versus *q* were obtained (**Figure 5-S3C**). The Yoneda wing is a narrow band of enhanced scattering signals due to the X-ray wave guiding effect occurring when the incidence angle is close to the critical angle of the substrate.[345-346] To generate the nucleation rates (J_n) from *I(q)* vs *q* plots, two methods were used: the GISAXS invariant method and GISAXS intensity fitting method. A detailed comparison of the strengths and limitations of these two methods is available in the Supporting Information (5-S2). For the GISAXS invariant method, the invariant (Q) is defined as $Q = (\frac{1}{2\pi^2}) \int I(q) q^2 dq$ for isotropic SAXS,[328] which is proportional to

the total volume of nanoparticles, and is also proportional to the total particle number when nucleation is dominant and particle growth is negligible. The linear fitting of relative changes of Q over the experimental time provides J_n from the slope. For the GISAXS intensity fitting method, the relationship between $I(q)$ vs q can be expressed as[293, 306, 320]

$$I(q) = kN \cdot \Delta\rho^2 \cdot \int D(R)V^2(R)P(q,R)dR \cdot [I_{pow}q^{-p} + S(q)] \quad , \qquad \textbf{(eq 5.4)}$$

where k is the experimental constant, N is the total particle number, $\Delta\rho$ is the electron density difference between particles and the background, $D(R)$ is the nucleus size distribution, $V(R)$ is the particle volume, $P(q,R)$ is the form factor, $I_{pow}q^{-p}$ is the power law (for aggregated particles), and $S(q)$ is the structure factor ($S(q)$ = 1 for dilute systems). A polydisperse sphere model with the Schultz size distribution was assumed in this study. Linear fitting of the relative changes in the total particle number N (in arbitrary units) over the experimental time provided J_n from the slope. From CNT, after taking the natural logarithm of both sides of **eq 5.1**, the equation can be rewritten as[306]

$$\ln(J_n) = \ln(J_0) - \frac{16\pi {v_m}^2 {\alpha'}^3}{3{k_B}^3 T^3 \sigma^2} = \ln(J_0) - \frac{B}{\sigma^2} \quad , \qquad \textbf{(eq 5.5)}$$

and the effective interfacial energy can be calculated by

$$\alpha' = \left(\frac{B \cdot 3{k_B}^3 T^3}{16\pi {v_m}^2}\right)^{1/3} \quad . \qquad \textbf{(eq 5.6)}$$

After obtaining J_n at different σ, the relationship between $\ln(J_n)$ and $1/\sigma^2$ was linearly fitted, thus providing the values of B and α'. Next, to calculate E_a , combining **eqs 5.1** and **5.3** provides

$$J_n = A \cdot \exp\left(-\frac{E_a}{k_B T}\right) \cdot \exp\left(-\frac{\Delta g_n}{k_B T}\right) \quad . \qquad \textbf{(eq 5.7)}$$

Note that if k_B is used, then E_a and Δg_n are both in units of J/molecule, so to convert them into units of J/mol, k_B was replaced with the ideal gas constant R (R=$N_A \cdot k_B$, 8.3144598 J/mol·K,

N_A=6.02214076×10^{23}).[324, 326] After taking the natural logarithm of both sides of **eq 5.7** and substituting R for k_B , we have

$$\ln(J_n) = \ln(A) - \frac{E_a + \Delta g_n}{RT} \quad . \qquad \textbf{(eq 5.8)}$$

After obtaining J_n at different T, the relationship between $\ln(J_n)$ and $1/T$ was linearly fitted, providing the values of E_a+Δg_n. After calculating Δg_n from **eq 5.2**, the values of E_a were obtained. A more detailed description of GISAXS data analysis is in the Supporting Information (5-S2).

5.2.5 *Ex situ* atomic force microscopy (AFM)

To observe the heterogeneously formed nuclei, *ex situ* tapping mode atomic force microscopy (AFM, Veeco Inc., Nanoscope V multimode SPM) was conducted for quartz reacted under the same conditions as in the GISAXS measurements (**Table 5.1**). Detailed information on AFM experiments and sample preparation can be found in the Supporting Information (5-S5).

5.3 Results and discussion

5.3.1 *In situ* GISAXS observations

GISAXS 1D patterns for selected time and conditions are presented in **Figure 5.2**. In 5 minutes (300 seconds), the scattering intensities of all five conditions increased, indicating continuous heterogeneous nucleation of iron(III) (hydr)oxide nanoparticles. The scattering intensities correlate to the total volume of particles on the substrate surface, and the shapes of the scattering intensity curves are related to the particle size and particle shape.[320] In **Figure 5.2A−C**, a faster increase in scattering intensity is observed for higher pH values, indicating faster nucleation rates at higher supersaturations. The value of the scattering vector q at the bend in the 1D scattering curves is reciprocally related to particle size. Thus, a bend in the higher q range

indicates a smaller average radius of gyration (R_g). Comparing the three pH systems, it is clear that at higher supersaturations, the bend locations for the curves shift to higher q ranges, suggesting a smaller R_g. Because *in situ* GISAXS was monitoring the particle scattering intensities starting before nucleation, it can be assumed that the early R_g values are close to the critical nucleus size (r_c). With the assumption, we found that smaller R_g and r_c observed for higher supersaturations are consistent with classical nucleation theory ($r_c = \frac{2v_m\alpha'}{k_BT\sigma}$). Furthermore, for each pH condition, the bend locations for the curves did not shift significantly in 300 seconds, indicating that, within this time period, particle nucleation was dominant over particle growth.

To obtain particle sizes, the scattering curves were fitted with a polydisperse sphere model (**eq 5.4**),[293, 320] providing the values of R_g. Particle size fitting was not performed for scattering obtained at 30 and 60 seconds because of the low scattering intensities-to-noise ratio. From 90 seconds to 300 seconds, the *in situ* average R_g values of the particles were 3.0 ± 0.3, 2.7 ± 0.3, and 2.4 ± 0.1 nm at pH 3.3, 3.6, and 3.9 (25ºC), respectively. **Figure 5.2D** and **5.2E** show the GISAXS scattering pattern of two additional temperatures (12ºC and 35ºC) at pH 3.3. Comparing **Figure 5.2A** with **Figure 5.2D** and **5.2E**, a faster increase of scattering intensity and faster nucleation rates are seen for higher temperatures. In addition, R_g slightly decreases at higher temperatures (3.2 ± 0.3 nm for pH 3.3 at 12ºC, 2.9 ± 0.2 nm for pH 3.3 at 35ºC), although the differences in R_g were within the experimental error range. Additional GISAXS figures for replicate experiments of all conditions are available in the Supporting Information (**Figure 5-S4**). Beam effects on iron(III) (hydr)oxide nucleation were checked by comparing the GISAXS scattering of locations receiving X-rays with that of locations not receiving X-rays (**Figure 5-S5**). No difference was observed, indicating that the brief X-ray beam exposure did not significantly affect the iron(III) (hydr)oxide nucleation behavior.

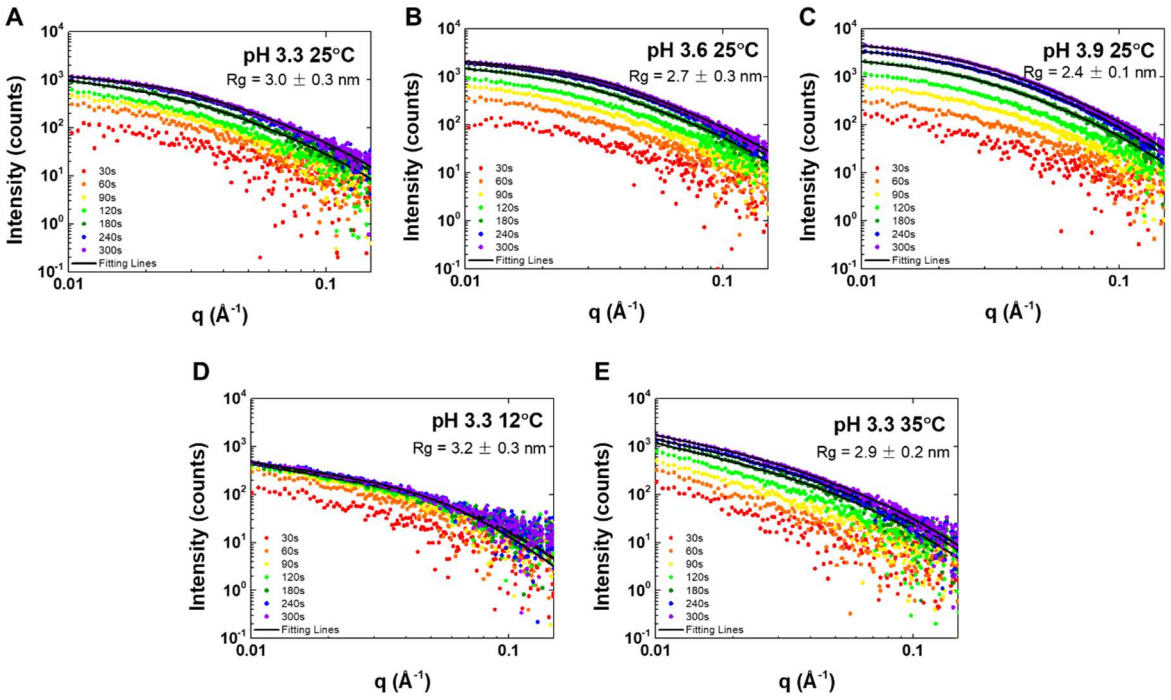

Figure 5.2 Representative GISAXS 1D plots of iron(III) (hydr)oxide heterogeneous nucleation on quartz: (**A**) pH 3.3 at 25ºC; (**B**) pH 3.6 at 25ºC; (**C**) pH 3.9 at 25ºC; (**D**) pH 3.3 at 12ºC; (**E**) pH 3.3 at 35ºC. Black lines are curves fitted by using software in MatLab developed in the APS at sector 12-ID-B. Time points from 90 seconds to 300 seconds were fitted. The fitting results of 90 seconds and 120 seconds were not plotted to clearly show the difference in the intensity pattern increase in the five conditions.

5.3.2 *Ex situ* AFM observations of iron(III) (hydr)oxide nucleation on quartz substrates

Tapping mode AFM measurements of the iron(III) (hydr)oxide nucleation on quartz show that the particle size changes systematically with different pH and temperature conditions (**Figure 5.3**). Analysis of more than 50 primary nanoparticles in each condition reveals that the average particle heights of primary particles in five systems were 1.5 ± 0.2 nm (pH 3.3 at 25ºC), 1.3 ± 0.3 nm (pH 3.6 at 25ºC), 1.2 ± 0.3 nm (pH 3.9 at 25ºC), 1.5 ± 0.3 nm (pH 3.3 at 12ºC), and 1.4 ± 0.2 nm (pH 3.3 at 35ºC). The term "primary particle" is used to differentiate newly nucleated particles (red arrow, **Figure 5.3A**) from particles with bigger sizes (blue arrow, **Figure 5.3A**). Observed in each condition, these bigger particles, with average sizes in the range of 10−20 nm, did not affect

the GISAXS analysis of primary particles because their scattering is beyond the experimental q range of 0.01−0.15 $Å^{-1}$. Additional tests using an inverted GISAXS cell confirmed that these bigger particles were mainly grown from primary particles after nucleation rather than resulting from gravitational settlement of homogeneously precipitated particles (detailed discussion is in Supporting Information, 5-S5). The trends of primary particle sizes in AFM observations were consistent with those observed by *in situ* GISAXS. In addition, for systems with higher supersaturations and temperatures, the AFM observations show that the particle densities on quartz increased, consistent with GISAXS observations, as the total particle volume (scattering intensity) increased. Note that although the size trends, as a function of supersaturation and temperature, are consistent for both AFM and GISAXS analyses, the absolute sizes from AFM measurements (1.2−1.5 nm) were smaller than those from GISAXS measurements (2.4−3.2 nm) (**Table 5-S1**). This difference could result from the dehydration of the *ex situ* samples. In addition, AFM measures the vertical heights of particles, while GISAXS measures the in-plane (horizontal) radii of gyration of particles. Therefore, the height from AFM and the radii from GISAXS may not be the same.

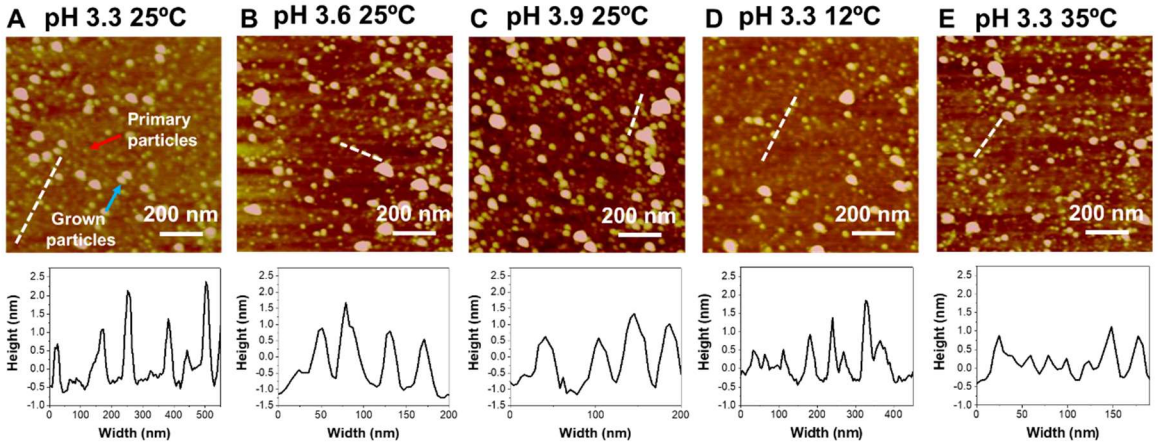

Figure 5.3 Representative AFM height mode images (1 μm × 1 μm) (color scale: 5 nm) of iron(III) (hydr)oxide heterogeneous nucleation on quartz in five conditions: (**A**) pH 3.3 at 25ºC, (**B**) pH 3.6 at 25ºC, (**C**) pH 3.9 at 25ºC, (**D**) pH 3.3 at 12ºC, and (**E**) pH 3.3 at 35ºC. The red arrow in (**A**) indicates an example

of a "primary particle", and the blue arrow in (**A**) indicates an example of the bigger particles, which were mainly attributed to particle growth.

5.3.3 Effective interfacial energy (α') calculations

To obtain α' of iron(III) (hydr)oxide heterogeneous nucleation on quartz, both the GISAXS invariant method and the GISAXS fitting method were used. For the invariant method, when nucleation is dominant over particle growth, Q is proportional to the total particle number. **Figure 5.4A** shows the evolution of Q values in the q range of 0.01–0.2 $Å^{-1}$ under three pH conditions at 25ºC from 30 seconds to 900 seconds. No apparent induction time was observed under our experimental conditions. From 90 seconds to 300 seconds, the invariant Q followed an approximately linear trend, suggesting that during this time range, particle nucleation was dominant over particle growth. Starting from 300 seconds, the increase of invariant Q in the three systems slowed, which implied the active growth of nucleated particles. Thus, from 90 seconds to 300 seconds, the invariant Q was proportional to the total particle number. The slope obtained from a linear regression of this time range provides the time-resolved total particle number change rate within the given time range, i.e., the nucleation rates (J_n), of the three systems. **Figure 5.4C** shows the correlation between J_n derived from the invariant method and the supersaturations (σ) under the three pH conditions at 25ºC. The fitting method uses **eq 5.4** to provide the total particle number (N). **Figure 5.4B** shows the evolution of fitted N values of the three pH conditions from 90 seconds to 300 seconds. The linear regression of N versus time generates J_n. **Figure 5.4D** shows the correlation between J_n derived from the fitting method and the supersaturations (σ) under the three pH conditions at 25ºC. Next, the slopes' B values obtained from the two methods were used to calculate α' by using **eq 5.6** (**Table 5.2**). Further, nucleation phase information from GIWAXS showed two peaks of 6-line ferrihydrite (1.51 Å at $2\theta = 62^{o}$ and 1.47 Å at $2\theta = 63^{o}$)[347] for iron(III)

(hydr)oxides in the three pH systems at 25°C (**Figure 5-S7**), but the other four peaks of 6-line ferrihydrite were not observed, suggesting that the iron(III) (hydr)oxide heterogeneous nucleation on quartz was poorly crystallized ferrihydrite-like iron (III) (hydr)oxide. In this study, several previously proposed formulas for ferrihydrite were used to calculate its molecular volume (v_m): $Fe(OH)_3$,[348] $Fe_5HO_8 \cdot 4H_2O$[349-351], and $5Fe_2O_3 \cdot 9H_2O$.[352-353] The density value used for ferrihydrite is 3.96 g/cm^3.[349, 351] Different values of ferrihydrite's molecular volume provided varied effective interfacial energies. From invariant calculations, they were 33.5 ± 0.1 mJ/m^2 for $Fe(OH)_3$, 12.3 ± 0.1 mJ/m^2 for $Fe_5HO_8 \cdot 4H_2O$, and 7.8 ± 0.1 mJ/m^2 for $5Fe_2O_3 \cdot 9H_2O$. From the fitting method, they were 34.6 ± 0.2 mJ/m^2 for $Fe(OH)_3$, 12.7 ± 0.1 mJ/m^2 for $Fe_5HO_8 \cdot 4H_2O$, and 8.0 ± 0.1 mJ/m^2 for $5Fe_2O_3 \cdot 9H_2O$. The derived α' are similar from these two invariant and fitting approaches, but the different molecular volumes based on varied chemical formula can provide different α' values. With increasing molecular volume and hydration degree, the α' needed for iron(III) (hydr)oxide to form heterogeneous nuclei on quartz decreased. The obtained α' (from fitting method) was also converted to the substrate−ferrihydrite interfacial free energy, α_{sn}, by using **eq 5-S3** in the Supporting Information: 152 mJ/m^2 ($Fe(OH)_3$), 122 mJ/m^2 ($Fe_5HO_8 \cdot 4H_2O$), and 115 mJ/m^2 ($5Fe_2O_3 \cdot 9H_2O$).

The obtained α' of iron(III) (hydr)oxide heterogeneous nucleation on quartz (7.8−34.6 mJ/m^2) was found to be slightly smaller than those of other crystal phases' nucleation on quartz, such as calcite (47 mJ/m^2),[306] vaterite (32 mJ/m^2),[306] and $Mn(OH)_2$(s) (71 mJ/m^2)[330]. It is also smaller than that of homogeneously nucleated iron oxyhydroxide (70−160 mJ/m^2),[331] and smaller than the surface energies of homogeneously formed and fully crystalized iron oxides, including goethite (380−1920 mJ/m^2)[333-335] and hematite (510−2630 mJ/m^2)[333], but close to the reported values of homogeneously formed hydrated $Fe(OH)_2$ (20 mJ/m^2)[333] and calcium phosphate (5−19

mJ/m^2) mineralization in/on collagen fibrils.[354] One possible reason for the smaller α' of iron(III) (hydr)oxide nucleation on quartz is that the highly hydrated and poorly crystalized structure of initially formed iron(III) (hydr)oxide nuclei decreases their heterogeneous nucleation energy barrier. It was found that the interfacial energies of Mn (hydr)oxide decreased by 20%−50% because of adsorbed water molecules on the surface.[355] Comparing ferrihydrite with other crystal phases, the number of surface-bound water molecules is significantly higher,[356] which might help to decrease its surface energy. Note that the obtained α' values of iron(III) (hydr)oxide are dependent on its formula and molecular volume (v_m). Therefore, when using the α' value for modelling iron(III) (hydr)oxide's formation, its formula should also be provided simultaneously.

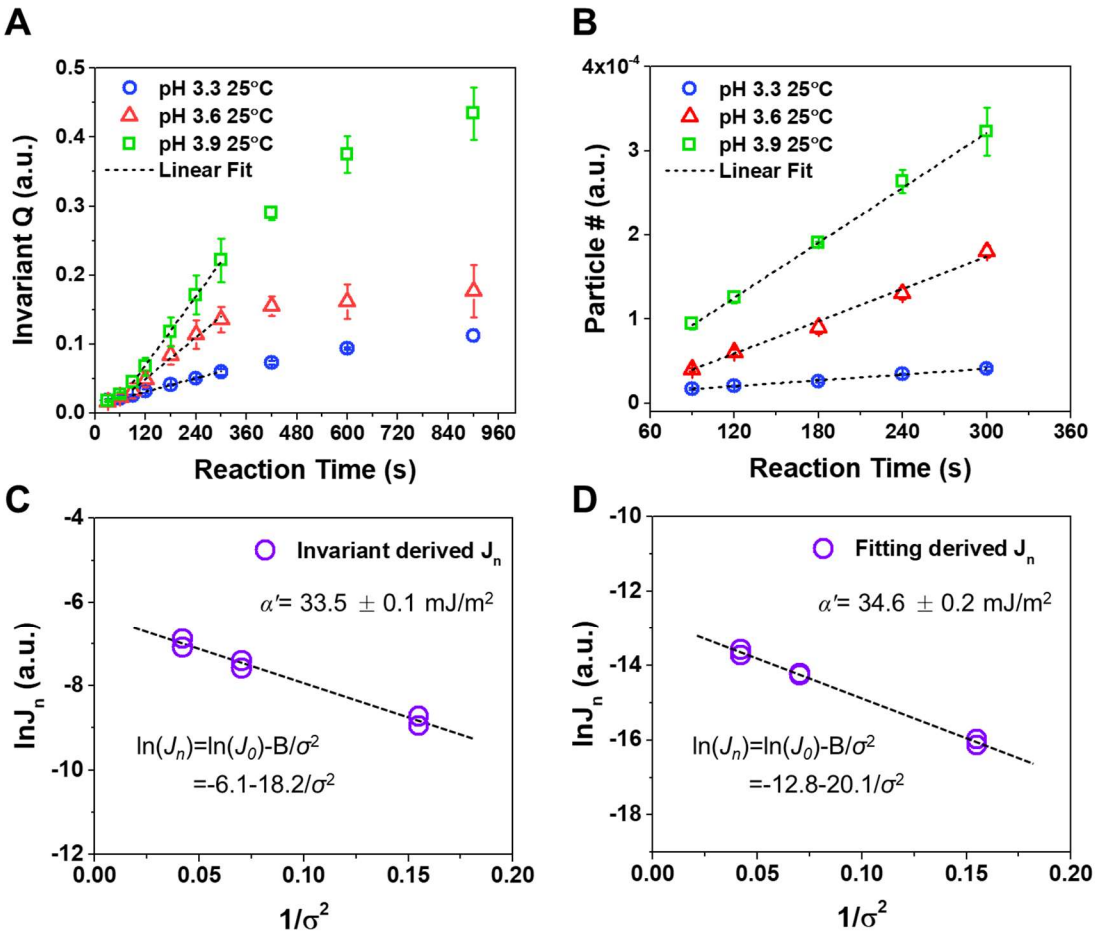

Figure 5.4 Mathematical calculations to obtain effective interfacial energy. (**A**) Invariant Q evolution of three pH conditions at 25ºC. Black dotted lines are the linear regression of Q values from 90 seconds to 300 seconds. Error bars represent the standard errors from triplicate GISAXS tests. (**B**) Total particle number (in arbitrary units) evolution of three pH conditions at 25ºC from GISAXS fitting. Black dotted lines are linear regressions of particle numbers from 90 seconds to 300 seconds. (**C**) and (**D**) Regression of nucleation rates (J_n) with supersaturations (σ) derived from the GISAXS invariant and fitting method, respectively.

Table 5.2 Effective interfacial energy and apparent activation energy of iron(III) (hydr)oxide heterogeneous nucleation on the (110) surface of quartz.

Ferrihydrite	Molecular weight (g/mol)	Density (g/cm^3)	Molecular volume (cm^3/molecule)	α' (invariant, mJ/m^2)[a]	α' (fitting, mJ/m^2)[a]	E_a (invariant, kJ/mol)[b]	E_a (fitting, kJ/mol)[b]
$Fe(OH)_3$[348]	106.85	3.96	4.48×10^{-23}	33.5±0.1	34.6±0.2	34.1±6.6	32.8±1.8
$Fe_5HO_8\cdot4H_2O$[349-351]	480.25	3.96	2.01×10^{-22}	12.3±0.1	12.7±0.1	34.2±6.6	32.8±1.8
$5Fe_2O_3\cdot9H_2O$[352-353]	960.5	3.96	4.03×10^{-22}	7.8±0.1	8.0±0.1	34.0±6.6	32.8±1.8

[a]The error ranges come from uncertainties related to the weighted linear regression of $\ln(J_n)$ vs $1/\sigma^2$. [b]The error ranges come from uncertainties related to the weighted linear regression of $\ln(J_n)$ vs $1/T$.

5.3.4 Apparent activation energy (E_a) and kinetic factor calculations

To obtain E_a of iron(III) (hydr)oxide heterogeneous nucleation on quartz, the GISAXS scattering spectra of different temperature conditions were analyzed by both the invariant and fitting methods. Figure 5A shows the evolution of invariant Q for three temperature conditions at pH 3.3 from 30 seconds to 900 seconds. The slopes obtained from a linear regression of invariant Q in the time range of 90 seconds to 300 seconds provide J_n of the three temperature conditions, as shown in Figure 5C. GISAXS fitting of the scattering patterns from 90 seconds to 300 seconds also provides J_n (**Figure 5.5B** and **5.5D**) under the three temperature conditions. Further, the correlation between J_n and T was linearly fitted to obtain the slope, which provided the $E_a+\Delta g_n$ values from **eq 5.8** (41.2 ± 6.1 kJ/mol from the invariant method, 40.5 ± 1.2 kJ/mol from the fitting method). For ferrihydrite in the form of $Fe(OH)_3$, using **eq 5.2**, the thermodynamic energy barrier (Δg_n) in the temperature range of 12−35°C was calculated to be 7.0 ± 0.6 kJ/mol from the invariant method and 7.8 ± 0.6 kJ/mol from the fitting method. The Δg_n values from both methods for all three ferrihydrite formulas are available in the SI (**Table 5-S2**). Subtraction of Δg_n from the sum of $E_a+\Delta g_n$ gave the kinetic energy barrier value, E_a: 34.1 ± 6.6 kJ/mol from the invariant method for $Fe(OH)_3$, and 32.8 ± 1.8 kJ/mol from the fitting method (**Table 5.2**). For the iron(III) (hydr)oxide phases in the different temperature systems, the 1.51 Å peak at $2\theta = 62^\circ$ and the 1.47 Å at $2\theta = 63^\circ$ peak of 6-line ferrihydrite were observed for pH 3.3 at 25°C and 35°C. For pH 3.3 at 12 °C, the 1.51 Å peak at $2\theta = 62^\circ$ was observed, suggesting that these iron(III) (hydr)oxides were also poorly crystallized ferrihydrite-like iron (III) (hydr)oxides (**Figure 5-S7**).

Then, using a calibration method reported before,[326] kinetic factors A and J_0 in **eq 5.3** were calculated (detailed calculation is in the Supporting Information, 5-S10). With the E_a

obtained from the fitting method (32.8 ± 1.8 kJ/mol), J_0 was calculated to be $10^{14.5\pm0.3}$ nuclei/m^2·min at 25ºC, which is in the similar range of reported values of other heterogeneous mineral nucleation systems at room temperature including $10^{13.5\pm0.7}$ nuclei/m^2·min of silica and $10^{16.1\pm1.0}$ nuclei/m^2·min of $CaCO_3$.[326, 337]

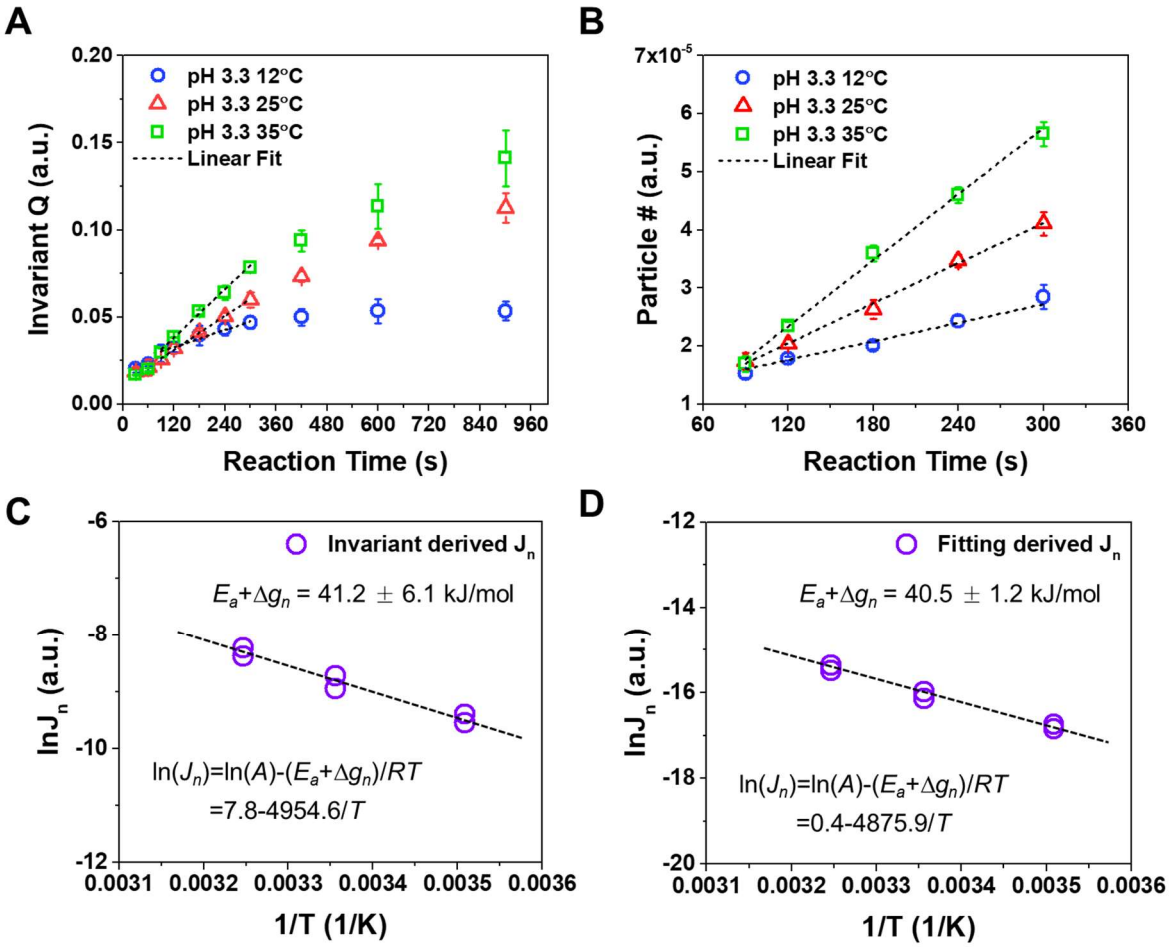

Figure 5.5 Mathematical calculations to obtain apparent activation energy. (**A**) Invariant Q evolution of three temperature conditions at pH 3.3. Black dotted lines are linear regressions of Q values from 90 seconds to 300 seconds. Error bars represent the standard errors from triplicate GISAXS tests. (**B**) Total particle number (in arbitrary units) evolution for three temperature conditions at pH 3.3, from the GISAXS fitting method. Black dotted lines are the linear regressions of particle numbers from 90 seconds to 300 seconds. (**C**) and (**D**) Regression of nucleation rates (J_n) with temperatures (T) derived from the GISAXS invariant and fitting method, respectively.

5.4 Conclusions and environmental implications

Here, we obtained the effective interfacial and apparent activation energies of iron(III) (hydr)oxide heterogeneous nucleation on a quartz surface by utilizing time-resolved GISAXS. The flow-through system ensured a constant water chemistry (e.g., reactant concentrations, supersaturations) for iron (III) (hydr)oxide nucleation during experiments. Time-resolved GISAXS allows accurate quantification of heterogeneous nucleation rates on surfaces. Using both the invariant and the fitting methods and employing CNT, the obtained nucleation rates successfully provide α' (the thermodynamic parameter) and E_a (the kinetic energy barrier), which can be useful for interpreting, predicting, and controlling iron(III) (hydr)oxide's formation in aquatic environments.

In natural and engineered aquatic environments, iron(III) (hydr)oxide is ubiquitous and serves as an important sequester for contaminants.[62, 92, 308-309] For example, in MAR, iron(III) (hydr)oxide formed from the dissolution of arsenic-bearing iron sulfide minerals can adsorb arsenic and decrease arsenic mobility.[92, 171] Considering that the recovered water from MAR is an important groundwater supply for agricultural irrigation,[357] the extents, sizes, formation kinetics, and distribution of iron(III) (hydr)oxide are thus important to model and monitor for arsenic control. However, in most reactive transport simulations, the nucleation of iron(III) (hydr)oxide is simply neglected; instead, bulk precipitation (only growth) is often used as an approximation.[358-360] In this case, overlooking the nucleation process can prevent accurate simulation of the arsenic mobility because of a lack of accurate modelling of the secondary precipitate's size, rate, and distribution. Without knowing the sizes of the initially formed iron(III) (hydr)oxide nuclei, the estimation of specific surface area will be inaccurate, which makes calculating the contaminant adsorption amount inaccurate. In addition, the

thermodynamic and kinetic energy barriers determine whether iron(III) (hydr)oxide nuclei can form on a certain type of mineral surface, and further determine the distribution of iron(III) (hydr)oxide in subsurface systems. For example, Hu et al. observed that the heterogeneous nucleation of iron(III) (hydr)oxide on corundum was faster than that on quartz and mica, which was attributed to the lower precipitate−substrate interfacial energy for corundum.[338] Li et al. found that the α' of calcium carbonate formation on mica was smaller than that on quartz, resulting in faster and more calcium carbonate nucleation on mica than on quartz.[306] For all these reasons, nucleation needs to be included in reactive transport models, which requires the thermodynamic and kinetic parameters of nucleation as important inputs. For example, Li et al. have successfully incorporated the α' and E_a of calcium carbonate heterogeneous nucleation on quartz into a numerical model to simulate calcium carbonate formation in a cement system.[340] Similarly, the α' and E_a of iron(III) (hydr)oxide heterogeneous nucleation on quartz obtained here can also be applied in reactive transport models in the future to predict iron(III) (hydr)oxide's formation and its distribution at solid–liquid interfaces.

In situ GISAXS, which provides fundamental thermodynamic and kinetic information about heterogeneous nucleation on substrates, will be crucial for solid–liquid interfacial science and engineering. While the use of the (110) surface of quartz in this work is a useful starting point, future studies can expand to determine the interfacial and activation energies of iron(III) (hydr)oxide heterogeneous nucleation on other minerals (e.g., mica, corundum, feldspar). Future studies can also explore surfaces with more morphological complexity. They can alter surface roughness by changing step densities, apply coatings of different chemical functional groups (e.g., amine-, carboxyl-, hydroxyl-), and add complexing agents (e.g., abundant oxyanions, organic matter) to the solution. For example,

previous studies have shown that both organic matter, either coated on surfaces[297] or in solution,[73, 92] and abundant anions (e.g., Cl^-,[300] NO_3^-,[300] AsO_4^{3-},[64] PO_4^{3-},[64] HCO_3^-[171]),[64, 171, 300] can have significant effects on iron(III) (hydr)oxide heterogeneous nucleation. Analyzing the interfacial and activation energies of iron(III) (hydr)oxide precipitation on chemically and physically different surfaces or in the presence of diverse water components will provide a more comprehensive understanding of the affinity for iron(III) (hydr)oxide to precipitate on different surfaces and enable better prediction of iron(III) (hydr)oxide precipitate's distribution in dynamic environmental systems.

In addition, for engineered applications, substrates can be modified to decrease or increase the interfacial and activation energies of iron(III) (hydr)oxide heterogeneous nucleation so as to better control the formation of iron(III) (hydr)oxide on substrates. For example, efforts can be made to control the nucleation of iron(III) (hydr)oxide on substrates for heterogeneously catalyzing Fenton reactions.[317] In this case, the interfacial energy can be decreased by substrate modification so as to decrease the critical nucleation size of iron(III) (hydr)oxide and increase its specific surface area. Further, considering that iron(III) (hydr)oxide is a common foulant in membrane separation processes, such as membrane distillation (MD)[361] and reverse osmosis (RO)[362], the membrane surface can be modified to increase the interfacial and activation energies of iron(III) (hydr)oxide precipitation, thus increasing the thermodynamic and kinetic energy barriers of iron(III) (hydr)oxide formation. An accurate *in situ* determination of the interfacial and activation energies of heterogeneous nucleation on substrates is important for predicting and controlling the size, nucleation rate, and distribution of nuclei in diverse natural and engineered aqueous environments.

Acknowledgments

We are grateful for support received from the National Science Foundation Environmental Chemical Science Program (CHE-1214090). The Nano Research Facility and the Institute of Materials Science & Engineering at Washington University in St. Louis provided their facilities for the experiments. Use of the Advanced Photon Source (Sector 12 ID-B for GISAXS) at the Argonne National Laboratory was supported by the U.S. Department of Energy, Office of Science, Office of Basic Energy Sciences, under Contract no. DE-AC02-06CH11357. We thank Prof. James Ballard for carefully reviewing our manuscript and thank the Environmental NanoChemistry Group members for valuable discussions.

Supporting information for Chapter 5

5-S1. GISAXS experiments.

Quartz substrate preparation. Quartz wafers were cut into 5 mm × 5 mm squares using a slow diamond saw (MTI Corp., CA), then cleaned thoroughly using acetone, Nochromix (Godax Laboratories Inc., MD), sulfuric acid, and deionized water (DI, resistivity > 18.2 MΩ-cm). Tapping mode atomic force microscopy (AFM, Veeco Inc., Nanoscope V multimode SPM) was used to confirm the clean surface of the quartz after the cleaning processes (Figure 5-S1).

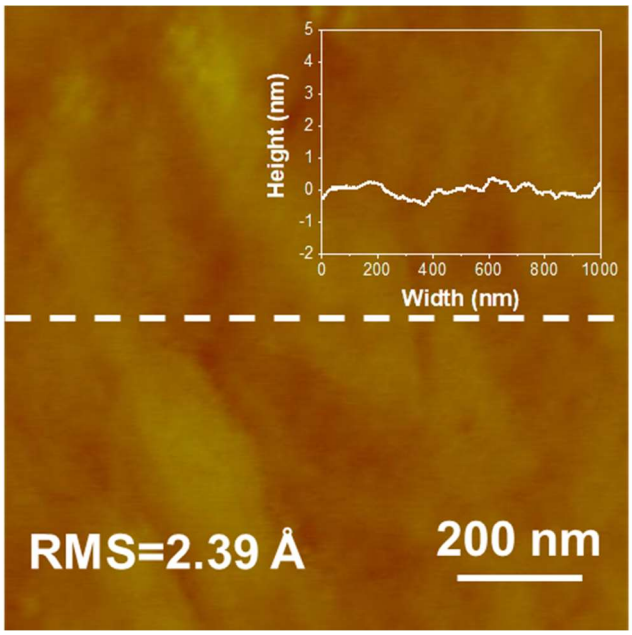

Figure 5-S1. Tapping mode AFM image (1 μm × 1 μm) of an unreacted clean (110) surface of a quartz substrate (color scale: 5 nm).

Solution chemistry. To initiate iron(III) (hydr)oxide nucleation, two reaction solutions were created from reagent grade $Fe(NO_3)_3 \cdot 9H_2O$ and $NaNO_3$, respectively. Before mixing, the pH of the $Fe(NO_3)_3$ solution was adjusted using HNO_3 (ACS grade, VWR) to ~2, to avoid iron(III) (hydr)oxide precipitation. The supersaturations with respect to ferrihydrite, defined as $\sigma = \ln(IAP/K_{sp})$, were calculated by Visual MINTEQ (Ver. 3.1) using the thermo.vdb database file. To measure the nucleation rates of iron(III) (hydr)oxide in a flow-through system, pH 3.6 and an 0.1 mM iron(III) concentration at room temperature (25ºC) were also chosen as starting conditions ($\sigma = 3.77$). First, to obtain α', two other pH conditions, pH 3.3 ($\sigma = 2.54$, 25ºC) and pH 3.9 ($\sigma = 4.87$, 25ºC), were employed to provide decreased and increased supersaturations, respectively, which led to different J_n. All three pH systems were supersaturated with respect to ferrihydrite ($\sigma > 0$). The pH of the $NaNO_3$ solution was controlled using NaOH (ACS grade, VWR) to make sure that the pH of the mixed solution reached the desired value. No pH values higher than 3.9 were used because the system at high pH was dominated by the fast nucleation of iron(III) (hydr)oxides in solution (homogeneous nucleation), which could block flows through tubing and significantly change the actual iron(III) concentrations in the cell. Further, a pH lower than 3.3 would cause nucleation rates too slow to form a measurable amount of heterogeneous nuclei within the practical experimental time. To obtain E_a, two other temperature conditions, 12ºC and 35ºC, were imposed at pH 3.3. The concentrations of $Fe(NO_3)_3$ solution at the lower and higher temperatures were tuned slightly to obtain the same supersaturation ($\sigma = 2.54$) of the mixed solution as that at 25ºC.

***In situ* GISAXS measurements.** GISAXS experiments were conducted at the beamline 12-ID-B of the Advanced Photon Source (Argonne National Laboratory, USA). Kapton film was used for both incoming and scattered X-ray beams to transmit through. The scattered X-

ray photons were collected by a 2-dimensional Pilatus 2 M detector (Dectris Ltd., Baden, Switzerland). The incident X-ray energy was 13.3 keV, and the sample-to-detector distance was 2.02 m, allowing a scattering vector q range of 0.0005 to 0.4 $Å^{-1}$. To ensure high surface sensitivity, the incidence angle was set to 0.11°, providing 98.8% reflectivity. Before each measurement, the quartz substrate was aligned parallel with respect to the X-ray beam, and a background image was taken of the clean quartz surface in DI water at the incidence angle. To start nucleation, $Fe(NO_3)_3$ and $NaNO_3$ solutions were pumped by two peristaltic pumps (model WPX1-F1/8S4−C, Welco Co. Ltd., Tokyo, Japan) into a micromixer (residence time < 1 s), and then pumped into the GISAXS cell at a constant flow rate of 5.6 mL/min to generate a measurable number of heterogeneous nuclei within a reasonable experimental time. This flow rate had been used by our previous flow-through study on calcium carbonate nucleation,[306] where it caused no bubbles inside the tubing and was fast enough to maintain constant water chemistry inside the cell. Timekeeping started when the mixed solution entered into the GISAXS cell and contacted the quartz. The pH of mixed solutions were monitored before and after the reaction, and the pH fluctuation was found to be less than 0.1 from the target value. For temperature experiments, the batch solutions of $Fe(NO_3)_3$ and $NaNO_3$ were either pre-heated in the tubing using a heating plate or pre-cooled with a water/ice mixture. Then, the tubing covered with insulating foam was connected to the GISAXS cell to start experiments. The temperatures of mixed solutions were monitored before and after the reaction, using a benchtop controller thermocouple probe (OMEGA CSI32K-C24, US) with a response time of 5 s and resolution of ± 0.5°C. The temperature fluctuation was less than 1°C from the target value. GISAXS 2D patterns were taken after the well-mixed solution entered into the cell, using a brief X-ray exposure (10 seconds at each measurement time point) to minimize beam effects. At least triplicate GISAXS

experiments were conducted for each condition. After each GISAXS experiment, grazing incidence wide angle X-ray scattering (GIWAXS) was used to identify the phases of newly formed iron(III) (hydr)oxide heterogeneous nanoparticles on the quartz substrate.

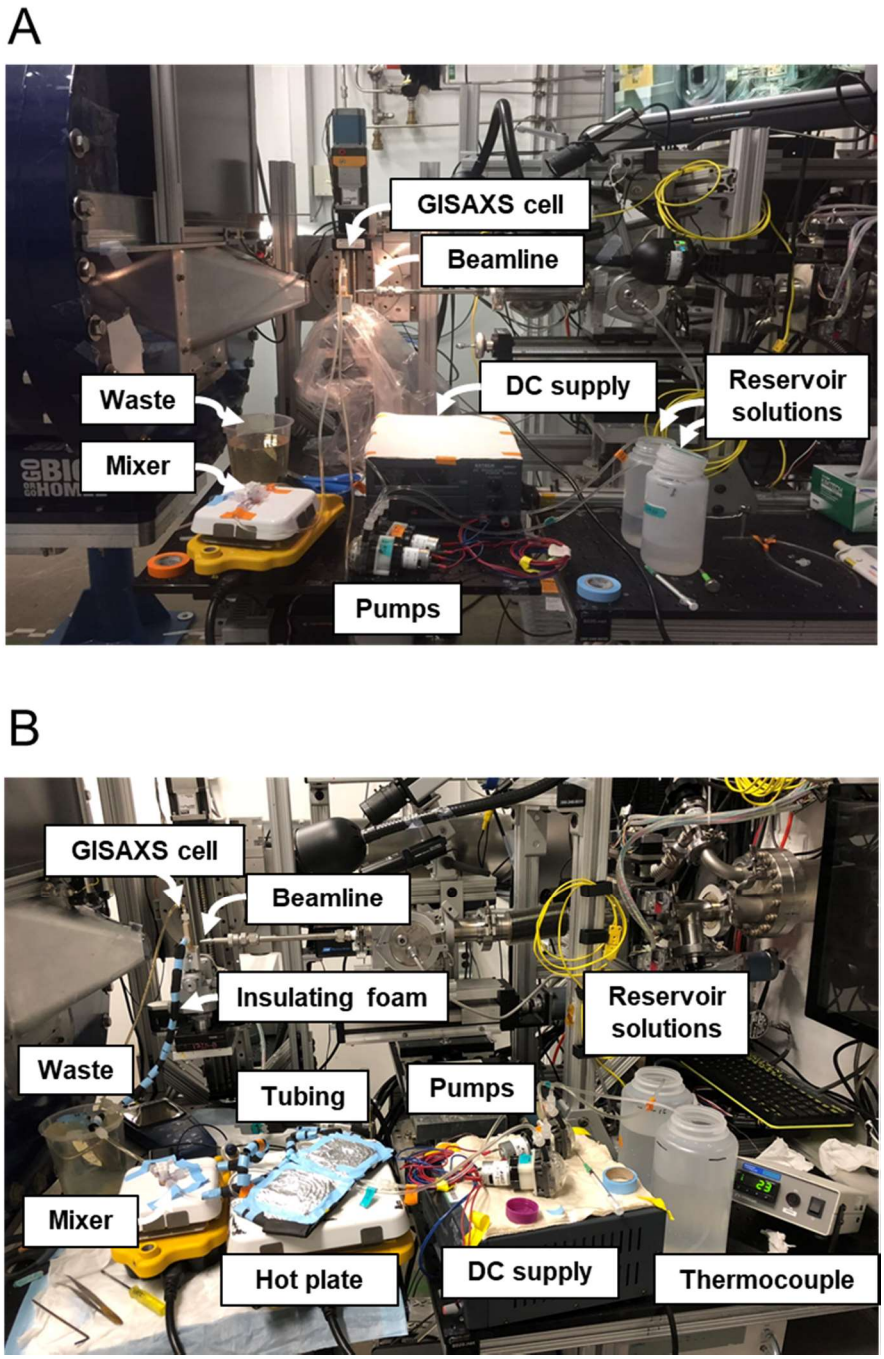

Figure 5-S2. Experimental setup at beamline 12-ID-B at APS for (A) interfacial energy measurements and (B) apparent activation energy measurements.

5-S2. GISAXS data analysis.

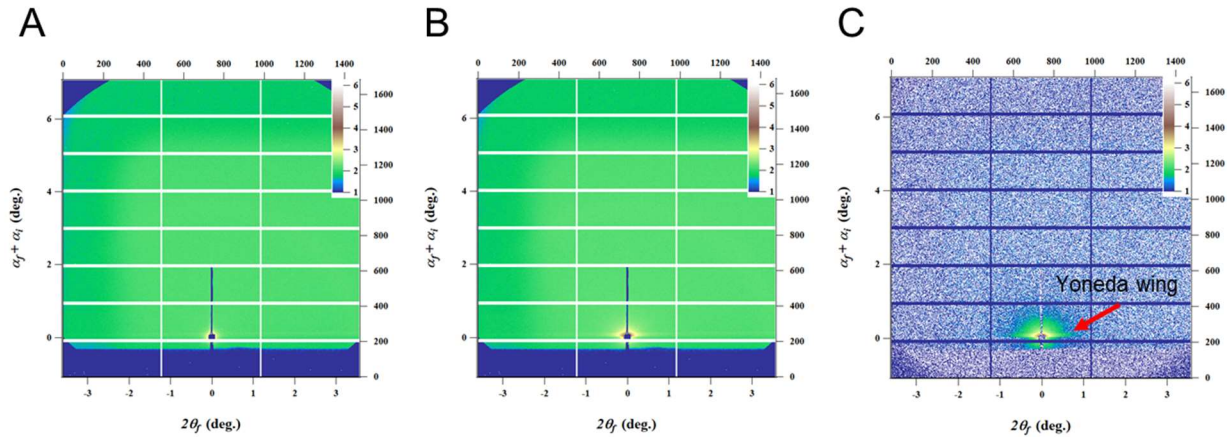

Figure 5-S3. (A) Representative GISAXS 2D image of background measured using DI water in the GISAXS cell. (B) Representative GISAXS 2D image measured for iron(III) (hydr)oxide nucleation reactions in the GISAXS cell. (C) Representative GISAXS 2D image after subtracting the background for iron(III) (hydr)oxide nucleation reactions in the GISAXS cell. A clear Yoneda wing is seen as the red arrow points out. GISAXS 1 D plots were obtained by line-cutting the Yoneda wing using GISAXSshop software in Igor 6.3.

GISAXS fitting. After background intensities from DI water scattering were subtracted, GISAXS 2D images were cut along the Yoneda wing and 1D plots of scattering intensity (I) versus q were made (Figure S3). Then, using the following relationship between $I(q)$ and q, $I(q) = N \cdot \Delta\rho^2 \cdot \int D(R)V^2(R)P(q,R)dR \cdot [I_{pow}q^{-p} + S(q)]$, the GISAXS 1D plots were fitted using the gui_2schultzand1Sq software in MatLab (MATLAB R2015a).[306] The term for aggregates, $I_{pow}q^{-p}$, can be moved out from the bracket and simply added when primary particles of the aggregates are agglomerated. A polydisperse sphere model with the Schultz size distribution was used. Five parameters were fitted simultaneously: total particle number (N), the mode (μ) and variance (σ^2) of the Schultz distribution D(R), the power law factor (I_{pow}), and the power law slope (p). The fitted the Schultz distribution D(μ, σ) was used to calculate the radius of gyration (R_g) by[306]

$$R_g = \mu\sqrt{\frac{3(z+8)(z+7)}{5(z+1)^2}}, \quad \textbf{(eq 5-S1)}$$

where

$$z = (\frac{\mu}{\sigma})^2 - 1\ . \quad \textbf{(eq 5-S2)}$$

Comparison of GISAXS invariant and fitting method. Nucleation rates (J_n) can be analyzed by the invariant method and the fitting method. The former uses the rate of increase of the invariant, Q, while the latter uses the rate of increase in the total particle number, N. The use of Q in GISAXS requires a caution and can be used only when particles are randomly oriented on substrate or spherical in shape. The fitting method is a more direct approach to obtain nucleation rates, while the invariant method is based on the assumption that invariant Q is proportional to the total particle number. This difference suggests that the invariant method suits only a system where nucleation is dominant over growth. In a system where both nucleation and growth happen, the fitting method is recommended because it separates the nucleation and growth by directly providing the total particle number N and particle size R_g. However, the fitting method does require high signal-to-noise ratios (strong scattering intensities) to ensure the fitting's accuracy. Additional assumptions need to be made for the fitting method, including the particle size distribution model and whether the system is a diluted one ($S(q)$=1). In our three pH systems, during the time period of 90 seconds to 300 seconds, particle nucleation was dominant over particle growth, and the signal-to-noise ratios were high, therefore these two approaches both work fine. While the two approaches obtain nucleation rates differently, and the absolute values of J_n were different, the slopes of $\ln(J_n)$ over $1/\sigma^2$ and the derived effective interfacial energies from these two approaches are still comparable.

5-S3. GISAXS replicate results.

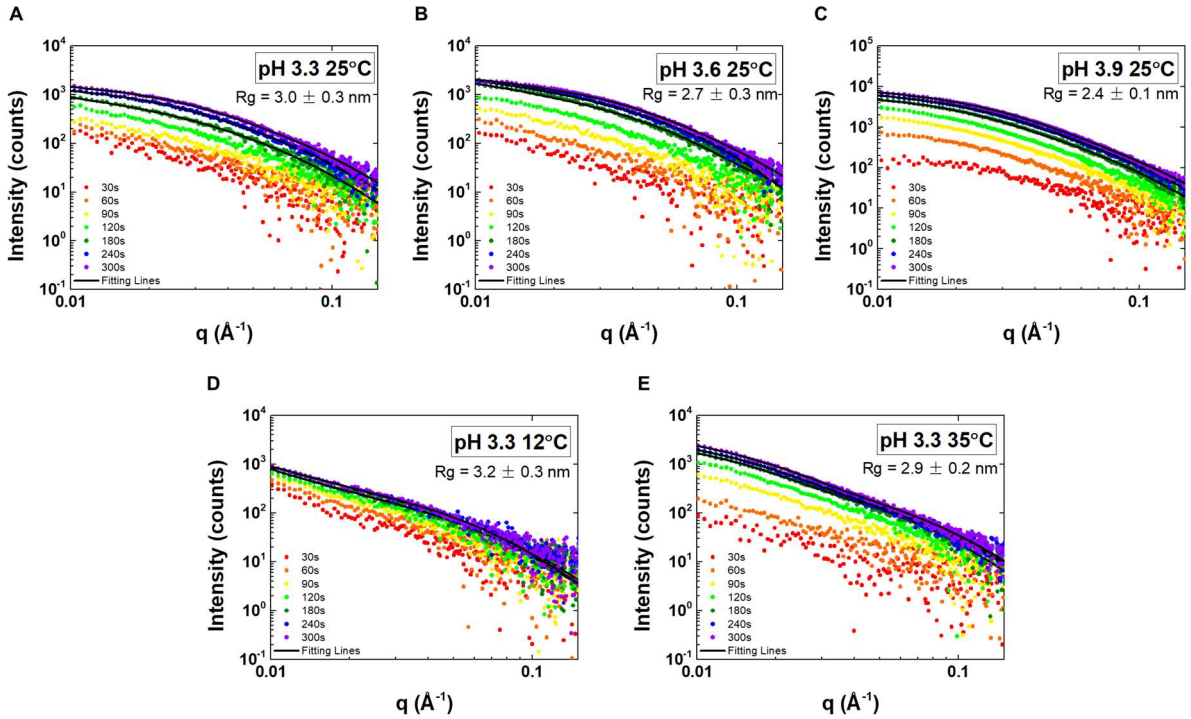

Figure 5-S4. GISAXS replicate results for (A) pH 3.3 (25ºC), (B) pH 3.6 (25ºC), (C) pH 3.9 (25ºC), (D) pH 3.3 (12ºC), and (E) pH 3.3 (35ºC). Black lines are curves fitted by using software in MatLab developed in APS at sector 12-ID-B. Time points from 90 seconds to 300 seconds were fitted. The fitting results for 90 seconds and 120 seconds are not shown to more clearly demonstrate the differences in the intensity pattern increase in the five conditions.

5-S4. GISAXS beam effects confirmation.

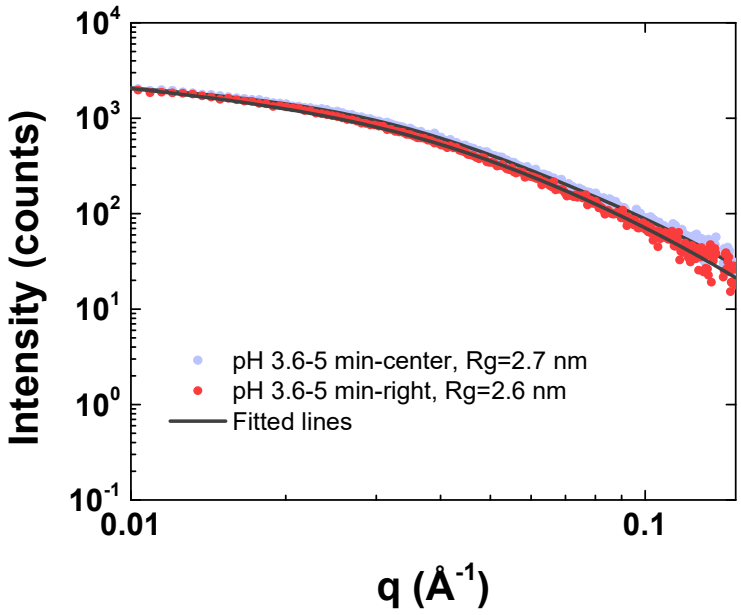

Figure 5-S5. GISAXS scattering from quartz reacted for 300 seconds (5 minutes) at pH 3.6 . The center position (light blue, at the center of the quartz) was the location on quartz exposed to X-rays during the experiment. The right position (red, 1 mm from the center of the quartz) was not exposed to X-rays during the experiment.

5-S5. AFM experiments.

AFM sample preparation and measurement. To observe the heterogeneous nuclei particles, *ex situ* tapping mode atomic force microscopy (AFM, Veeco Inc., Nanoscope V multimode SPM) was conducted. The AFM measurements were conducted on quartz reacted for 5 minutes because the GISAXS results indicated that nucleation was dominant over particle growth within 5 minutes, and therefore AFM measurements of samples reacted for 5 minutes could show clearly the particle size of newly formed nanoparticles. After reaction, the quartz substrate was taken out of the GISAXS cell, gently rinsed with ethanol, and dried with pure nitrogen gas. To prevent nanoparticle dissolution by DI water, ethanol was used instead. To obtain quantitative information about the average sizes of the precipitates, the heights of at least 50 nanoparticles in each condition were analyzed using Nanoscope 7.20 software (Veeco Inc.).

AFM measurement for quartz reacted in an inverted GISAXS cell. To evaluate whether the bigger particles observed in AFM were from primary particle growth or the result of gravitational settlement of homogeneously precipitated particles, additional AFM experiments were conducted with an inverted GISAXS cell in which the quartz was at the on top and solution contacted the quartz surface from below (Figure 5-S6). This inverted configuration kept homogeneously precipitated particles from collecting on the quartz. However, particles with sizes of 10−20 nm still appeared after 5 minutes of reaction, indicating that they had mainly grown from primary particles after nucleation rather than resulting from gravitational settlement of homogeneously precipitated particles. There is, however, a caveat that, even in the inverted geometry, some homogeneously nucleated particles can also be collected by Brownian motion.

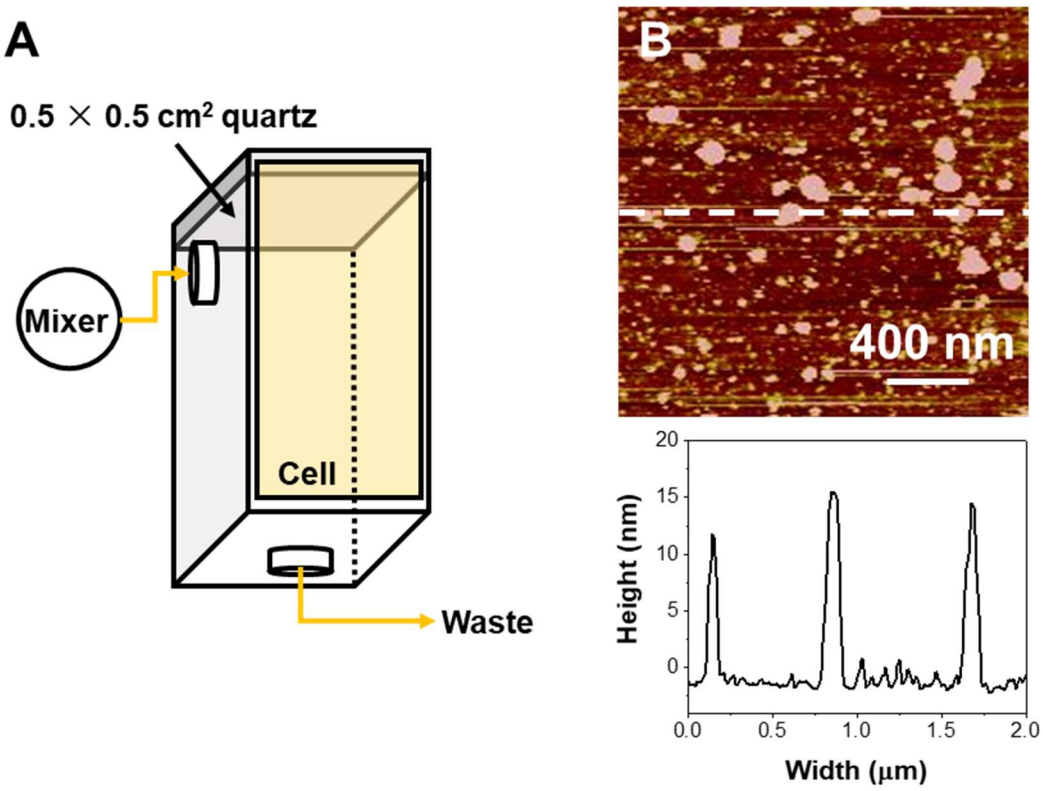

Figure 5-S6. (A) Experimental setup of AFM experiments with quartz reacted in an inverted GISAXS cell, with the quartz on top and the solution at bottom. (B) AFM image (2 μm × 2 μm) of the quartz after reaction for 5 minutes at pH 3.6 (color scale: 5 nm).

5-S6. Calculation of the substrate−nucleation interfacial free energy α_{sn}.

The effective interfacial energy obtained, α',is a combination of the liquid-nucleation interfacial free energy, α_{ln}, the liquid−substrate interfacial free energy, α_{ls}, and the substrate−nucleation interfacial free energy, α_{sn}.[328] For spherical particles, these combine to give α' by[328]

$$\alpha' = \alpha_{ln} \frac{2(1-cos\ ) - sin^2\theta \frac{\alpha_{ls}-\alpha_{sn}}{\alpha_{ln}}}{2^{2/3}(2-3cos\theta+cos^3\theta)^{2/3}}, \qquad \textbf{(eq 5-S3)}$$

where θ is the contact angle of the nuclei on the substrate. To calculate the substrate-nucleation interfacial free energy, α_{sn}, we need to find values for α_{ls}, α_{ln}, and θ. The water−quartz interfacial free energy, α_{ls}, has been determined by a previous study to be α_{ls} =

335 mJ/m^2.[363] We used a reported value for the water−ferrihydrite interfacial free energy, $\alpha_{ln,}$ of 186 mJ/m^2.[332] This number was calculated by Hiemstra[332], who used a surface enthalpy value for ferrihydrite (H_{surf} = 107 mJ/m^2) calculated by Pinney et al. (used Fe_5O_8H for ferrihydrite)[350] and the entropy of ferrihydrite ($-TS_{surf}$ = 79 mJ/m^2) measured by Snow et al. (used $FeOOH \cdot 0.027H_2O$ for ferrihydrite).[364] For small particle sizes, contact angles are hard to measure directly. Therefore, we used the AFM vertical heights of particles and GISAXS's in-plane (horizontal) radii of gyration of particles (lateral dimensions) to roughly calculate the contact angles of iron(III) (hydr)oxide heterogeneous nucleation on quartz (Table S1). This relationship has been successfully used previously to calculate the contact angles of $Mn(OH)_2$ heterogeneous nucleation on quartz:[365]

$$\theta = 2\arctan\left(\frac{H_{AFM}}{R_{GISAXS}}\right), \qquad \textbf{(eq 5-S4)}$$

The contact angle of iron(III) (hydr)oxide heterogeneous nucleation on quartz was 52.1° ± 10.6°. Using the numbers provided above, the quartz−ferrihydrite interfacial free energy, $\alpha_{sn,}$ was variously calculated to be 152 ± 13 mJ/m^2 ($Fe(OH)_3$), 122 ± 18 mJ/m^2 ($Fe_5HO_8 \cdot 4H_2O$), and 115 ± 19 mJ/m^2 ($5Fe_2O_3 \cdot 9H_2O$). It should be noted that the value of the water−ferrihydrite interfacial free energy, $\alpha_{ln,}$ from Hiemstra[332] was calculated using two different ferrihydrite formulas, so this number could have errors. Nevertheless, the calculation of α_{sn} presented here provides a guideline for estimated interfacial energy values, and their trends among different conditions can be compared.

Table 5-S1. AFM heights, GISAXS radii of gyration, and calculated contact angles of iron(III) (hydr)oxide heterogeneous nucleation on quartz under different conditions. Considering that the iron(III) (hydr)oxide nanoparticle sizes were extremely small, a small change in H or R_g would cause a significant change of contact angles and their large error bars. The difference in contact angles among the five systems was within the error bars, and so it would be difficult to conclude that there is any trend among these systems.

Size (nm)	AFM height (H)	GISAXS radii of gyration (R_g)	θ (º)
pH 3.3 25ºC	1.5 ± 0.2	3.0 ± 0.3	53.1 ± 10.7
pH 3.6 25ºC	1.3 ± 0.3	2.7 ± 0.3	51.4 ± 15.3
pH 3.9 25ºC	1.2 ± 0.3	2.4 ± 0.1	53.1 ± 13.3
pH 3.3 12ºC	1.5 ± 0.3	3.2 ± 0.3	50.2 ± 12.9
pH 3.3 35ºC	1.4 ± 0.2	2.9 ± 0.2	51.5 ± 9.5

5-S7. GIWAXS results.

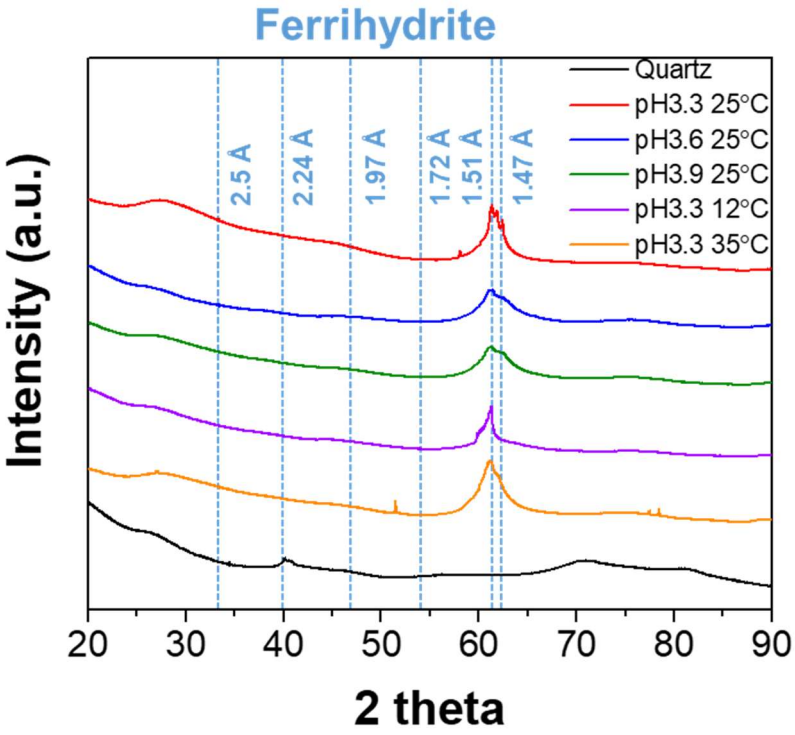

Figure 5-S7. GIWAXS patterns of unreacted quartz and quartz reacted for 15 minutes during *in situ* GISAXS experiments in different conditions. The vertical dotted blue lines indicate reference peak locations of 6-line ferrihydrite, including 2.5 Å, 2.24 Å, 1.97 Å, 1.72 Å, 1.51 Å, and 1.47 Å.[347] Only two peaks of 6-line ferrihydrite were observed, possibly the result of both poorly crystalline phase formation and oriented epitaxial heterogeneous nucleation of iron(III) (hydr)oxide on quartz.[366]

5-S8. Thermodynamic energy barrier (Δg_n).

Table 5-S2. Thermodynamic energy barrier (Δg_n) of iron(III) (hydr)oxide heterogeneous nucleation on quartz at different temperatures and pH 3.3.

Δg_n (kJ/mol)	Temperature (ºC)	$Fe(OH)_3$[a]	$Fe_5HO_8 \cdot 4H_2O$[a]	$5Fe_2O_3 \cdot 9H_2O$[a]
Invariant method	12	7.6 ± 0.1	7.6 ± 0.2	7.8 ± 0.2
	25	7.0 ± 0.1	7.0 ± 0.2	7.1 ± 0.3
	35	6.5 ± 0.1	6.5 ± 0.2	6.7 ± 0.3
Fitting method	12	8.4 ± 0.1	8.4 ± 0.2	8.4 ± 0.3
	25	7.7 ± 0.2	7.7 ± 0.2	7.7 ± 0.3
	35	7.2 ± 0.2	7.2 ± 0.2	7.2 ± 0.3

[a] The error ranges result from the ranges of interfacial energy, α'.

5-S9. Discussion of surface charge and water contact angle contributions to nucleation trends in three pH systems.

To evaluate how surface charge and hydrophilicity contribute to the observed nucleation trends under three pH conditions, we measured zeta potentials and water contact angles. Table S3 shows the zeta potentials (mV) of suspended quartz powders and homogeneously formed iron(III) (hydr)oxide precipitates under three pH conditions with 10 mM $NaNO_3$. Quartz powders were prepared by grinding a quartz (110) substrate purchased from MTI. Quartz powders were negatively charged at pH 3.3−3.9, consistent with the pH_{iep} reported for quartz (pH ~2−3).[338] With higher pH, the zeta potential of quartz decreased slightly to more negative values. Iron(III) (hydr)oxide precipitates were positively charged, consistent with the pH_{iep} reported for ferrihydrite (pH ~7−8).[338] With higher pH, the zeta potential of iron(III) (hydr)oxide precipitates slightly decreased to more neutral values.

Within the experimental pH range, electrostatic attractive forces existed between iron(III) (hydr)oxide precipitate and quartz, but did not vary significantly. Further, the measured water contact angles on the quartz surface (Figure S8) were similar. Based on these results, surface charge and hydrophilicity made minor contributions to the observed nucleation trends. Supersaturation was the main contributor to the different nucleation trends.

Table 5-S3. Measured zeta potentials (mV) of suspended quartz powders and homogeneously formed iron(III) (hydr)oxide precipitates in three pH conditions with 10 mM $NaNO_3$.

Zeta potentials (mV)	3.3	3.6	3.9
Quartz	-12.3 ± 1.6	-13.9 ± 1.2	-15.0 ± 1.1
Iron(III) (hydr)oxide	26.0 ± 2.7	25.7 ± 1.9	25.1 ± 1.0

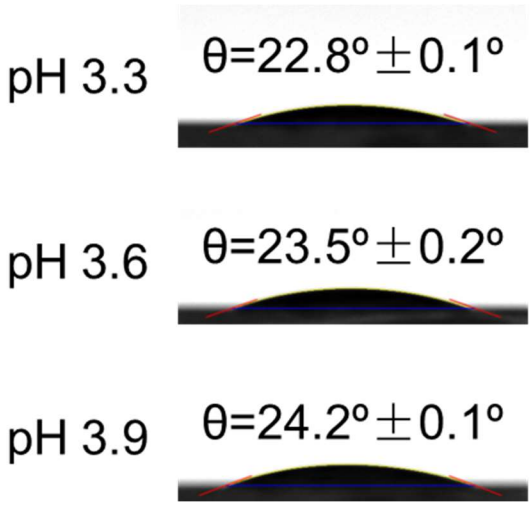

Figure 5-S8. Water contact angles on the quartz surface. The water drops contained 10 mM $NaNO_3$ with pH controlled by HNO_3.

5-S10. Calibration of GISAXS fitting results with AFM imaging and calculation of kinetic factors *A* and J_0.

The GISAXS fitting method obtained particle numbers (a.u.) can be converted to absolute nucleus numbers using a method used before for $CaCO_3$ nucleation system by calibration of GISAXS data with AFM images.[326] Figure 5-S9 shows the calibration of GISAXS fitted particle numbers in relative units with AFM particle numbers (nuclei/μm^2) counted from AFM images (both are from 5 minutes results). Error bars for the data points are particle number deviations from three 1×1 μm^2 scan areas on a single substrate. The linear fitting line is known to cross (0,0), where no nuclei were formed on substrate, and no GISAXS signal should be observed. The linear fitting of 5 experimental conditions' results and (0,0) generates the correction factor from x-axis values to y-axis values of $(2.35 \pm 0.18) \times 10^6$, with a Pearson's r=0.94. Further, the absolute value of the pre-exponential kinetic factor, *A*, can be obtained using the calibrated nucleation rates in the unit of nuclei/μm^2 • s. The value of *A* is 2.2×10^6 nuclei/μm^2·s, or 2.2×10^{18} nuclei/m^2·s. Then, using E_a obtained from fitting method (32.8 ± 1.8 kJ/mol), J_0 can be calculated using eq 5.3 and eq 5.8 to be $10^{14.5\pm0.3}$ nuclei/m^2·min at 25ºC. This J_0 value of heterogeneous iron(III) (hydr)oxide nucleation is in the similar range of reported values of other mineral nucleation systems including $10^{13.5\pm0.7}$ nuclei/m^2·min at room temperature for heterogeneous silica nucleation,[337] and $10^{16.1\pm1.0}$ nuclei/m^2·min at room temperature for heterogeneous $CaCO_3$ nucleation.[326]

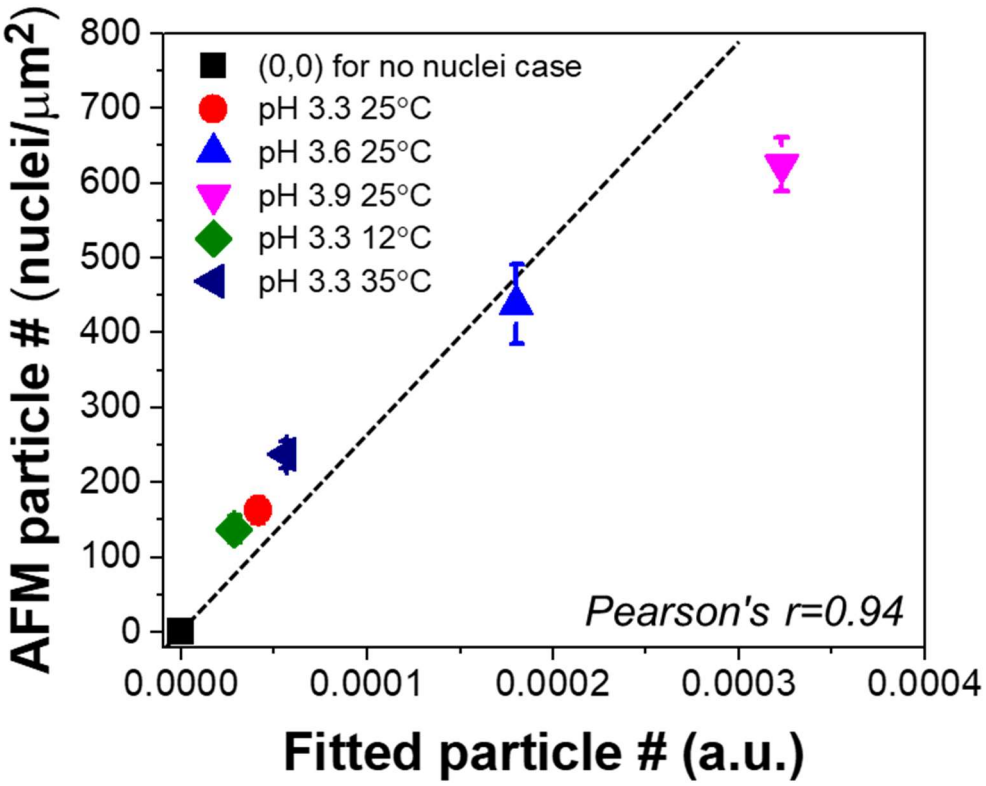

Figure 5-S9. Calibration of GISAXS fitted particle numbers (a.u.) with AFM particle numbers (nuclei/μm^2).

Chapter 6. Localized heating with a photothermal polydopamine coating facilitates a novel membrane distillation process

Reproduced from Ref. 93 with permission from The Royal Society of Chemistry:[93] Wu, X., Jiang, Q., Ghim, D., Singamaneni, S.,* Jun, Y. S*. Localized Heating by a Photothermal Polydopamine Coating Facilitates a Novel Membrane Distillation Process, *Journal of Materials Chemistry A*, **2018**, 18799-18807. DOI: 10.1039/c8ta05738a. Copyright 2018 Royal Society of Chemistry.

Abstract

From here, we turn our focus from fundamental studies to engineered applications, using the knowledge that we have obtained. **Chapters 6 & 7** are focused on **System 3**, which concerns the development of nature-inspired nanomaterial-based membranes for sustainable desalination by using membrane distillation (MD). In **Chapter 6**, we develop a simple, stable, and scalable PDA-coated polyvinylidene fluoride (PVDF) membrane for photothermal membrane distillation. Solar-driven membrane distillation using photothermal membranes is of considerable interest for future water desalination systems. However, the low energy efficiency, complex synthesis, and instability of current photothermal materials hinder their further development and practicability. In this study, for the first time, we demonstrate a simple, stable, and scalable polydopamine (PDA) coated polyvinylidene fluoride (PVDF) membrane for highly efficient solar-driven membrane distillation. Our membrane shows the best energy efficiency among existing photothermal membranes (45%), and the highest water flux (0.49 $kg/m^2 \cdot h$) using a direct contact membrane distillation (DCMD) system under 0.75 kW/m^2 solar irradiation. Such performance was facilitated by the PDA coating, whose broad light absorption and outstanding photothermal conversion properties enable higher transmembrane temperature and increased driving force for vapor transport. In addition, the excellent hydrophobicity achieved by fluoro-silanization gives the membrane great wetting resistance and high salt rejection. More importantly, the robustness of our membrane, stemming from the excellent underwater adhesion of the PDA, makes the composite membrane an outstanding candidate for real-world applications.

6.1 Introduction

Rapidly increasing population, economic development, and water contamination have resulted in unprecedented global fresh water demands.[367-369] To augment the freshwater supply and alleviate water scarcity, desalination of seawater and brackish water, which comprise 97.5% of the total water on earth,[370] has been extensively implemented by many countries in the past few decades.[19, 371] Over 19,000 water desalination plants have been built globally, reaching an estimated capacity of 100 million m^3/day by 2017.[372] Water desalination technologies include those without phase change processes, such as reverse osmosis (RO)[373-375] and electrodialysis (ED),[376-377] and those that involve phase change processes, such as thermal distillation (i.e., boiling)[378-379] and membrane distillation (MD).[23-24, 380]

Membrane distillation, an advantageous thermally-driven membrane technology, generates clean water based on the vapor pressure difference between the two sides of a porous hydrophobic membrane.[381-382] In direct contact membrane distillation (DCMD), the most common MD configuration, water evaporates on the hot feed water side of the membrane surface, diffuses across the microporous membrane, and condenses on the cold distillate side.[74, 81] MD can be operable under conditions with lower temperatures than boiling and lower pressures than RO,[22, 383] leading to decreased electricity input and less fouling or corrosion problems.[381] Moreover, less sophisticated equipment and pretreatment systems facilitate MD to possess small footprint, compactness, and high modularity.[22, 381, 383-384] The use of renewable energy sources to heat feed saline water, such as waste heat from power plants[381, 385] and solar energy by implementing solar thermal collection systems,[83, 386-389] further incentivizes MD's application for sustainable water desalination. However, one of

the main challenges of conventional MD is temperature polarization, which results in a lowered surface temperature at the membrane-feed water interface with respect to its bulk water value.[74, 390-391] Consequently, the cross-membrane temperature difference is decreased, reducing the driving force for mass transport and undermining the overall MD performance.[85]

Most recently, light-driven localized heating at membrane surfaces that incorporate photothermal materials (e.g., Ag nanoparticles, carbon black, and nitrocellulose) has provided a means to alleviate the concerns brought by the influence of temperature polarization.[21, 85, 392] With the integration of photothermal materials, localized heating can be efficiently generated from incident light (especially, renewable solar irradiation), which helps to increase and maintain the membrane surface temperature at the membrane-feed water interface. The MD system using photothermal membranes can significantly reduce the electricity input, while possessing other advantages of conventional MD processes such as less fouling problems and the modularity to combine with other systems.[381] However, the photothermal materials demonstrated so far have several limitations which hinder their further development and commercial practicability. For example, Ag nanoparticles are prone to delamination or leakage from membranes into water.[85] The dissolution of photothermal material will restrict its utilization for certain MD configurations (e.g., vacuum membrane distillation), and also lead to the potential impairment of the membrane's photothermal performance during long term applications. On the other hand, the bilayer structure of carbon black coating on the membrane surface makes the carbon black membrane exhibit low photothermal conversion efficiency.[21] Besides, the synthesis methods of these composite membranes are often complex, involving phase inversion or electrospinning processes, which may be cost and energy intensive.

Herein, we demonstrate, for the first time, a simple, stable, and highly effective PDA coated polyvinylidene fluoride (PVDF) membrane for solar-driven membrane distillation. Polydopamine, as a mussel-inspired polymer,[393] has been extensively applied in surface modifications owing to its inherent and robust adhesive properties and hydrophilic nature.[394] Polydopamine can be easily coated on surfaces, regardless of their initial surface energy, making the synthesis simple and cost-effective.[395] The PDA coating on organic substrates is extremely stable under harsh conditions, including ultrasonication or acidic pH (<1), which makes the long-term commercial application of PDA-coated materials viable.[393] Similar to those of naturally occurring eumelanin,[396-400] PDA also exhibits broad light absorption and remarkable photothermal conversion properties,[401-402] which ensures its potential application for highly efficient solar-based seawater desalination. Moreover, the biocompatibility,[403-404] low toxicity and biodegradable nature of PDA make it an environmentally benign material for water purification[398, 405] and biomedical applications.[406-407] Previously, PDA has been applied for seawater desalination techniques, such as forward osmosis and nanofiltration, to increase the permeate flux facilitated by only exploiting its hydrophilic nature.[408-409] However, there is still plenty of room to utilize PDA for solar-driven seawater desalination applications considering its superb photothermal properties, especially in solar-driven membrane distillation. The solar-driven MD system using PDA in this study shows the best thermal efficiency to date among currently reported photothermal MD systems, and the highest water flux using a DCMD system among currently reported solar-driven MD studies. The simple, stable, and highly effective photothermal membrane introduced in this study can help to expand PDA's application and provide a promising option to alleviate the global fresh water scarcity problems.

6.2 Experimental section

6.2.1 Synthesis of FTCS-PDA-PVDF membrane

A PDA coating on a commercial hydrophilic polyvinylidene fluoride (PVDF) membrane (0.45 μm pore size, 110 μm thickness, MilliporeSigma) was achieved via self-polymerization of PDA.[393, 396] Hydrophilic PVDF was chosen for easier PDA coating. Dopamine (DA, 2 mg/mL) was dissolved in 10 mM Tris-HCl (pH 8.5), and PVDF membranes were dipped in the solution. The solution was shaken (VWR Orbital Shaker, Model 3500) for 24 hours before the membrane was taken out and rinsed using deionized (DI) water (18.2 MΩ-cm, Barnstead Ultrapure water systems). The self-polymerization process was repeated for 7 days until the entire surface of the PVDF was uniformly coated by PDA (**Figure 6-S1**). Then, the membrane was rinsed with DI water and dried under N_2 gas. Next, the PDA-PVDF membrane was exposed to (tridecafluoro-1,1,2,2-tetrahydrooctyl)-trichlorosilane (FTCS) vapor at 70 °C for 3 hours, resulting in a dense coverage of PDA-PVDF by hydrophobic FTCS fluoro-silane.[76, 410].

6.2.2 Characterization of FTCS-PDA-PVDF membrane

Scanning electron microscopy (SEM; OVA NanoSEM 230, FEI) was used to image the morphology and microstructure of the FTCS-PDA-PVDF membrane surface and its cross-section at an acceleration voltage of 10 kV. The chemical composition of PDA and FTCS on the PVDF surface were identified using an attenuated total reflection Fourier transform infrared (ATR-FTIR; Thermo Scientific Nicolet Nexus 470 spectrometer equipped with a diamond crystal) spectroscopy and a Raman spectroscopy (inVia confocal Raman spectroscope, Renishaw, equipped with 514 nm wavelength diode laser). The reference peaks

for FTIR are shown in **Table 6-S1**. X-ray photoelectron spectroscopy (XPS, PHI 5000 VersaProbe II, Ulvac-PHI with monochromatic Al Kα radiation (1486.6 eV)) was utilized to identify the N 1s, C 1s, and Si 2p peaks for the PDA-FTCS-PDA membrane. The surface roughness (root-mean-square, RMS) was measured using tapping mode AFM (Veeco Inc., Nanoscope V multimode SPM) and analyzed using the Nanoscope 7.20 software (Veeco Inc.). For each membrane, triplicate locations on the sample surface were measured to determine the roughness. The gravimetric method was used to quantify the porosity (ε) of the PDA-PVDF membrane.[77, 411-412] Three 2 cm × 2 cm pieces were cut from a PDA-PVDF membrane sheet, weighed dry, and then submerged in DI water for 1 week before being taken out and weighed again wet. The porosity was calculated using the equation below to get the average values for triplicate samples:

$$\varepsilon = \frac{w_2 - w_1}{\rho_w V}, \qquad \textbf{(eq 6.1)}$$

where ε is the porosity (%), w_2 (g) is the weight of the wet membrane, w_1 (g) is the weight of the dry membrane, ρ_w (g/cm^3) is the liquid density (DI water), and V (cm^3) is the volume of the membrane. ImageJ 1.80 software (National Institutes of Health, Bethesda, Maryland, USA) was used to determine the average pore diameter of pristine PVDF and FTCS-PDA-PVDF membranes by taking measurements of 100 pores from the SEM top surface images. A mean and a standard deviation were calculated for each size distribution. Considering that both pristine PVDF and PDA-PVDF are hydrophilic (contact angle ≈ 0º, **Figure 6.1A**), it is difficult to evaluate the effect of the altered pore size and porosity by PDA coating on the membrane wetting property or MD performance. The actual amount of FTCS on the FTCS-PVDF (contact angle ≈ 120º) and FTCS-PDA-PVDF (contact angle ≈ 125º)

membranes could be different, which also makes it difficult to attribute the slight wetting resistance increase of FTCS-PDA-PVDF only to the PDA coating.

6.2.3 Measuring the optical properties and surface temperature of FTCS-PDA-PVDF membranes

The transmittance and reflectance of FTCS-PVDF and FTCS-PDA-PVDF membranes were measured using a micro-spectrophotometer (QDI 302, CRAIC Technologies) coupled to a Leica microscope (DM 4000M, Leica Microsystems). The surface temperatures of the FTCS-PVDF and FTCS-PDA-PVDF membranes were measured by an infrared camera (IR camera, Ti 100, FLUKE) after 600 secs light illumination using a solar simulator (Newport 66921 Arc Lamp) under both unfocused and focused irradiations (**Figure 6-S3**). Triplicate 1 cm × 1 cm pieces were cut from the membranes of interest and measured. The surface temperature of the membrane with water on top (water thickness = 8 mm) was monitored using a benchtop controller thermocouple probe (OMEGA CSI32K-C24, US) with a response time of 5 s and resolution of ±0.5 °C

6.2.4 Direct contact membrane distillation experiments

DCMD experiments were carried out using a specially designed membrane distillation module. The setup of the system is shown in **Figure 6-S4**. The membrane distillation module consists of a 2-mm-thick quartz window with a diameter of 5 cm on the feed side to allow light illumination. A 1-mm-thick aluminum platform was placed in between the feed side and distillate side to support the membrane. The cross-flow velocities in the feed and distillate channels were 3.6 mL/min and 16.2 mL/min, respectively. Both DI

water and 0.5 M NaCl aqueous solution (ACS grade, BDH, PA) were used as feed water, stored in a 500-mL Erlenmeyer flask, and DI water was used for the distillate stream at the bottom of the membrane. The 0.5 M salinity was chosen to mimic the average salinity of seawater.[413] The feed and distillate were continuously circulated through the membrane module using two peristaltic pumps respectively (Welco WPX1-F1 and Stenner 85MHP5). The flow rate of the feed water was changed by monitoring the DC supply (Extech 382203) controlling the feed pump. The distillate reservoir was kept on a weighing balance (Sartorius ELT402) to measure the collected permeate at 1 min intervals. The distillate reservoir was capped during MD tests to reduce the effects of evaporation. During solar MD tests, the light from the solar simulator (Newport 66921 Arc Lamp) was oriented to the membrane surface using a mirror. The light intensities at the membrane surface were measured to be 0.75 (unfocused) and 7.0 kW/m^2 (focused using a magnifying lens) by a spectroradiometer (SpectriLight ILT 950). The diameters of the active irradiation areas were 5 cm and 1.5 cm for 0.75 kW/m^2 and 7.0 kW/m^2 intensities, respectively. The solar efficiency was calculated by the following equation:

$$\eta = \frac{\dot{m} H_{vap}}{I}, \qquad \textbf{(eq 6.2)}$$

where η is solar efficiency, $\dot{m}$ is the permeate flux (kg/m^2·h), H_{vap} is the enthalpy change (2,454 kJ/kg) from liquid to vapor, and I is the power density of the incident light (kJ/m^2·h).[21].

6.2.5 Stability tests of the FTCS-PDA-PVDF membrane

The chemical and mechanical stability of the FTCS-PDA-PVDF membrane was tested at three pH values (pH 4, 7, and 10), using both ultrasonic agitation for 6 hours (Bransonic 3510R, 335W) and vigorous shaking for 30 days (VWR Orbital Shaker, Model

3500) (**Figure 6-S6A**). Triplicate 1 cm × 1 cm pieces were cut from the membrane and measured. The contact angles of the membrane after testing in pure water and saline water, were measured using a contact angle analyzer (Phoenix 300, Surface Electro Optics Co. Ltd) over 10 cycles of MD tests (1 cycle = 1 hour) (**Figure 6-S6B**). After every 2 cycles, the membrane was washed using DI water, dried using N_2 gas, and weighed to reveal the mass variation during MD tests. A chloride probe (VWR 89231-632) was used to measure the salt concentration in both the feed and distillate during 0.5 M NaCl MD tests. SEM images were further measured for the FTCS-PDA-PVDF membrane after MD tests to evaluate the morphology and microstructure alteration.

6.3 Results and Discussion

6.3.1 FTCS-PDA-PVDF membrane synthesis and characterization

Polydopamine coating on a commercial hydrophilic PVDF membrane (0.45 μm pore size; MilliporeSigma) can be easily achieved via a self-polymerization process (**Figure 6.1A** and **Figure 6-S1**).[393, 396] The PVDF membrane has been widely used for MD systems,[382] and in our work, hydrophilic PVDF was chosen to achieve easier and more efficient PDA coating owing to PDA's hydrophilic nature. With 2 mg/mL dopamine (DA) in 10 mM Tris-HCl (pH 8.5) solution, the self-polymerization process was repeated for 7 days to ensure that the entire surface of the PVDF was uniformly coated by PDA (**Figure 6-S1**). The uniformity coating of PDA on PVDF surface can minimize the influence of light illumination spot on the membrane's photothermal reactivity. The amount of PDA coating can be tuned by varying the number of coating cycles, and the final weight percentage of PDA on PVDF after 7 cycles was quantified to be 9.7±0.5 wt% by measuring the weight difference of the membrane

before and after polymerization. With the additional coating of PDA, the porosity (ε) of the PDA-PVDF membrane decreased slightly (73.2% ± 2.6%, compared with 82.1% ± 4.2% for a pristine PVDF membrane, measured by a gravimetric method).[77, 411-412] Hydrophobicity is important for MD membranes because it resists pore wetting, ensures the passage of only the vapor phase through the membrane pores, and enhances the salt rejection performance of the membrane.[81] The hydrophobicity of PDA-coated PVDF membrane was increased by a facile fluoro-silanization method using (tridecafluoro-1,1,2,2-tetrahydrooctyl)-trichlorosilane (FTCS),[76, 410] leading to a water contact angle of 125.5º. The above processes are evident in a morphological investigation carried out by scanning electron microscopy (SEM) and contact angle measurements, which clearly show a uniform and dense coating of PDA on the microporous PVDF surface and cross-section (**Figure 6.1B-G**), and the successful hydrophobic modification of FTCS, respectively (inset in **Figure 6.1A**). ImageJ analysis of surface SEM images (×5000 magnification) indicates that an average surface pore size of FTCS-PDA-PVDF membrane was 0.96 ± 0.42 μm by taking measurements of 100 pores.[414-415] The average pore size of FTCS-PDA-PVDF membrane became larger compared with pristine PVDF membrane (0.46 ± 0.13 μm, confirmed by SEM images), which can be due to the fact that the PDA coating closed the smaller pores rather than the bigger pores, making the average pore size increase (**Figure 6.1B** and **6.1E**). Consequently, the pore numbers calculated from SEM images also decreased from $2.6 \times 10^7/cm^2$ of pristine PVDF membrane to $1.1 \times 10^6/cm^2$ of FTCS-PDA-PVDF membrane.

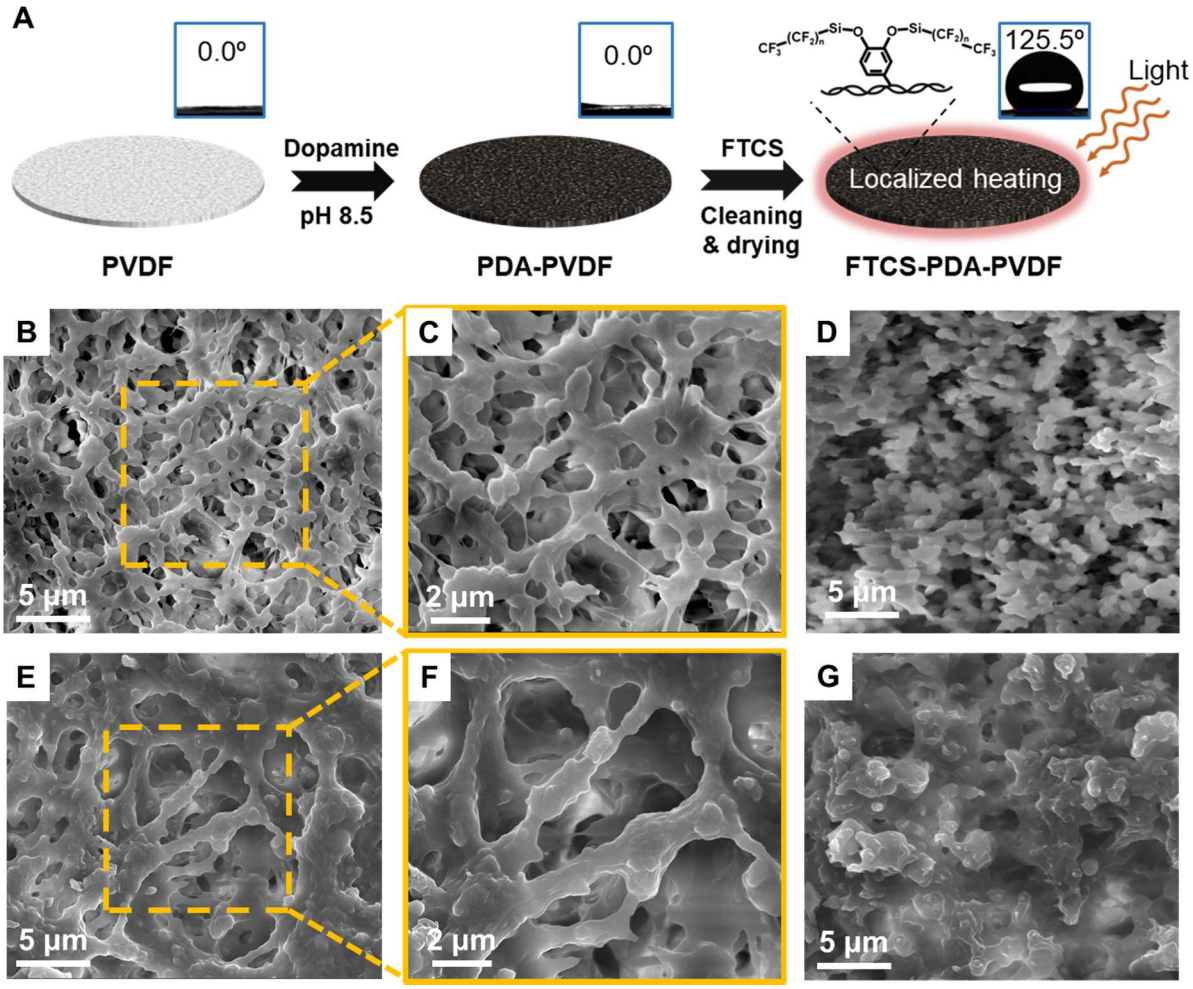

Figure 6.1 (**A**) Schematic depicting the synthesis of the FTCS-PDA-PVDF membrane. SEM images of the pristine PVDF membrane surface (**B** and **C**) and cross-section (**D**). SEM images of the FTCS-PDA-PVDF membrane surface (**E** and **F**) and cross-section (**G**).

To further understand the chemical composition of the synthesized FTCS-PDA-PVDF membrane, we have performed attenuated total reflection Fourier transform infrared (ATR-FTIR) spectroscopy measurements (**Figure 6.2A**). The characteristic N-H and C=C peaks of PDA on PVDF at 1520 and 1610 cm^{-1},[416-419] and the Si-O peak of FTCS at 1010 cm^{-1},[420-421] respectively indicated the successful coating of PDA and the FTCS modification. The ATR-FTIR reference peaks for PDA coating on PVDF are summarized in **Table 6-S1**. Raman spectroscopy also showed peaks of PDA at 1350 and 1573 cm^{-1} (**Figure 6-S2A**),

corresponding to the stretching and deformation of PDA's catechol groups.[422-423] X-ray photoelectron spectroscopy (XPS) revealed the chemical composition difference between pristine PVDF and FTCS-PDA-PVDF, based on the N 1s, Si 2p, and C 1s peaks (**Figure 6.2B–D**). As shown in **Figure 6.2B**, a new N 1s peak emerged at 398–402 eV for the FTCS-PDA-PVDF, corresponding to the N-C and N-H bonds of PDA layers on the surface of PVDF membrane.[424] The new emerging Si 2p peak of FTCS-PDA-PVDF at 103.8 eV (**Figure 6.2C**) showed the Si-O bond of FTCS on the PDA-PVDF surface.[425] Within the broad C 1s peak (**Figure 6.2D**), the increased relative ratio of $–CF_2–$ (290.2 eV) over $–CH_2–$ (285.2 eV) and the newly appeared $–CF_3$ peak (292.3 eV) from FTCS-PDA-PVDF were attributed to the fluorinated tails of FTCS on the PVDF surface.[426] Further, to evaluate the PDA coating effects on surface roughness, the root-mean-square (RMS) roughnesses of both FTCS-PDA-PVDF (179 ± 12 nm) and pristine PVDF (498 ± 31 nm) membranes were acquired by measuring tapping mode atomic force microscopy (AFM) images (**Figure 6-S2B**). The lowered surface roughness after PDA coating can be attributed to the partial filling of large pores in the PVDF membrane with PDA, which can also be observed in SEM images.

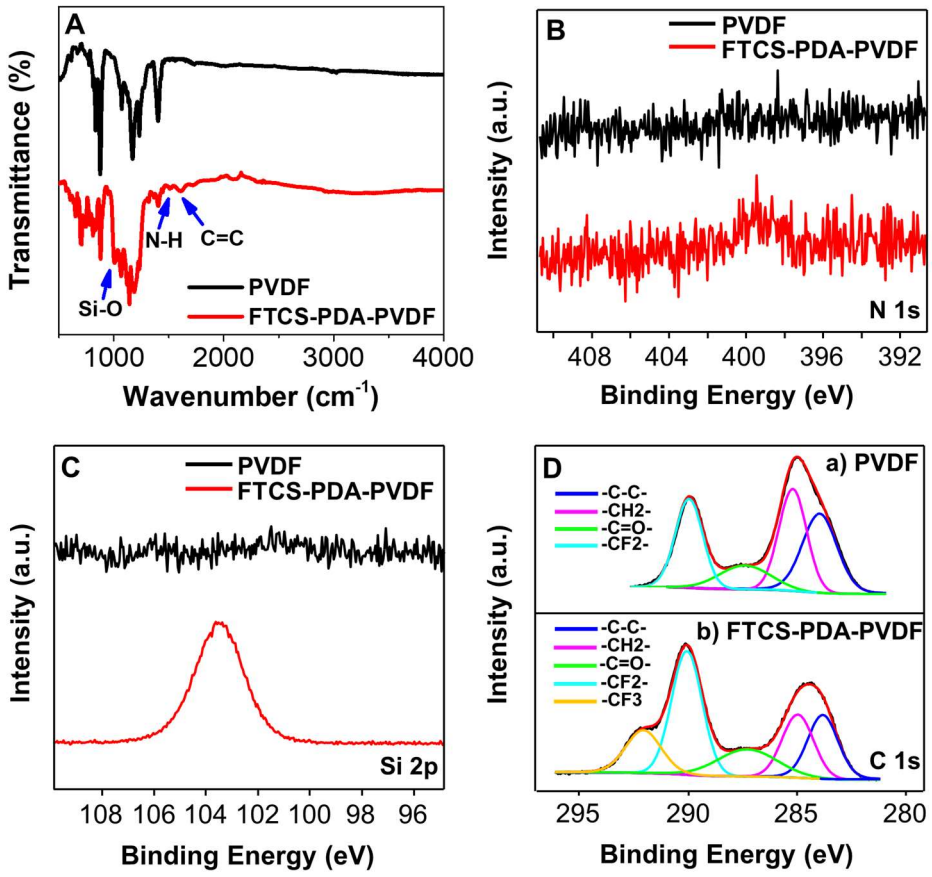

Figure 6.2 Characterization of the FTCS-PDA-PVDF membrane. (**A**) ATR-FTIR spectra of the pristine PVDF and the FTCS-PDA-PVDF membranes. XPS spectra of the pristine PVDF and the FTCS-PDA-PVDF membranes showing the N 1s (**B**), Si 2p (**C**), and C 1s (**D**) peaks.

6.3.2 Light absorption and photothermal conversion of the FTCS-PDA-PVDF membrane

In light-to-heat conversion by photothermal materials, the light absorption properties are of crucial importance. Hence, following the chemical characterization, the transmittance and reflectance measurements of the FTCS-PDA-PVDF membrane were carried out in the range of 450–800 nm, using a micro-spectrophotometer (**Figure 6.3A** and **6.3B**). The light absorption properties of pristine PVDF membranes modified only by FTCS (FTCS-PVDF) and by PDA (PDA-PVDF) were also measured for comparison. The FTCS-PVDF membrane

showed high transmittance (~17.1%) and reflectance (~27.6%) in the visible region, which indicated relatively low light extinction (~55.3%). On the other hand, after PDA coating, the PDA-PVDF and FTCS-PDA-PVDF membranes exhibited extremely small optical transmittance (~0.4% for PDA-PVDF, and ~0.1% for FTCS-PDA-PVDF) and reflectance (~2.6% for PDA-PVDF, and ~3.7% for FTCS-PDA-PVDF) in the visible region, indicating a large optical extinction (~97.0% for PDA-PVDF, and ~96.2% for FTCS-PDA-PVDF) by the membrane. This excellent light extinction property, which was mainly attributed to light absorption by the PDA coating and light scattering by the membrane's porous structure,[394, 399] underlies the light-to-heat conversion of the FTCS-PDA-PVDF membrane.

Further, to probe the photothermal conversion performance of the FTCS-PDA-PVDF membrane, the surface temperatures of dry FTCS-PVDF, PDA-PVDF, and FTCS-PDA-PVDF were measured by an infrared (IR) camera under light illumination from a solar simulator (**Figure 6.3C** and **6.3D**). Two light intensities were used to represent unfocused and focused illumination, and the power densities were measured to be 0.75 (~0.7 sun) and 7.0 kW/m^2 (~7 sun) respectively by a spectroradiometer (**Figure 6-S3**). After 600 secs illumination, the surface equilibrium temperature of dry FTCS-PDA-PVDF increased from room temperature (20 ºC) to ~35 ºC (at 0.75 kW/m^2) and to ~97 ºC (at 7.0 kW/m^2). The surface temperature of the dry PDA-PVDF membrane also increased from 20 ºC to ~35 ºC (0.75 kW/m^2) and to ~96 ºC (7.0 kW/m^2). In comparison, the dry FTCS-PVDF membrane surface temperature increased only from 20 ºC to ~23 ºC (0.75 kW/m^2) and to ~27 ºC (7.0 kW/m^2) under the same irradiation conditions. To evaluate the photothermal conversion properties of the membranes under water, the surface temperatures of membranes with water on top (8 mm distance from the membrane to the air/water interface) were also monitored using a benchtop controller thermocouple probe. For membranes immersed in water, the

temperature increases on the top of the membrane surface were smaller than those of dry membranes. Under water, after 600 sec illumination, the surface equilibrium temperature of FTCS-PDA-PVDF membrane increased from 20 ºC to ~26 ºC (0.75 kW/m^2) and to ~32 ºC (7.0 kW/m^2), and the temperature of PDA-PVDF membrane increased from 20 ºC to ~25 ºC (0.75 kW/m^2) and to ~31 ºC (7.0 kW/m^2), while the temperature of FTCS-PVDF membrane increased only from 20 ºC to ~22 ºC (0.75 kW/m^2) and to ~24 ºC (7.0 kW/m^2). The water on top of the membrane absorbed and scattered photons passing through, thus reducing the number of photons absorbed by the PDA coating on the membrane. The above results confirmed that the PDA coating on the PVDF surface exhibited high photothermal conversion and can be utilized for localized heating under solar irradiation.

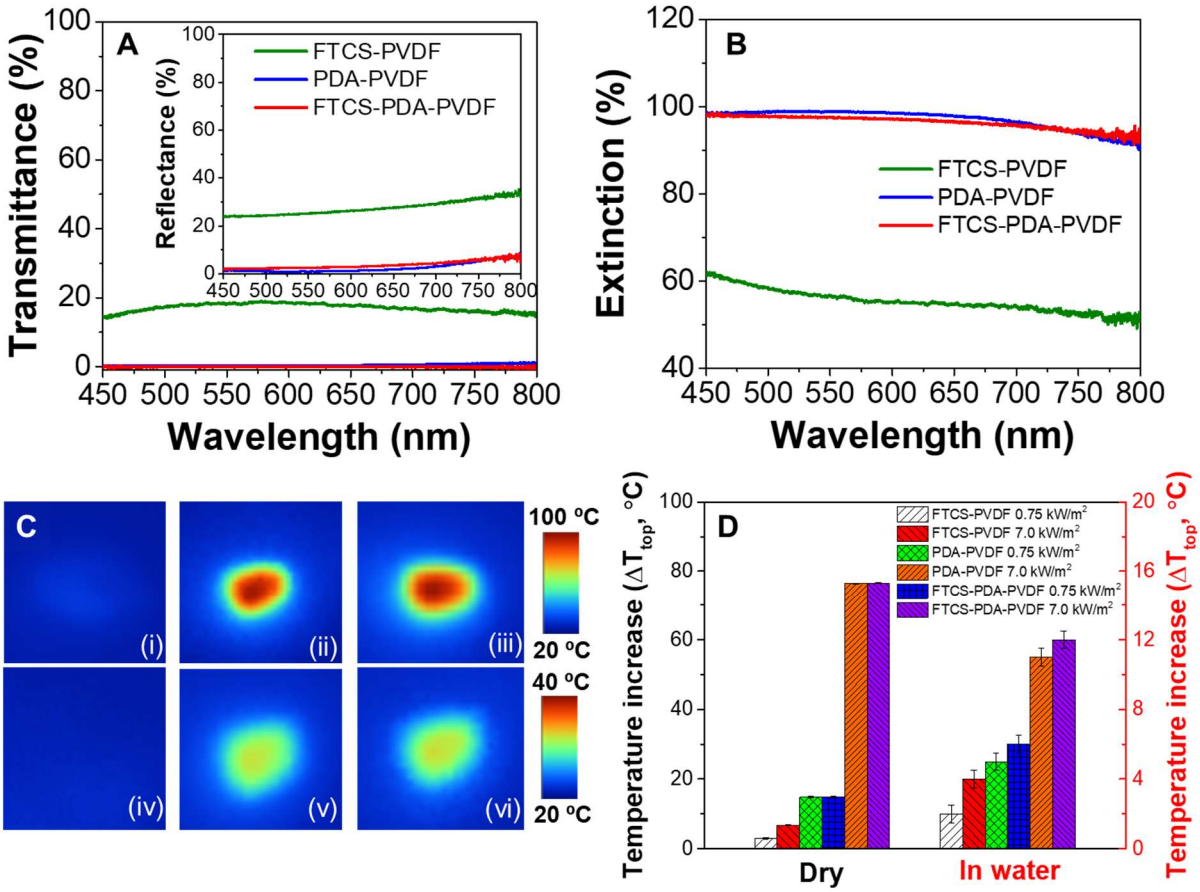

Figure 6.3 Optical and thermal properties of the FTCS-PDA-PVDF membrane. (**A**) Transmittance and (*inset*) reflectance spectra of the FTCS-PVDF, PDA-PVDF, and FTCS-PDA-PVDF membranes. (**B**) Light extinction spectra of the FTCS-PVDF, PDA-PVDF, and FTCS-PDA-PVDF membranes. (**C**) IR camera images of the FTCS-PVDF membrane under illumination of 7.0 kW/m^2 (**i**), 0.75 kW/m^2 (**iv**), the PDA-PVDF membrane under illumination of 7.0 kW/m^2 (ii), 0.75 kW/m^2 (**v**), and the FTCS-PDA-PVDF membrane under 7.0 kW/m^2 (**iii**), and 0.75 kW/m^2 (**vi**) after 600 sec illumination. (**D**) Surface temperature increase (ΔT, ºC) from room temperature (20 ºC) of the FTCS-PVDF, PDA-PVDF, and FTCS-PDA-PVDF membranes, after 600 sec illumination at 7.0 kW/m^2 and 0.75 kW/m^2, both under dry conditions and under water (water thickness = 8 mm).

6.3.3 Solar-driven membrane distillation performance of the FTCS-PDA-PVDF membrane

The solar-driven membrane distillation performance of the FTCS-PDA-PVDF membrane was tested in a specially designed direct contact membrane distillation (DCMD) module (**Figure 6.4A** and **Figure 6-S4**). The distillate (DI water, 20 ºC) was circulated with

a flow rate of 16.2 mL/min, and the increasing weight of the distillate was measured continuously by a balance to quantify the amount of collected water. To test the membrane distillation performance within 60 minutes (**Figure 6.4B** and **6.4C**) under different salinities, both pure water and highly saline water (0.5 M NaCl) were used as feed water (20 ºC) with a flow rate of 3.6 mL/min. Here, the 0.5 M salinity was chosen to mimic the average salinity of seawater.[413] The FTCS-PVDF membrane was used as a control membrane for comparison. For the FTCS-PDA-PVDF membrane with pure water, the water flux was 0.58 kg/m^2·h under 0.75 kW/m^2 irradiation. On the other hand, for the FTCS-PVDF membrane, the water flux was only 0.12 kg/m^2·h under identical irradiation, which is 3.8 times lower than that of the FTCS-PDA-PVDF membrane. With higher irradiation intensity (7.0 kW/m^2), the water flux of the FTCS-PDA-PVDF membrane increased to 5.17 kg/m^2·h, 12.6 times higher than that of FTCS-PVDF membrane (0.38 kg/m^2·h) under identical irradiation. In comparison, the water flux collected with saline feed water was lower than that of pure water for both the FTCS-PVDF and FTCS-PDA-PVDF membranes. The water fluxes for the FTCS-PDA-PVDF membrane were 0.49 and 4.23 kg/m^2·h under 0.75 and 7.0 kW/m^2 irradiations, significantly higher than those of the FTCS-PVDF membrane (0.09 and 0.22 kg/m^2·h). The lower water flux with saline water was due to the lower vapor pressure being in equilibrium with the feed, resulting in a lower vapor pressure difference across the membrane.[427-428] To put the FTCS-PDA-PVDF membrane in real-world use perspective, with saline water, a permeate flux rate of ~0.49 kg/m^2·h, and an active area of ~1 × 1 m^2, our solar MD system could generate 3.92 L/day under 0.75 kW/m^2 irradiation, with 8 h of sunlight time and at ~20 ºC ambient temperature. This outstanding solar-driven MD performance of the FTCS-PDA-PVDF membrane makes it highly attractive for efficient and sustainable desalination process.

The feed flow rate is crucial for MD efficiency because it affects the heat transfer in the feed channel and the temperature polarization effects on the membrane surface.[382] Therefore, to evaluate the influence of feed flow rate on the solar-driven MD performance, we also measured the permeate water flux with varied feed flow rates (1.5–8.1 mL/min) for FTCS-PDA-PVDF membranes (**Figure 6.4D**, **Figure 6-S5**) with simulated solar irradiation. The tests were conducted in triplicate, using a new membrane each time. With 0.75 kW/m^2 irradiation, the fluxes with pure water and saline water decreased from 0.66 and 0.57 kg/m^2·h to 0.49 and 0.43 kg/m^2·h, respectively, when the feed flow rate increased from 1.5 to 8.1 mL/min. With 7.0 kW/m^2 irradiation, the fluxes with pure water and saline water decreased from 5.89 and 4.87 kg/m^2·h to 4.18 and 3.51 kg/m^2·h, respectively (**Figure 6-S5A-B**). As shown in the schematic diagram comparing conventional MD and solar-driven MD in Fig. S5C†, for conventional MD systems, the permeate water flux increases with an increasing feed water flow rate, owing to better mixing in the flow channel and decreased temperature polarization effects.[391, 429] Contrarily, in the solar-driven MD system, the permeate water flux decreased with increasing feed water flow rate. With higher feed flow rate, the heat loss from the heated membrane top surface to the bulk feed water was faster, leading to a smaller temperature gradient across the membrane. Similar trends have been reported in a recent study using carbon black as photothermal material.[21] However, with feed flow rates of 1.5–8.1 mL/min and irradiation of 0.75 kW/m^2, the permeate flux with saline feed water (0.5 M NaCl) of our membrane (0.43–0.57 kg/m^2·h) was about twice as high as that reported for the carbon black membrane (~0.21–0.27 kg/m^2·h) under similar conditions.[21]

The solar conversion efficiency (η), which describes the overall membrane thermal efficiency, was defined as the ratio of the energy needed to generate permeate flux over the total energy input by solar irradiation (I, kJ/m^2·h) (same as the gained output ratio, see

detailed description in the section 6-S4 in Supporting formation). The energy needed for permeate flux was calculated by multiplying the permeate flux ($\dot{m}$, kg/m^2·h) by the evaporation enthalpy change (H_{vap}, 2,454 kJ/kg) of water.[21] As shown in **Figure 6.4E**, with a pure water flow rate of 3.6 mL/min, the solar conversion efficiency of the FTCS-PDA-PVDF membrane was calculated to be 53% under 0.75 kW/m^2 irradiation, much higher than the 10% of FTCS-PVDF under identical irradiation. When the feed flow rates were adjusted from 1.5 to 8.1 mL/min, the solar efficiencies decreased from 60% to 44%. At a flow rate of 3.6 mL/min with saline water, the solar conversion efficiencies of FTCS-PDA-PVDF membranes were 45% and 41% under 0.75 and 7.0 kW/m^2 irradiations, respectively. For both pure water and saline water, the solar efficiencies decreased when using larger feed flow rates. Previous studies have used silver nanoparticles, nitrocellulose, and carbon black as photothermal materials for light-driven MD systems with excellent flux penetration and solar conversion efficiencies.[21, 85, 392] However, our FTCS-PDA-PVDF membrane exhibited even higher solar conversion efficiency (45% for saline water under 0.75 kW/m^2 irradiation) than membranes using silver nanoparticles (36.9%),[85] nitrocellulose (31.8%)[392] and carbon black (21.5%)[21] (**Table 6-S2**). The outstanding solar conversion efficiency of the FTCS-PDA-PVDF membrane compared with other recently reported membranes can be mainly attributed to three factors: (i) The superior light absorption properties of PDA. Polydopamine has wider light absorption range than Ag nanoparticles, which absorb light mainly in the UV range.[85] (ii) The high surface temperature on the top of membrane owing to the excellent photothermal conversion properties of PDA, even with a thick water layer on top of the membrane surface. PDA is known to convert 99% of the absorbed photon energy into heat within 50 ps.[397] (iii) The high density and uniformity of the PDA coating on the PVDF membrane surface as shown in SEM images. The uniform self-polymerization of dopamine

and the excellent adhesion of PDA to a multitude of surfaces foster *'proximal'* photothermal conversion activity. Such proximal photothermal conversion leads to an increased transmembrane temperature and a larger vapor pressure difference across the membrane. In contrast, in the previous work using a carbon black layer on top of the PVDF membrane, the light-absorbing layer is far from the PVDF membrane surface, decreasing the transmembrane temperature and the driving force for vapor transport.[21]

In terms of solar conversion efficiency, although our membrane achieved the highest efficiency among existing photothermal MD membranes, it is relatively lower than those of photothermal steam generation membranes.[398, 430-431] The main reasons behind the lower efficiency in photothermal MD are the top water layer interference and conductive heat loss. With water thickness ranging from 1.5–8 mm in existing photothermal MD systems (**Table 6-S2**), this top water layer can reduce the number of photons absorbed by the photothermal membrane and thus lead to a lower membrane surface temperature. In addition, the floating feed water system further increases the conductive heat loss, while for photothermal steam generation, the untreated water under the evaporators is often in a stagnant system. Although the efficiencies of current photothermal steam generation are higher, the steam collection still remains as the challenge before its large scale applications. In the future, efforts should be put into increasing the solar conversion efficiency of photothermal MD by developing new MD modules or membranes to exalt its competitiveness among all the photothermal desalination techniques. Furthermore, photothermal MD can be more advantageous when it is used for flowback water treatment from unconventional oil and gas recovery systems, which already contain high temperature water (e.g., ~60–70 ºC).[432] The high temperature feed water along with photothermal temperature rise, makes the overall MD process more efficient.

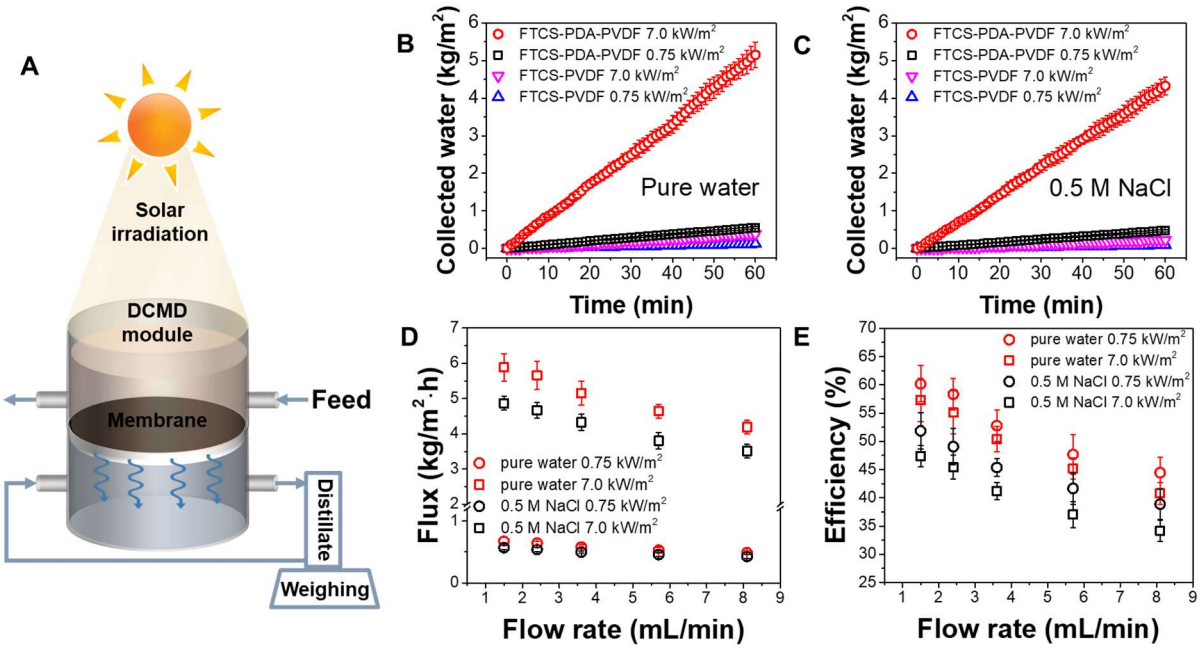

Figure 6.4 (**A**) Schematic depicting the solar-driven DCMD system. Collected water (kg/m2) using the FTCS-PVDF and the FTCS-PDA-PVDF membrane using both pure water (**B**) and 0.5 M NaCl saline water (**C**) under different solar irradiations. Flux (**D**) and efficiency (**E**) of solar-driven DCMD system using the FTCS-PDA-PVDF membrane with varying feed flow rates, using both pure water and 0.5 M NaCl saline water under different solar irradiations. Triplicate membrane samples were tested in all cases.

6.3.4 Chemical and mechanical stability of the FTCS-PDA-PVDF membrane

The chemical and mechanical stability of the FTCS-PDA-PVDF membrane was investigated further by subjecting it to both ultrasonic agitation for 6 hours and vigorous shaking for 30 days at three pH values (pH 4, 7, and 10) (**Figure 6-S6A**). Even after these extreme stress tests, the FTCS-PDA-PVDF membrane did not exhibit discernible signs of disintegration or loss of PDA coating from the surface. The morphology of the FTCS-PDA-PVDF membrane remained unaltered after 10 cycling tests with pure water and saline water, as shown by the SEM images of the FTCS-PDA-PVDF membrane surface (**Figure 6-S6B-C**). Then, to evaluate the potential changes in membrane wetting after several MD cycles,

the contact angles of pure water and saline water on the membrane were measured (**Figure 6-S6D**). For an unused FTCS-PDA-PVDF membrane, the contact angles were 125.5º ± 1.9º and 126.1º ± 1.6º for pure water and saline water, respectively. After 10 cycles of MD tests (1 hr × 10 times), the contact angles for pure water and saline water were 124.3º ± 1.5º and 125.4º ± 1.3º, indicating less than 1% variation in the contact angle. Pore wetting problems have constrained the use of many MD membranes for long term or large scale applications.[382] However, the excellent and stable hydrophobicity of the FTCS-PDA-PVDF membrane, owing to the covalent and dense FTCS fluoro-silane, confers long-lasting and stable wetting resistance. The variation of membrane mass was also smaller than 1% over 10 cycles of MD tests using saline water with focused irradiation (7.0 kW/m^2) (**Figure 6-S6E**). The salt rejection was larger than 99.9% over 10 cycles of MD tests using saline water under both unfocused (0.75 kW/m^2) and focused (7.0 kW/m^2) irradiations (**Figure 6-S6E**). This high salt rejection of FTCS-PDA-PVDF membrane can be attributed to the operation conditions of the DCMD (low hydrostatic pressure), and to the excellent hydrophobicity and wetting resistance of the membrane. Furthermore, the flux performance of FTCS-PDA-PVDF membrane remained stable over 10 cycles of MD tests (less than 5% variation, **Figure 6-S6F**). The remarkable chemical and mechanical stability of the FTCS-PDA-PVDF membrane, owing to the strong adhesion between PDA and the PVDF surface,[394, 416] can lessen environmental concerns or the need for further treatment caused by the possible detachment of photothermal materials from the membrane surface, and increase the longevity of membranes for long term solar MD applications.

6.4 Conclusions and environmental implications

In summary, we present a simple, stable, and highly effective photothermal membrane for solar-driven membrane distillation. Owing to the remarkable light absorption and outstanding photothermal conversion properties of the PDA coating, the FTCS-PDA-PVDF membrane exhibited excellent solar membrane distillation performance (efficiency of 45% under 0.75 kW/m^2 irradiation). The FTCS-PDA-PVDF membrane exhibited a 4.23 $kg/m^2 \cdot h$ permeate flux under 7.0 kW/m^2 irradiation, a 19-fold enhancement over FTCS-PVDF membrane. In addition, the proximal polymerization process that leads to strong adhesion between PDA and the PVDF surface resulted in the excellent chemical and mechanical robustness and stability of the FTCS-PDA-PVDF membrane, which allows its utilization in long term solar MD applications. In comparison with recently reported photothermal membranes which utilized phase inversion or electrospinning processes,[21, 85] PDA polymerization would be a much easier way to achieve proximal photothermal conversion activity. The simplicity of the PDA coating method also makes the membrane attractive for future commercial applications. From engineering perspectives, with built-up systems with multiple industrial-scale tanks, the final coated-membrane area can be significantly larger than other existing membrane modification methods to achieve a similar extent of photothermal performance. In the future, efforts can be put into expediting the PDA polymerization by optimizing the reaction conditions and designing better mixing systems. Coupled with renewable and sustainable solar irradiation, the highly efficient photothermal membrane introduced here can provide a promising option to alleviate the global water crisis.

Acknowledgments

We are grateful for the support received from the National Science Foundation Environmental Engineering Program (CBET-1604542). We wish to thank the Institute of Materials Science and Engineering (IMSE) in Washington University in St. Louis for the use of XPS. We also thank the Nano Research Facility (NRF) at Washington University in St. Louis for use of SEM. We thank Mr. James Linders at Machine Shop of Department of Chemistry at Washington University in St. Louis for helping the design and building of MD module, and Prof. James Ballard for carefully reviewing our manuscript. Lastly, we also thank the Environmental NanoChemistry Group members for providing valuable discussions and suggestions for this paper.

Supporting information for Chapter 6

Supporting figures and tables

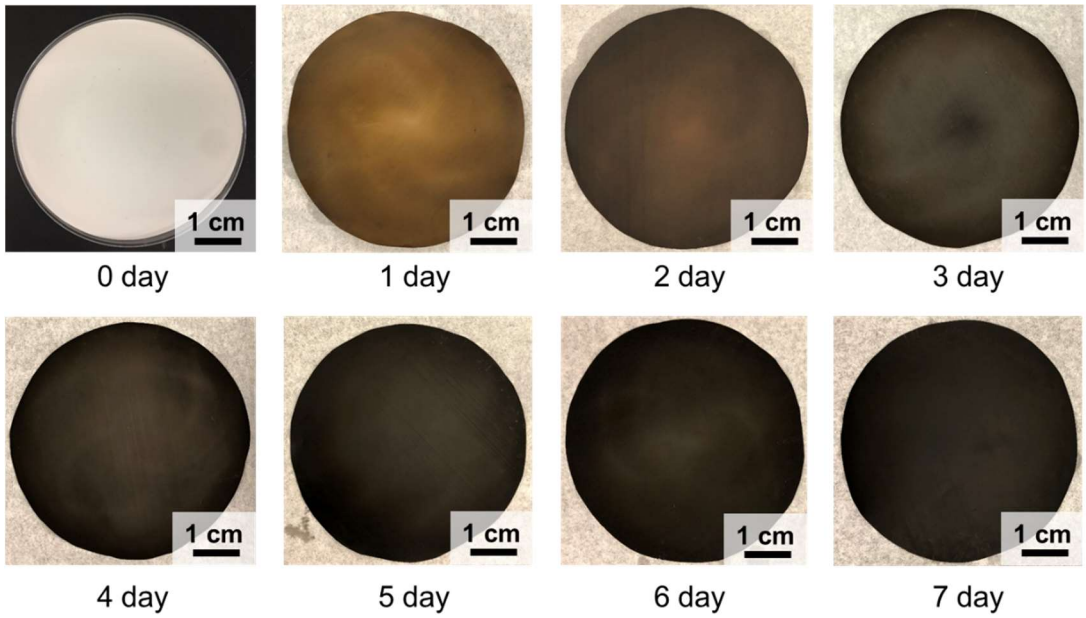

Figure 6-S1. Optical images showing the color change of the PVDF surface during the 7-day PDA self-polymerization process.

Table 6-S1. ATR-FTIR reference peaks for PDA coating on PVDF.

	FTIR peak positions (cm^{-1})				
N-H bending vibrations	1510	1490	1506	1540	1520
C=C resonance vibrations in the aromatic ring	1600	1610	1600	1645	1610
O-H and NH_2 stretching vibrations	3100-3600	3100-3600	3100-3600	3000-3700	3100-3600
Reference	Jiang et al., 2011[417]	Cao et al., 2014[416]	Shao et al., 2014[418]	Sun et al., 2017[419]	This study

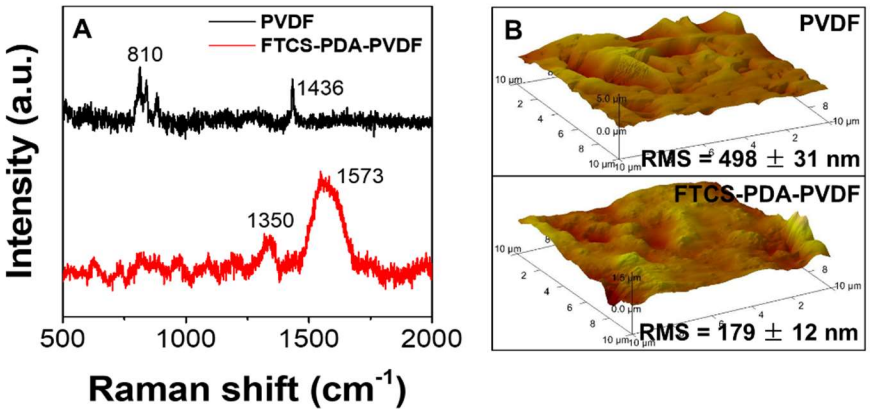

Figure 6-S2. (A) Raman spectra of pristine PVDF and FTCS-PDA-PVDF membranes; (B) Tapping mode AFM images (10 μm × 10 μm) showing the surface roughness (RMS) of pristine PVDF and FTCS-PDA-PVDF membranes.

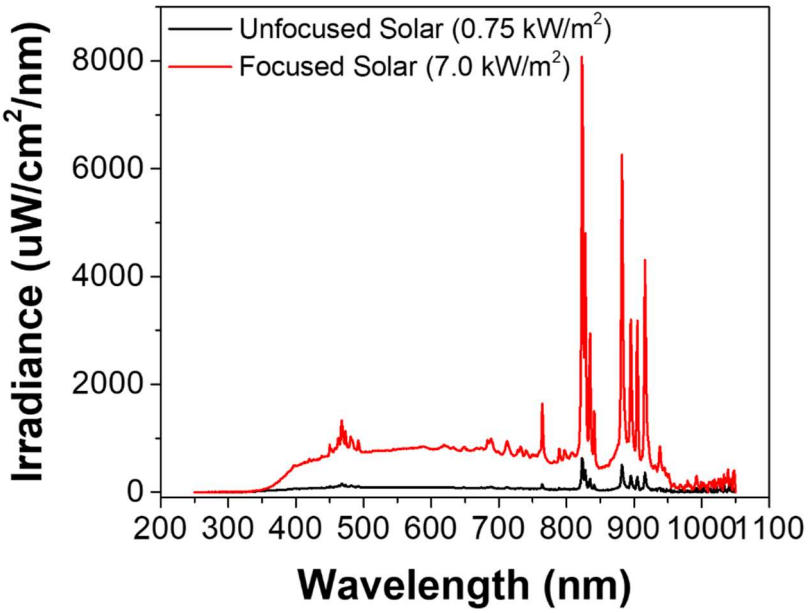

Figure 6-S3. Solar irradiance spectra of the solar simulator for unfocused (0.75 kW/m^2) and focused (7.0 kW/m^2) conditions.

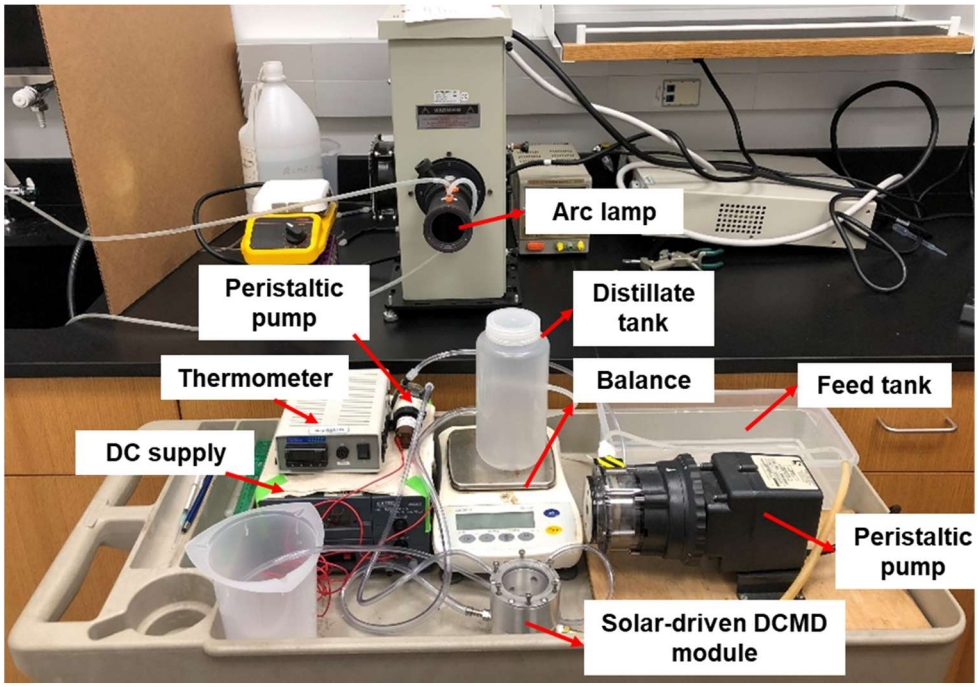

Figure 6-S4. Photo of the portable solar-driven direct contact membrane distillation system.

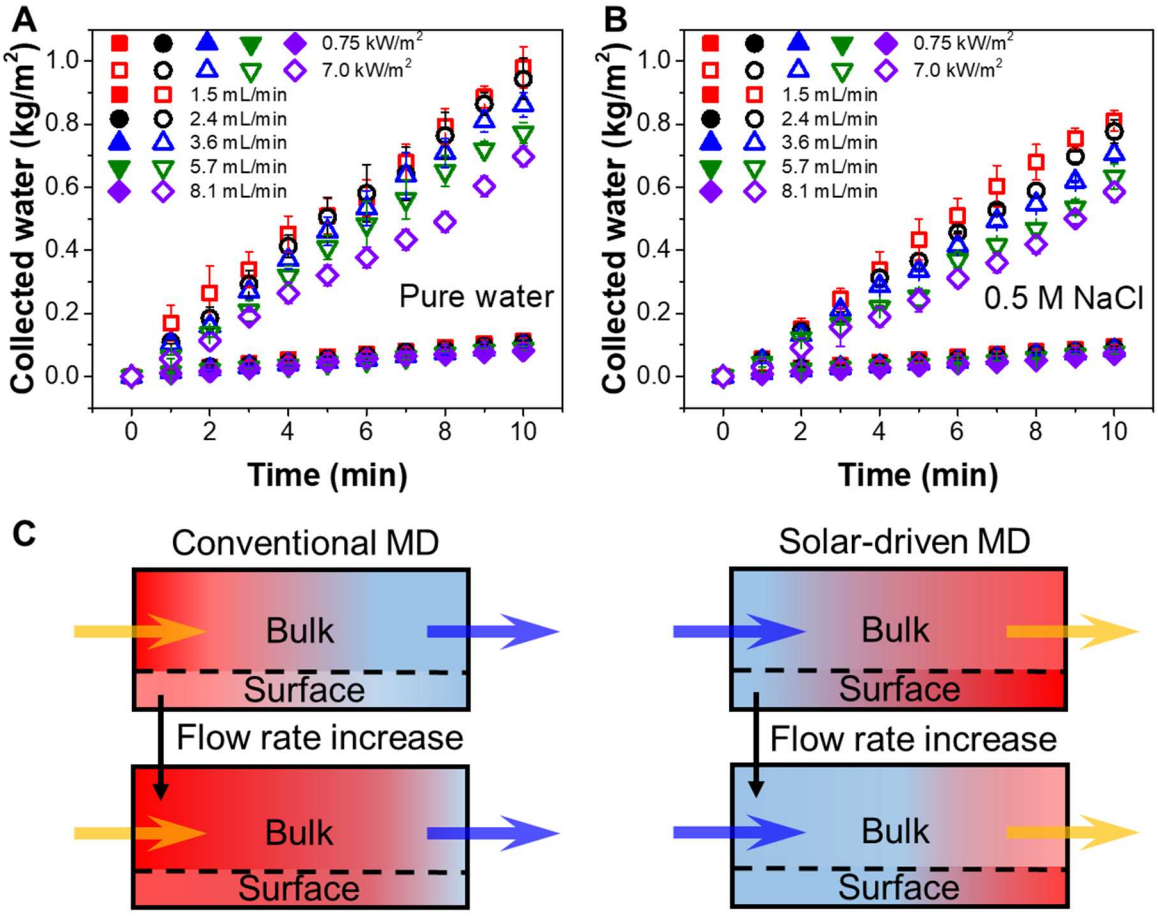

Figure 6-S5. Collected water (kg/m^2) for DCMD using pure water (A) and 0.5 M NaCl (B) with various feed flow rates (1.5–8.1 mL/min). (C) Schematic illustration depicting the temperature change in the feed side of a conventional MD system and solar-driven MD system with different feed flow rates. Red depicts high temperature and blue depicts low temperature.

Table 6-S2. Comparison with other current photothermal MD membranes.

Materials	MD system[a]	Efficiency	T_{top} [b] (ºC)	Thickness of H_2O on top (mm)	Flux (kg/m^2 h)	Energy source	Hydrophobicity	Paper
PVDF-PVA-5.5wt%BC	DCMD	21.45%	20.8	1.5	0.22	solar	NA	Dongare et al., 2017[21]
PVDF-25%Ag NPs	VMD	29.6%	54.3	NA	25.7	UV	80.3º±3.6º	Politano et al., 2017[85]
Millipore nitrocellulose membrane	AGMD	31.8%	42–72[c]	4	0.35	solar	NA	Summers et al., 2013[392]
FTCS-PDA-PVDF	DCMD	45%	26	8	0.49	solar	126.1º±1.6º	This study

[a] VMD stands for vacuum membrane distillation. AGMD stands for air gap membrane distillation.
[b] Water temperatures of feed inlet and distillate for Dongare et al. and this study are 20 ºC. Politano et al. used an inlet of ~28 ºC. Summers et al. used an inlet of 26–30 ºC and a distillate of 20 ºC.
[c] Summers et al. used an electric heater besides the solar system.

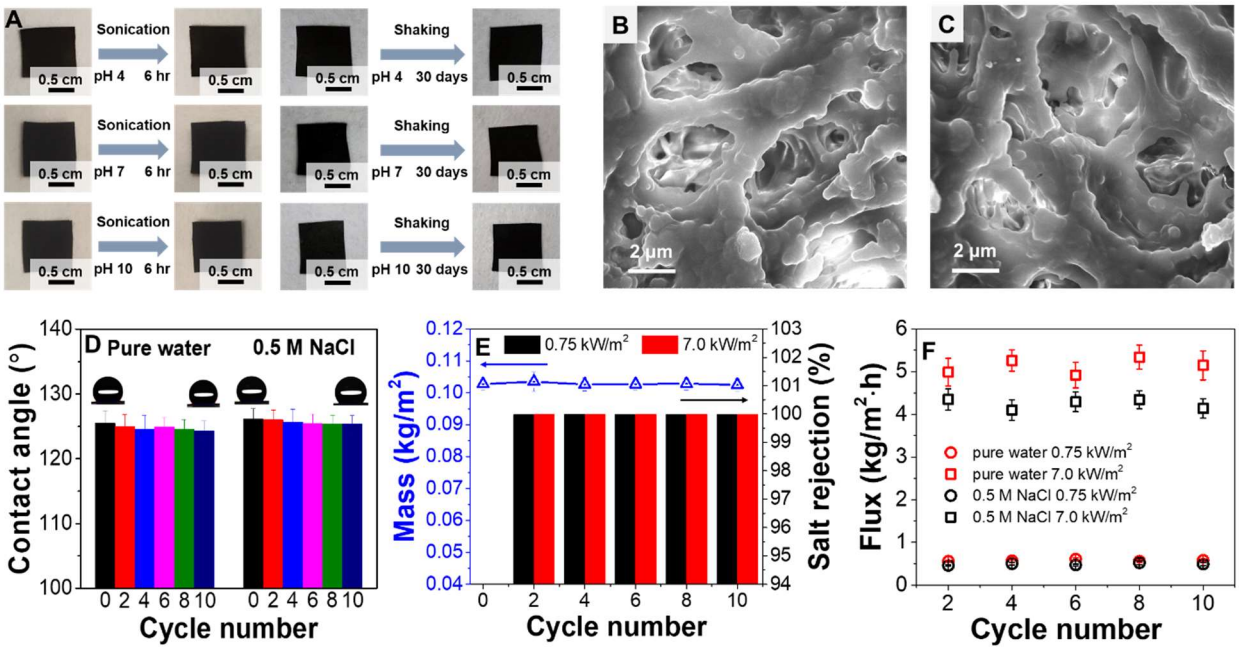

Figure 6-S6. (A) Photographs showing the chemical and mechanical stability of FTCS-PDA-PVDF membrane with ultra-sonication and shaking for an extended duration. SEM images of FTCS-PDA-PVDF membrane surface after 10 cycles using (B) pure water and (C) 0.5 M NaCl. (D) Contact angles of FTCS-PDA-PVDF membrane over 10 cycles of MD tests using pure water and 0.5 M NaCl. (E) *(Left y-axis)* Mass change of FTCS-PDA-PVDF membrane over 10 cycles of MD tests using 0.5 M NaCl, with 7.0 kW/m^2 irradiation; *(right y-axis)* Salt rejection of FTCS-PDA-PVDF membrane over 10 cycles of MD tests using 0.5 M NaCl, with both 0.75 and 7.0 kW/m^2 irradiations. (F) Flux performance of FTCS-PDA-PVDF membrane over 10 cycles of MD tests using pure water and 0.5 M NaCl, with both 0.75 and 7.0 kW/m^2 irradiations. Triplicate membrane samples were tested.

Chapter 7. Thermally-Engineered Polydopamine-Bacterial Nanocellulose Bilayered Membrane for Photothermal Membrane Distillation

Abstract

In **Chapter 6**, we described a photothermal membrane distillation performance of a simple, stable, and scalable PDA-coated polyvinylidene fluoride (PVDF) membrane. Here in **Chapter 7**, to further improve solar conversion efficiency, we continue to develop our membrane by changing the commercial PVDF membrane for a highly porous bacterial nanocellulose (BNC) aerogel membrane. The membrane performance for photothermal membrane distillation is enhanced by a thermally-engineered bilayered structure. Solar energy holds great promise for sustainable desalination to alleviate global water scarcity. Recently developed solar steam generation relying on interfacial evaporators has high solar energy-to-steam efficiency (60–90%), but its vapor collection efficiency is low, typically ~30%. Here, we present a solar-driven photothermal membrane distillation (PMD) system that offers easy and highly efficient clean vapor generation, condensation, and collection. The photothermal membrane is thermally-engineered to incorporate a bilayer structure composed of two environmentally-sustainable materials, polydopamine (PDA) particles and bacterial nanocellulose (BNC). The optimally sized PDA particles on top maximize sunlight absorption and sunlight-to-heat conversion, and the bottom BNC aerogel insulating layer achieves high vapor permeability and low conductive heat loss. This thermally-engineered design enables a permeate flux of 1.0 kg m^{-2} h^{-1} under 1 sun irradiation, and a record high solar energy-to-collected water efficiency of 68%, without ancillary heat or heat recovery systems. Moreover, the membrane shows effective bactericidal activity and allows easy cleaning, increasing its lifespan. This study provides a paradigm for using photothermal material incorporated in an aerogel to sustainably purify water. Using solar energy, the PMD

system presented here can also provide decentralized desalination for remote or underdeveloped areas, and can support resilient community development.

7.1 Introduction

Water scarcity presents a top challenge to human society.[433-435] To alleviate water scarcity, desalination of seawater or brackish water has been implemented extensively.[19, 375] Most current desalination techniques, including thermal distillation,[378] reverse osmosis (RO),[373] and electrodialysis (ED),[376] are centralized systems that have high installation and maintenance costs, and require large amounts of electrical energy.[436] In developing countries, rural communities, and disaster areas that lack electricity, solar-driven water desalination is regarded as a promising technique.[437] Recently, solar steam generation by using interfacial evaporators has gained much attention with high solar energy-to-steam (SE/S) efficiencies (~60–90%).[438-440] However, the lack of efficient vapor condensation and clean water collection systems decreases the overall solar energy-to-collected water (SE/CW) efficiencies of current evaporators to only ~30%,[441] which may constrain their reliable and sustainable freshwater production.

To address this challenge, here, we present a photothermal membrane distillation (PMD) system, driven by solar energy, that offers easy vapor condensation and water collection. Membrane distillation (MD) is a promising membrane-based thermally-driven desalination technique.[442] In traditional MD, the saline feed water is heated to achieve a temperature difference (ΔT) between the two sides of a hydrophobic membrane. The resulting vapor pressure difference (ΔP) drives the water to vaporize on the hot feed side, pass through the porous membrane, and condense on the cold distillate side.[442] However, external energy sources are needed to heat the feed water.

In PMD, a membrane embedded with light-absorbing photothermal materials can utilize solar energy to drive the MD process by interfacial heating. The photothermal membrane harvests solar energy at the saline water–membrane interface, generates localized heat, and provides a high transmembrane temperature gradient for efficient vapor transport.[21, 93] Compared with other solar-based desalination techniques, PMD possesses several key advantages. First, the high hydrophobicity of the membrane in PMD offers excellent salt rejection and low salt-fouling. Second, combined with systematically developed and already commercialized MD systems, such as direct contact, air gap, and vacuum membrane distillation (DCMD, AGMD, VMD), PMD can offer easy, scalable, and highly efficient clean water collection.

To improve the SE/CW efficiency of PMD membrane, three important aspects need to be addressed: excellent light-to-heat conversion, high vapor permeability, and low conductive heat loss. In this work, polydopamine (PDA) particles with an optimal size for maximizing sunlight absorption in the visible range are used as the photothermal material. The superb light absorption and photothermal conversion properties of these PDA particles create a high transmembrane temperature difference and a vapor transport driving force. Then, bacterial nanocellulose (BNC), known for its outstanding mechanical strength and scalability, is used as the supporting layer to entangle and retain the PDA particles. More importantly, the microporous structure of BNC enables high vapor permeability and reduces the conductive heat loss from the solar absorber layer to the underlying distillate. This thermally-engineered bilayered membrane achieves a permeate flux of 1.0 kg m^{-2} h^{-1} under 1 sun irradiation (1 kW m^{-2}) and the highest SE/CW efficiency of 68% among reports when treating saline water (20ºC, 0.5 M NaCl) without ancillary heat or heat recovery systems. The membrane also exhibits effective self-disinfection under light illumination, mitigating the

concern of bio-fouling. Using sustainable solar energy, the PMD system presented here, with a bilayered aerogel structure facilitating highly energy-efficient water purification, can provide easy, cheap, decentralized, and sustainable desalination solutions for households, remote areas, ships, or disaster regions. The PMD system can also help to realize Sustainable Development Goals (SDGs) set by the United Nations,[443] using affordable and clean solar energy to provide freshwater for resilient communities.

7.2 Experimental section

7.2.1 Fabrication of a hydrophobic bilayered polydopamine-bacterial nanocellulose aerogel membrane

Figure 7.1A demonstrates the fabrication procedure for a hydrophobic bilayered membrane using bacterial nanocellulose and PDA. *Gluconacetobacter hansenii* was cultured to form a BNC hydrogel, using a method reported earlier.[444] Polydopamine particles were prepared using a method reported by Lu and co-workers.[445] By controlling the ratio of ammonia to dopamine monomers, the PDA particle size was optimized to ensure the overlap of PDA optical absorption with the solar spectrum in the visible range.[398] As indicated by a scanning electron microscopy (SEM) image, the synthesized PDA particles were spherical, with an average diameter of ~1 μm (**Figure 7.1B**). PDA particles were dispersed in bacterial growth medium and added onto the top of the BNC hydrogel, forming a PDA/BNC layer. The hydrogel was cleaned and freeze-dried to obtain a bilayered PDA/BNC membrane. To make the membrane hydrophobic, the PDA/BNC membrane was later exposed to (tridecafluoro-1,1,2,2-tetrahydrooctyl)-trichlorosilane (FTCS) vapor at 70°C for 6 hours, resulting in a coverage of FTCS fluorosilane functional groups. Using a contact angle

analyzer (Phoenix 300, Surface Electro Optics Co. Ltd), the water contact angle of the FTCS-PDA/BNC bilayered membrane was measured to be 125º (**Figure 7.1C**). More detailed preparation information on the hydrophobic bilayered membrane is available in the Supporting Information (7-S1).

7.2.2 Membrane characterization

The FTCS-PDA/BNC membrane surface and cross-section morphology and microstructure were characterized using a scanning electron microscopy (SEM; OVA NanoSEM 230, FEI). The chemical composition of PDA and FTCS on the BNC were identified using X-ray photoelectron spectroscopy (XPS, PHI 5000 VersaProbe II, Ulvac-PHI) and Raman spectroscopy (inVia Raman Microscope, Renishaw). For XPS measurements, Al Kα monochromator radiation was used to measure the C 1s, F 1s, and N 1s spectra of pure BNC, PDA/BNC, and FTCS-PDA/BNC membranes. A gravimetric method was used to quantify the porosity (ε) of BNC and PDA/BNC membranes, as described in detail in SI (7-S2).[77, 446]

7.2.3 Optical and photothermal conversion property measurements

The transmittance and reflectance of the BNC and FTCS-PDA/BNC membranes were measured using a micro-spectrophotometer (QDI 302, CRAIC Technologies) coupled to a Leica microscope (DM 4000M, Leica Microsystems). An infrared camera (IR camera, Ti 100, FLUKE) was used to quantify the surface temperature increase of BNC and FTCS-PDA/BNC membranes within 120 secs under light illumination via a solar simulator (Newport 66921 Arc Lamp). Two light illumination intensities were chosen in this study: 1

kW m^{-2} (~1 sun) and 9 kW m^{-2} (~9 sun), as measured by a spectroradiometer (SpectriLight ILT 950). The membrane surface temperature increase with water on top (water thickness = 8 mm) was monitored using a benchtop controller thermocouple probe (±0.5°C resolution, OMEGA CSI32K-C24, US) after 600 secs at each light illumination.

7.2.4 Photothermal membrane distillation tests

The PMD performance of the BNC and FTCS-PDA/BNC membranes was tested in a direct contact membrane distillation (DCMD) module. A schematic of the PMD unit is provided in SI (7-S3). For PMD tests using room temperature feed water (20ºC), 0.5 M NaCl was used to mimic the average salinity of seawater.[413] DI water (20ºC) was used as the distillate. The distillate reservoir was kept on a weighing balance (Sartorius ELT402) to measure the collected permeate amount. During PMD tests, simulated solar light was oriented perpendicularly to the membrane surface, with intensities controlled at 1 kW m^{-2} (1 sun) and 9 kW m^{-2} (9 sun). For PMD tests combined with hot feed water, the NaCl solution was heated to 45 ºC and 65 ºC (±1 ºC) using a hot plate (Thermo Scientific HP131225). A chloride probe (VWR 89231-632) was used to test the salt rejection of the membranes. Detailed PMD information is available in the SI (7-S3). The solar energy to collected water (SE/CW) efficiency calculation is available in the SI (7-S3).

7.2.5 Stability tests of the FTCS-PDA/BNC membrane

The chemical and mechanical stability of the FTCS-PDA/BNC membrane (SI 7-S4) was tested at three pH values (pH 3, 7, and 10), using vigorous shaking for 30 days (VWR Orbital Shaker, Model 3500). These pH values were chosen to mimic natural and engineered aqueous systems.[447] The UV−Vis absorbance of the solution in which the FTCS-PDA/BNC

membrane was immersed was measured at pH 7 before and after ultrasonic agitation for 6 hours in a 35ºC ultrasonication bath (Fisher Scientific, Model FS6). No significant change was observed. Over 5 cycles of PMD tests (1 cycle = 1 hour), the contact angles, salt rejection, and collected permeate fluxes were monitored. SEM images were again measured for the FTCS-PDA/BNC membrane after PMD tests to evaluate its morphology and microstructure alteration.

7.2.6 Self-disinfection activity measurements

To identify the self-disinfection property of the FTCS-PDA/BNC membrane, four conditions were tested to simulate actual PMD processes: (i) a membrane contacted with water contaminated by bacteria, (ii) a membrane contacted with water contaminated by bacteria during PMD, (iii) a membrane illuminated by light after feed water had drained from the top of the membrane, and (iv) a membrane after washing in DI water. The FTCS-PDA/BNC membrane was submerged in solution containing MG 1655 *E. coli* (>324 live cells/mL) for 1 hour to test condition (i). To test condition (ii), FTCS-PDA/BNC membrane with *E. coli* contaminated water on top was exposed to simulated sunlight (1 kW/m^2) for 1 hour. To test condition (iii), after being submerged in *E. coli* contaminated water for 1 hour, FTCS-PDA/BNC membrane was removed and exposed to simulated sunlight (1 kW m^{-2}) for 10 minutes. Condition (iv) was tested by washing FTCS-PDA/BNC membrane in DI water for 5 minutes after light illumination treatment as in condition (iii). In each condition, the FTCS-PDA/BNC membrane after test was exposed to fluorescent dyes (Molecular Probes Live/Dead Bacterial cell viability kit, Thermo Fisher Scientific) for 30 minutes and then imaged under a Leica microscope (DM 4000M, Leica microsystems) to identify live (blue fluorescent filter, 340−380 nm) and dead (green fluorescent filter, 450−490 nm) cells.

Detailed information on bacterial solution preparation and self-disinfection tests is available in the SI (7-S4).

7.3 Results and discussion

7.3.1 Fabrication of the bilayered PMD membrane

The hydrophobic bilayered membrane was fabricated by first culturing *Gluconacetobacter hansenii* to form a BNC hydrogel (**Figure 7.1a**).[444] To ensure that the PDA optical absorption overlapped with the solar spectrum in the visible range (**Figure 7-S1**), PDA particles were synthesized with an optimal size (~1 μm diameter, **Figure 7.1b**).[398, 445] The prepared PDA particles were added onto the top of the growing BNC layer, where they were entangled by BNC nanofibrils during *in situ* growth, forming a PDA/BNC layer. The bilayered hydrogel was then cleaned and freeze-dried to obtain a bilayered PDA/BNC aerogel membrane. To make the membrane hydrophobic, the PDA/BNC membrane was exposed to (tridecafluoro-1,1,2,2-tetrahydrooctyl)-trichlorosilane (FTCS) vapor, which resulted in a coverage of fluoro-functional groups on the membrane surface and a water contact angle of 125º (**Figure 7.1c**). For comparison, we also prepared a pristine BNC aerogel membrane, which contained interconnected nanofibrils with diameters in the range of 20–100 nm (**Figure 7.1e,f**). A cross-section SEM image of the pristine BNC membrane shows its layered and microporous structure in the z-direction. Top surface SEM images of FTCS-PDA/BNC membrane (**Figure 7.1i,j**) show the spherical PDA particles entangled inside the BNC nanofibrils. A cross-section of FTCS-PDA/BNC membrane exhibits a bilayered structure (**Figure 7.1k**), with a clear interface between the PDA-loaded BNC and pristine BNC layers. While the pristine BNC and FTCS-PDA/BNC membranes have similar overall

thicknesses (~250 μm) (**Figure 7-S2**), the FTCS-PDA/BNC membrane comprises a ~30 μm PDA-loaded BNC layer and a ~220 μm pristine BNC layer (**Figure 7-S2b**). Confirmed by gravimetric measurements, the porosities (ε) of the pristine BNC (~98%) and PDA/BNC (~93%) are higher than those of commercially available polyvinylidene difluoride (PVDF) membranes (50–70%)[446, 448]. The weight percentage of PDA particles in the entire bilayered FTCS-PDA/BNC membrane was measured to be ~56%, and the weight percentage of PDA particles in the PDA/BNC layer as the top layer of the bilayered FTCS-PDA/BNC membrane reached ~91 wt%. Detailed calculation of PDA wt% and the characterization of the FTCS-PDA/BNC membrane by XPS and Raman measurements are available in the Supplementary Information (7-S2).

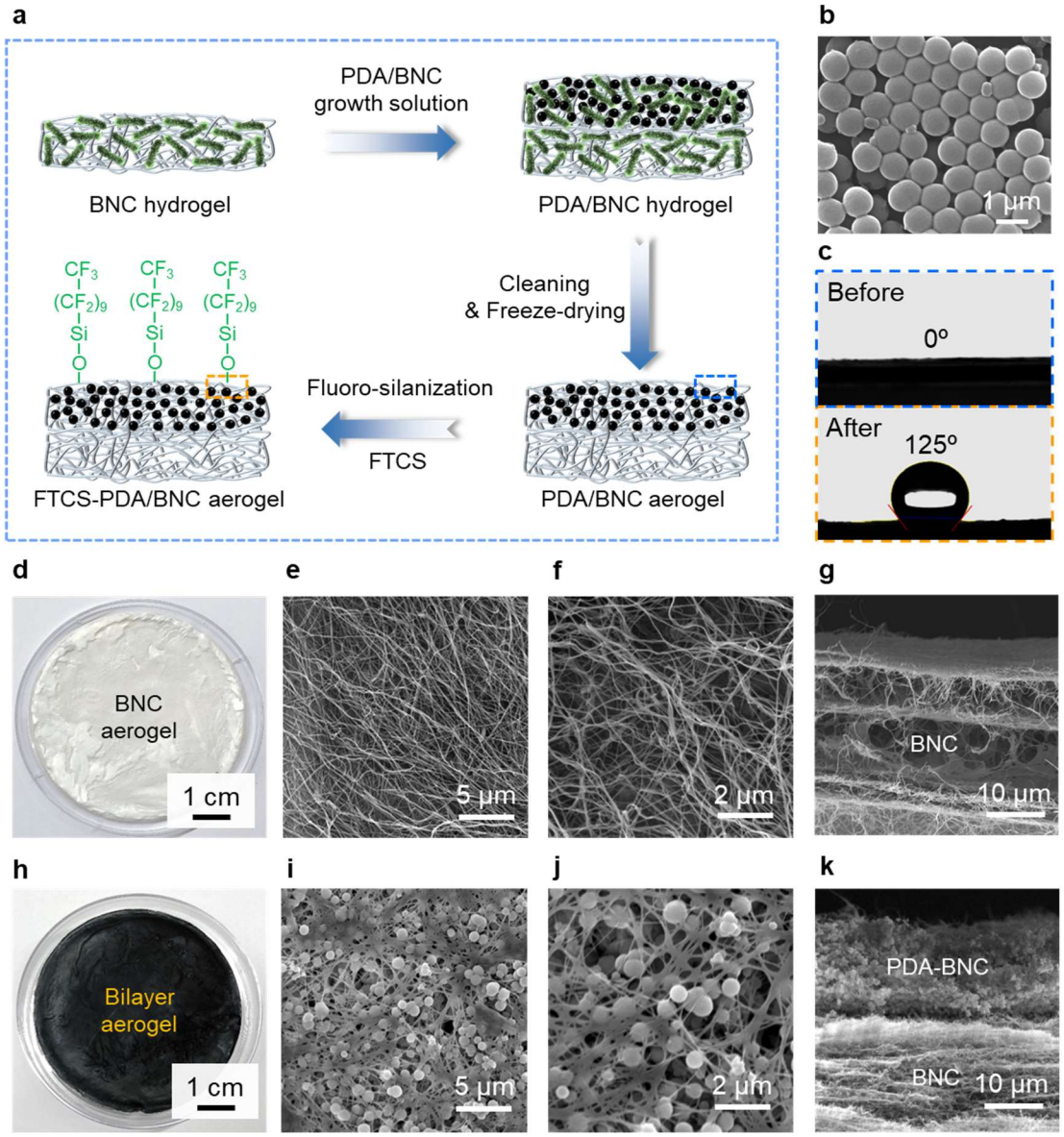

Figure 7.1 Fabrication and characterization of the bilayered FTCS-PDA/BNC aerogel membrane. (**a**) Schematic illustration showing the fabrication processes of the FTCS-PDA/BNC aerogel membrane. (**b**) SEM image of PDA particles with a diameter of ~1 μm. (**c**) Water contact angle images of PDA/BNC aerogel membrane before and after FTCS treatment. Optical images of pristine BNC aerogel membrane (**d**) and FTCS-PDA/BNC aerogel membrane (**h**). Top surface SEM images of pristine BNC aerogel membrane (**e** and **f**) and FTCS-PDA/BNC aerogel membrane (**i** and **j**). Cross-section SEM images of pristine BNC (**g**) and FTCS-PDA/BNC (**k**) aerogel membranes.

7.3.2 Optical and photothermal conversion properties

In PMD membranes, high light absorption is essential for light-to-heat conversion. The optical transmittance and reflectance of the pristine BNC and FTCS-PDA/BNC membranes were measured in the range of 450–750 nm (**Figure 7.2a,b**). The pristine BNC exhibited a light transmittance of ~59% and a reflectance of ~11%, leading to a light extinction of ~30%. In contrast, after PDA particles were loaded, FTCS-PDA/BNC showed extremely low light transmittance (~0%), and reflectance (~2%), which resulted in a high light extinction (~98%) in the visible range. Such a high light extinction of the FTCS-PDA/BNC membrane, attributed to the superb light absorption of PDA particles inside the BNC network, results in excellent light-to-heat conversion by the bilayered membrane.

Besides its light absorption, the photothermal conversion activity of a photothermal membrane determines its ability to transform direct solar light into thermal energy. In a test, the FTCS-PDA/BNC membrane was exposed to simulated solar light at two illumination intensities: 1 kW m^{-2} (~1 sun) and 9 kW m^{-2} (~9 suns). As indicated by IR images (**Figure 7.2c**), the surface temperature of FTCS-PDA/BNC membrane increased rapidly from ~24ºC to ~78ºC during 10 seconds under 1 sun, and increased to ~256ºC during 40 seconds under 9 suns; both temperatures then remained constant over the remainder of the 120 seconds duration of the test (**Figure 7.2d**). In contrast, over 120 seconds, the surface temperature of pristine BNC membrane slowly increased from ~24ºC to ~29ºC under 1 sun and to ~39ºC under 9 suns. For PMD membranes, high under-water surface temperature increase of the membrane is essential for their performance. Therefore, the photothermal conversion activity of the FTCS-PDA/BNC membrane under ambient temperature water (20ºC, 8 mm distance from the membrane surface to the air/water interface) was monitored (**Figure 7.2e**). Under water, after 600 seconds illumination, the pristine BNC membrane showed a surface

equilibrium temperature of ~24ºC under 1 sun, and ~26ºC under 9 suns. In stark contrast, the FTCS-PDA/BNC membrane exhibited much higher surface equilibrium temperatures of ~33ºC under 1 sun and ~52ºC under 9 suns.

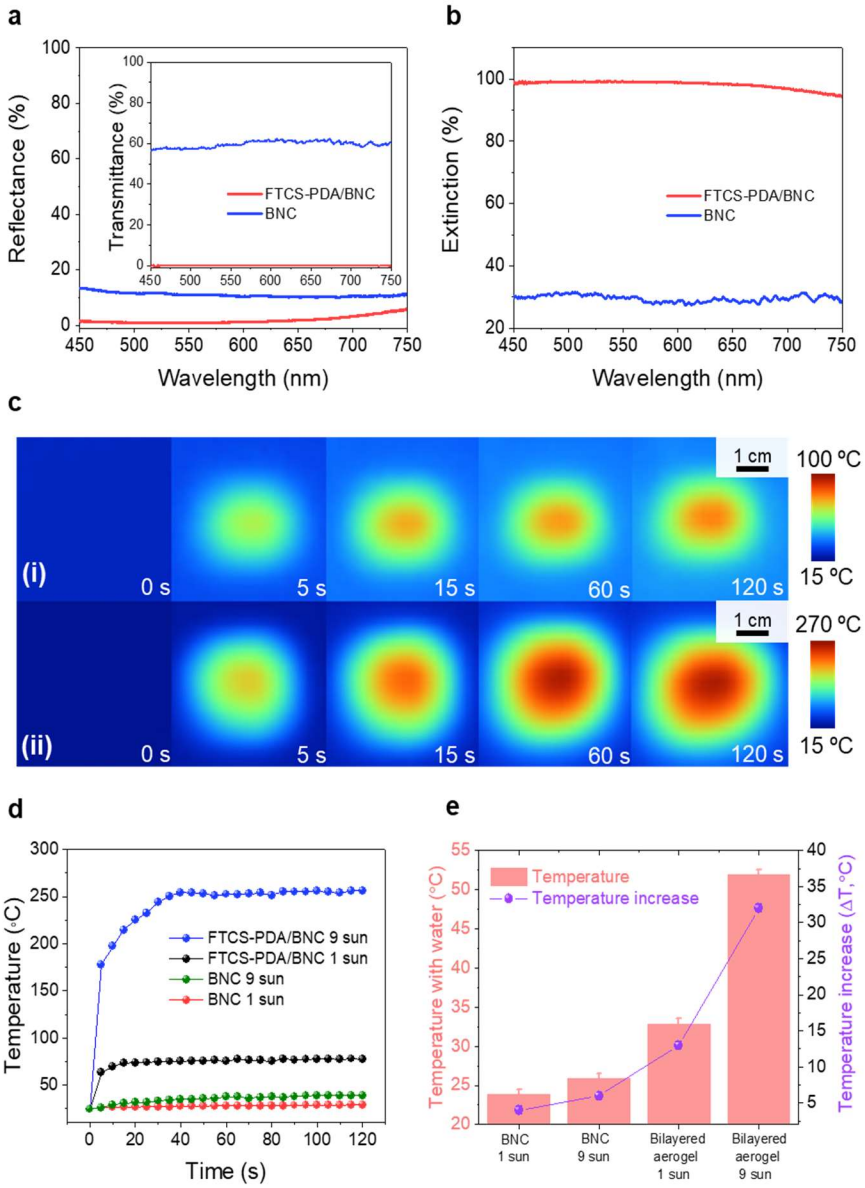

Figure 7.2 Optical properties of the bilayered aerogel membranes. (**a**) Light reflectance and transmittance of pristine BNC and FTCS-PDA/BNC aerogel membranes. (**b**) Light extinction of pristine BNC and FTCS-PDA/BNC aerogel membranes. (**c**) IR camera images of FTCS-PDA/BNC membrane over 120 seconds under two light irradiations: 1 kW m^{-2} (**i**) and 9 kW m^{-2} (**ii**). (**d**) Temperature increase of dry pristine BNC and dry FTCS-PDA/BNC aerogel membranes under the two light irradiations. (**e**) Temperature (left y axis) and temperature increase (right y axis) of pristine

BNC and FTCS-PDA/BNC aerogel membranes with water on top (water thickness = 8 mm) under the two light irradiations.

7.3.3 Photothermal membrane distillation

The PMD tests were carried out in a direct contact membrane distillation (DCMD) module with a solar simulator (**Figure 7.3a** and **Figure 7-S5**). Highly saline water (0.5 M NaCl, 20ºC) at ambient temperature was used as the feed water and circulated on top of the membrane at a flow rate of 3.6 mL min^{-1}. On the other side of the membrane, the distillate (DI water, 20ºC) was circulated at a flow rate of 16.2 mL min^{-1}, and the amount of collected water was quantified continuously using a balance. Pristine BNC treated with FTCS (FTCS-BNC) was used as the control membrane for comparison. Under 1 sun irradiation, the FTCS-PDA/BNC membrane achieved a water flux of 1.0 kg m^{-2} h^{-1} (**Figure 7.3b**), 10 times higher than that of the FTCS-BNC membrane (0.1 kg m^{-2} h^{-1}). With higher light power density (9 sun), the water flux of the FTCS-PDA/BNC membrane increased to 9.4 kg m^{-2} h^{-1} (**Figure 7.3b**), 23 times higher than that of the FTCS-BNC membrane (0.4 kg m^{-2} h^{-1}). Over 5 cycles (1 hour for each cycle), the water permeate fluxes from FTCS-PDA/BNC membrane remained stable under both solar irradiation conditions (**Figure 7.3c**). The SE/CW efficiencies (η) were calculated to be 68% and 72% for FTCS-PDA/BNC membrane under 1 sun and 9 sun respectively, much higher than those of FTCS-BNC membrane under identical irradiations (**Figure 7.3d**). These efficiencies are comparable to the SE/S efficiencies from previous interfacial steam evaporators (~60–90%),[437, 439] but significantly higher than their SE/CW efficiencies (~30%) when condensation and collection systems were employed.[441]

Both the permeate flux (1.0 kg m^{-2} h^{-1}) and the SE/CW efficiency (68%) of FTCS-PDA/BNC membrane are also noticeably higher than previously reported PMD membranes when treating ambient temperature feed water under similar irradiations (**Figure 7.3e**). For

example, a PDA-coated PVDF (PDA-PVDF) membrane achieved a 0.49 kg m^{-2} h^{-1} flux with an efficiency of 45% under 0.75 sun[93], while a carbon black-PVDF (CB-PVDF) composite membrane showed a flux of 0.22 kg m^{-2} h^{-1} and an efficiency of 21% under 0.7 sun[21]. The higher permeate flux and SE/CW efficiency of FTCS-PDA/BNC membrane can be attributed to three mechanisms: (1) The optimized PDA particle size allows better light absorption, and the *in situ* incorporation of PDA particles in the BNC matrix during its bacteria-mediated growth enables a higher density of PDA in the membrane surface. (2) The BNC membrane has higher vapor permeability than PVDF membranes. The greater porosity of the BNC membrane (98%) than that of benchmark PVDF membranes (50–70%)[446, 448] helps to reduce mass transport resistance and increase permeability. It has been reported that the intrinsic permeability of BNC is 52% higher than that of PVDF membrane.[76] (3) Conductive heat loss from the membrane top surface to the distillate is decreased by the higher porosity and lower thermal conductivity of the BNC aerogel structure. The thermal conductivity of BNC aerogel (0.027 W m^{-1} K^{-1}) is significantly smaller than that of the benchmark PVDF membrane (0.089 W m^{-1} K^{-1}), and even close to the thermal conductivity of air at room temperature (0.024 W m^{-1} K^{-1}).[76, 398] This lower conductive heat loss helps to maintain a high temperature gradient across the membrane, which facilitates a larger vapor pressure difference and mass transport driving force.

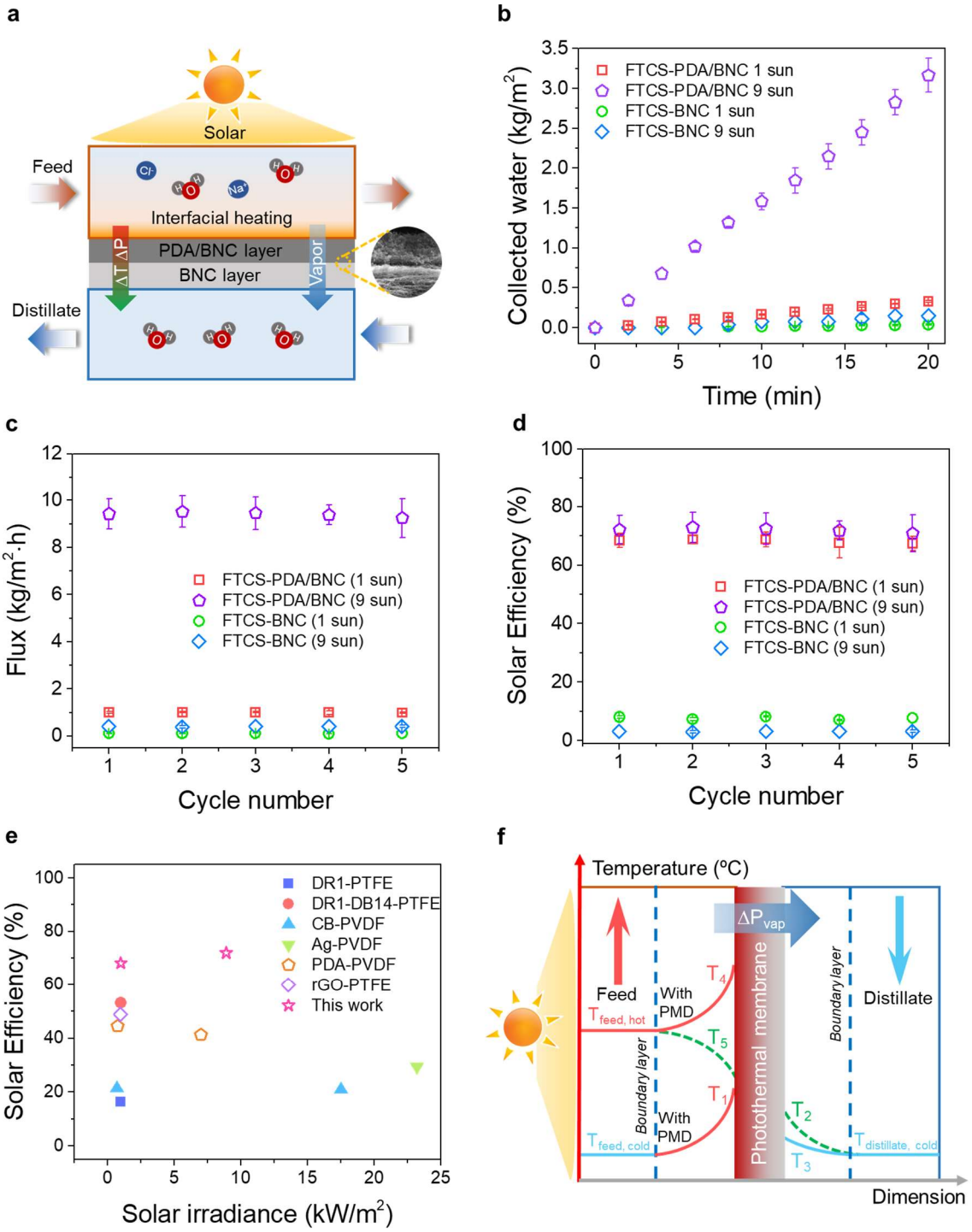

Figure 7.3 Photothermal membrane distillation (PMD) tests. (**a**) Schematic showing the PMD system using a bilayer FTCS-PDA/BNC aerogel membrane. (**b**) The collected water (kg m^{-2}) from FTCS-BNC and FTCS-PDA/BNC aerogel membranes during PMD tests under two light irradiations: 1 kW m^{-2} and 9 kW m^{-2}. (**c**) Water fluxes of FTCS-BNC and FTCS-PDA/BNC aerogel membranes during 5 cycles of PMD tests. Each cycle lasted 1 hour. (**d**) Solar energy to collected water (SE/CW) efficiencies of FTCS-BNC and FTCS-PDA/BNC aerogel membranes during 5 cycles of PMD tests. (**e**) A comparison of SE/CW efficiencies between our work and previous PMD works using ambient

temperature feed water. DR1-PTFE: disperse red 1 (DR1) modified PTFE (polytetrafluoroethylene) membrane.[449] DR1-DB14-PTFE: DR1 and disperse blue 14 (DB14) modified PTFE membrane.[450] CB-PVDF: carbon black modified PVDF membrane.[21] Ag-PVDF: silver nanoparticles modified PVDF membrane.[85] PDA-PVDF: PDA coated PVDF membrane.[93] rGO-PTFE: reduced graphene oxide modified PTFE membrane.[451] (**f**) Schematic diagram of the temperature profile in PMD systems, including the use of ambient temperature or hot feed water, and photothermal membranes with or without a heat insulation layer.

7.3.4 Chemical and mechanical stability of the bilayered PMD membrane

The chemical and mechanical stability of FTCS-PDA/BNC membrane was further tested to show its robustness for long term PMD applications. After being exposed to solutions at three different pH values (pH 3, 7, and 10) and under vigorous shaking for 30 days, FTCS-PDA/BNC membrane did not show signs of disintegration or loss of the PDA particles from the surface (**Figure 7-S6a**). UV−Vis measurement confirmed that there was no detachment of PDA particles from the membrane after ultrasonication for 6 hours in a 35 ºC ultrasonication bath (**Figure 7-S6b**). After 5 cycles of PMD tests, the morphology and microstructure of the FTCS-PDA/BNC membrane remained unaltered, as indicated by SEM observation (**Figure 7-S6c**). The contact angles of the FTCS-PDA/BNC membrane remained high and showed less than 2% variation during over 5 cycles, confirming the excellent and stable wetting resistance of the membrane (**Figure 7-S6d**). The stable hydrophobicity, owing to the strong covalent Si-O bond from the silanization reaction, prevents the deformation of membrane into hydrogel during PMD. The salt rejection was larger than 99.9% over 5 cycles of PMD tests using saline water (**Figure 7-S6d**). Our previous study showed that PDA particles deposited into BNC matrix *via* vacuum filtration was unstable under shaking, while the *in situ* growth strategy enabled BNC nanofibrils to strongly entangle the PDA particles and mechanically lock them in the fibril network.[398] The remarkable stability of FTCS-PDA/BNC membrane lessens concerns of the possible detachment of photothermal materials

from the membrane surface, and also makes the membrane promising for long term PMD applications.

7.3.5 Temperature profiles in a PMD system

In a PMD system, the temperature profile at the local membrane surface is different from that in conventional MD systems. **Figure 7.3f** illustrates the temperature profile in a PMD system, including the use of ambient temperature or hot feed water, and photothermal membranes with or without a heat insulation layer. When PMD uses ambient temperature feed water, the membrane surface temperature increase (T_1) at the feed side results only from the photothermal activity of the membrane. Therefore, solar energy is the primary energy source for such a configuration. Without a heat insulation layer, the membrane surface temperature at the distillate side (T_2) can be close to T_1 at the feed side due to conductive heat transport, making the temperature gradient (ΔT), and consequently the vapor pressure gradient (ΔP) between the two sides of the membrane to be low. The addition of a heat insulation layer at the bottom of the photothermal layer helps to minimize the conductive heat loss from the feed side to the distillate side, which lowers the distillate side's membrane surface temperature (T_3) and offers a larger ΔT to facilitate faster vapor transport. In PMD applications, the combination of photothermal membranes and low grade heat energy sources, such as waste heat from large power plants and oil and gas recovery systems, can further increase PMD's efficiency due to less heat loss from the membrane surface to the feed water. The PMD performance of the FTCS-PDA/BNC membrane was also tested with feed water temperatures of 45 ºC and 65 ºC, simulating, respectively, the temperatures in the condenser streams of U.S. power plants[452] and in produced water from oil and gas recovery systems[432] (**Figure 7-S7**). With 45 ºC and 65 ºC feed water, the FTCS-PDA/BNC membrane achieved

fluxes of 9.1 and 16.7 kg m^{-2} h^{-1} with SE/CW efficiencies of 81.3% and 91.9%, respectively. For a PMD system combined with hot feed water, the membrane surface temperature (T_4 in **Figure 7.3f**) is improved from T_1. In addition, the surface temperature increase from photothermal activity alleviates the temperature polarization effect that occurs in conventional MD (T_5). The heat flux in PMD systems with different categories is summarized in **Figure 7-S8a, b, and c**.

7.3.6 Solar photothermal self-disinfection

In water purification filtration processes, biofouling decreases membrane performance in the long term.[453] In conventional MD, biofouling can cause vapor-pressure depression due to the very small pore structure of the biofouling layer.[454] Herein, we show that the FTCS-PDA/BNC membrane can effectively kill bacteria on the membrane surface under light illumination during PMD operation. To test the bactericidal ability, the FTCS-PDA/BNC membrane was first immersed into a solution containing *E. coli* bacteria (>324 live cells/mL) to simulate an extreme situation of membrane operation in water contaminated with bacteria (**Figure 7.4a**). We employed fluorescence live/dead staining to investigate the bactericidal efficacy of the membrane. In this control experiment under dark conditions, after 1 hour, a substantial amount of live bacteria was observed on the membrane surface, as indicated by the green fluorescence (**Figure 7.4a1**) and a SEM image of the membrane surface (**Figure 7.4a3**), and no dead bacteria were detected, as indicated by the absence of red fluorescence (**Figure 7.4a2**). Then, to simulate *in situ* PMD operation (**Figure 7.4b**), light irradiation (1 kW m^{-2}) was applied to the membrane in contact with water containing bacteria. After 1 hour, compared to the previous condition (*i.e.,* before the PMD operation), fewer live bacteria were observed on the membrane (**Figure 7.4b1**), while dead bacteria

increased significantly (**Figure 7.4b2**). A SEM image indicated the presence of both live bacteria (green arrow) and dead bacteria (red arrow) on the membrane surface (**Figure 7.4b3**). The increase in dead bacteria on the membrane surface is attributed to the photothermal activity of PDA particles and the resulting higher local surface temperature under light illumination. It should be noted that not all the bacteria could be killed during *in situ* PMD, possibly due to the continuous attachment of new live bacteria from the water onto the membrane surface. However, the observed microbial inactivation suggests locally high temperatures on the membrane surface, which were enough to partially kill *E. coli* adhered to the film. To kill the entire microorganisms on membrane, the feed water was drained, and the membrane was further exposed to light irradiation (1 kW m^{-2}) (**Figure 7.4c**). After just 10 minutes exposure, the bacteria on the FTCS-PDA/BNC membrane exhibited only red fluorescence (dead bacteria) and no live bacteria were observable (**Figure 7.4c1-3**), which indicated that the photothermal activity and the associated temperature rise of the FTCS-PDA/BNC aerogel membrane without water on top was sufficient to kill all the bacteria on the surface. **Figure 7.4d** shows that after washing the membrane in DI water for 5 minutes, no live or dead bacteria was detectable on the membrane surface. This result indicates that the dead bacteria on membrane surface can be easily removed. Thermogravimetric analysis (TGA) confirmed that the chemical composition of the FTCS-PDA/BNC membrane did not alter much after the bactericidal treatment (**Figure 7-S9**). Complementary tests using FTCS-BNC membrane as a control showed that neither light alone nor the FTCS coating alone killed bacteria within the experimental time (**Figure 7-S10**). Therefore, the excellent bactericidal ability of the FTCS-PDA/BNC membrane was mainly attributed to the photothermal activity of PDA particles and the associated high membrane local temperature. This demonstrates the excellent anti-biofouling performance of the FTCS-PDA/BNC

membrane upon light exposure, showing good promise for long term water purification applications. In addition, the solar photothermal disinfection property of the FTCS-PDA/BNC membrane can be used for water disinfection when treating bio-contaminated water.

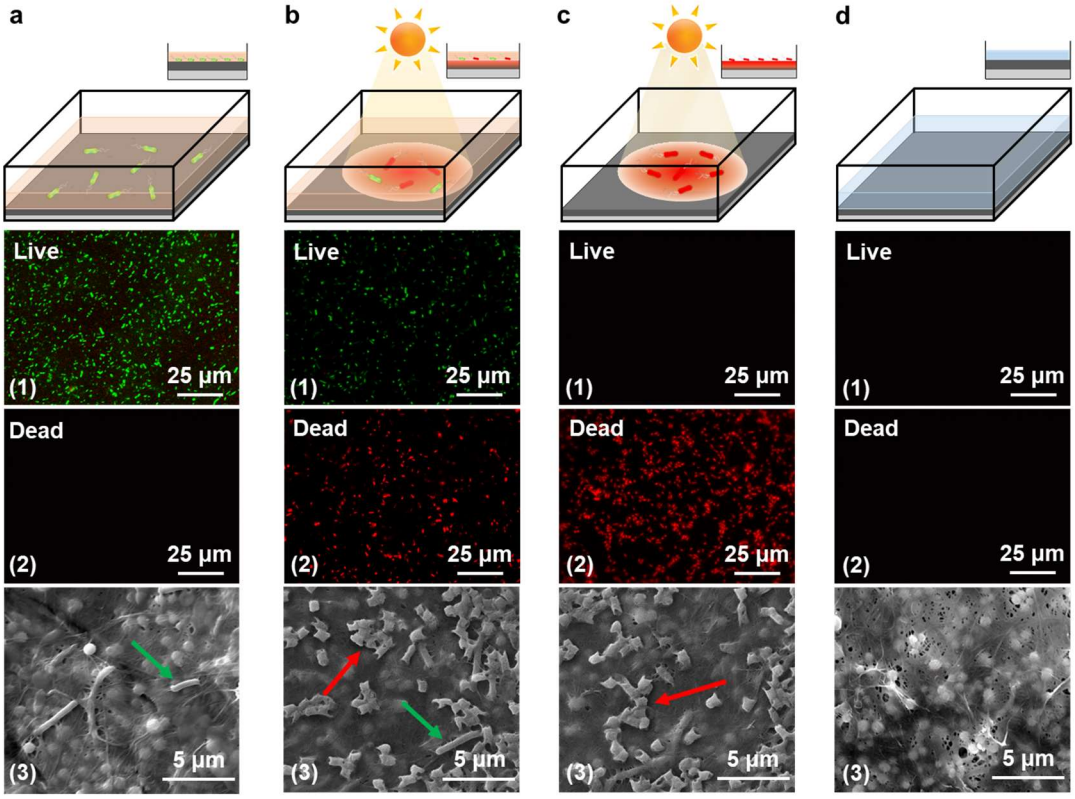

Figure 7.4 Self-disinfection activity measurements. Schematic, fluorescence, and SEM images of (**a**) FTCS-PDA/BNC membrane after exposure to water contaminated with *E. coli* for 1 hour, (**b**) FTCS-PDA/BNC membrane after *in situ* PMD operation for 1 hour with water contaminated with *E. coli*, (**c**) FTCS-PDA/BNC membrane after the water contaminated with *E. coli* was drained from the top surface, and the membrane was exposed to solar light (1 kW m^{-2}) for 10 minutes, (**d**) FTCS-PDA/BNC membrane after exposure to light and washing using DI water.

7.4 Conclusions and environmental implications

Here, we demonstrate the high performance of a bilayered FTCS-PDA/BNC membrane for PMD. Both PDA and BNC are biodegradable and biocompatible, so that this membrane can be an excellent choice for minimizing non-degradable polymeric wastes.[398]

The bilayered membrane achieved a permeate flux of 1.0 kg m^{-2} h^{-1} under 1 sun irradiation, with a high SE/CW efficiency (68%). The superb optical absorption and photothermal conversion properties of PDA particles loaded inside BNC matrix provide a high transmembrane temperature difference and driving force for vapor transport. The thermally-engineered strategy of using a highly porous and low thermally conductive BNC layer facilitates high vapor permeability and inhibits conductive heat loss from the feed side to the distillate side. The strong chemically-bonded fluorosilane functional groups on the membrane surface allow only vapor transport and provide high salt rejection (>99.9%). Furthermore, the self-disinfection activity of the bilayered membrane under solar light effectively resists live microbial accumulations and their biofilm formation on the membrane, which increases the longevity of membrane performance and reduces the membrane replacement cost. Using renewable solar energy, the bilayered membrane with biocompatible materials (both PDA and BNC) holds great promise for easy, scalable, sustainable, and decentralized water purification to alleviate water scarcity, especially for households or resilient communities in remote, rural, or disaster areas.

Acknowledgments

We are grateful for the support received from the National Science Foundation Environmental Engineering Program (CBET-1604542). We wish to thank the Institute of Materials Science and Engineering (IMSE) and Nano Research Facility (NRF) in Washington University in St. Louis for the use of XPS and SEM, respectively. We also thank Prof. James Ballard for carefully reviewing our manuscript. Lastly, we thank the Environmental NanoChemistry Group members for providing valuable discussions and suggestions for this paper.

Supporting information for Chapter 7

7-S1. Synthesis of FTCS-PDA/BNC bilayered aerogel membrane

To synthesize a BNC hydrogel, first, #1765 medium (16 ml), containing 2% (w/v) glucose, 0.5% (w/v) yeast extract, 0.5% (w/v) peptone, 0.27% (w/v) disodium phosphate and 0.5% (w/v) citric acid, was used to culture *Gluconacetobacter hansenii* (ATCC®53582) in test tubes at 30 °C under shaking at 250 rpm. The bacterial culture solution (3 ml, incubated 3 days) was added to the #1765 medium (5 ml) to make a total 8 ml of bacterial growth solution. The solution was subsequently transferred to a 6 cm petri dish and incubated at room temperature without disturbance. After 5 days, a thin BNC hydrogel (~220 μm of thickness) was obtained.

To ensure a good overlap of PDA particles' optical absorption with the solar spectrum in the visible range (Supplementary Information Fig. 1), PDA particles were synthesized with an optimal size (~1 μm diameter).[398] Ammonia solution (NH_4OH, 0.14 ml, 28–30%) was mixed with 31.5 ml of DI water (> 18.2 MΩ·cm), followed by addition of 14 ml of ethanol to the above mixture. After stirring for 30 minutes, dopamine hydrochloride solution (3.5 ml, 0.05 g ml^{-1}) was added into the above solution. After stirring for 30 hours at room temperature, the PDA particles were collected by centrifugation (7000 rpm, 20 min) and washed three times with water and dispersed in DI water (40 ml).

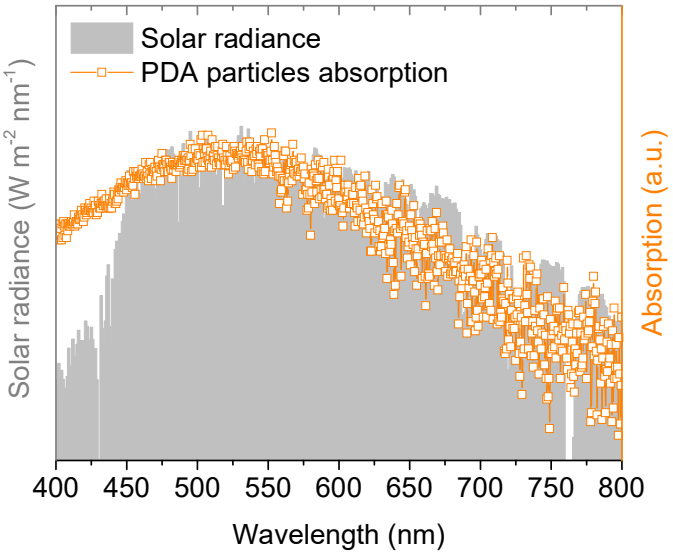

Figure 7-S1 Solar spectral irradiance (AM 1.5 G) (gray, left Y axis) and the absorption of PDA particles (orange, right Y axis).

To synthesize the bilayered PDA/BNC hydrogel membrane, PDA particles in DI water was centrifuged, collected, and dispersed in bacterial growth medium (5 ml), then added on top of the previously synthesized BNC hydrogel. After 24 hours, a thin PDA/BNC layer (~30 μm) formed. The bilayered hydrogel was then harvested and washed in boiling water for 2 hours, then dialyzed in DI water for two days. The purified PDA/BNC bilayer was freeze-dried overnight to obtain the PDA/BNC bilayered aerogel membrane. Lastly, to make the aerogel membrane hydrophobic, the PDA/BNC aerogel membrane was exposed to (tridecafluoro-1,1,2,2-tetrahydrooctyl)-trichlorosilane (FTCS) vapor at 70°C for 6 hours, resulting in a coverage of hydrophobic FTCS fluorosilane functional groups on the PDA/BNC aerogel membrane.[76, 410]

7-S2. Characterization of FTCS-PDA/BNC bilayered aerogel membrane.

To quantify the porosity (ε) of the PDA/BNC membrane, a gravimetric method was used.[77, 446] Three 2 cm × 2 cm pieces were cut from a PDA/BNC membrane, weighed dry, and then submerged in DI water for 1 week before being taken out and weighed again wet. The porosity was calculated using the equation below to get the average values for triplicate samples:

$$\varepsilon = \frac{w_2 - w_1}{\rho_w V}, \quad \textbf{(eq 7-S1)}$$

where ε is the porosity (%), w_2 (g) is the weight of the wet membrane, w_1 (g) is the weight of the dry membrane, ρ_w (g/cm^3) is the liquid density (DI water), and V (cm^3) is the volume of the membrane. It should be noted that the porosity of the PDA/BNC membrane is the average porosity of the pristine BNC layer and the PDA-loaded BNC layer. Due to similar synthesis methods, we anticipate that the BNC layer in the PDA/BNC membrane would have a similar porosity to the pristine BNC membrane.

The weight percentage of PDA particles in terms of the entire PDA/BNC membrane was calculated by measuring the weight of pristine BNC (w_{BNC}) membrane and PDA/BNC ($w_{PDA\text{-}BNC}$) membrane with the same size and the same thickness (**Figure 7-S2**):

$$PDA\ wt\% = \frac{w_{PDA/BNC} - w_{BNC}}{w_{PDA/BNC}}. \quad \textbf{(eq 7-S2)}$$

The PDA wt% in terms of the PDA/BNC layer of the PDA/BNC membrane was calculated using the following equation:

$$PDA\ wt\%' = \frac{w_{PDA/BNC} - w_{BNC}}{w_{PDA/BNC} - \frac{w_{BNC}}{Thickness_{BNC}} \times Thickness_{BNC\ Layer}}, \quad \textbf{(eq 7-S3)}$$

where $Thickness_{BNC}$ is the thickness of the pristine BNC membrane (~250 μm), and $Thickness_{BNC\ layer}$ is the thickness of the BNC layer in the PDA/BNC bilayer membrane (~220 μm).

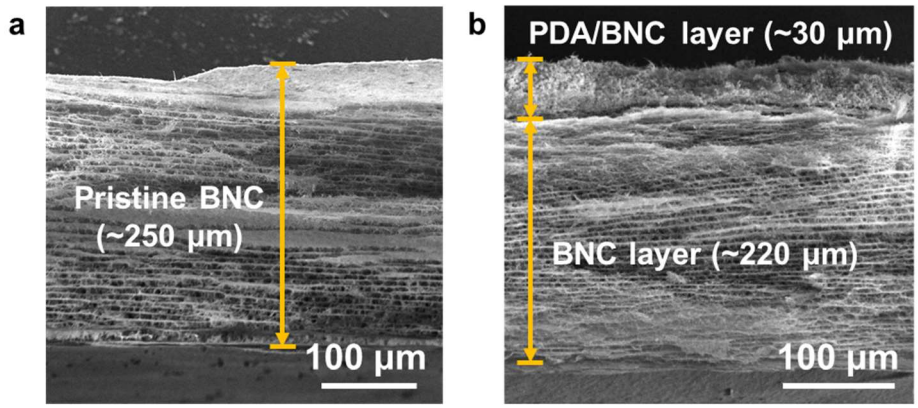

Figure 7-S2. SEM images showing cross-sections of the pristine BNC (a) and FTCS-PDA/BNC (b) aerogel membranes.

Scanning electron microscopy (SEM; OVA NanoSEM 230, FEI) was used to image the morphology and microstructure of the FTCS-PDA/BNC aerogel membrane surface and its cross-section at an acceleration voltage of 10 kV. The chemical composition of PDA and FTCS on the BNC surface were identified using an X-ray photoelectron spectroscopy (XPS, PHI 5000 VersaProbe II, Ulvac-PHI with monochromatic Al Kα radiation (1486.6 eV)) and a Raman spectroscope (inVia confocal Raman spectroscope, Renishaw, equipped with 514 nm wavelength diode laser). For XPS measurements, Al Kα monochromator radiation was used to measure the C 1s, F 1s, and N 1s spectra of the FTCS-PDA/BNC membrane. The newly appeared C 1s peaks at 291.4 and 293.6 eV corresponded to the $–CF_2–$ and $–CF_3$ functional groups of FTCS, respectively (Figure 7-S3a).[426] The increased peak intensity at 399.9 eV in N 1s indicated the indole or pyrrole N-H bonds from PDA particles (Figure 7-

S3c).[455-456] In the Raman spectra (Figure 7-S3d), the two new peaks at 1350 and 1573 cm^{-1} correspond to the stretching and deformation of the catechol groups of PDA, respectively.[423] XPS and Raman results indicate successful loading of PDA particles and fluoro-silane coating in the FTCS-PDA/BNC membrane.

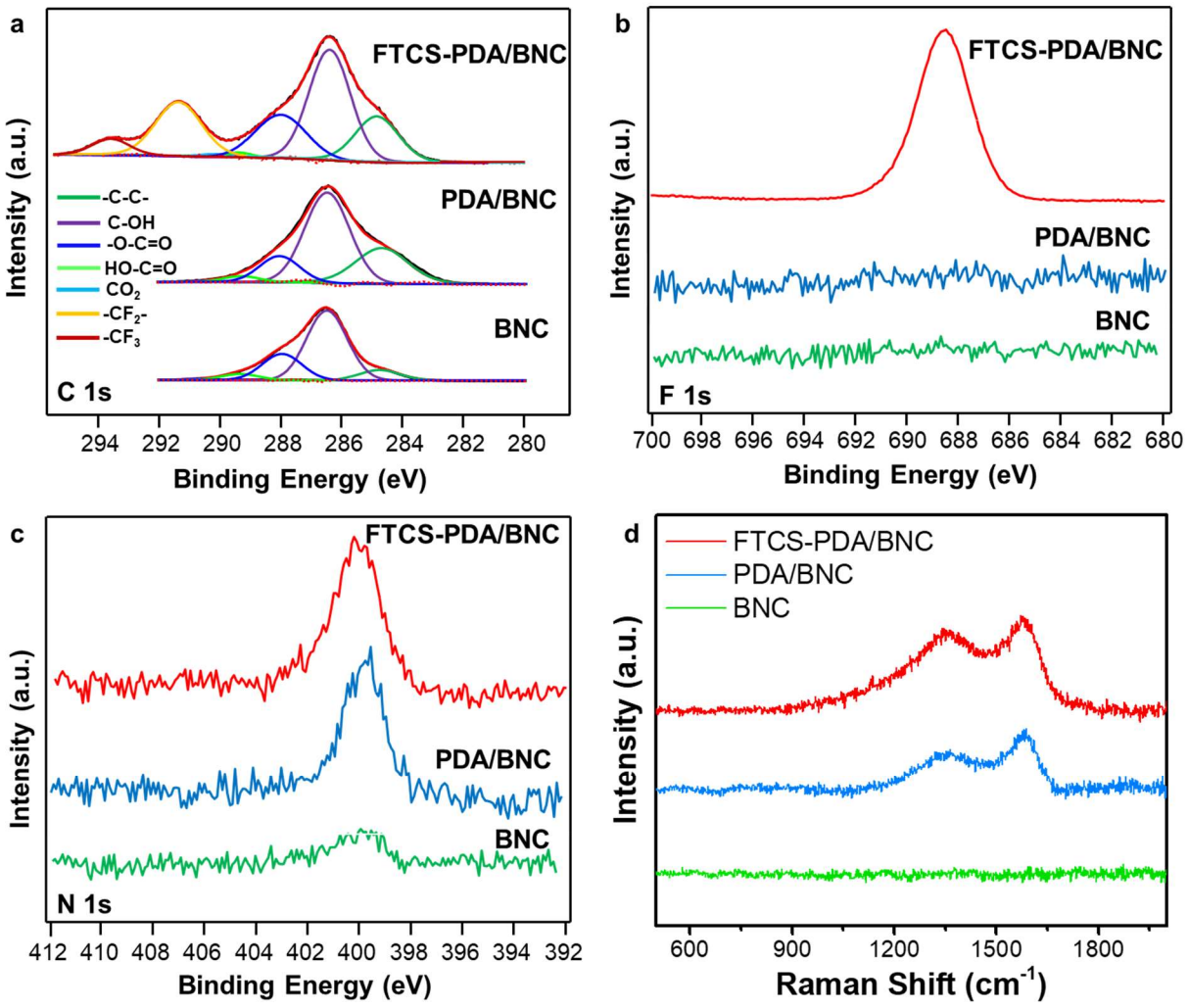

Figure 7-S3. XPS spectra of the pristine BNC, PDA/BNC, and FTCS-PDA/BNC, showing the C 1s (a), F 1s (b), and N 1s (c) peaks. Raman spectra of BNC, PDA/BNC, and FTCS-PDA/BNC (d).

The transmittance and reflectance of the pristine BNC and FTCS-PDA/BNC aerogel membranes were measured using a micro-spectrophotometer (QDI 302, CRAIC

Technologies) coupled to a Leica microscope (DM 4000M, Leica Microsystems). The surface temperatures of the pristine BNC and FTCS-PDA/BNC aerogel membranes were measured by an infrared camera (IR camera, Ti 100, FLUKE) after 600 secs light illumination using a solar simulator (Newport 66921 Arc Lamp) under two irradiations: 1 kW m^{-2} (1 sun) and 9 kW m^{-2} (9 sun), as measured by a spectroradiometer (SpectriLight ILT 950). Triplicate 1 cm × 1 cm pieces were cut from the membranes and measured. SI Fig. 4 shows the IR images of a pristine BNC membrane under two irradiations. The surface temperature of the membrane with water on top (water thickness = 8 mm) was monitored using a benchtop controller thermocouple probe (OMEGA CSI32K-C24, US) with a response time of 5 s and resolution of ±0.5 °C.

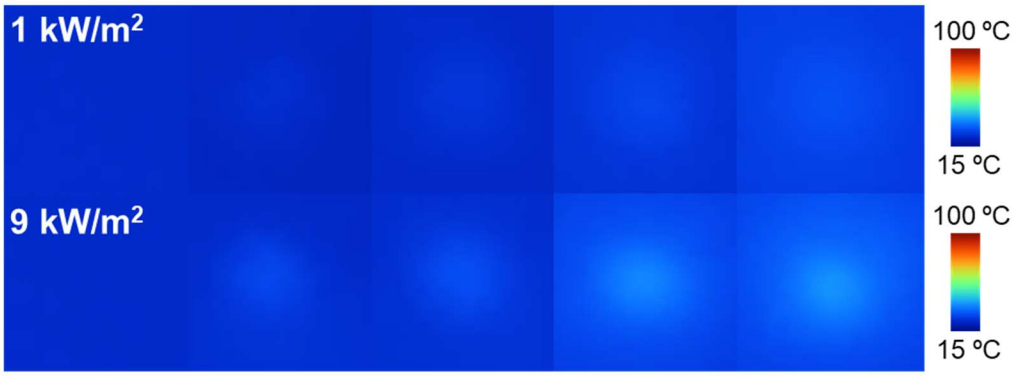

Figure 7-S4. IR **images** of a pristine BNC membrane under two irradiations: 1 kW m^{-2} (top) and 9 kW m^{-2} (bottom).

7-S3. Photothermal membrane distillation tests.

The photothermal membrane distillation performance of FTCS-PDA/BNC aerogel membrane was tested in a direct contact membrane distillation (DCMD) module. The setup of the system is shown in Figure 7-S5. The membrane distillation module consists of a 2-mm-thick quartz window with a diameter of 5 cm on the feed side to allow light illumination.

A 1-mm-thick aluminum platform was placed in between the feed side and distillate side to support the membrane. The cross-flow velocities in the feed and distillate channels were 3.6 mL/min and 16.2 mL/min, respectively. The distillate flow rate was larger than the feed flow rate to minimize the temperature increase of the distillate. We used 0.5 M NaCl aqueous solution (ACS grade, BDH, PA) as feed water, stored in a 500-mL Erlenmeyer flask. DI water was used for the distillate stream at the bottom of the membrane. The 0.5 M salinity was chosen to mimic the average salinity of seawater.[413] The feed and distillate were continuously circulated through the membrane module using two peristaltic pumps, respectively, a Welco WPX1-F1 and a Stenner 85MHP5. The flow rate of the feed water was changed by monitoring the DC supply (Extech 382203) controlling the feed pump. The distillate reservoir was kept on a weighing balance (Sartorius ELT402) to measure the collected permeate at 2 minute intervals. The distillate reservoir was capped during MD tests to reduce the effects of evaporation. During PMD tests, the light from the solar simulator (Newport 66921 Arc Lamp) was oriented perpendicularly to the membrane surface using a mirror. The light intensities at the membrane surface were measured to be 1 kW/m^2 and 9 kW/m^2 (focused using a magnifying lens) by a spectroradiometer (SpectriLight ILT 950). The solar energy-to-collected water (SE/CW) efficiency used in this work is defined as the ratio of the energy used in generating water flux in PMD over the total energy input by solar irradiation, and is calculated by the following equation:

$$\eta = \frac{\dot{m} H_{vap}}{I}, \qquad \textbf{(eq 7-S4)}$$

where η is the solar efficiency, $\dot{m}$ is the permeate flux (kg m^{-2} h^{-1}), H_{vap} is the enthalpy change (2,454 kJ kg^{-1}) from liquid to vapor, and I is the power density of the incident light

(kJ m^{-2} $-h^{-1}$).[21] The SE/CW efficiency used in this study is also the gain output ratio (GOR) or the overall solar energy efficiency of the system.

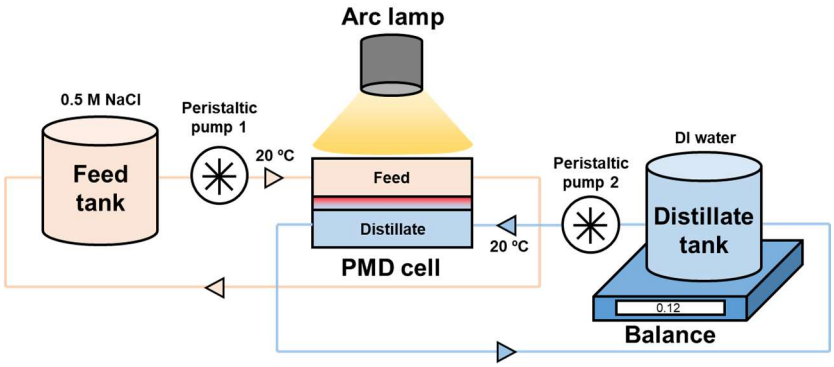

Figure 7-S5. Schematic of the photothermal direct contact membrane distillation system.

7-S4. Chemical and mechanical stability tests.

The chemical and mechanical stability of FTCS-PDA/BNC aerogel membrane was further tested to show its robustness for long term PMD applications. After being exposed to solutions at three different pH values (pH 3, 7, and 10) under vigorous shaking for 30 days (VWR Orbital Shaker, Model 3500), FTCS-PDA/BNC membrane did not show signs of disintegration or loss of the PDA particles from the surface (Figure 7-S6a). UV−Vis measurement confirmed that there was no detachment of PDA particles from the membrane after ultrasonication for 6 hours in a 35 ºC ultrasonication bath (Figure 7-S6b) (Fisher Scientific, Model FS6). Triplicate 1 cm × 1 cm membrane pieces were tested. After 5 cycles of PMD tests (1 cycle = 1 hour), the morphology and microstructure of the FTCS-PDA/BNC membrane remained unaltered, as indicated by SEM observation (Figure 7-S6c). The contact angles of the FTCS-PDA/BNC membrane, measured using a contact angle analyzer (Phoenix 300, Surface Electro Optics Co. Ltd), remained high and showed less than 2% variation over 5 cycles, confirming the excellent and stable wetting resistance of the membrane (Figure 7-S6d). A chloride probe (VWR 89231-632) was used to measure the salt concentration in both

the feed (C_{feed}) and distillate ($C_{distillate}$) during PMD tests, and the salt rejection calculated using the following equation was larger than 99.9% over 5 cycles of PMD tests using saline water:

$$Salt\ rejection\% = \frac{C_{feed} - C_{distillate}}{C_{feed}}, \quad \textbf{(eq 7-S5)}$$

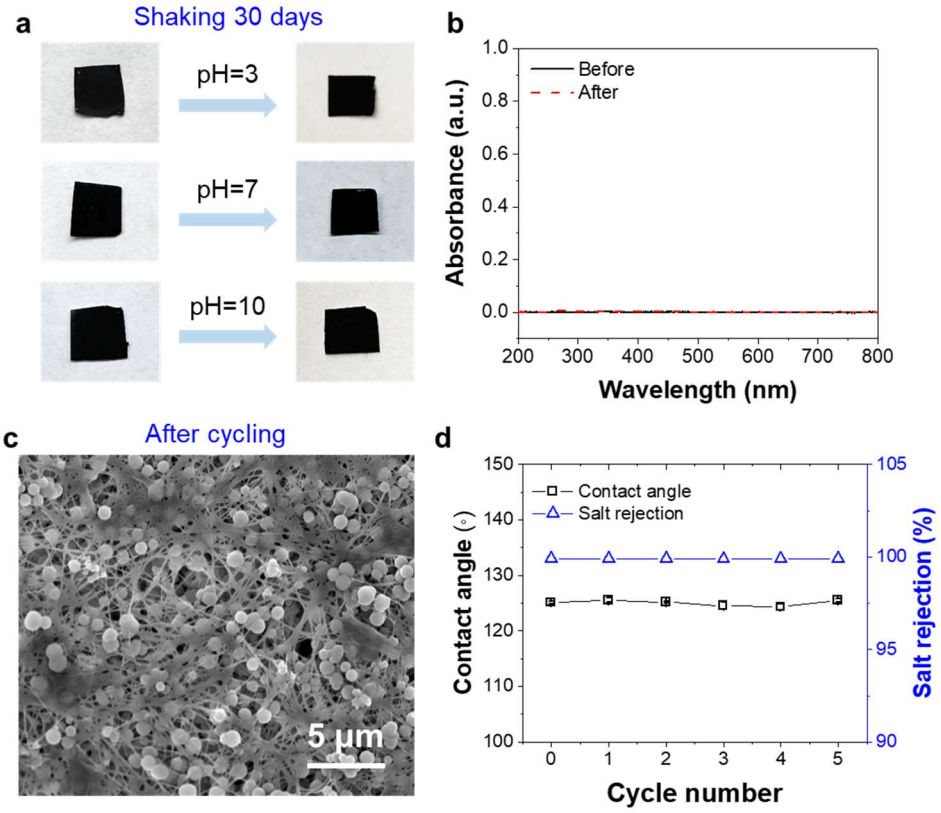

Figure 7-S6. Stability tests of FTCS-PDA/BNC membrane. (a) Optical images showing the FTCS-PDA/BNC membrane surface alteration after vigorous shaking for 30 days under three pH conditions. (b) UV−Vis absorbance spectra of FTCS-PDA/BNC membrane immersed solutions (at pH 7) before and after ultrasonic agitation for 6 hours in a 35ºC ultrasonication bath. (c) Surface morphology of FTCS-PDA/BNC membrane after 5 cycles of PMD tests (1 hour/cycle). (d) Alterations of contact angles and salt rejections of FTCS-PDA/BNC membrane during 5 cycles of PMD tests. Error bars from triplicate tests were smaller than the symbols.

7-S5. PMD tests with hot feed water.

In PMD applications, the combination of photothermal membranes and low grade heat energy sources, such as waste heat from large power plants and oil and gas recovery systems, can further increase PMD's efficiency due to less heat loss from the membrane surface to the feed water. Two hot feed water temperatures, 45 ºC and 65 ºC, were tested in PMD, respectively simulating the temperatures in condenser streams of U.S. power plants,[452] and in produced water from oil and gas recovery systems.[432, 457] The NaCl feed solution was heated to 45 ºC and 65 ºC using a hot plate (Thermo Scientific HP131225). Under dark condition, the FTCS-PDA/BNC membrane achieved water fluxes of 7.9 kg m^{-2} h^{-1} and 15.3 kg m^{-2} h^{-1} with 45 ºC and 65 ºC feed water, respectively (Figure 7-S7a), close to those of FTCS-BNC membrane (8.1 and 15.4 kg m^{-2} h^{-1}). With additional solar irradiation (1 sun), the fluxes of the FTCS-PDA/BNC membrane increased to 9.1 and 16.7 kg m^{-2} h^{-1} with 45 ºC and 65 ºC feed water, respectively. The higher permeate flux with additional solar light was attributed to the increased membrane surface temperature, which helped to alleviate temperature polarization effects in the boundary layer and increase the transmembrane temperature gradient. The solar energy to collected water (SE/CW) efficiencies with hot feed water (η') were calculated using the following equation modified from eq 7-S4:

$$\eta' = \frac{(\dot{m}_{with\ solar} - \dot{m}_{without\ solar}) \cdot H_{vap}}{I}, \qquad \textbf{(eq 7-S6)}$$

where $\dot{m}_{with\ solar}$ and $\dot{m}_{without\ solar}$ are the permeate fluxes (kg m^{-2} h^{-1}) under solar irradiation and dark conditions, respectively. The solar conversion efficiencies of FTCS-PDA/BNC membrane were 81.3% and 91.9% with 45 ºC and 65 ºC hot feed water, respectively (Figure 7-S7b), which are among the highest reported SE/CW efficiencies for PMD systems with hot water sources (Figure 7-S8d). As compared with PMD systems using ambient temperature feed water, the combination of PMD with low grade heat energy sources

can further increase the water purification rate and thermal efficiency of PMD, making it more reliable in real applications where these energy sources are available.

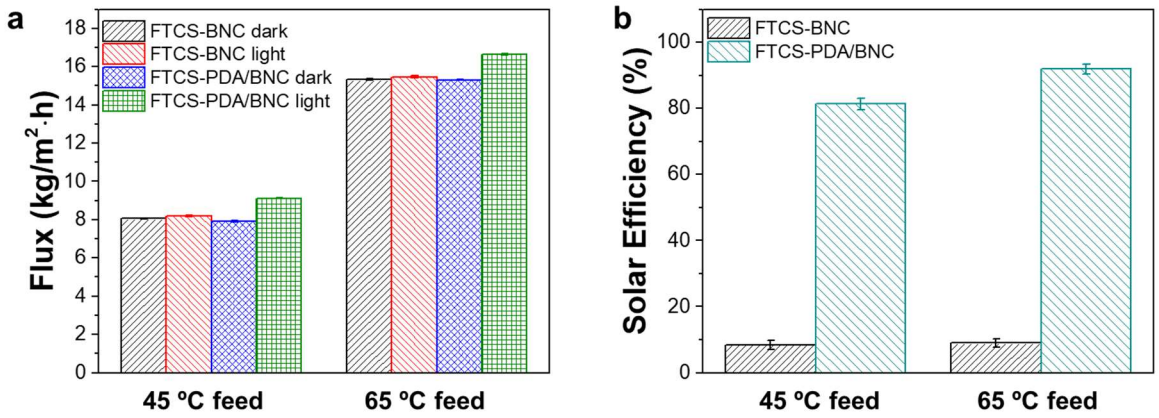

Figure 7-S7. (a) PMD fluxes of FTCS-PDA/BNC and FTCS-BNC membranes with hot feed water (0.5 M NaCl, 45 ºC and 65 ºC) under both dark and light (1 sun) conditions. (b) The SE/CW efficiencies of FTCS-PDA/BNC and FTCS-BNC membranes with hot feed water.

7-S6. Comparison of different PMD systems.

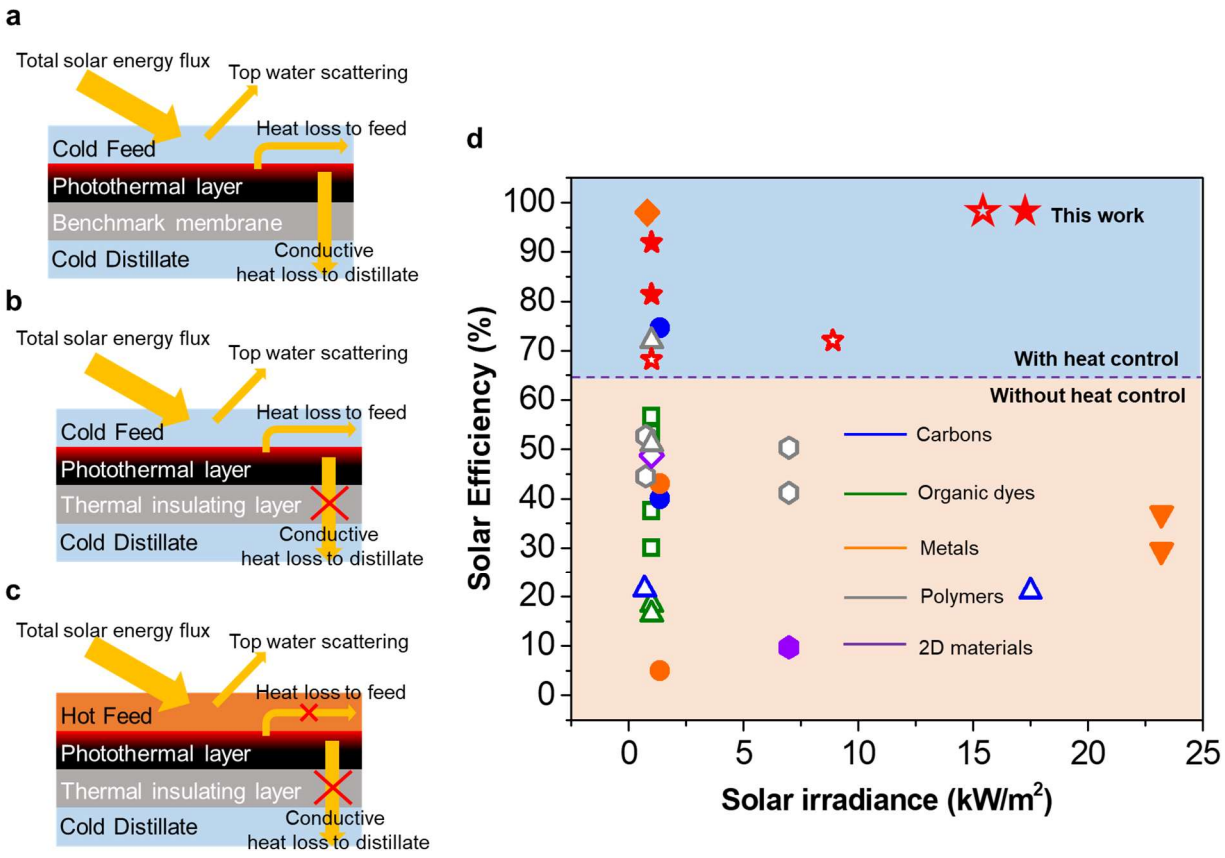

Figure 7-S8. Heat flux charts in PMD systems. (a) PMD using ambient temperature feed and distillate, and benchmark membranes coated with photothermal materials. (b) PMD using ambient temperature feed and distillate, and thermal insulating membranes coated with photothermal materials. (c) PMD using hot feed and ambient temperature distillate, and thermal insulating membranes coated with photothermal materials. (d) Comparison of SE/CW efficiencies among reported PMD systems. Current PMD membranes include photothermal materials such as carbon materials,[21, 458] organic dyes,[449-450, 459] metals,[85, 458, 460] polymers,[93, 461] and 2D materials[451, 462]. To increase the SE/CW efficiencies, various heat control strategies have been used, including (i) combining PMD systems with hot feed water (solid labels),[85, 458, 460, 462] (ii) using a heat insulating layer (this study), and (iii) using latent heat recovery systems.[461] The blue area in the chart includes the SE/CW efficiencies from PMD systems that use one of the heat control strategies as described above, while the orange area in the chart includes the SE/CW efficiencies from PMD systems that have no heat control strategies.

7-S7. Self-disinfection property measurement.

MG 1655 *E. coli* was grown in Luria−Bertani liquid medium at 37 ºC. All cultures were in 125 mL baffled shake flasks (25 mL working volume, shaking at 225 rpm). Cells in log phase (>324 live cells/mL) were harvested after 24 hours of incubation and then used for bactericidal tests. To identify the self-disinfection property of the FTCS-PDA/BNC membrane, four conditions were tested to simulate actual PMD processes: (i) a membrane contacted with water contaminated by bacteria, (ii) a membrane contacted with water contaminated by bacteria during PMD, (iii) a membrane illuminated by light after feed water had drained from the top of the membrane, and (iv) a membrane after washing in DI water. The FTCS-PDA/BNC membrane was submerged into solution containing MG 1655 *E. coli* for 1 hour to test condition (i). To test condition (ii), FTCS-PDA/BNC membrane with E. coli contaminated water on top was exposed to simulated sunlight (1 kW m^{-2}) for 1 hour. To test condition (iii), after being submerged in *E. coli* contaminated water for 1 hour, FTCS-PDA/BNC membrane was removed and exposed to simulated sunlight (1 kW m^{-2}) for 10 minutes. Condition (iv) was tested by washing FTCS-PDA/BNC membrane in DI water for 5 minutes after light illumination as in condition (iii). In each condition, the FTCS-PDA/BNC membrane after test was exposed to fluorescent dyes (Molecular Probes Live/Dead Bacterial cell viability kit, Thermo Fisher Scientific) for 30 minutes and then imaged under a Leica microscope (DM 4000M, Leica microsystems) to identify live (blue fluorescent filter, 340−380 nm) and dead (green fluorescent filter, 450−490 nm) cells. To show the stability of FTCS-PDA/BNC membrane during disinfection test, thermogravimetric analysis (TGA) was performed using a TA Instruments Q5000 IR thermogravimetric analyzer in nitrogen gas at a rate of 5 °C/min (Figure 7-S9). The FTCS-PDA/BNC membrane started to decompose at temperature around 300 °C, confirming its thermal stability during photothermal water

treatment applications, where the membrane temperature is usually <100 °C. Additional control self-disinfection tests using the FTCS-BNC membrane showed that it cannot kill bacteria after exposure to water contaminated with *E. coli* for 1 hour (Figure 7-S10a), or after *in situ* PMD operation for 1 hour with water contaminated with *E. coli* (Figure 7-S10b), or after the water contaminated with *E. coli* was drained from the top surface, and then exposed to solar light (1 kW m^{-2}) for 10 minutes (Figure 7-S10c). These control experiments indicated that neither light alone nor the FTCS coating alone killed bacteria within the experimental time. Therefore, the bactericidal ability of the FTCS-PDA/BNC membrane was mainly attributed to the photothermal activity of PDA particles under solar light.

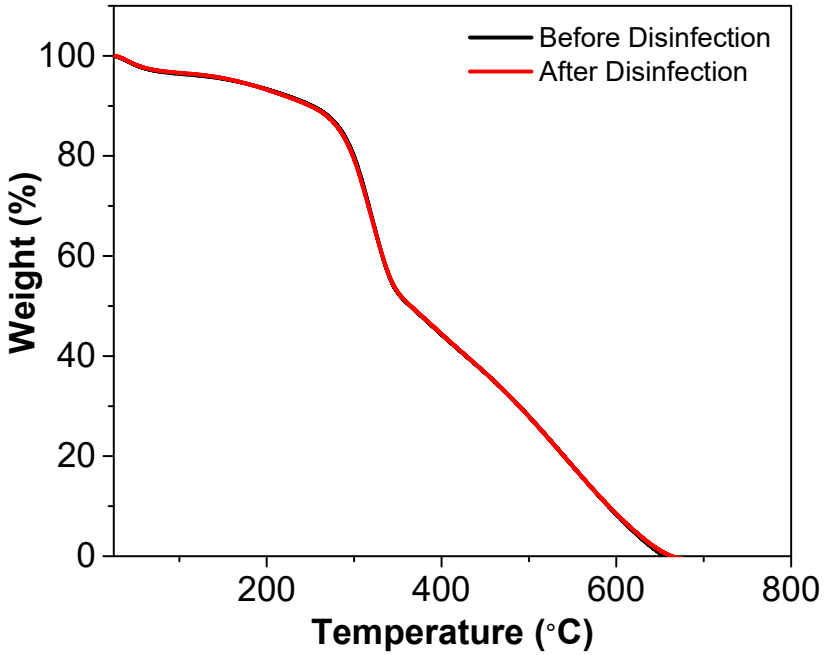

Figure 7-S9. TGA of FTCS-PDA/BNC membrane before and after self-disinfection tests.

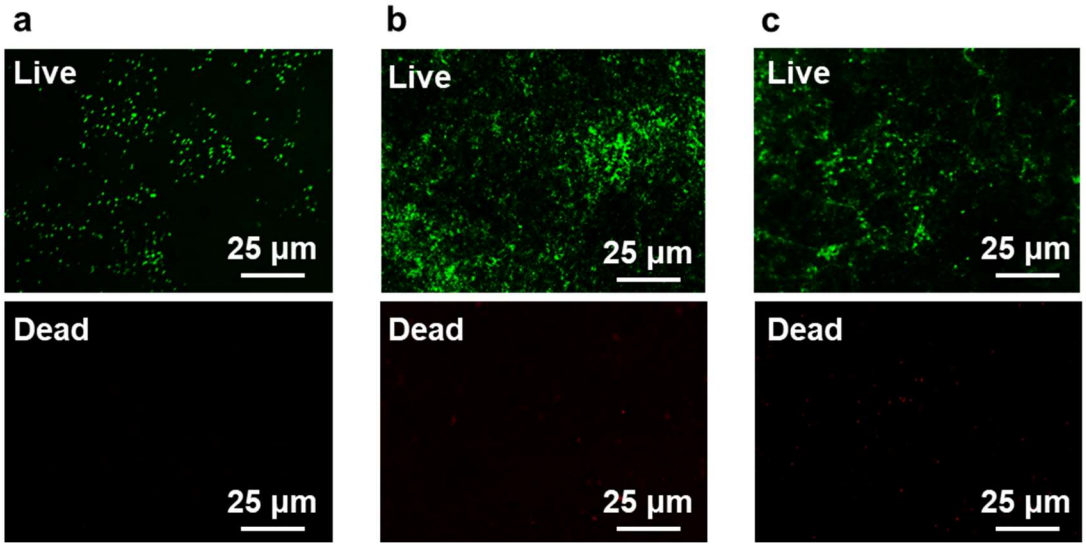

Figure 7-S10. Fluorescence images of (a) FTCS-BNC membrane after exposure to water contaminated with *E. coli* for 1 hour, (b) FTCS-BNC membrane after *in situ* PMD operation for 1 hour with water contaminated with *E. coli*, and (c) FTCS-BNC membrane after the water contaminated with *E. coli* was drained from the top surface, and then exposed to solar light (1 kW m^{-2}) for 10 minutes.

Chapter 8. Conclusions and future directions

8.1 Conclusions

To obtain a better understanding of the chemistry of nanoscale solids and organic matter in sustainable water management systems, this thesis has systematically investigated the solid–liquid interfacial interactions among nanoparticles and different water constituents (e.g., reactive species and organic matter) in water treatment or subsurface systems. Further, it has applied the knowledge obtained from fundamental mechanistic studies of nanoscale interfacial reactions to develop nanomaterial-based membranes for sustainable water treatment. Specifically, we have examined the surface chemistry of engineered nanoparticles in advanced oxidation processes (AOPs), the arsenic mobilization from arsenic-bearing iron sulfide minerals in managed aquifer recharge (MAR), the thermodynamic and kinetic parameters of iron (hydr)oxide nucleation on earth abundant mineral surfaces, and the applications of nature-inspired photothermal material for sustainable seawater desalination using membrane distillation (MD). Linking three engineered water management systems, **System 1** AOPs, **System 2** MAR, and **System 3** MD, provides a comprehensive understanding of the physicochemical transformation of nanomaterials that will enable a better control of their fate and transport. Ultimately, it will speed the development of next generation of the sustainable water treatment techniques based on nanotechnology.

Using **System 1**, we focused on investigating the surface chemistry of a model engineered nanomaterial, CeO_2 NPs, in a UV/H_2O_2 process with co-existing NOM. The findings indicated that before entering into AOPs, NOM stabilized CeO_2 NPs via surface complexation between the COO^- functional groups of NOM and CeO_2 surfaces, reversing the zeta potentials of CeO_2 NPs and maintaining the electrostatic repulsive forces between

them. After they entered into the UV/H_2O_2 treatment, the colloidal stability of CeO_2 NPs was reduced with neutralized zeta potentials of CeO_2 NPs and decreased electrostatic repulsive forces between NPs. NOM complexed with CeO_2 NPs acted as a protective layer, making the impacts of UV/H_2O_2 treatment insignificant in a short reaction period. In the long term, superoxide radicals dominated in neutralizing the surface charge of CeO_2, leading to the sedimentation of NPs. The new findings in **System 1** offer insights into the surface chemistry of ENMs in advanced water treatment processes where NOM and ROS are present.

Using **System 2**, we investigated arsenic mobilization in a MAR process operating in the presence of abundant oxyanions and dissolved organic matter. For oxyanions, phosphate showed time-dependent effects on arsenic mobility. In a short period (6 hours), relative to the control system that contained only sodium nitrate, phosphate increased arsenic mobility by promoting FeAsS dissolution. However, over a longer experimental time (7 days), phosphate decreased arsenic mobility by forming a greater extent of secondary minerals (maghemite, γ-Fe_2O_3, and phosphosiderite, $FePO_4 \cdot 2H_2O$) and offering more adsorption sites for arsenic. During the entire 7-day reaction, silicate increased the arsenic mobility, and bicarbonate decreased the arsenic mobility. For DOM, SRDOM decreased arsenic mobility in the short term (<6 hours) by inhibiting FeAsS dissolution, but increased arsenic mobility over a longer experimental time (7 days) by inhibiting secondary iron(III) (hydr)oxide precipitation and decreasing arsenic adsorption onto iron(III) (hydr)oxide. GISAXS measurements indicated that SRDOM decreased iron(III) (hydr)oxide nucleus sizes and growth rates. A combined analysis of SRDOM and other proteinaceous or labile DOM (alginate, polyaspartate, and glutamate) indicated that DOM with higher molecular weights caused more increased arsenic mobility. The new observations in **System 2** advance our understanding of the impacts of the oxyanions and DOM in injected water on arsenic mobility

and secondary precipitate formation during MAR operation. In addition, by using a flow-through, time-resolved, and *in situ* GISAXS method, the effective interfacial and apparent activation energies of iron(III) (hydr)oxide heterogeneous nucleation on quartz were experimentally obtained. The detection of iron(III) (hydr)oxide nucleation rates under different supersaturations (pH 3.3−3.6) and temperatures (12−35ºC) led to quantification of α' and E_a. These thermodynamic and kinetic values benefit the use of reactive transport models to understand and predict iron(III) (hydr)oxide's formation at mineral–water interfaces, as well as its effects on pollutants' fate and transport in natural and engineered water systems.

Studying **System 3**, we developed nature-inspired photothermal membranes for sustainable desalination using membrane distillation. In particular, photothermal membrane distillation (PMD) was developed, which utilized a photothermal membrane embedded with light-absorbing photothermal materials to harvest solar energy and generate localized heat at the water-membrane interface. Polydopamine (PDA), with easy synthesis, biocompatibility, and excellent light-to-heat conversion, was used as the photothermal material to develop several PMD membranes with high solar conversion efficiencies. First, a simple, stable, and scalable PDA-coated PVDF membrane was synthesized for PMD, with a high solar energy conversion efficiency (45%) and a high water flux (0.49 $kg/m^2 \cdot h$) under 0.75 kW/m^2 solar irradiation. The PDA coating on the membrane facilitated broad light absorption and outstanding photothermal conversion. Further, to increase the solar energy conversion efficiency, bacterial nanocellulose (BNC) was utilized to decrease heat conductive loss from the photothermal layer to the cold distillate. A new photothermal membrane was thermally-engineered to incorporate a bilayer structure composed of two environmentally-sustainable materials, PDA particles and BNC. This thermally-engineered design enabled a permeate

flux of 1.0 kg/m^2·h under 1 sun irradiation, and a record high solar energy-to-collected water efficiency of 68%, without ancillary heat or heat recovery systems. In addition, the membrane showed effective bactericidal activity and allowed easy cleaning. The findings from **System 3** offer potential solutions to providing potable water and alleviating water stress in remote or underdeveloped areas using sustainable solar energy and decentralized water treatment techniques that require less energy input and cost.

To conclude, the work in this dissertation offers an in-depth and mechanistic understanding of solid-liquid interfacial interactions including nanoparticles and different water constituents (e.g., organic matter) in water treatment or subsurface systems, and provides additional insights into designing new membranes that can utilize sustainable solar energy to treat water. The findings will help fill the current knowledge gaps regarding the fate of nanoscale solids and organic matter in water management systems, which will in turn benefit the design of the next generation of safer and more sustainable water treatment systems.

8.2 Recommended future directions

Our new findings have provided an improved understanding of solid–liquid interfacial interactions including nanoparticles and different water constituents (e.g., organic matter) in water treatment or subsurface systems, and have also provided additional insights into designing new membranes which can utilize sustainable energy source to treat water. Building on this work, the following future research directions are recommended.

First, more attention should be paid to the physicochemical transformation of nanomaterials and contaminants in environments and to their impacts on eco-systems. The widespread applications of engineered nanomaterials (ENMs) will inevitably lead to their release into the environment, including the air, soil, and surface and ground water, and into engineered water treatment systems. In these systems, the nanomaterials' surface chemistry might be changed by various components, including light (UV or sunlight), abundant cations (Ca, Mn, Fe) or anions (Cr, As, P), dissolved organic matter (DOM), reactive species (including reactive oxygen species (ROS) or hyalogen species (RHS)), and earth-abundant mineral surfaces. DOM, including natural organic matter (NOM) and soluble microbial products (SMPs), may have different complexation affinities towards ENMs based on DOM's functional group compositions and molecular weight distributions. The adsorption of DOM, and potential redox reactions between ENMs and cations/anions, ROS/RHS, and light, might lead to ENMs' dissolution, colloidal stability alteration, and functional property changes (including changes in surface charge, porosity, optical properties, and biocompatibility with ecological systems). The physicochemical transformation of emerging nanomaterials in natural and engineered water systems should be systematically investigated, including polymeric and 2D nanomaterials, and recalcitrant contaminants such as micro- and

nano-plastics. In addition, new *in situ* detection methods should be developed to better quantitatively follow the physicochemical transformation of nanomaterials. The physicochemical transformation of nanomaterials and contaminants in environments at interfaces can be studied by AFM-assisted force measurements[463] or X-ray scattering[464] to follow the interaction between nanomaterials and different surfaces, as well as the structural changes of nanomaterials during redox reactions.

Second, for arsenic control and arsenopyrite dissolution in managed aquifer recharge systems, our work found that maghemite was the main secondary mineral phase from arsenopyrite dissolution in oxidative environments. However, whether maghemite precipitates directly or is transformed from less crystalline iron (hydr)oxide phases during arsenopyrite dissolution is still in contention. Future *in situ* study can investigate the phase transformation of secondary mineral precipitates from arsenopyrite dissolution. Different phases of secondary Fe-containing mineral phases (e.g., ferrihydrite, magnetite, maghemite, and hematite) will have various adsorption affinities towards arsenic. For example, more crystalized forms of iron(III) (hydr)oxides have been shown to possess lower adsorption capacity towards arsenic.[304] Thus, the phase transformation pathway of secondary mineral precipitates from arsenopyrite dissolution should be carefully studied to provide a better understanding of arsenic mobility at different time stages. In addition, a clear delineation of the fate of each element (iron, arsenic, and sulfur) and a quantitative description of the mass balance of each element during arsenopyrite dissolution will benefit a comprehensive understanding of arsenic mobility in MAR. Furthermore, considering that (bi)carbonate species dissolved from calcite or other metal carbonates dominate in controlling the groundwater water chemistry in many MAR sites, it is important to systematically study the effects of (bi)carbonate on arsenopyrite dissolution. For example, the effects of different

bicarbonate concentrations and pH on arsenic mobility and arsenic adsorption onto secondary iron(III) (hydr)oxide precipitates can be studied.

Regarding iron(III) (hydr)oxide heterogeneous nucleation on earth abundant mineral surfaces, future efforts can incorporate the interfacial and activation energies of iron(III) (hydr)oxide on quartz into reactive transport models to predict iron(III) (hydr)oxide's formation in MAR, acid mine drainage, or hydraulic fracturing systems. Future studies can also focus on measuring the interfacial and activation energies of iron(III) (hydr)oxide on other surfaces besides quartz (e.g., mica, corundum, feldspar). Therefore, when analyzing a more complex system where several substrates are available, these thermodynamic and kinetic parameters can be compared to provide an improved understanding of the affinity of iron(III) (hydr)oxide precipitate towards different surfaces and to obtain a better prediction of iron(III) (hydr)oxide precipitate distribution. Moreover, for engineered applications, substrates can be modified to control the formation of iron(III) (hydr)oxide by tuning the interfacial and activation energies. For example, the interfacial energy can be decreased to decrease the critical nucleation size of iron(III) (hydr)oxide and increase its specific surface area when it is used for heterogeneously catalyzing Fenton reactions.[317] Further, in membrane processes, the membrane surface can be modified to increase the interfacial and activation energy of iron(III) (hydr)oxide precipitation, thus increasing the thermodynamic and kinetic energy barriers of iron(III) (hydr)oxide formation and resisting its fouling on the membrane.

Third, using the knowledge obtained from fundamental mechanistic studies, novel membranes that are stable, scalable, and sustainable can be developed for next generation water treatment. An ideal membrane would have high chemical and mechanical stability with long-term robustness when it encounters reactive species or light, and will not have significant organic/inorganic/biological fouling problems. To be scalable, a membrane must

be both cheap and easily and quickly synthesized. Most importantly, to be sustainable, the membrane must not adversely affect the surrounding environment, especially eco-systems, while at the same time maintaining high water treatment performance. Such a membrane must also mainly or solely use sustainable energy sources, including solar energy. Membrane technologies, including ultrafiltration, microfiltration, nanofiltration, reverse osmosis, membrane distillation, forward distillation, and capacitive deionization, can be incorporated with novel nanomaterials and ideal system designs to solve the water crisis. Membrane distillation (MD) in particular can be a potential decentralized water treatment for remote areas or underdeveloped regions by using renewable heat sources, including solar energy. Using photothermal membranes, MD can treat saline, brackish, and wastewater with low cost and reduced electricity input. Resource recovery using MD has been promising due to its capability to treat highly contaminated water. For example, MD has been used to recovery resources including phosphorus,[465] ammonia,[466] and minerals[467] from wastewater or hypersaline water. Facilitated by the photothermal effect, PMD can also have the potential to recover useful resources with reduced electricity input than conventional MD. In the future, photothermal materials can also be incorporated with photocatalytic or electro-conductive materials to generate synergetic effects, including photo-disinfection[468] and Joule heating[469] for MD. Membranes incorporating nature-inspired materials (e.g., wood and cellulose) particularly interesting: they are highly abundant, cheap, scalable, biocompatible, and meet the requirements of sustainable membrane design. In terms of membrane structure modifications, effects of membrane's porosity or pore size on membrane performance should be studied. Increasing membrane porosity or the nominal pore diameter can increase membrane's vapor permeability,[470] light absorption (by increasing the light traveling distance inside materials),[471-472] and reduce conductive heat transfer,[442] therefore enhancing the

thermal efficiency of the membrane. However, increasing membrane's porosity or the nominal pore diameter might also cause easier wetting and a reduction in the mechanical strength of the membrane.[442] In addition, efforts can be put into understanding fouling mechanisms (e.g., organic, bacteria, and mineral fouling) of newly developed membranes and further surface modifications to resist fouling. In terms of improving MD's operation efficiency towards real applications, better systematic design (e.g., residence time, MD configuration, water thickness) can be done to offer improved water recovery rate and vapor condensation efficiency.

In summary, the work presented in this dissertation provides a mechanistic basis for future studies on solid–liquid interfacial chemistry, colloidal chemistry, soil/aquifer remediation, rock/fluid interaction, and the design of novel sustainable membranes for water purification and desalination. In the future, with an improved fundamental mechanistic understanding of the physicochemical transformation of nanomaterials and contaminants in environments and their impacts on eco-systems, and advanced material design and applications for water treatment, eventually more sustainable water management systems can be built to provide safe and clean water.

References

1. Ripl, W., Water: the bloodstream of the biosphere. *Phil. Trans. Royal Soc. London B* **2003,** *358* (1440), 1921-1934.
2. Cosgrove, W. J.; Rijsberman, F. R., *World water vision: making water everybody's business*. Routledge: 2014.
3. Hanjra, M. A.; Qureshi, M. E., Global water crisis and future food security in an era of climate change. *Food Policy* **2010,** *35* (5), 365-377.
4. Schwarzenbach, R. P.; Egli, T.; Hofstetter, T. B.; von Gunten, U.; Wehrli, B., Global water pollution and human health. *Annu. Rev. Environ. Res.* **2010,** *35*, 109-136.
5. Vörösmarty, C. J.; McIntyre, P. B.; Gessner, M. O.; Dudgeon, D.; Prusevich, A.; Green, P.; Glidden, S.; Bunn, S. E.; Sullivan, C. A.; Reidy Liermann, C., Global threats to human water security and river biodiversity. *Nature* **2010,** *467* (7315), 555.
6. Richter, B. D.; Mathews, R.; Harrison, D. L.; Wigington, R., Ecologically sustainable water management: managing river flows for ecological integrity. *Ecological App.* **2003,** *13* (1), 206-224.
7. Clara, M.; Strenn, B.; Gans, O.; Martinez, E.; Kreuzinger, N.; Kroiss, H., Removal of selected pharmaceuticals, fragrances and endocrine disrupting compounds in a membrane bioreactor and conventional wastewater treatment plants. *Water Res.* **2005,** *39* (19), 4797-4807.
8. Michael, I.; Rizzo, L.; McArdell, C.; Manaia, C.; Merlin, C.; Schwartz, T.; Dagot, C.; Fatta-Kassinos, D., Urban wastewater treatment plants as hotspots for the release of antibiotics in the environment: a review. *Water Res.* **2013,** *47* (3), 957-995.
9. Patterson, J. W., Industrial wastewater treatment technology. **1985**.
10. Koivunen, J.; Siitonen, A.; Heinonen-Tanski, H., Elimination of enteric bacteria in biological–chemical wastewater treatment and tertiary filtration units. *Water Res.* **2003,** *37* (3), 690-698.
11. Dillon, P., Future management of aquifer recharge. *Hydrogeo. J.* **2005,** *13* (1), 313-316.
12. Dillon, P.; Pavelic, P.; Page, D.; Beringen, H.; Ward, J., Managed aquifer recharge. *An introduction Waterlines Report Series* **2009,** (13).
13. Wang, S.; Patel, M.; Dunivin, B.; Clark, J.; Foellmi, S.; Dipietro, C., Post‐treatment Optimization to Enhance Groundwater Recharge Operations. *J. Am. Water Works Assoc.* **2015,** *107* (5), 87-92.
14. Bullard, M. G.; Widdowson, M.; Salazar-Benites, G.; Heisig-Mitchell, J.; Nelson, A.; Bott, C., Managed Aquifer Recharge: Transport and Attenuation in a Coastal Plain Aquifer. *Screen* **2019,** *1* (505), 530.
15. Wilson, K. E.; Hochuli, S.; Lehman, P., Planning for Regional Water Supply Needs in Florida through an Integrated Loop Pipeline System. In *Pipelines 2008: Pipeline Asset Management: Maximizing Performance of our Pipeline Infrastructure*, 2008; pp 1-10.
16. Levantesi, C.; La Mantia, R.; Masciopinto, C.; Böckelmann, U.; Ayuso-Gabella, M. N.; Salgot, M.; Tandoi, V.; Van Houtte, E.; Wintgens, T.; Grohmann, E., Quantification of pathogenic microorganisms and microbial indicators in three wastewater reclamation and managed aquifer recharge facilities in Europe. *Sci. Total Environ.* **2010,** *408* (21), 4923-4930.
17. Vanderzalm, J.; Dillon, P.; Barry, K.; Miotlinski, K.; Kirby, J.; La Salle, C. L. G., Arsenic mobility and impact on recovered water quality during aquifer storage and recovery using reclaimed water in a carbonate aquifer. *App. Geochem.* **2011,** *26* (12), 1946-1955.
18. Drewes, J. E., Ground water replenishment with recycled water—water quality improvements during managed aquifer recharge. *Ground Water* **2009,** *47* (4), 502-505.
19. Elimelech, M.; Phillip, W. A., The future of seawater desalination: energy, technology, and the environment. *Science* **2011,** *333* (6043), 712-717.
20. Bennett, A., 50 th Anniversary: Desalination: 50 years of progress. *Filtration Separation* **2013,** *50* (3), 32-39.

21. Dongare, P. D.; Alabastri, A.; Pedersen, S.; Zodrow, K. R.; Hogan, N. J.; Neumann, O.; Wu, J.; Wang, T.; Deshmukh, A.; Elimelech, M., Nanophotonics-enabled solar membrane distillation for off-grid water purification. *Proc. Natl. Acad. Sci.* **2017,** *114* (27), 6936-6941.
22. Goh, P.; Matsuura, T.; Ismail, A.; Hilal, N., Recent trends in membranes and membrane processes for desalination. *Desalination* **2016,** *391*, 43-60.
23. Alkhudhiri, A.; Darwish, N.; Hilal, N., Membrane distillation: a comprehensive review. *Desalination* **2012,** *287*, 2-18.
24. Lawson, K. W.; Lloyd, D. R., Membrane distillation. *J. Membr. Sci.* **1997,** *124* (1), 1-25.
25. Koch, B.; Dittmar, T., From mass to structure: an aromaticity index for high‐resolution mass data of natural organic matter. *Rapid Commun. Mass Spectrom.* **2006,** *20* (5), 926-932.
26. Keller, A. A.; McFerran, S.; Lazareva, A.; Suh, S., Global life cycle releases of engineered nanomaterials. *J. Nanopart. Res.* **2013,** *15* (6), 1-17.
27. Colvin, V. L., The potential environmental impact of engineered nanomaterials. *Nature Biotechnol.* **2003,** *21* (10), 1166.
28. Limbach, L. K.; Bereiter, R.; Müller, E.; Krebs, R.; Gälli, R.; Stark, W. J., Removal of oxide nanoparticles in a model wastewater treatment plant: influence of agglomeration and surfactants on clearing efficiency. *Environ. Sci. Technol.* **2008,** *42* (15), 5828-5833.
29. Gottschalk, F.; Sonderer, T.; Scholz, R. W.; Nowack, B., Modeled environmental concentrations of engineered nanomaterials (TiO_2, ZnO, Ag, CNT, fullerenes) for different regions. *Environ. Sci. Technol.* **2009,** *43* (24), 9216-9222.
30. Pradeep, T., Noble metal nanoparticles for water purification: a critical review. *Thin Solid Films* **2009,** *517* (24), 6441-6478.
31. Qu, X.; Alvarez, P. J.; Li, Q., Applications of nanotechnology in water and wastewater treatment. *Water Res.* **2013,** *47* (12), 3931-3946.
32. Zhong, L. S.; Hu, J. S.; Liang, H. P.; Cao, A. M.; Song, W. G.; Wan, L. J., Self‐Assembled 3D flowerlike iron oxide nanostructures and their application in water treatment. *Adv. Mater.* **2006,** *18* (18), 2426-2431.
33. Chen, J.; Gu, B.; LeBoeuf, E. J.; Pan, H.; Dai, S., Spectroscopic characterization of the structural and functional properties of natural organic matter fractions. *Chemosphere* **2002,** *48* (1), 59-68.
34. Matilainen, A.; Gjessing, E. T.; Lahtinen, T.; Hed, L.; Bhatnagar, A.; Sillanpää, M., An overview of the methods used in the characterisation of natural organic matter (NOM) in relation to drinking water treatment. *Chemosphere* **2011,** *83* (11), 1431-1442.
35. Ritchie, J. D.; Perdue, E. M., Proton-binding study of standard and reference fulvic acids, humic acids, and natural organic matter. *Geochim. Cosmochim. Acta* **2003,** *67* (1), 85-96.
36. Leenheer, J. A.; Croué, J.-P., Peer reviewed: characterizing aquatic dissolved organic matter. ACS Publications: 2003.
37. Jarusutthirak, C.; Amy, G.; Croué, J.-P., Fouling characteristics of wastewater effluent organic matter (EfOM) isolates on NF and UF membranes. *Desalination* **2002,** *145* (1), 247-255.
38. Kikuchi, T.; Fujii, M.; Terao, K.; Jiwei, R.; Lee, Y. P.; Yoshimura, C., Correlations between aromaticity of dissolved organic matter and trace metal concentrations in natural and effluent waters: A case study in the Sagami River Basin, Japan. *Sci. Total Environ.* **2017,** *576*, 36-45.
39. Aiken, G. R.; Hsu-Kim, H.; Ryan, J. N., Influence of dissolved organic matter on the environmental fate of metals, nanoparticles, and colloids. *Environ. Sci. Technol.* **2011,** *45* (8), 3196-3201.
40. Gu, B.; Schmitt, J.; Chen, Z.; Liang, L.; McCarthy, J. F., Adsorption and desorption of natural organic matter on iron oxide: mechanisms and models. *Environ. Sci. Technol.* **1994,** *28* (1), 38-46.
41. Tiller, C. L.; O'Melia, C. R., Natural organic matter and colloidal stability: models and measurements. *Colloids Surf., A* **1993,** *73*, 89-102.
42. Murphy, E. M.; Zachara, J. M.; Smith, S. C.; Phillips, J. L., The sorption of humic acids to mineral surfaces and their role in contaminant binding. *Sci. Total Environ.* **1992,** *117*, 413-423.

43. Delay, M.; Dolt, T.; Woellhaf, A.; Sembritzki, R.; Frimmel, F. H., Interactions and stability of silver nanoparticles in the aqueous phase: Influence of natural organic matter (NOM) and ionic strength. *J. Chromatogr., A* **2011,** *1218* (27), 4206-4212.
44. Hyung, H.; Fortner, J. D.; Hughes, J. B.; Kim, J.-H., Natural organic matter stabilizes carbon nanotubes in the aqueous phase. *Environ. Sci. Technol.* **2007,** *41* (1), 179-184.
45. Louie, S. M.; Tilton, R. D.; Lowry, G. V., Effects of molecular weight distribution and chemical properties of natural organic matter on gold nanoparticle aggregation. *Environ. Sci. Technol.* **2013,** *47* (9), 4245-4254.
46. Keller, A. A.; Wang, H.; Zhou, D.; Lenihan, H. S.; Cherr, G.; Cardinale, B. J.; Miller, R.; Ji, Z., Stability and aggregation of metal oxide nanoparticles in natural aqueous matrices. *Environ. Sci. Technol.* **2010,** *44* (6), 1962-1967.
47. Andreozzi, R.; Caprio, V.; Insola, A.; Marotta, R., Advanced oxidation processes (AOP) for water purification and recovery. *Catal. Today* **1999,** *53* (1), 51-59.
48. Parsons, S., *Advanced oxidation processes for water and wastewater treatment*. IWA publishing: 2004.
49. Stasinakis, A., Use of selected advanced oxidation processes (AOPs) for wastewater treatment—a mini review. *Global NEST J.* **2008,** *10* (3), 376-385.
50. Bielski, B. H.; Cabelli, D. E.; Arudi, R. L.; Ross, A. B., Reactivity of HO_2/O^{-2} radicals in aqueous solution. *J. Phys. Chem. Ref. Data* **1985,** *14* (4), 1041-1100.
51. Buxton, G. V.; Greenstock, C. L.; Helman, W. P.; Ross, A. B., Critical review of rate constants for reactions of hydrated electrons, hydrogen atoms and hydroxyl radicals ($\cdot OH/\cdot O^-$) in aqueous solution. *J. Phys. Chem. Ref. Data* **1988,** *17* (2), 513-886.
52. Christensen, H.; Sehested, K.; Corfitzen, H., Reactions of hydroxyl radicals with hydrogen peroxide at ambient and elevated temperatures. *J. Phys. Chem.* **1982,** *86* (9), 1588-1590.
53. Labille, J.; Masion, A.; Ziarelli, F.; Rose, J.; Brant, J.; Villiéras, F.; Pelletier, M.; Borschneck, D.; Wiesner, M. R.; Bottero, J.-Y., Hydration and dispersion of C60 in aqueous systems: the nature of water− fullerene interactions. *Langmuir* **2009,** *25* (19), 11232-11235.
54. Wang, C.; Shang, C.; Ni, M.; Dai, J.; Jiang, F., (Photo) chlorination-Induced Physicochemical Transformation of Aqueous Fullerene n C60. *Environ. Sci. Technol.* **2012,** *46* (17), 9398-9405.
55. Wu, J.; Alemany, L. B.; Li, W.; Benoit, D.; Fortner, J. D., Photoenhanced transformation of hydroxylated fullerene (fullerol) by free chlorine in water. *Environ.Sci. Nano* **2017,** *4* (2), 470-479.
56. Wu, J.; Li, W.; Fortner, J. D., Photoenhanced oxidation of C60 aggregates (nC60) by free chlorine in water. *Environ.Sci. Nano* **2017,** *4* (1), 117-126.
57. Reed, K.; Cormack, A.; Kulkarni, A.; Mayton, M.; Sayle, D.; Klaessig, F.; Stadler, B., Exploring the properties and applications of nanoceria: is there still plenty of room at the bottom? *Environ. Sci. Nano.* **2014,** *1* (5), 390-405.
58. Sarathy, S.; Mohseni, M., The fate of natural organic matter during UV/H_2O_2 advanced oxidation of drinking water A paper submitted to the Journal of Environmental Engineering and Science. *Can. J. Civ. Eng.* **2008,** *36* (1), 160-169.
59. Sarathy, S. R.; Mohseni, M., The impact of UV/H_2O_2 advanced oxidation on molecular size distribution of chromophoric natural organic matter. *Environ. Sci. Technol.* **2007,** *41* (24), 8315-8320.
60. Thomson, J.; Roddick, F. A.; Drikas, M., Vacuum ultraviolet irradiation for natural organic matter removal. *J. Water Supply Res. T.* **2004,** *53* (4), 193-206.
61. Amy, G.; Drewes, J., Soil aquifer treatment (SAT) as a natural and sustainable wastewater reclamation/reuse technology: fate of wastewater effluent organic matter (EfOM) and trace organic compounds. *Environ. Monitor. Assess.* **2007,** *129* (1), 19-26.
62. Neil, C. W.; Yang, Y. J.; Schupp, D.; Jun, Y.-S., Water chemistry impacts on arsenic mobilization from arsenopyrite dissolution and secondary mineral precipitation: implications for managed aquifer recharge. *Environ. Sci. Technol.* **2014,** *48* (8), 4395-4405.

63. Schreiber, M.; Gotkowitz, M.; Simo, J.; Freiberg, P., Mechanisms of arsenic release to ground water from naturally occurring sources, eastern Wisconsin. In *Arsenic in Ground Water*, Springer: 2003; pp 259-280.
64. Neil, C. W.; Lee, B.; Jun, Y.-S., Different Arsenate and Phosphate Incorporation Effects on the Nucleation and Growth of Iron (III)(Hydr) oxides on Quartz. *Environ. Sci. Technol.* **2014,** *48* (20), 11883-11891.
65. Jung, H.; Jun, Y.-S., Ionic strength-controlled mn (hydr) oxide nanoparticle nucleation on quartz: effect of aqueous $Mn(OH)_2$. *Environ. Sci. Technol.* **2016,** *50* (1), 105-113.
66. Hu, Y.; Neil, C.; Lee, B.; Jun, Y.-S., Control of heterogeneous Fe (III)(hydr) oxide nucleation and growth by interfacial energies and local saturations. *Environ. Sci. Technol* **2013,** *47* (16), 9198-9206.
67. Neil, C. W.; Yang, Y. J.; Jun, Y.-S., Arsenic mobilization and attenuation by mineral–water interactions: implications for managed aquifer recharge. *J. Environ. Monit.* **2012,** *14* (7), 1772-1788.
68. Neil, C. W.; Jun, Y.-S., Fe^{3+} Addition Promotes Arsenopyrite Dissolution and Iron (III)(Hydr) oxide Formation and Phase Transformation. *Environ. Sci. Technol. Let.* **2015,** *3* (1), 30-35.
69. Rauch-Williams, T.; Hoppe-Jones, C.; Drewes, J., The role of organic matter in the removal of emerging trace organic chemicals during managed aquifer recharge. *Water Res.* **2010,** *44* (2), 449-460.
70. Johnson, S. B.; Yoon, T. H.; Brown, G. E., Adsorption of organic matter at mineral/water interfaces: 5. Effects of adsorbed natural organic matter analogues on mineral dissolution. *Langmuir* **2005,** *21* (7), 2811-2821.
71. Chi, F.-H.; Amy, G. L., Kinetic study on the sorption of dissolved natural organic matter onto different aquifer materials: the effects of hydrophobicity and functional groups. *J. Colloid Interf. Sci.* **2004,** *274* (2), 380-391.
72. Specht, C.; Kumke, M.; Frimmel, F., Characterization of NOM adsorption to clay minerals by size exclusion chromatography. *Water Res.* **2000,** *34* (16), 4063-4069.
73. Neil, C. W.; Ray, J. R.; Lee, B.; Jun, Y.-S., Fractal aggregation and disaggregation of newly formed iron (III)(hydr) oxide nanoparticles in the presence of natural organic matter and arsenic. *Environ. Sci. Nano* **2016,** *3* (3), 647-656.
74. Phattaranawik, J.; Jiraratananon, R.; Fane, A., Heat transport and membrane distillation coefficients in direct contact membrane distillation. *J. Mem. Sci.* **2003,** *212* (1), 177-193.
75. Wang, K. Y.; Chung, T.-S.; Gryta, M., Hydrophobic PVDF hollow fiber membranes with narrow pore size distribution and ultra-thin skin for the fresh water production through membrane distillation. *Chem. Eng. Sci.* **2008,** *63* (9), 2587-2594.
76. Leitch, M. E.; Li, C.; Ikkala, O.; Mauter, M. S.; Lowry, G. V., Bacterial nanocellulose aerogel membranes: novel high-porosity materials for membrane distillation. *Environ. Sci. Technol. Lett.* **2016,** *3* (3), 85-91.
77. Efome, J. E.; Baghbanzadeh, M.; Rana, D.; Matsuura, T.; Lan, C. Q., Effects of superhydrophobic SiO_2 nanoparticles on the performance of PVDF flat sheet membranes for vacuum membrane distillation. *Desalination* **2015,** *373*, 47-57.
78. Liao, Y.; Wang, R.; Fane, A. G., Engineering superhydrophobic surface on poly (vinylidene fluoride) nanofiber membranes for direct contact membrane distillation. *J. Mem. Sci.* **2013,** *440*, 77-87.
79. Prince, J.; Singh, G.; Rana, D.; Matsuura, T.; Anbharasi, V.; Shanmugasundaram, T., Preparation and characterization of highly hydrophobic poly (vinylidene fluoride)–clay nanocomposite nanofiber membranes (PVDF–clay NNMs) for desalination using direct contact membrane distillation. *J. Mem. Sci.* **2012,** *397*, 80-86.
80. Razmjou, A.; Arifin, E.; Dong, G.; Mansouri, J.; Chen, V., Superhydrophobic modification of TiO_2 nanocomposite PVDF membranes for applications in membrane distillation. *J. Mem. Sci.* **2012,** *415*, 850-863.

81. Drioli, E.; Ali, A.; Macedonio, F., Membrane distillation: Recent developments and perspectives. *Desalination* **2015,** *356*, 56-84.
82. Koschikowski, J.; Wieghaus, M.; Rommel, M., Solar thermal driven desalination plants based on membrane distillation. *Water Sci. Tech. Water Supply* **2003,** *3* (5-6), 49-55.
83. Chen, T.-C.; Ho, C.-D., Immediate assisted solar direct contact membrane distillation in saline water desalination. *J. Mem. Sci.* **2010,** *358* (1), 122-130.
84. Hausmann, A.; Sanciolo, P.; Vasiljevic, T.; Weeks, M.; Duke, M., Integration of membrane distillation into heat paths of industrial processes. *Chem. Eng. J.* **2012,** *211*, 378-387.
85. Politano, A.; Argurio, P.; Di Profio, G.; Sanna, V.; Cupolillo, A.; Chakraborty, S.; Arafat, H. A.; Curcio, E., Photothermal membrane distillation for seawater desalination. *Adv. Mater.* **2017,** *29* (2).
86. Summers, E. K.; Lienhard V, J. H., A novel solar-driven air gap membrane distillation system. *Desalination Water Treat.* **2013,** *51* (7-9), 1344-1351.
87. Turchi, C. S.; Ollis, D. F., Photocatalytic degradation of organic water contaminants: mechanisms involving hydroxyl radical attack. *J. Cata.* **1990,** *122* (1), 178-192.
88. Christl, I.; Kretzschmar, R., Relating ion binding by fulvic and humic acids to chemical composition and molecular size. 1. Proton binding. *Environ. Sci. Technol.* **2001,** *35* (12), 2505-2511.
89. Milne, C. J.; Kinniburgh, D. G.; Tipping, E., Generic NICA-Donnan model parameters for proton binding by humic substances. *Environ. Sci. Technol.* **2001,** *35* (10), 2049-2059.
90. Weng, L.; Van Riemsdijk, W. H.; Koopal, L. K.; Hiemstra, T., Adsorption of humic substances on goethite: comparison between humic acids and fulvic acids. *Environ. Sci. Technol.* **2006,** *40* (24), 7494-7500.
91. Wu, X.; Neil, C. W.; Kim, D.; Jung, H.; Jun, Y.-S., Co-effects of UV/H_2O_2 and natural organic matter on the surface chemistry of cerium oxide nanoparticles. *Environ.Sci. Nano* **2018,** *5* (10), 2382-2393.
92. Wu, X.; Bowers, B.; Kim, D.; Lee, B.; Jun, Y.-S., Dissolved Organic Matter Affects Arsenic Mobility and Iron (III)(hydr) oxide Formation: Implications for Managed Aquifer Recharge. *Environ. Sci. Technol.* **2019**.
93. Wu, X.; Jiang, Q.; Ghim, D.; Singamaneni, S.; Jun, Y.-S., Localized heating with a photothermal polydopamine coating facilitates a novel membrane distillation process. *J. Mater. Chem. A* **2018,** *6* (39), 18799-18807.
94. Barton, L. E.; Auffan, M.; Bertrand, M.; Barakat, M.; Santaella, C.; Masion, A.; Borschneck, D.; Olivi, L.; Roche, N.; Wiesner, M. R., Transformation of pristine and citrate-functionalized CeO2 nanoparticles in a laboratory-scale activated sludge reactor. *Environ. Sci. Technol.* **2014,** *48* (13), 7289-7296.
95. Barton, L. E.; Auffan, M.; Olivi, L.; Bottero, J.-Y.; Wiesner, M. R., Heteroaggregation, transformation and fate of CeO2 nanoparticles in wastewater treatment. *Environ. Pollut.* **2015,** *203*, 122-129.
96. Collin, B.; Auffan, M.; Johnson, A. C.; Kaur, I.; Keller, A. A.; Lazareva, A.; Lead, J. R.; Ma, X.; Merrifield, R. C.; Svendsen, C., Environmental release, fate and ecotoxicological effects of manufactured ceria nanomaterials. *Environ. Sci. Nano.* **2014,** *1* (6), 533-548.
97. Gómez-Rivera, F.; Field, J. A.; Brown, D.; Sierra-Alvarez, R., Fate of cerium dioxide (CeO2) nanoparticles in municipal wastewater during activated sludge treatment. *Bioresour. Technol.* **2012,** *108*, 300-304.
98. Grassian, V. H.; Haes, A. J.; Mudunkotuwa, I. A.; Demokritou, P.; Kane, A. B.; Murphy, C. J.; Hutchison, J. E.; Isaacs, J. A.; Jun, Y.-S.; Karn, B., NanoEHS–defining fundamental science needs: no easy feat when the simple itself is complex. *Environ. Sci. Nano.* **2016,** *3* (1), 15-27.
99. Lin, W.; Huang, Y.-w.; Zhou, X.-D.; Ma, Y., Toxicity of cerium oxide nanoparticles in human lung cancer cells. *Int. J. Toxicol.* **2006,** *25* (6), 451-457.
100. Park, E.-J.; Choi, J.; Park, Y.-K.; Park, K., Oxidative stress induced by cerium oxide nanoparticles in cultured BEAS-2B cells. *Toxicology* **2008,** *245* (1), 90-100.

101. Pera-Titus, M.; Garcıa-Molina, V.; Baños, M. A.; Giménez, J.; Esplugas, S., Degradation of chlorophenols by means of advanced oxidation processes: a general review. *Appl. Catal., B* **2004,** *47* (4), 219-256.
102. Hirst, S. M.; Karakoti, A. S.; Tyler, R. D.; Sriranganathan, N.; Seal, S.; Reilly, C. M., Anti‐inflammatory Properties of Cerium Oxide Nanoparticles. *Small* **2009,** *5* (24), 2848-2856.
103. Celardo, I.; De Nicola, M.; Mandoli, C.; Pedersen, J. Z.; Traversa, E.; Ghibelli, L., Ce^{3+} ions determine redox-dependent anti-apoptotic effect of cerium oxide nanoparticles. *ACS Nano* **2011,** *5* (6), 4537-4549.
104. Das, M.; Patil, S.; Bhargava, N.; Kang, J.-F.; Riedel, L. M.; Seal, S.; Hickman, J. J., Auto-catalytic ceria nanoparticles offer neuroprotection to adult rat spinal cord neurons. *Biomaterials* **2007,** *28* (10), 1918-1925.
105. Heckert, E. G.; Karakoti, A. S.; Seal, S.; Self, W. T., The role of cerium redox state in the SOD mimetic activity of nanoceria. *Biomaterials* **2008,** *29* (18), 2705-2709.
106. Pirmohamed, T.; Dowding, J. M.; Singh, S.; Wasserman, B.; Heckert, E.; Karakoti, A. S.; King, J. E.; Seal, S.; Self, W. T., Nanoceria exhibit redox state-dependent catalase mimetic activity. *Chem. Commun.* **2010,** *46* (16), 2736-2738.
107. Laabs, C. N.; Amy, G. L.; Jekel, M., Understanding the size and character of fouling-causing substances from effluent organic matter (EfOM) in low-pressure membrane filtration. *Environ. Sci. Technol.* **2006,** *40* (14), 4495-4499.
108. Shon, H.; Vigneswaran, S.; Snyder, S., Effluent Organic Matter (EfOM) in Wastewater: Constituents, Effects, and Treatment. *Crit. Rev. Env. Sci. Technol.* **2006,** *36* (4), 327-374.
109. Bazri, M. M.; Barbeau, B.; Mohseni, M., Impact of UV/H2O2 advanced oxidation treatment on molecular weight distribution of NOM and biostability of water. *Water Res.* **2012,** *46* (16), 5297-5304.
110. Chin, A.; Bérubé, P., Removal of disinfection by-product precursors with ozone-UV advanced oxidation process. *Water Res.* **2005,** *39* (10), 2136-2144.
111. Drewes, J. E.; Fox, P., Fate of natural organic matter (NOM) during groundwater recharge using reclaimed water. *Water Sci. Technol.* **1999,** *40* (9), 241-248.
112. Jarusutthirak, C.; Amy, G., Role of soluble microbial products (SMP) in membrane fouling and flux decline. *Environ. Sci. Technol.* **2006,** *40* (3), 969-974.
113. Liu, J.-l.; Li, X.-y.; Xie, Y.-f.; Tang, H., Characterization of soluble microbial products as precursors of disinfection byproducts in drinking water supply. *Sci. Total Environ.* **2014,** *472*, 818-824.
114. Shen, Y.-x.; Xiao, K.; Liang, P.; Sun, J.-y.; Sai, S.-j.; Huang, X., Characterization of soluble microbial products in 10 large-scale membrane bioreactors for municipal wastewater treatment in China. *J. Membr. Sci. Technol.* **2012,** *415*, 336-345.
115. Sposito, G. *The surface chemistry of soils*; 1984.
116. Furman, O.; Usenko, S.; Lau, B. L., Relative importance of the humic and fulvic fractions of natural organic matter in the aggregation and deposition of silver nanoparticles. *Environ. Sci. Technol.* **2013,** *47* (3), 1349-1356.
117. Stankus, D. P.; Lohse, S. E.; Hutchison, J. E.; Nason, J. A., Interactions between natural organic matter and gold nanoparticles stabilized with different organic capping agents. *Environ. Sci. Technol.* **2010,** *45* (8), 3238-3244.
118. Quik, J. T.; Lynch, I.; Van Hoecke, K.; Miermans, C. J.; De Schamphelaere, K. A.; Janssen, C. R.; Dawson, K. A.; Stuart, M. A. C.; Van De Meent, D., Effect of natural organic matter on cerium dioxide nanoparticles settling in model fresh water. *Chemosphere* **2010,** *81* (6), 711-715.
119. Zhang, Z.; Gao, P.; Qiu, Y.; Liu, G.; Feng, Y.; Wiesner, M., Transport of cerium oxide nanoparticles in saturated silica media: influences of operational parameters and aqueous chemical conditions. *Scientific reports* **2016,** *6*.

120. Collin, B.; Oostveen, E.; Tsyusko, O. V.; Unrine, J. M., Influence of natural organic matter and surface charge on the toxicity and bioaccumulation of functionalized ceria nanoparticles in Caenorhabditis elegans. *Environ. Sci. Technol.* **2014,** *48* (2), 1280-1289.
121. Kroll, A.; Behra, R.; Kaegi, R.; Sigg, L., Extracellular polymeric substances (EPS) of freshwater biofilms stabilize and modify CeO2 and Ag nanoparticles. *PLoS One* **2014,** *9* (10), e110709.
122. Yang, L.; Shin, H.-S.; Hur, J., Estimating the concentration and biodegradability of organic matter in 22 wastewater treatment plants using fluorescence excitation emission matrices and parallel factor analysis. *Sensors* **2014,** *14* (1), 1771-1786.
123. Westerhoff, P.; Mezyk, S. P.; Cooper, W. J.; Minakata, D., Electron pulse radiolysis determination of hydroxyl radical rate constants with Suwannee River fulvic acid and other dissolved organic matter isolates. *Environ. Sci. Technol.* **2007,** *41* (13), 4640-4646.
124. Neil, C. W.; Ray, J. R.; Lee, B.; Jun, Y.-S., Fractal aggregation and disaggregation of newly formed iron (III)(hydr) oxide nanoparticles in the presence of natural organic matter and arsenic. *Environ.Sci. Nano* **2016,** *3* (3), 647-656.
125. Chang, M.-W.; Chung, C.-C.; Chern, J.-M.; Chen, T.-S., Dye decomposition kinetics by UV/H_2O_2: initial rate analysis by effective kinetic modelling methodology. *Chem. Eng. Sci.* **2010,** *65* (1), 135-140.
126. Liu, X.; Ray, J. R.; Neil, C. W.; Li, Q.; Jun, Y.-S., Enhanced Colloidal Stability of CeO_2 Nanoparticles by Ferrous Ions: Adsorption, Redox Reaction, and Surface Precipitation. *Environ. Sci. Technol.* **2015,** *49* (9), 5476-5483.
127. Daneshvar, N.; Behnajady, M.; Mohammadi, M. K. A.; Dorraji, M. S., UV/H_2O_2 treatment of Rhodamine B in aqueous solution: Influence of operational parameters and kinetic modeling. *Desalination* **2008,** *230* (1), 16-26.
128. Muruganandham, M.; Swaminathan, M., Photochemical oxidation of reactive azo dye with UV–H_2O_2 process. *Dyes Pigm.* **2004,** *62* (3), 269-275.
129. Park, P. W.; Ledford, J. S., Effect of crystallinity on the photoreduction of cerium oxide: A study of CeO_2 and Ce/Al_2O_3 catalysts. *Langmuir* **1996,** *12* (7), 1794-1799.
130. Schierbaum, K.-D., Ordered ultra-thin cerium oxide overlayers on Pt (111) single crystal surfaces studied by LEED and XPS. *Surf. Sci.* **1998,** *399* (1), 29-38.
131. Deshpande, S.; Patil, S.; Kuchibhatla, S. V.; Seal, S., Size dependency variation in lattice parameter and valency states in nanocrystalline cerium oxide. *Appl. Phys. Lett.* **2005,** *87* (13), 133113-133113.
132. Zhang, F.; Wang, P.; Koberstein, J.; Khalid, S.; Chan, S.-W., Cerium oxidation state in ceria nanoparticles studied with X-ray photoelectron spectroscopy and absorption near edge spectroscopy. *Surf. Sci.* **2004,** *563* (1), 74-82.
133. Aguila, A.; O'Shea, K. E.; Tobien, T.; Asmus, K.-D., Reactions of hydroxyl radical with dimethyl methylphosphonate and diethyl methylphosphonate. A fundamental mechanistic study. *J. Phys. Chem. A.* **2001,** *105* (33), 7834-7839.
134. McCord, J. M.; Fridovich, I., Superoxide dismutase an enzymic function for erythrocuprein (hemocuprein). *J. Biol. Chem.* **1969,** *244* (22), 6049-6055.
135. Chen, J.; Xiu, Z.; Lowry, G. V.; Alvarez, P. J., Effect of natural organic matter on toxicity and reactivity of nano-scale zero-valent iron. *Water Res.* **2011,** *45* (5), 1995-2001.
136. Deonarine, A.; Hsu-Kim, H., Precipitation of mercuric sulfide nanoparticles in NOM-containing water: Implications for the natural environment. *Environ. Sci. Technol.* **2009,** *43* (7), 2368-2373.
137. Hyung, H.; Kim, J.-H., Natural organic matter (NOM) adsorption to multi-walled carbon nanotubes: effect of NOM characteristics and water quality parameters. *Environ. Sci. Technol.* **2008,** *42* (12), 4416-4421.
138. Celardo, I.; Pedersen, J. Z.; Traversa, E.; Ghibelli, L., Pharmacological potential of cerium oxide nanoparticles. *Nanoscale* **2011,** *3* (4), 1411-1420.

139. Karakoti, A. S.; Singh, S.; Kumar, A.; Malinska, M.; Kuchibhatla, S. V.; Wozniak, K.; Self, W. T.; Seal, S., PEGylated nanoceria as radical scavenger with tunable redox chemistry. *J. Am. Chem. Soc.* **2009,** *131* (40), 14144-14145.
140. Korsvik, C.; Patil, S.; Seal, S.; Self, W. T., Superoxide dismutase mimetic properties exhibited by vacancy engineered ceria nanoparticles. *Chem. Commun.* **2007,** (10), 1056-1058.
141. Singh, S.; Dosani, T.; Karakoti, A. S.; Kumar, A.; Seal, S.; Self, W. T., A phosphate-dependent shift in redox state of cerium oxide nanoparticles and its effects on catalytic properties. *Biomaterials* **2011,** *32* (28), 6745-6753.
142. Kumar, E.; Selvarajan, P.; Balasubramanian, K., Preparation and studies of cerium dioxide (CeO_2) nanoparticles by microwave-assisted solution method. *Recent Res. Sci. Technol.* **2010,** *2* (4).
143. Li, C.; Sakata, Y.; Arai, T.; Domen, K.; Maruya, K.-i.; Onishi, T., Adsorption of carbon monoxide and carbon dioxide on cerium oxide studied by Fourier-transform infrared spectroscopy. Part 2.—Formation of formate species on partially reduced CeO_2 at room temperature. *J. Chem. Soc., Faraday Trans. 1* **1989,** *85* (6), 1451-1461.
144. Li, C.; Sakata, Y.; Arai, T.; Domen, K.; Maruya, K.-i.; Onishi, T., Carbon monoxide and carbon dioxide adsorption on cerium oxide studied by Fourier-transform infrared spectroscopy. Part 1.—Formation of carbonate species on dehydroxylated CeO_2, at room temperature. *J. Chem. Soc., Faraday Trans. 1* **1989,** *85* (4), 929-943.
145. Cho, J.; Amy, G.; Pellegrino, J.; Yoon, Y., Characterization of clean and natural organic matter (NOM) fouled NF and UF membranes, and foulants characterization. *Desalination* **1998,** *118* (1), 101-108.
146. Papageorgiou, S. K.; Kouvelos, E. P.; Favvas, E. P.; Sapalidis, A. A.; Romanos, G. E.; Katsaros, F. K., Metal–carboxylate interactions in metal–alginate complexes studied with FTIR spectroscopy. *Carbohydr. Res.* **2010,** *345* (4), 469-473.
147. Sun, W.-L.; Xia, J.; Li, S.; Sun, F., Effect of natural organic matter (NOM) on Cu (II) adsorption by multi-walled carbon nanotubes: relationship with NOM properties. *Chem. Eng. J.* **2012,** *200*, 627-636.
148. Guan, X.-H.; Shang, C.; Chen, G.-H., ATR-FTIR investigation of the role of phenolic groups in the interaction of some NOM model compounds with aluminum hydroxide. *Chemosphere* **2006,** *65* (11), 2074-2081.
149. Bond, T.; Goslan, E. H.; Parsons, S. A.; Jefferson, B., A critical review of trihalomethane and haloacetic acid formation from natural organic matter surrogates. *Environ. Technol. Rev.* **2012,** *1* (1), 93-113.
150. Croue, J.-P.; Korshin, G. V.; Benjamin, M. M., *Characterization of natural organic matter in drinking water*. American Water Works Association: 2000.
151. Bensalem, A.; Bozon-Verduraz, F.; Delamar, M.; Bugli, G., Preparation and characterization of highly dispersed silica-supported ceria. *Appl. Catal., A* **1995,** *121* (1), 81-93.
152. Hamoudi, S.; Larachi, F. ç.; Adnot, A.; Sayari, A., Characterization of spent MnO_2/CeO_2 wet oxidation catalyst by TPO–MS, XPS, and S-SIMS. *J. Catal.* **1999,** *185* (2), 333-344.
153. Chen, H.; Sayari, A.; Adnot, A.; Larachi, F. ç., Composition–activity effects of Mn–Ce–O composites on phenol catalytic wet oxidation. *Appl. Catal., B* **2001,** *32* (3), 195-204.
154. Laachir, A.; Perrichon, V.; Badri, A.; Lamotte, J.; Catherine, E.; Lavalley, J. C.; El Fallah, J.; Hilaire, L.; Le Normand, F.; Quéméré, E., Reduction of CeO_2 by hydrogen. Magnetic susceptibility and Fourier-transform infrared, ultraviolet and X-ray photoelectron spectroscopy measurements. *J. Chem. Soc., Faraday Trans.* **1991,** *87* (10), 1601-1609.
155. Larachi, F. ç.; Pierre, J.; Adnot, A.; Bernis, A., Ce 3d XPS study of composite $Ce_xMn_{1-x}O_{2-y}$ wet oxidation catalysts. *Appl. Surf. Sci.* **2002,** *195* (1), 236-250.
156. Scholes, F.; Hughes, A.; Hardin, S.; Lynch, P.; Miller, P., Influence of hydrogen peroxide in the preparation of nanocrystalline ceria. *Chem. Mater.* **2007,** *19* (9), 2321-2328.

157. Dai, Y.; Manthiram, A.; Campion, A.; Goodenough, J., X-ray-photoelectron-spectroscopy evidence for peroxide in 1: 2: 3 copper oxides containing disordered or excess oxygen. *Phys. Rev. B* **1988,** *38* (7), 5091.
158. Lamontagne, B.; Roy, D.; Sporken, R.; Caudano, R., Identification of the adsorption sites of molecular oxygen on Si (111) using XPS. *Progress in surface science* **1995,** *50* (1-4), 315-324.
159. Campbell, C. T., An XPS study of molecularly chemisorbed oxygen on Ag (111). *Surf. Sci.* **1986,** *173* (2-3), L641-L646.
160. Hughes, A.; Taylor, R.; Hinton, B.; Wilson, L., XPS and SEM characterization of hydrated cerium oxide conversion coatings. *Surface and Interface Analysis* **1995,** *23* (7‐8), 540-550.
161. Soria, J.; Martinez-Arias, A.; Conesa, J., Effect of oxidized rhodium on oxygen adsorption on cerium oxide. *Vacuum* **1992,** *43* (5-7), 437-440.
162. Boehm, H., Acidic and basic properties of hydroxylated metal oxide surfaces. *Disc. Faraday Soc.* **1971,** *52*, 264-275.
163. Goldberg, S., Competitive adsorption of arsenate and arsenite on oxides and clay minerals. *Soil Sci. Soc. Am. J.* **2002,** *66* (2), 413-421.
164. Asati, A.; Santra, S.; Kaittanis, C.; Perez, J. M., Surface-charge-dependent cell localization and cytotoxicity of cerium oxide nanoparticles. *ACS nano* **2010,** *4* (9), 5321-5331.
165. Karakoti, A.; Monteiro-Riviere, N.; Aggarwal, R.; Davis, J.; Narayan, R. J.; Self, W.; McGinnis, J.; Seal, S., Nanoceria as antioxidant: synthesis and biomedical applications. *Jom* **2008,** *60* (3), 33-37.
166. Tarnuzzer, R. W.; Colon, J.; Patil, S.; Seal, S., Vacancy engineered ceria nanostructures for protection from radiation-induced cellular damage. *Nano Lett.* **2005,** *5* (12), 2573-2577.
167. Hailstone, R.; DiFrancesco, A.; Leong, J.; Allston, T.; Reed, K., A study of lattice expansion in CeO_2 nanoparticles by transmission electron microscopy. *J. Phys. Chem. C* **2009,** *113* (34), 15155-15159.
168. Huang, X.; Beck, M. J., Determining the oxidation state of small, hydroxylated metal-oxide nanoparticles with infrared absorption spectroscopy. *Chem. Mater.* **2015,** *27* (8), 2965-2972.
169. IHSS, The International Humic Substances Society.
170. Rogers, N. J.; Franklin, N. M.; Apte, S. C.; Batley, G. E.; Angel, B. M.; Lead, J. R.; Baalousha, M., Physico-chemical behaviour and algal toxicity of nanoparticulate CeO_2 in freshwater. *Environ. Chem.* **2010,** *7* (1), 50-60.
171. Wu, X.; Burnell, S.; Neil, C. W.; Kim, D.; Zhang, L.; Jung, H.; Jun, Y.-S., Effects of Phosphate, Silicate, and Bicarbonate on Arsenopyrite Dissolution and Secondary Mineral Precipitation. *ACS Earth Space Chem.* **2020**.
172. Siebert, S.; Burke, J.; Faures, J.-M.; Frenken, K.; Hoogeveen, J.; Döll, P.; Portmann, F. T., Groundwater use for irrigation–a global inventory. *Hydro. Earth System Sci.* **2010,** *14* (10), 1863-1880.
173. Borchers, J. W.; Carpenter, M., Land Subsidence from groundwater use in California. *California Water Foundation Full Report of Findings/April 2014* **2014,** *151*.
174. Zaveri, E.; Grogan, D. S.; Fisher-Vanden, K.; Frolking, S.; Lammers, R. B.; Wrenn, D. H.; Prusevich, A.; Nicholas, R. E., Invisible water, visible impact: groundwater use and Indian agriculture under climate change. *Environ. Res. Lett.* **2016,** *11* (8), 084005.
175. Cao, G.; Zheng, C.; Scanlon, B. R.; Liu, J.; Li, W., Use of flow modeling to assess sustainability of groundwater resources in the North China Plain. *Water Resour. Res.* **2013,** *49* (1), 159-175.
176. Famiglietti, J.; Lo, M.; Ho, S.; Bethune, J.; Anderson, K.; Syed, T.; Swenson, S.; De Linage, C.; Rodell, M., Satellites measure recent rates of groundwater depletion in California's Central Valley. *Geophys. Res. Lett.* **2011,** *38* (3).
177. Erban, L. E.; Gorelick, S. M.; Zebker, H. A., Groundwater extraction, land subsidence, and sea-level rise in the Mekong Delta, Vietnam. *Environ. Sci. Technol. Lett.* **2014,** *9* (8), 084010.

178. Ferguson, G.; Gleeson, T., Vulnerability of coastal aquifers to groundwater use and climate change. *Nat. Clim. Chang.* **2012,** *2* (5), 342.
179. Jones, G. W.; Pichler, T., Relationship between pyrite stability and arsenic mobility during aquifer storage and recovery in southwest central Florida. *Environ. Sci. Technol.* **2007,** *41* (3), 723-730.
180. Reich, M.; Becker, U., First-principles calculations of the thermodynamic mixing properties of arsenic incorporation into pyrite and marcasite. *Chem. Geo.* **2006,** *225* (3), 278-290.
181. Utsunomiya, S.; Peters, S. C.; Blum, J. D.; Ewing, R. C., Nanoscale mineralogy of arsenic in a region of New Hampshire with elevated As-concentrations in the groundwater. *Am. Mineral.* **2003,** *88* (11-12), 1844-1852.
182. McNab Jr, W. W.; Singleton, M. J.; Moran, J. E.; Esser, B. K., Ion exchange and trace element surface complexation reactions associated with applied recharge of low-TDS water in the San Joaquin Valley, California. *Appl. Geochem.* **2009,** *24* (1), 129-137.
183. McKibben, M.; Tallant, B.; Del Angel, J., Kinetics of inorganic arsenopyrite oxidation in acidic aqueous solutions. *App. Geochem.* **2008,** *23* (2), 121-135.
184. Walker, F. P.; Schreiber, M. E.; Rimstidt, J. D., Kinetics of arsenopyrite oxidative dissolution by oxygen. *Geochim. Cosmochim. Acta* **2006,** *70* (7), 1668-1676.
185. Yu, Y.; Zhu, Y.; Gao, Z.; Gammons, C. H.; Li, D., Rates of Arsenopyrite Oxidation by Oxygen and Fe (III) at pH 1.8− 12.6 and 15− 45° C. *Environ. Sci. Technol.* **2007,** *41* (18), 6460-6464.
186. Neil, C. W.; Jun, Y.-S., Fe^{3+} Addition Promotes Arsenopyrite Dissolution and Iron (III)(Hydr) oxide Formation and Phase Transformation. *Environ. Sci. Technol. Lett.* **2015,** *3* (1), 30-35.
187. Wu, X.; Bowers, B.; Kim, D.; Lee, B.; Jun, Y.-S., Dissolved Organic Matter Affects Arsenic Mobility and Iron (III)(hydr) oxides Formation: Implications for Managed Aquifer Recharge. *Environ. Sci. Technol.* **2019,** *53* (24), 14357-14367.
188. Bekele, E.; Toze, S.; Patterson, B.; Higginson, S., Managed aquifer recharge of treated wastewater: Water quality changes resulting from infiltration through the vadose zone. *Water Res.* **2011,** *45* (17), 5764-5772.
189. Meng, X.; Bang, S.; Korfiatis, G. P., Effects of silicate, sulfate, and carbonate on arsenic removal by ferric chloride. *Water Res.* **2000,** *34* (4), 1255-1261.
190. Waltham, C. A.; Eick, M. J., Kinetics of arsenic adsorption on goethite in the presence of sorbed silicic acid. *Soil Sci. Soc. Am. J.* **2002,** *66* (3), 818.
191. Arai, Y.; Sparks, D.; Davis, J., Effects of dissolved carbonate on arsenate adsorption and surface speciation at the hematite−water interface. *Environ. Sci. Technol.* **2004,** *38* (3), 817-824.
192. Gao, Y.; Mucci, A., Acid base reactions, phosphate and arsenate complexation, and their competitive adsorption at the surface of goethite in 0.7 M NaCl solution. *Geochim. Cosmochim. Acta* **2001,** *65* (14), 2361-2378.
193. Carabante, I.; Grahn, M.; Holmgren, A.; Hedlund, J., In situ ATR–FTIR studies on the competitive adsorption of arsenate and phosphate on ferrihydrite. *J. Colloid Interface Sci.* **2010,** *351* (2), 523-531.
194. Kish, M. M.; Viola, R. E., Oxyanion specificity of aspartate-β-semialdehyde dehydrogenase. *Inorganic Chem.* **1999,** *38* (4), 818-820.
195. Jain, A.; Loeppert, R. H., Effect of competing anions on the adsorption of arsenate and arsenite by ferrihydrite. *J. Environ. Quality* **2000,** *29* (5), 1422-1430.
196. Manning, B. A.; Goldberg, S., Modeling competitive adsorption of arsenate with phosphate and molybdate on oxide minerals. *Soil Sci. Soc. Am. J.* **1996,** *60* (1), 121-131.
197. Zheng, Y.; Van Geen, A.; Stute, M.; Dhar, R.; Mo, Z.; Cheng, Z.; Horneman, A.; Gavrieli, I.; Simpson, H.; Versteeg, R., Geochemical and hydrogeological contrasts between shallow and deeper aquifers in two villages of Araihazar, Bangladesh: Implications for deeper aquifers as drinking water sources. *Geochim. Cosmochim. Acta* **2005,** *69* (22), 5203-5218.
198. Pfeifer, H.-R.; Gueye-Girardet, A.; Reymond, D.; Schlegel, C.; Temgoua, E.; Hesterberg, D. L.; Chou, J. W., Dispersion of natural arsenic in the Malcantone watershed, Southern Switzerland:

field evidence for repeated sorption–desorption and oxidation ‐ reduction processes. *Geoderma* **2004,** *122* (2), 205-234.
199. Lin, C.; Banin, A., Effect of long-term effluent recharge on phosphate sorption by soils in a wastewater reclamation plant. *Water Air Soil Pollution* **2005,** *164* (1), 257-273.
200. Iler, R., The chemistry of silica.,(Wiley-Interscience: New York). **1979**.
201. Robinson, R. B.; Reed, G. D.; Frazier, B., Iron and manganese sequestration facilities using sodium silicate. *AWWA J.* **1992**, 77-82.
202. Waychunas, G. A.; Jun, Y.-S.; Eng, P. J.; Ghose, S. K.; Trainor, T. P., Anion sorption topology on hematite: comparison of arsenate and silicate. *Developments in Earth and Environmental Sciences* **2007,** *7*, 31-65.
203. Stumm, W.; Morgan, J. J., *Aquatic chemistry: chemical equilibria and rates in natural waters*. John Wiley & Sons: 2012; Vol. 126.
204. Anawar, H. M.; Akai, J.; Sakugawa, H., Mobilization of arsenic from subsurface sediments by effect of bicarbonate ions in groundwater. *Chemosphere* **2004,** *54* (6), 753-762.
205. Appelo, C.; Van der Weiden, M.; Tournassat, C.; Charlet, L., Surface complexation of ferrous iron and carbonate on ferrihydrite and the mobilization of arsenic. *Environ. Sci. Technol.* **2002,** *36* (14), 3096-3103.
206. Holm, T. R., EFFECTS OF CO_3^{2-}/bicarbonate, Si, and PO_4^{3-} on Arsenic sorption to HFO. *AWWA J.* **2002,** *94* (4), 174-181.
207. Radu, T.; Subacz, J. L.; Phillippi, J. M.; Barnett, M. O., Effects of dissolved carbonate on arsenic adsorption and mobility. *Environ. Sci. Technol.* **2005,** *39* (20), 7875-7882.
208. Wilkie, J. A.; Hering, J. G., Adsorption of arsenic onto hydrous ferric oxide: effects of adsorbate/adsorbent ratios and co-occurring solutes. *Colloids Surf., A* **1996,** *107*, 97-110.
209. Bruno, J.; Stumm, W.; Wersin, P.; Brandberg, F., On the influence of carbonate in mineral dissolution: I. The thermodynamics and kinetics of hematite dissolution in bicarbonate solutions at T=25 C. *Geochim. Cosmochim. Acta* **1992,** *56* (3), 1139-1147.
210. McGuire, M. M.; Banfield, J. F.; Hamers, R. J., Quantitative determination of elemental sulfur at the arsenopyrite surface after oxidation by ferric iron: mechanistic implications. *Geochem. Transa.* **2001,** *2* (4), 25-29.
211. Asta, M. P.; Cama, J.; Ayora, C.; Acero, P.; de Giudici, G., Arsenopyrite dissolution rates in O_2-bearing solutions. *Chem. Geol.* **2010,** *273* (3-4), 272-285.
212. Aronniemi, M.; Sainio, J.; Lahtinen, J., Chemical state quantification of iron and chromium oxides using XPS: the effect of the background subtraction method. *Surf. Sci.* **2005,** *578* (1), 108-123.
213. Descostes, M.; Mercier, F.; Thromat, N.; Beaucaire, C.; Gautier-Soyer, M., Use of XPS in the determination of chemical environment and oxidation state of iron and sulfur samples: constitution of a data basis in binding energies for Fe and S reference compounds and applications to the evidence of surface species of an oxidized pyrite in a carbonate medium. *App. Surf. Sci.* **2000,** *165* (4), 288-302.
214. Lin, T.-C.; Seshadri, G.; Kelber, J. A., A consistent method for quantitative XPS peak analysis of thin oxide films on clean polycrystalline iron surfaces. *App. Surf. Sci.* **1997,** *119* (1), 83-92.
215. Grosvenor, A.; Kobe, B.; Biesinger, M.; McIntyre, N., Investigation of multiplet splitting of Fe 2p XPS spectra and bonding in iron compounds. *Surf. Inter. Ana.* **2004,** *36* (12), 1564-1574.
216. Yamashita, T.; Hayes, P., Analysis of XPS spectra of Fe^{2+} and Fe^{3+} ions in oxide materials. *App. Surf. Sci.* **2008,** *254* (8), 2441-2449.
217. Seah, M.; Brown, M., Validation and accuracy of software for peak synthesis in XPS. *J. Electron Spectro. Related Phenomena* **1998,** *95* (1), 71-93.
218. Courtin-Nomade, A.; Bril, H.; Bény, J.-M.; Kunz, M.; Tamura, N., Sulfide oxidation observed using micro-Raman spectroscopy and micro-X-ray diffraction: The importance of water/rock ratios and pH conditions. *Am. Mineral.* **2010,** *95* (4), 582-591.

219. Jia, Y.; Xu, L.; Fang, Z.; Demopoulos, G. P., Observation of surface precipitation of arsenate on ferrihydrite. *Environ. Sci. Technol.* **2006,** *40* (10), 3248-3253.
220. Kharbish, S.; Libowitzky, E.; Beran, A., The effect of As-Sb substitution in the Raman spectra of tetrahedrite-tennantite and pyrargyrite-proustite solid solutions. *Eur. J. Mineral.* **2007,** *19* (4), 567-574.
221. De Faria, D.; Venâncio Silva, S.; De Oliveira, M., Raman microspectroscopy of some iron oxides and oxyhydroxides. *J. Raman Spectrosc.* **1997,** *28* (11), 873-878.
222. Hanesch, M., Raman spectroscopy of iron oxides and (oxy) hydroxides at low laser power and possible applications in environmental magnetic studies. *Geophys. J. Int.* **2009,** *177* (3), 941-948.
223. Mazzetti, L.; Thistlethwaite, P., Raman spectra and thermal transformations of ferrihydrite and schwertmannite. *J. Raman Spectrosc.* **2002,** *33* (2), 104-111.
224. Likodimos, V.; Stergiopoulos, T.; Falaras, P.; Kunze, J.; Schmuki, P., Phase composition, size, orientation, and antenna effects of self-assembled anodized titania nanotube arrays: A polarized micro-Raman investigation. *J. Phys. Chem. C* **2008,** *112* (33), 12687-12696.
225. Roca, A. G.; Marco, J. F.; Morales, M. d. P.; Serna, C. J., Effect of nature and particle size on properties of uniform magnetite and maghemite nanoparticles. *J. Phys. Chem. C* **2007,** *111* (50), 18577-18584.
226. Lumsdon, D.; Meeussen, J.; Paterson, E.; Garden, L.; Anderson, P., Use of solid phase characterisation and chemical modelling for assessing the behaviour of arsenic in contaminated soils. *Appl. Geochem.* **2001,** *16* (6), 571-581.
227. Nesbitt, H.; Muir, I., Oxidation states and speciation of secondary products on pyrite and arsenopyrite reacted with mine waste waters and air. *Mineral. Petrol.* **1998,** *62* (1-2), 123-144.
228. Das, S.; Hendry, M. J., Application of Raman spectroscopy to identify iron minerals commonly found in mine wastes. *Chem. Geol.* **2011,** *290* (3-4), 101-108.
229. Sato, R. K.; McMillan, P. F., An infrared and Raman study of the isotopic species of. alpha.-quartz. *J. Phys. Chem.* **1987,** *91* (13), 3494-3498.
230. Zaghib, K.; Julien, C., Structure and electrochemistry of $FePO_4 \cdot 2H_2O$ hydrate. *J. Power Sources* **2005,** *142* (1-2), 279-284.
231. Hyeon, T.; Lee, S. S.; Park, J.; Chung, Y.; Na, H. B., Synthesis of highly crystalline and monodisperse maghemite nanocrystallites without a size-selection process. *J. Am. Chem. Soc.* **2001,** *123* (51), 12798-12801.
232. Zhang, L.; Zhu, Y.; Wu, X.; Jun, Y.-S., Effects of sulfate on biotite interfacial reactions under high temperature and high CO_2 pressure. *Phys. Chem. Chem. Phys.* **2019,** *21* (12), 6381-6390.
233. Montoro, L.; Rosolen, J.; Shin, J.; Passerini, S., Investigations of natural pyrite in solvent-free polymer electrolyte, lithium metal batteries. *Electrochim. Acta* **2004,** *49* (20), 3419-3427.
234. Borgnino, L.; Giacomelli, C. E.; Avena, M. J.; De Pauli, C. P., Phosphate adsorbed on Fe (III) modified montmorillonite: Surface complexation studied by ATR-FTIR spectroscopy. *Colloids Surf., A* **2010,** *353* (2), 238-244.
235. Tejedor-Tejedor, M. I.; Anderson, M. A., The protonation of phosphate on the surface of goethite as studied by CIR-FTIR and electrophoretic mobility. *Langmuir* **1990,** *6* (3), 602-611.
236. Zhang, L.; Kim, D.; Kim, Y.; Wan, J.; Jun, Y.-S., Effects of phosphate on biotite dissolution and secondary precipitation under conditions relevant to engineered subsurface processes. *Phys. Chem. Chem. Phys.* **2017,** *19* (44), 29895-29904.
237. Miot, J.; Benzerara, K.; Morin, G.; Kappler, A.; Bernard, S.; Obst, M.; Férard, C.; Skouri-Panet, F.; Guigner, J.-M.; Posth, N., Iron biomineralization by anaerobic neutrophilic iron-oxidizing bacteria. *Geochim. Cosmochim. Acta* **2009,** *73* (3), 696-711.
238. Fan, R.; Short, M. D.; Zeng, S.-J.; Qian, G.; Li, J.; Schumann, R. C.; Kawashima, N.; Smart, R. S. C.; Gerson, A. R., The formation of silicate-stabilized passivating layers on pyrite for reduced acid rock drainage. *Environ. Sci. Technol.* **2017,** *51* (19), 11317-11325.
239. Kargbo, D. M.; Atallah, G.; Chatterjee, S., Inhibition of pyrite oxidation by a phospholipid in the presence of silicate. *Environ. Sci. Technol.* **2004,** *38* (12), 3432-3441.

240. Swedlund, P. J.; Webster, J. G., Adsorption and polymerisation of silicic acid on ferrihydrite, and its effect on arsenic adsorption. *Water Res.* **1999,** *33* (16), 3413-3422.
241. Guan, X.; Dong, H.; Ma, J.; Jiang, L., Removal of arsenic from water: Effects of competing anions on As (III) removal in $KMnO_4$–Fe (II) process. *Water Res.* **2009,** *43* (15), 3891-3899.
242. Kaegi, R.; Voegelin, A.; Folini, D.; Hug, S. J., Effect of phosphate, silicate, and Ca on the morphology, structure and elemental composition of Fe (III)-precipitates formed in aerated Fe (II) and As (III) containing water. *Geochim. Cosmochim. Acta* **2010,** *74* (20), 5798-5816.
243. Kinsela, A. S.; Jones, A. M.; Bligh, M. W.; Pham, A. N.; Collins, R. N.; Harrison, J. J.; Wilsher, K. L.; Payne, T. E.; Waite, T. D., Influence of dissolved silicate on rates of Fe (II) oxidation. *Environ. Sci. Technol.* **2016,** *50* (21), 11663-11671.
244. Voegelin, A.; Kaegi, R.; Frommer, J.; Vantelon, D.; Hug, S. J., Effect of phosphate, silicate, and Ca on Fe (III)-precipitates formed in aerated Fe (II)-and As (III)-containing water studied by X-ray absorption spectroscopy. *Geochim. Cosmochim. Acta* **2010,** *74* (1), 164-186.
245. Kim, M.-J.; Nriagu, J.; Haack, S., Carbonate ions and arsenic dissolution by groundwater. *Environ. Sci. Technol.* **2000,** *34* (15), 3094-3100.
246. Nickson, R.; McArthur, J.; Ravenscroft, P.; Burgess, W.; Ahmed, K., Mechanism of arsenic release to groundwater, Bangladesh and West Bengal. *App. Geochem.* **2000,** *15* (4), 403-413.
247. Welch, A. H.; Lico, M. S., Factors controlling As and U in shallow ground water, southern Carson Desert, Nevada. *App. Geochem.* **1998,** *13* (4), 521-539.
248. Welch, A. H.; Westjohn, D.; Helsel, D. R.; Wanty, R. B., Arsenic in ground water of the United States: occurrence and geochemistry. *Ground water* **2000,** *38* (4), 589-604.
249. Fakhreddine, S.; Dittmar, J.; Phipps, D.; Dadakis, J.; Fendorf, S., Geochemical triggers of arsenic mobilization during managed aquifer recharge. *Environ. Sci. Technol.* **2015,** *49* (13), 7802-7809.
250. Bhargava, G.; Gouzman, I.; Chun, C.; Ramanarayanan, T.; Bernasek, S., Characterization of the "native" surface thin film on pure polycrystalline iron: A high resolution XPS and TEM study. *Appl. Surf. Sci.* **2007,** *253* (9), 4322-4329.
251. Gui, Q.; Sun, L.; Liu, L.; Wu, X.; Chu, P. K., d 0 ferromagnetism in black phosphorous oxide caused by surface PO bonds. *Appl. Phys. Lett.* **2016,** *108* (9), 091602.
252. Puziy, A.; Poddubnaya, O.; Socha, R.; Gurgul, J.; Wisniewski, M., XPS and NMR studies of phosphoric acid activated carbons. *Carbon* **2008,** *46* (15), 2113-2123.
253. Jensen, D. S.; Kanyal, S. S.; Madaan, N.; Vail, M. A.; Dadson, A. E.; Engelhard, M. H.; Linford, M. R., Silicon (100)/SiO_2 by XPS. *Surf. Sci. Spectra* **2013,** *20* (1), 36-42.
254. Arai, Y.; Sparks, D. L., ATR–FTIR spectroscopic investigation on phosphate adsorption mechanisms at the ferrihydrite–water interface. *J. Colloid Interface Sci.* **2001,** *241* (2), 317-326.
255. Abdelghany, A.; ElBatal, F.; ElBatal, H.; EzzElDin, F., Optical and FTIR structural studies of CoO-doped sodium borate, sodium silicate and sodium phosphate glasses and effects of gamma irradiation-a comparative study. *J. Mole. Struc.* **2014,** *1074*, 503-510.
256. Liao, L.-F.; Lien, C.-F.; Shieh, D.-L.; Chen, M.-T.; Lin, J.-L., FTIR study of adsorption and photoassisted oxygen isotopic exchange of carbon monoxide, carbon dioxide, carbonate, and formate on TiO_2. *J. Phys. Chem. B* **2002,** *106* (43), 11240-11245.
257. Criado, M.; Palomo, A.; Fernández-Jiménez, A., Alkali activation of fly ashes. Part 1: Effect of curing conditions on the carbonation of the reaction products. *Fuel* **2005,** *84* (16), 2048-2054.
258. Alley, W. M.; Healy, R. W.; LaBaugh, J. W.; Reilly, T. E., Flow and storage in groundwater systems. *Science* **2002,** *296* (5575), 1985-1990.
259. Famiglietti, J. S., The global groundwater crisis. *Nat. Clim. Change* **2014,** *4* (11), 945-948.
260. Famiglietti, J.; Lo, M.; Ho, S.; Bethune, J.; Anderson, K.; Syed, T.; Swenson, S.; De Linage, C.; Rodell, M., Satellites measure recent rates of groundwater depletion in California's Central Valley. *Geophys. Res. Lett.* **2011,** *38* (3), L03403.

261. Feng, W.; Zhong, M.; Lemoine, J. M.; Biancale, R.; Hsu, H. T.; Xia, J., Evaluation of groundwater depletion in North China using the Gravity Recovery and Climate Experiment (GRACE) data and ground‐based measurements. *Water Resour. Res.* **2013,** *49* (4), 2110-2118.
262. Rodell, M.; Velicogna, I.; Famiglietti, J. S., Satellite-based estimates of groundwater depletion in India. *Nature* **2009,** *460* (7258), 999.
263. Konikow, L. F.; Kendy, E., Groundwater depletion: A global problem. *Hydrogeol. J.* **2005,** *13* (1), 317-320.
264. Dillon, P.; Pavelic, P.; Page, D.; Beringen, H.; Ward, J., Managed aquifer recharge. *An introduction Waterlines Report Series* **2009,** *13*.
265. Corkhill, C.; Vaughan, D., Arsenopyrite oxidation–A review. *Appl. Geochem.* **2009,** *24* (12), 2342-2361.
266. Maeng, S. K.; Sharma, S. K.; Lekkerkerker-Teunissen, K.; Amy, G. L., Occurrence and fate of bulk organic matter and pharmaceutically active compounds in managed aquifer recharge: a review. *Water Res.* **2011,** *45* (10), 3015-3033.
267. Seitzinger, S. P.; Styles, R. M.; Lauck, R.; Mazurek, M. A., Atmospheric pressure mass spectrometry: a new analytical chemical characterization method for dissolved organic matter in rainwater. *Environ. Sci. Technol.* **2003,** *37* (1), 131-137.
268. Pabich, W. J.; Valiela, I.; Hemond, H. F., Relationship between DOC concentration and vadose zone thickness and depth below water table in groundwater of Cape Cod, USA. *Biogeochemistry* **2001,** *55* (3), 247-268.
269. Quanrud, D. M.; Hafer, J.; Karpiscak, M. M.; Zhang, J.; Lansey, K. E.; Arnold, R. G., Fate of organics during soil-aquifer treatment: sustainability of removals in the field. *Water Res.* **2003,** *37* (14), 3401-3411.
270. Vanderzalm, J. L.; La Salle, C. L. G.; Dillon, P., Fate of organic matter during aquifer storage and recovery (ASR) of reclaimed water in a carbonate aquifer. *Appl. Geochem.* **2006,** *21* (7), 1204-1215.
271. Bauer, M.; Blodau, C., Mobilization of arsenic by dissolved organic matter from iron oxides, soils and sediments. *Sci. Total Environ.* **2006,** *354* (2-3), 179-190.
272. Redman, A. D.; Macalady, D. L.; Ahmann, D., Natural organic matter affects arsenic speciation and sorption onto hematite. *Environ. Sci. Technol.* **2002,** *36* (13), 2889-2896.
273. Buschmann, J.; Kappeler, A.; Lindauer, U.; Kistler, D.; Berg, M.; Sigg, L., Arsenite and arsenate binding to dissolved humic acids: influence of pH, type of humic acid, and aluminum. *Environ. Sci. Technol.* **2006,** *40* (19), 6015-6020.
274. Sharma, P.; Ofner, J.; Kappler, A., Formation of binary and ternary colloids and dissolved complexes of organic matter, Fe and As. *Environ. Sci. Technol.* **2010,** *44* (12), 4479-4485.
275. Sharma, P.; Rolle, M.; Kocar, B.; Fendorf, S.; Kappler, A., Influence of natural organic matter on As transport and retention. *Environ. Sci. Technol.* **2010,** *45* (2), 546-553.
276. Weng, L.; Van Riemsdijk, W. H.; Hiemstra, T., Effects of fulvic and humic acids on arsenate adsorption to goethite: experiments and modeling. *Environ. Sci. Technol.* **2009,** *43* (19), 7198-7204.
277. Chen, J.; Gu, B.; Royer, R. A.; Burgos, W. D., The roles of natural organic matter in chemical and microbial reduction of ferric iron. *Sci. Total Environ.* **2003,** *307* (1-3), 167-178.
278. Kulkarni, H. V.; Mladenov, N.; McKnight, D. M.; Zheng, Y.; Kirk, M. F.; Nemergut, D. R., Dissolved fulvic acids from a high arsenic aquifer shuttle electrons to enhance microbial iron reduction. *Sci. Total Environ.* **2018,** *615*, 1390-1395.
279. Chen, W.; Westerhoff, P.; Leenheer, J. A.; Booksh, K., Fluorescence excitation− emission matrix regional integration to quantify spectra for dissolved organic matter. *Environ. Sci. Technol.* **2003,** *37* (24), 5701-5710.
280. Wu, X.; Neil, C.; Kim, D.; Jung, H.; Jun, Y.-S., Co-effects of UV/H_2O_2 and Natural Organic Matter on the Surface Chemistry of Cerium Oxide Nanoparticles. *Environ. Sci. Nano* **2018,** *5* (10), 2382-2393.

281. Gaffney, J. S.; Marley, N. A.; Clark, S. B. *Humic and fluvic acids and organic colloidal materials in the environment*; ANL/ER/CP-89942; CONF-9608110-1
ON: DE96012697; TRN: 96:004712; Argonne National Lab., IL (United States): **1996**.
282. Barker, D. J.; Stuckey, D. C., A review of soluble microbial products (SMP) in wastewater treatment systems. *Water Res.* **1999,** *33* (14), 3063-3082.
283. Shon, H.; Vigneswaran, S.; Snyder, S., Effluent organic matter (EfOM) in wastewater: constituents, effects, and treatment. *Crit. Rev. Env. Sci. Tec.* **2006,** *36* (4), 327-374.
284. Cheng, H.; Hu, Y.; Luo, J.; Xu, B.; Zhao, J., Geochemical processes controlling fate and transport of arsenic in acid mine drainage (AMD) and natural systems. *J. Hazard. Mater.* **2009,** *165* (1-3), 13-26.
285. Donahue, R.; Hendry, M., Geochemistry of arsenic in uranium mine mill tailings, Saskatchewan, Canada. *Appl. Geochem.* **2003,** *18* (11), 1733-1750.
286. McGuire, M. M.; Banfield, J. F.; Hamers, R. J., Quantitative determination of elemental sulfur at the arsenopyrite surface after oxidation by ferric iron: mechanistic implications. *Geochem. T.* **2001,** *2* (1), 25-29.
287. Averett, R. C.; Leenheer, J.; McKnight, D. M.; Thorn, K. *Humic substances in the Suwannee River, Georgia; interactions, properties, and proposed structures*; USGPO; US Geological Survey, Map Distribution: **1994**.
288. Hong, J.; Liu, L.; Luo, Y.; Tan, W.; Qiu, G.; Liu, F., Photochemical oxidation and dissolution of arsenopyrite in acidic solutions. *Geochim. Cosmochim. Acta* **2018,** *239*, 173-185.
289. Jang, J.-H.; Dempsey, B. A., Coadsorption of arsenic (III) and arsenic (V) onto hydrous ferric oxide: effects on abiotic oxidation of arsenic (III), extraction efficiency, and model accuracy. *Environ. Sci. Technol.* **2008,** *42* (8), 2893-2898.
290. Qiu, G.; Gao, T.; Hong, J.; Tan, W.; Liu, F.; Zheng, L., Mechanisms of arsenic-containing pyrite oxidation by aqueous arsenate under anoxic conditions. *Geochim. Cosmochim. Acta* **2017,** *217*, 306-319.
291. De Winter, J. C., Using the Student's t-test with extremely small sample sizes. *Pract. Assess., Res. Eval.* **2013,** *18* (10).
292. Fenter, P.; Sturchio, N. C., Mineral–water interfacial structures revealed by synchrotron X-ray scattering. *Prog. Surf. Sci.* **2004,** *77* (5-8), 171-258.
293. Jun, Y.-S.; Lee, B.; Waychunas, G. A., In situ observations of nanoparticle early development kinetics at mineral−water interfaces. *Environ. Sci. Technol.* **2010,** *44* (21), 8182-8189.
294. Masscheleyn, P. H.; Delaune, R. D.; Patrick Jr, W. H., Effect of redox potential and pH on arsenic speciation and solubility in a contaminated soil. *Environ. Sci. Technol.* **1991,** *25* (8), 1414-1419.
295. De Faria, D.; Venâncio Silva, S.; De Oliveira, M., Raman microspectroscopy of some iron oxides and oxyhydroxides. *J Raman Spectrosc.* **1997,** *28* (11), 873-878.
296. Wang, S.; Mulligan, C. N., Effects of three low-molecular-weight organic acids (LMWOAs) and pH on the mobilization of arsenic and heavy metals (Cu, Pb, and Zn) from mine tailings. *Environ. Geochem. Hlth* **2013,** *35* (1), 111-118.
297. Ray, J. R.; Lee, B.; Baltrusaitis, J.; Jun, Y.-S., Formation of iron (III)(hydr) oxides on polyaspartate-and alginate-coated substrates: effects of coating hydrophilicity and functional group. *Environ. Sci. Technol.* **2012,** *46* (24), 13167-13175.
298. Teixeira, J., Small‐angle scattering by fractal systems. *J. Appl. Crystallogr.* **1988,** *21* (6), 781-785.
299. Robinson, D.; Earnshaw, J., Experimental study of colloidal aggregation in two dimensions. I. Structural aspects. *Phys. Rev. A* **1992,** *46* (4), 2045-2054.
300. Hu, Y.; Lee, B.; Bell, C.; Jun, Y.-S., Environmentally abundant anions influence the nucleation, growth, ostwald ripening, and aggregation of hydrous Fe (III) oxides. *Langmuir* **2012,** *28* (20), 7737-7746.

301. Kennedy, C.; Scott, S.; Ferris, F., Hydrothermal phase stabilization of 2-line ferrihydrite by bacteria. *Chem. Geol.* **2004,** *212* (3-4), 269-277.
302. Gunsolus, I. L.; Mousavi, M. P.; Hussein, K.; Bühlmann, P.; Haynes, C. L., Effects of humic and fulvic acids on silver nanoparticle stability, dissolution, and toxicity. *Environ. Sci. Technol.* **2015,** *49* (13), 8078-8086.
303. Hur, J.; Schlautman, M. A., Humic substance adsorptive fractionation by minerals and its subsequent effects on pyrene sorption isotherms. *J. Environ. Sci. Health Part A* **2006,** *41* (3), 343-358.
304. Park, H.; Myung, N. V.; Jung, H.; Choi, H., As (V) remediation using electrochemically synthesized maghemite nanoparticles. *J. Nanopart. Res.* **2009,** *11* (8), 1981-1989.
305. Jun, Y. S.; Lee, B., Total X‐Ray Scattering and Small‐Angle X‐ray Scattering for Determining the Structures, Sizes, Shapes, and Aggregation Extents of Iron (Hydr) oxide Nanoparticles. *Iron Oxides: From Nature to Applications* **2016**, 371-396.
306. Li, Q.; Fernandez-Martinez, A.; Lee, B.; Waychunas, G. A.; Jun, Y.-S., Interfacial energies for heterogeneous nucleation of calcium carbonate on mica and quartz. *Environ. Sci. Technol.* **2014,** *48* (10), 5745-5753.
307. Waychunas, G. A.; Kim, C. S.; Banfield, J. F., Nanoparticulate iron oxide minerals in soils and sediments: unique properties and contaminant scavenging mechanisms. *J. Nano. Res.* **2005,** *7* (4-5), 409-433.
308. Ferris, F.; Tazaki, K.; Fyfe, W., Iron oxides in acid mine drainage environments and their association with bacteria. *Chem. Geol.* **1989,** *74* (3-4), 321-330.
309. Jew, A. D.; Dustin, M. K.; Harrison, A. L.; Joe-Wong, C. M.; Thomas, D. L.; Maher, K.; Brown Jr, G. E.; Bargar, J. R., Impact of organics and carbonates on the oxidation and precipitation of iron during hydraulic fracturing of shale. *Energy & Fuels* **2017,** *31* (4), 3643-3658.
310. Ghauch, A.; Tuqan, A.; Assi, H. A., Antibiotic removal from water: elimination of amoxicillin and ampicillin by microscale and nanoscale iron particles. *Environ. Pollut.* **2009,** *157* (5), 1626-1635.
311. Hua, M.; Yang, B.; Shan, C.; Zhang, W.; He, S.; Lv, L.; Pan, B., Simultaneous removal of As (V) and Cr (VI) from water by macroporous anion exchanger supported nanoscale hydrous ferric oxide composite. *Chemosphere* **2017,** *171*, 126-133.
312. Neubauer, U.; Furrer, G.; Schulin, R., Heavy metal sorption on soil minerals affected by the siderophore desferrioxamine B: the role of Fe (III)(hydr) oxides and dissolved Fe (III). *Euro. J. Soil Sci.* **2002,** *53* (1), 45-55.
313. Stipp, S.; Hansen, M.; Kristensen, R.; Hochella Jr, M.; Bennedsen, L.; Dideriksen, K.; Balic-Zunic, T.; Leonard, D.; Mathieu, H.-J., Behaviour of Fe-oxides relevant to contaminant uptake in the environment. *Chem. Geol.* **2002,** *190* (1-4), 321-337.
314. Banfield, J. F.; Zhang, H., Nanoparticles in the environment. *Rev. Miner. Geochem.* **2001,** *44* (1), 1-58.
315. Cornell, R. M.; Schwertmann, U., *The iron oxides: structure, properties, reactions, occurrences and uses*. John Wiley & Sons: 2003.
316. Huffman, G.; Ganguly, B.; Zhao, J.; Rao, K.; Shah, N.; Feng, Z.; Huggins, F.; Taghiei, M. M.; Lu, F., Structure and dispersion of iron-based catalysts for direct coal liquefaction. *Energy & Fuels* **1993,** *7* (2), 285-296.
317. Pouran, S. R.; Raman, A. A. A.; Daud, W. M. A. W., Review on the application of modified iron oxides as heterogeneous catalysts in Fenton reactions. *J. Cleaner Product.* **2014,** *64*, 24-35.
318. Karthika, S.; Radhakrishnan, T.; Kalaichelvi, P., A review of classical and nonclassical nucleation theories. *Cryst. Growth Des.* **2016,** *16* (11), 6663-6681.
319. Chen, X.; Schröder, J.; Hauschild, S.; Rosenfeldt, S.; Dulle, M.; Förster, S., Simultaneous SAXS/WAXS/UV–vis study of the nucleation and growth of nanoparticles: a test of classical nucleation theory. *Langmuir* **2015,** *31* (42), 11678-11691.

320. Jun, Y.-S.; Kim, D.; Neil, C. W., Heterogeneous nucleation and growth of nanoparticles at environmental interfaces. *Acc. Chemi. Res.* **2016,** *49* (9), 1681-1690.
321. Sharifi Dehsari, H.; Heidari, M.; Halda Ribeiro, A.; Tremel, W.; Jakob, G.; Donadio, D.; Potestio, R.; Asadi, K., Combined Experimental and Theoretical Investigation of Heating Rate on Growth of Iron Oxide Nanoparticles. *Chem. Mater.* **2017,** *29* (22), 9648-9656.
322. Nielsen, M. H.; Aloni, S.; De Yoreo, J. J., In situ TEM imaging of $CaCO_3$ nucleation reveals coexistence of direct and indirect pathways. *Science* **2014,** *345* (6201), 1158-1162.
323. Habraken, W. J.; Tao, J.; Brylka, L. J.; Friedrich, H.; Bertinetti, L.; Schenk, A. S.; Verch, A.; Dmitrovic, V.; Bomans, P. H.; Frederik, P. M., Ion-association complexes unite classical and non-classical theories for the biomimetic nucleation of calcium phosphate. *Nature communications* **2013,** *4* (1), 1-12.
324. De Yoreo, J. J.; Vekilov, P. G., Principles of crystal nucleation and growth. *Rev. Miner. Geochem.* **2003,** *54* (1), 57-93.
325. Hu, Q.; Nielsen, M. H.; Freeman, C.; Hamm, L.; Tao, J.; Lee, J.; Han, T. Y.-J.; Becker, U.; Harding, J.; Dove, P., The thermodynamics of calcite nucleation at organic interfaces: Classical vs. non-classical pathways. *Fara. Discus.* **2012,** *159* (1), 509-523.
326. Li, Q.; Jun, Y.-S., The apparent activation energy and pre-exponential kinetic factor for heterogeneous calcium carbonate nucleation on quartz. *Comm. Chem.* **2018,** *1* (1), 56.
327. Li, Q.; Jun, Y.-S., Salinity-Induced Reduction of Interfacial Energies and Kinetic Factors during Calcium Carbonate Nucleation on Quartz. *J. Phys. Chem. C* **2019,** *123* (23), 14319-14326.
328. Fernandez-Martinez, A.; Hu, Y.; Lee, B.; Jun, Y.-S.; Waychunas, G. A., In situ determination of interfacial energies between heterogeneously nucleated $CaCO_3$ and quartz substrates: thermodynamics of CO_2 mineral trapping. *Environ. Sci. Technol.* **2012,** *47* (1), 102-109.
329. Pontoni, D.; Bolze, J.; Dingenouts, N.; Narayanan, T.; Ballauff, M., Crystallization of calcium carbonate observed in-situ by combined small-and wide-angle X-ray scattering. *J. Phy. Chem. B* **2003,** *107* (22), 5123-5125.
330. Jung, H.; Lee, B.; Jun, Y.-S., Structural match of heterogeneously nucleated $Mn(OH)_2$(s) nanoparticles on quartz under various pH conditions. *Langmuir* **2016,** *32* (41), 10735-10743.
331. Legg, B. A.; Zhu, M.; Zhang, H.; Waychunas, G.; Gilbert, B.; Banfield, J. F., A model for nucleation when nuclei are nonstoichiometric: understanding the precipitation of iron oxyhydroxide nanoparticles. *Cryst. Growth Des.* **2016,** *16* (10), 5726-5737.
332. Hiemstra, T., Formation, stability, and solubility of metal oxide nanoparticles: Surface entropy, enthalpy, and free energy of ferrihydrite. *Geochim. Cosmochim. Acta* **2015,** *158*, 179-198.
333. de Leeuw, N. H.; Cooper, T. G., Surface simulation studies of the hydration of white rust $Fe(OH)_2$, goethite α-FeO(OH) and hematite α-Fe_2O_3. *Geochim. Cosmochim. Acta* **2007,** *71* (7), 1655-1673.
334. Kashchiev, D.; Van Rosmalen, G., Nucleation in solutions revisited. *Crystal Res. Technol.* **2003,** *38* (7‐8), 555-574.
335. Steefel, C. I.; Van Cappellen, P., A new kinetic approach to modeling water-rock interaction: The role of nucleation, precursors, and Ostwald ripening. *Geochim. Cosmochim. Acta* **1990,** *54* (10), 2657-2677.
336. Nielsen, A. E., *Kinetics of precipitation*. Pergamon: 1964; Vol. 18.
337. Wallace, A. F.; DeYoreo, J. J.; Dove, P. M., Kinetics of silica nucleation on carboxyl-and amine-terminated surfaces: insights for biomineralization. *J. Am. Chem. Soc.* **2009,** *131* (14), 5244-5250.
338. Hu, Y.; Neil, C.; Lee, B.; Jun, Y.-S., Control of heterogeneous Fe (III)(hydr) oxide nucleation and growth by interfacial energies and local saturations. *Environ. Sci. Technol.* **2013,** *47* (16), 9198-9206.
339. Schmidbauer, M.; Grigoriev, D.; Hanke, M.; Schäfer, P.; Wiebach, T.; Köhler, R., Effects of grazing incidence conditions on the x-ray diffuse scattering from self-assembled nanoscale islands. *Phys. Rev. B* **2005,** *71* (11), 115324.

340. Li, Q.; Steefel, C. I.; Jun, Y.-S., Incorporating nanoscale effects into a continuum-scale reactive transport model for CO_2-deteriorated cement. *Environ. Sci. Technol.* **2017,** *51* (18), 10861-10871.
341. Li, Q.; Jew, A. D.; Kohli, A.; Maher, K.; Brown Jr, G. E.; Bargar, J. R., Thicknesses of Chemically Altered Zones in Shale Matrices Resulting from Interactions with Hydraulic Fracturing Fluid. *Energy & Fuels* **2019,** *33* (8), 6878-6889.
342. Bigham, J.; Schwertmann, U.; Pfab, G., Influence of pH on mineral speciation in a bioreactor simulating acid mine drainage. *Appl. Geochem.* **1996,** *11* (6), 845-849.
343. Stefánsson, A., Iron (III) hydrolysis and solubility at 25 C. *Environ. Sci. Technol.* **2007,** *41* (17), 6117-6123.
344. Michel, F. M.; Ehm, L.; Antao, S. M.; Lee, P. L.; Chupas, P. J.; Liu, G.; Strongin, D. R.; Schoonen, M. A.; Phillips, B. L.; Parise, J. B., The structure of ferrihydrite, a nanocrystalline material. *Science* **2007,** *316* (5832), 1726-1729.
345. Lee, B.; Seifert, S.; Riley, S. J.; Tikhonov, G.; Tomczyk, N. A.; Vajda, S.; Winans, R. E., Anomalous grazing incidence small-angle x-ray scattering studies of platinum nanoparticles formed by cluster deposition. *J. Chem. Phys.* **2005,** *123* (7), 074701.
346. Yoneda, Y., Anomalous surface reflection of X rays. *Phys. Rev.* **1963,** *131* (5), 2010.
347. Kukkadapu, R. K.; Zachara, J. M.; Fredrickson, J. K.; Smith, S. C.; Dohnalkova, A. C.; Russell, C. K., Transformation of 2-line ferrihydrite to 6-line ferrihydrite under oxic and anoxic conditions. *Am. Mineral.* **2003,** *88* (11-12), 1903-1914.
348. Navrotsky, A.; Mazeina, L.; Majzlan, J., Size-driven structural and thermodynamic complexity in iron oxides. *Science* **2008,** *319* (5870), 1635-1638.
349. Jambor, J. L.; Dutrizac, J. E., Occurrence and constitution of natural and synthetic ferrihydrite, a widespread iron oxyhydroxide. *Chem. Rev.* **1998,** *98* (7), 2549-2586.
350. Pinney, N.; Kubicki, J. D.; Middlemiss, D. S.; Grey, C. P.; Morgan, D., Density functional theory study of ferrihydrite and related Fe-oxyhydroxides. *Chem. Mater.* **2009,** *21* (24), 5727-5742.
351. Towe, K. M.; Bradley, W. F., Mineralogical constitution of colloidal "hydrous ferric oxides". *J. Colloid Interf. Sci.* **1967,** *24* (3), 384-392.
352. Cornell, R.; Giovanoli, R., The influence of copper on the transformation of ferrihydrite ($5Fe_2O_3 \cdot 9H_2O$) into crystalline products in alkaline media. *Polyhedron* **1988,** *7* (5), 385-391.
353. Jansen, E.; Kyek, A.; Schäfer, W.; Schwertmann, U., The structure of six-line ferrihydrite. *Appl. Phy. A* **2002,** *74* (1), s1004-s1006.
354. Kim, D.; Lee, B.; Thomopoulos, S.; Jun, Y.-S., The role of confined collagen geometry in decreasing nucleation energy barriers to intrafibrillar mineralization. *Nature Comm.* **2018,** *9* (1), 962.
355. Birkner, N.; Navrotsky, A., Thermodynamics of manganese oxides: Effects of particle size and hydration on oxidation-reduction equilibria among hausmannite, bixbyite, and pyrolusite. *Am. Mineral.* **2012,** *97* (8-9), 1291-1298.
356. Manceau, A.; Gates, W., Surface structural model for ferrihydrite. *Clays Clay Mineral.* **1997,** *45* (3), 448-460.
357. Dillon, P.; Arshad, M., Managed aquifer recharge in integrated water resource management. In *Integrated groundwater management*, Springer, Cham: 2016; pp 435-452.
358. Marie, P.; Géraldine, P.-C.; Dominique, T.; Alexandre, B.; Marina, A.; Jérome, P.; Benoît, D.; Jean-Christophe, M.; Shakeel, A.; Wolfram, K., Water quality evolution during managed aquifer recharge (MAR) in Indian crystalline basement aquifers: reactive transport modeling in the critical zone. *Pr Earth Planet Sci* **2014,** *10*, 82-87.
359. Nham, H. T. T.; Greskowiak, J.; Nödler, K.; Rahman, M. A.; Spachos, T.; Rusteberg, B.; Massmann, G.; Sauter, M.; Licha, T., Modeling the transport behavior of 16 emerging organic contaminants during soil aquifer treatment. *Sci. Total Environ.* **2015,** *514*, 450-458.
360. Wallis, I.; Prommer, H.; Pichler, T.; Post, V.; B. Norton, S.; Annable, M. D.; Simmons, C. T., Process-based reactive transport model to quantify arsenic mobility during aquifer storage and recovery of potable water. *Environ. Sci. Technol.* **2011,** *45* (16), 6924-6931.

361. Tijing, L. D.; Woo, Y. C.; Choi, J.-S.; Lee, S.; Kim, S.-H.; Shon, H. K., Fouling and its control in membrane distillation—A review. *J. Mem. Sci.* **2015,** *475*, 215-244.
362. Yiantsios, S. G.; Karabelas, A. J., An assessment of the Silt Density Index based on RO membrane colloidal fouling experiments with iron oxide particles. *Desalination* **2003,** *151* (3), 229-238.
363. Parks, G. A., Surface and interfacial free energies of quartz. *J. Geophys. Res.* **1984,** *89* (B6), 3997-4008.
364. Snow, C.; Lilova, K.; Radha, A.; Shi, Q.; Smith, S.; Navrotsky, A.; Boerio-Goates, J.; Woodfield, B., Heat capacity and thermodynamics of a synthetic two-line ferrihydrite, FeOOH· 0.027 H_2O. *J. Chem. Thermo.* **2013,** *58*, 307-314.
365. Jung, H.; Lee, B.; Jun, Y.-S., Structural match of heterogeneously nucleated Mn $(OH)_2$ (s) nanoparticles on quartz under various pH conditions. *Langmuir* **2016,** *32* (41), 10735-10743.
366. Holder, C. F.; Schaak, R. E., Tutorial on Powder X-ray Diffraction for Characterizing Nanoscale Materials. ACS Publications: 2019.
367. Alcamo, J.; Flörke, M.; Märker, M., Future long-term changes in global water resources driven by socio-economic and climatic changes. *Hydrolog. Sci. J.* **2007,** *52* (2), 247-275.
368. Arnell, N. W., Climate change and global water resources: SRES emissions and socio-economic scenarios. *Glob. Environ. Change* **2004,** *14* (1), 31-52.
369. Vörösmarty, C. J.; Green, P.; Salisbury, J.; Lammers, R. B., Global water resources: vulnerability from climate change and population growth. *Science* **2000,** *289* (5477), 284-288.
370. El-Dessouky, H. T.; Ettouney, H. M., *Fundamentals of salt water desalination*. Elsevier: 2002.
371. Shannon, M. A.; Bohn, P. W.; Elimelech, M.; Georgiadis, J. G.; Marinas, B. J.; Mayes, A. M., Science and technology for water purification in the coming decades. *Nature* **2008,** *452* (7185), 301.
372. IDA, 2016 – 2017 IDA Desalination Yearbook. *2016 – 2017 IDA Desalination Yearbook* **2017**.
373. Childress, A. E.; Elimelech, M., Effect of solution chemistry on the surface charge of polymeric reverse osmosis and nanofiltration membranes. *J. Membr. Sci.* **1996,** *119* (2), 253-268.
374. Fritzmann, C.; Löwenberg, J.; Wintgens, T.; Melin, T., State-of-the-art of reverse osmosis desalination. *Desalination* **2007,** *216* (1-3), 1-76.
375. Greenlee, L. F.; Lawler, D. F.; Freeman, B. D.; Marrot, B.; Moulin, P., Reverse osmosis desalination: water sources, technology, and today's challenges. *Water Res.* **2009,** *43* (9), 2317-2348.
376. Ortiz, J.; Sotoca, J.; Exposito, E.; Gallud, F.; Garcia-Garcia, V.; Montiel, V.; Aldaz, A., Brackish water desalination by electrodialysis: batch recirculation operation modeling. *J. Membr. Sci.* **2005,** *252* (1-2), 65-75.
377. Sadrzadeh, M.; Mohammadi, T., Sea water desalination using electrodialysis. *Desalination* **2008,** *221* (1-3), 440-447.
378. Khawaji, A. D.; Kutubkhanah, I. K.; Wie, J.-M., Advances in seawater desalination technologies. *Desalination* **2008,** *221* (1-3), 47-69.
379. Zhao, D.; Xue, J.; Li, S.; Sun, H.; Zhang, Q.-d., Theoretical analyses of thermal and economical aspects of multi-effect distillation desalination dealing with high-salinity wastewater. *Desalination* **2011,** *273* (2-3), 292-298.
380. Souhaimi, M. K.; Matsuura, T., *Membrane distillation: principles and applications*. Elsevier: 2011.
381. Deshmukh, A.; Boo, C.; Karanikola, V.; Lin, S.; Straub, A. P.; Tong, T.; Warsinger, D. M.; Elimelech, M., Membrane Distillation at the Water-Energy Nexus: Limits, Opportunities, and Challenges. *Energy Environ. Sci.* **2018**.
382. El-Bourawi, M.; Ding, Z.; Ma, R.; Khayet, M., A framework for better understanding membrane distillation separation process. *J. Membr. Sci.* **2006,** *285* (1-2), 4-29.

383. Camacho, L. M.; Dumée, L.; Zhang, J.; Li, J.-d.; Duke, M.; Gomez, J.; Gray, S., Advances in membrane distillation for water desalination and purification applications. *Water* **2013,** *5* (1), 94-196.
384. Chafidz, A.; Al-Zahrani, S.; Al-Otaibi, M. N.; Hoong, C. F.; Lai, T. F.; Prabu, M., Portable and integrated solar-driven desalination system using membrane distillation for arid remote areas in Saudi Arabia. *Desalination* **2014,** *345*, 36-49.
385. Dow, N.; Gray, S.; Zhang, J.; Ostarcevic, E.; Liubinas, A.; Atherton, P.; Roeszler, G.; Gibbs, A.; Duke, M., Pilot trial of membrane distillation driven by low grade waste heat: Membrane fouling and energy assessment. *Desalination* **2016,** *391*, 30-42.
386. Gálvez, J. B.; García-Rodríguez, L.; Martín-Mateos, I., Seawater desalination by an innovative solar-powered membrane distillation system: the MEDESOL project. *Desalination* **2009,** *246* (1-3), 567-576.
387. Hogan, P.; Fane, A.; Morrison, G., Desalination by solar heated membrane distillation. *Desalination* **1991,** *81* (1-3), 81-90.
388. Koschikowski, J.; Wieghaus, M.; Rommel, M., Solar thermal-driven desalination plants based on membrane distillation. *Desalination* **2003,** *156* (1-3), 295-304.
389. Qtaishat, M. R.; Banat, F., Desalination by solar powered membrane distillation systems. *Desalination* **2013,** *308*, 186-197.
390. Schofield, R.; Fane, A.; Fell, C., Heat and mass transfer in membrane distillation. *J. Membr. Sci.* **1987,** *33* (3), 299-313.
391. Schofield, R.; Fane, A.; Fell, C.; Macoun, R., Factors affecting flux in membrane distillation. *Desalination* **1990,** *77*, 279-294.
392. Summers, E. K., Experimental study of thermal performance in air gap membrane distillation systems, including the direct solar heating of membranes. *Desalination* **2013,** *330*, 100-111.
393. Lee, H.; Dellatore, S. M.; Miller, W. M.; Messersmith, P. B., Mussel-inspired surface chemistry for multifunctional coatings. *Science* **2007,** *318* (5849), 426-430.
394. Liu, Y.; Ai, K.; Lu, L., Polydopamine and its derivative materials: synthesis and promising applications in energy, environmental, and biomedical fields. *Chem. Rev.* **2014,** *114* (9), 5057-5115.
395. Kim, B. H.; Lee, D. H.; Kim, J. Y.; Shin, D. O.; Jeong, H. Y.; Hong, S.; Yun, J. M.; Koo, C. M.; Lee, H.; Kim, S. O., Mussel‐Inspired Block Copolymer Lithography for Low Surface Energy Materials of Teflon, Graphene, and Gold. *Adv. Mater.* **2011,** *23* (47), 5618-5622.
396. d'Ischia, M.; Napolitano, A.; Ball, V.; Chen, C.-T.; Buehler, M. J., Polydopamine and eumelanin: From structure–property relationships to a unified tailoring strategy. *Acc. Chem. Res.* **2014,** *47* (12), 3541-3550.
397. Forest, S. E.; Simon, J. D., Wavelength‐dependent Photoacoustic Calorimetry Study of Melanin. *Photochem. Photobiol.* **1998,** *68* (3), 296-298.
398. Jiang, Q.; Derami, H. G.; Ghim, D.; Cao, S.; Jun, Y.-S.; Singamaneni, S., Polydopamine-filled bacterial nanocellulose as a biodegradable interfacial photothermal evaporator for highly efficient solar steam generation. *J. Mater. Chem. A* **2017,** *5* (35), 18397-18402.
399. Riesz, J.; Sarna, T.; Meredith, P., Radiative relaxation in synthetic pheomelanin. *J. Phys. Chem. B* **2006,** *110* (28), 13985-13990.
400. Simon, J. D., Spectroscopic and dynamic studies of the epidermal chromophores trans-urocanic acid and eumelanin. *Acc. Chem. Res.* **2000,** *33* (5), 307-313.
401. Black, K. C.; Yi, J.; Rivera, J. G.; Zelasko-Leon, D. C.; Messersmith, P. B., Polydopamine-enabled surface functionalization of gold nanorods for cancer cell-targeted imaging and photothermal therapy. *Nanomedicine* **2013,** *8* (1), 17-28.
402. Liu, Y.; Ai, K.; Liu, J.; Deng, M.; He, Y.; Lu, L., Dopamine‐melanin colloidal nanospheres: an efficient near‐infrared photothermal therapeutic agent for in vivo cancer therapy. *Adv. Mater.* **2013,** *25* (9), 1353-1359.

403. Hong, S.; Kim, K. Y.; Wook, H. J.; Park, S. Y.; Lee, K. D.; Lee, D. Y.; Lee, H., Attenuation of the in vivo toxicity of biomaterials by polydopamine surface modification. *Nanomedicine* **2011,** *6* (5), 793-801.
404. Ku, S. H.; Ryu, J.; Hong, S. K.; Lee, H.; Park, C. B., General functionalization route for cell adhesion on non-wetting surfaces. *Biomaterials* **2010,** *31* (9), 2535-2541.
405. Zhang, C.; Wu, M.-B.; Wu, B.-H.; Yang, J.; Xu, Z.-K., Solar-driven self-heating sponges for highly efficient crude oil spill remediation. *J. Mater. Chem. A* **2018,** *6* (19), 8880-8885.
406. Lee, M.; Rho, J.; Lee, D. E.; Hong, S.; Choi, S. J.; Messersmith, P. B.; Lee, H., Water detoxification by a substrate‐bound catecholamine adsorbent. *ChemPlusChem* **2012,** *77* (11), 987-990.
407. Mrówczyński, R., Polydopamine-Based Multifunctional (Nano) materials for Cancer Therapy. *ACS Appl. Mater. Inter.* **2017,** *10* (9), 7541-7561.
408. Han, G.; Zhang, S.; Li, X.; Widjojo, N.; Chung, T.-S., Thin film composite forward osmosis membranes based on polydopamine modified polysulfone substrates with enhancements in both water flux and salt rejection. *Chem. Eng. Sci.* **2012,** *80*, 219-231.
409. Sun, G.; Chung, T.-S.; Jeyaseelan, K.; Armugam, A., Stabilization and immobilization of aquaporin reconstituted lipid vesicles for water purification. *Colloids Surf. B* **2013,** *102*, 466-471.
410. Jin, H.; Kettunen, M.; Laiho, A.; Pynnönen, H.; Paltakari, J.; Marmur, A.; Ikkala, O.; Ras, R. H., Superhydrophobic and superoleophobic nanocellulose aerogel membranes as bioinspired cargo carriers on water and oil. *Langmuir* **2011,** *27* (5), 1930-1934.
411. Khalifa, A.; Lawal, D.; Antar, M.; Khayet, M., Experimental and theoretical investigation on water desalination using air gap membrane distillation. *Desalination* **2015,** *376*, 94-108.
412. Kuila, U.; McCarty, D. K.; Derkowski, A.; Fischer, T. B.; Prasad, M., Total porosity measurement in gas shales by the water immersion porosimetry (WIP) method. *Fuel* **2014,** *117*, 1115-1129.
413. Loćiciga, H. A., Modern‐age buildup of CO_2 and its effects on seawater acidity and salinity. *Geophys. Res. Lett.* **2006,** *33* (10).
414. Sun, M.; Zucker, I.; Davenport, D. M.; Zhou, X.; Qu, J.; Elimelech, M., Reactive, Self-cleaning Ultrafiltration Membrane Functionalized with Iron Oxychloride (FeOCl) Nanocatalysts. *Environ. Sci. Technol.* **2018**.
415. Tiraferri, A.; Yip, N. Y.; Phillip, W. A.; Schiffman, J. D.; Elimelech, M., Relating performance of thin-film composite forward osmosis membranes to support layer formation and structure. *J. Membr. Sci.* **2011,** *367* (1-2), 340-352.
416. Cao, C.; Tan, L.; Liu, W.; Ma, J.; Li, L., Polydopamine coated electrospun poly (vinyldiene fluoride) nanofibrous membrane as separator for lithium-ion batteries. *J. Power Sources* **2014,** *248*, 224-229.
417. Jiang, J.; Zhu, L.; Zhu, L.; Zhu, B.; Xu, Y., Surface characteristics of a self-polymerized dopamine coating deposited on hydrophobic polymer films. *Langmuir* **2011,** *27* (23), 14180-14187.
418. Shao, L.; Wang, Z. X.; Zhang, Y. L.; Jiang, Z. X.; Liu, Y. Y., A facile strategy to enhance PVDF ultrafiltration membrane performance via self-polymerized polydopamine followed by hydrolysis of ammonium fluotitanate. *J. Membr. Sci.* **2014,** *461*, 10-21.
419. Sun, D.; Zhu, Y.; Meng, M.; Qiao, Y.; Yan, Y.; Li, C., Fabrication of highly selective ion imprinted macroporous membranes with crown ether for targeted separation of lithium ion. *Sep. Purif. Technol.* **2017,** *175*, 19-26.
420. Al-Oweini, R.; El-Rassy, H., Synthesis and characterization by FTIR spectroscopy of silica aerogels prepared using several $Si(OR)_4$ and $R''Si(OR')_3$ precursors. *J. Mol. Struct* **2009,** *919* (1-3), 140-145.
421. Gupta, P.; Dillon, A.; Bracker, A.; George, S., FTIR studies of H_2O and D_2O decomposition on porous silicon surfaces. *Surf. Sci.* **1991,** *245* (3), 360-372.
422. Cheng, G.; Zheng, S.-Y., Construction of a high-performance magnetic enzyme nanosystem for rapid tryptic digestion. *Sci Rep.* **2014,** *4*, 6947.

423. Ryu, J.; Ku, S. H.; Lee, H.; Park, C. B., Mussel‐inspired polydopamine coating as a universal route to hydroxyapatite crystallization. *Adv. Funct. Mater.* **2010,** *20* (13), 2132-2139.
424. Cui, J.; Zhang, Y.; Wang, Y.; Ding, J.; Yu, P.; Yan, Y.; Li, C.; Zhou, Z., Fabrication of lithium ion imprinted hybrid membranes with antifouling performance for selective recovery of lithium. *New J. Chem.* **2018,** *42* (1), 118-128.
425. Wu, Y.; Lu, J.; Meng, M.; Dai, J.; Lin, X.; Gao, J.; Li, C.; Yan, Y., Bioinspired synthesis of pDA/SiO_2-based porous ciprofloxacin-imprinted nanocomposite membrane by a polydopamine-assisted organic-inorganic method. *Chem. Eng. J.* **2017,** *309*, 263-271.
426. Ren, L.-F.; Xia, F.; Chen, V.; Shao, J.; Chen, R.; He, Y., TiO_2-FTCS modified superhydrophobic PVDF electrospun nanofibrous membrane for desalination by direct contact membrane distillation. *Desalination* **2017,** *423*, 1-11.
427. Martínez-Díez, L.; Vazquez-Gonzalez, M. I., Temperature and concentration polarization in membrane distillation of aqueous salt solutions. *J. Membr. Sci.* **1999,** *156* (2), 265-273.
428. Winter, D.; Koschikowski, J.; Wieghaus, M., Desalination using membrane distillation: Experimental studies on full scale spiral wound modules. *J. Membr. Sci.* **2011,** *375* (1-2), 104-112.
429. Cath, T. Y.; Adams, V. D.; Childress, A. E., Experimental study of desalination using direct contact membrane distillation: a new approach to flux enhancement. *J. Membr. Sci.* **2004,** *228* (1), 5-16.
430. Chen, C.; Li, Y.; Song, J.; Yang, Z.; Kuang, Y.; Hitz, E.; Jia, C.; Gong, A.; Jiang, F.; Zhu, J.; Yang, B.; Xie, J.; Hu, L., Highly flexible and efficient solar steam generation device. *Adv. Mater.* **2017,** *29* (30), 1701756.
431. Hu, X.; Xu, W.; Zhou, L.; Tan, Y.; Wang, Y.; Zhu, S.; Zhu, J., Tailoring Graphene Oxide‐Based Aerogels for Efficient Solar Steam Generation under One Sun. *Adv. Mater.* **2017,** *29* (5), 1604031.
432. Acharya, H. R.; Henderson, C.; Matis, H.; Kommepalli, H.; Moore, B.; Wang, H., Cost effective recovery of low-TDS frac flowback water for re-use. *DOE Report DE-FE0000784* **2011**, 100.
433. Mekonnen, M. M.; Hoekstra, A. Y., Four billion people facing severe water scarcity. *Sci. Adv.* **2016,** *2* (2), e1500323.
434. Schewe, J.; Heinke, J.; Gerten, D.; Haddeland, I.; Arnell, N. W.; Clark, D. B.; Dankers, R.; Eisner, S.; Fekete, B. M.; Colón-González, F. J., Multimodel assessment of water scarcity under climate change. *Proc. Natl. Acad. Sci.* **2014,** *111* (9), 3245-3250.
435. Van Loon, A. F.; Gleeson, T.; Clark, J.; Van Dijk, A. I.; Stahl, K.; Hannaford, J.; Di Baldassarre, G.; Teuling, A. J.; Tallaksen, L. M.; Uijlenhoet, R., Drought in the Anthropocene. *Nat. Geosci.* **2016,** *9* (2), 89.
436. Lee, K. P.; Arnot, T. C.; Mattia, D., A review of reverse osmosis membrane materials for desalination—development to date and future potential. *J. Membr. Sci.* **2011,** *370* (1-2), 1-22.
437. Jun, Y.-S.; Wu, X.; Ghim, D.; Jiang, Q.; Cao, S.; Singamaneni, S., Photothermal Membrane Water Treatment for Two Worlds. *Acc. Chem. Res.* **2019,** *52* (5), 1215-1225.
438. Chen, C.; Kuang, Y.; Hu, L., Challenges and opportunities for solar evaporation. *Joule* **2019**.
439. Ghasemi, H.; Ni, G.; Marconnet, A. M.; Loomis, J.; Yerci, S.; Miljkovic, N.; Chen, G., Solar steam generation by heat localization. *Nat. Commun.* **2014,** *5*, 4449.
440. Shang, W.; Deng, T., Solar steam generation: steam by thermal concentration. *Nat. Energy* **2016,** *1* (9), 16133.
441. Ni, G.; Zandavi, S. H.; Javid, S. M.; Boriskina, S. V.; Cooper, T. A.; Chen, G., A salt-rejecting floating solar still for low-cost desalination. *Energy Environ. Sci.* **2018,** *11* (6), 1510-1519.
442. Deshmukh, A.; Boo, C.; Karanikola, V.; Lin, S.; Straub, A. P.; Tong, T.; Warsinger, D. M.; Elimelech, M., Membrane Distillation at the Water-Energy Nexus: Limits, Opportunities, and Challenges. *Energy Environ. Sci.* **2018,** *11*, 1177-1196.
443. Lu, Y.; Nakicenovic, N.; Visbeck, M.; Stevance, A.-S., Policy: Five priorities for the UN sustainable development goals. *Nat. News* **2015,** *520* (7548), 432.

444. Jiang, Q.; Tian, L.; Liu, K. K.; Tadepalli, S.; Raliya, R.; Biswas, P.; Naik, R. R.; Singamaneni, S., Bilayered biofoam for highly efficient solar steam generation. *Adv. Mater.* **2016,** *28* (42), 9400-9407.
445. Ai, K.; Liu, Y.; Ruan, C.; Lu, L.; Lu, G. M., Sp2 C‐Dominant N‐Doped Carbon Sub‐micrometer Spheres with a Tunable Size: A Versatile Platform for Highly Efficient Oxygen‐Reduction Catalysts. *Adv. Mater.* **2013,** *25* (7), 998-1003.
446. Wang, Z.; Yu, H.; Xia, J.; Zhang, F.; Li, F.; Xia, Y.; Li, Y., Novel GO-blended PVDF ultrafiltration membranes. *Desalination* **2012,** *299*, 50-54.
447. Jiang, Q.; Ghim, D.; Cao, S.; Tadepalli, S.; Liu, K.-K.; Kwon, H.; Luan, J.; Min, Y.; Jun, Y.-S.; Singamaneni, S., Photothermally Active Reduced Graphene Oxide/Bacterial Nanocellulose Composites as Biofouling-Resistant Ultrafiltration Membranes. *Environ. Sci. Technol.* **2018,** *53* (1), 412-421.
448. Yan, L.; Li, Y. S.; Xiang, C. B.; Xianda, S., Effect of nano-sized Al_2O_3-particle addition on PVDF ultrafiltration membrane performance. *J. Membr. Sci.* **2006,** *276* (1-2), 162-167.
449. Fujiwara, M., Water desalination using visible light by disperse red 1 modified PTFE membrane. *Desalination* **2017,** *404*, 79-86.
450. Fujiwara, M.; Kikuchi, M., Solar desalination of seawater using double-dye-modified PTFE membrane. *Water Res.* **2017,** *127*, 96-103.
451. Huang, L.; Pei, J.; Jiang, H.; Hu, X., Water desalination under one sun using graphene-based material modified PTFE membrane. *Desalination* **2018,** *442*, 1-7.
452. Gingerich, D. B.; Mauter, M. S., Quantity, quality, and availability of waste heat from United States thermal power generation. *Environ. Sci. Technol.* **2015,** *49* (14), 8297-8306.
453. Herzberg, M.; Elimelech, M., Biofouling of reverse osmosis membranes: role of biofilm-enhanced osmotic pressure. *J. Membr. Sci.* **2007,** *295* (1-2), 11-20.
454. Goh, S.; Zhang, Q.; Zhang, J.; McDougald, D.; Krantz, W. B.; Liu, Y.; Fane, A. G., Impact of a biofouling layer on the vapor pressure driving force and performance of a membrane distillation process. *J. Membr. Sci.* **2013,** *438*, 140-152.
455. Feng, J.; Fan, H.; Zha, D.-a.; Wang, L.; Jin, Z., Characterizations of the formation of polydopamine-coated halloysite nanotubes in various pH environments. *Langmuir* **2016,** *32* (40), 10377-10386.
456. Liebscher, J. r.; Mrówczyński, R.; Scheidt, H. A.; Filip, C.; Hădade, N. D.; Turcu, R.; Bende, A.; Beck, S., Structure of polydopamine: a never-ending story? *Langmuir* **2013,** *29* (33), 10539-10548.
457. Shaffer, D. L.; Arias Chavez, L. H.; Ben-Sasson, M.; Romero-Vargas Castrillón, S.; Yip, N. Y.; Elimelech, M., Desalination and reuse of high-salinity shale gas produced water: drivers, technologies, and future directions. *Environ. Sci. Technol.* **2013,** *47* (17), 9569-9583.
458. Wu, J.; Zodrow, K. R.; Szemraj, P. B.; Li, Q., Photothermal nanocomposite membranes for direct solar membrane distillation. *J. Mater. Chem. A* **2017,** *5* (45), 23712-23719.
459. Fujiwara, M.; Imura, T., Photo induced membrane separation for water purification and desalination using azobenzene modified anodized alumina membranes. *ACS Nano* **2015,** *9* (6), 5705-5712.
460. Ang, E. H.; Tan, Y. Z.; Chew, J. W., Three-Dimensional Plasmonic Spacer Enables Highly Efficient Solar-Enhanced Membrane Distillation of Seawater. *J. Mater. Chem. A* **2019**.
461. Xue, G.; Chen, Q.; Lin, S.; Duan, J.; Yang, P.; Liu, K.; Li, J.; Zhou, J., Highly efficient water harvesting with optimized solar thermal membrane distillation device. *Global Chal.* **2018,** *2* (5-6), 1800001.
462. Tan, Y. Z.; Wang, H.; Han, L.; Tanis-Kanbur, M. B.; Pranav, M. V.; Chew, J. W., Photothermal-enhanced and fouling-resistant membrane for solar-assisted membrane distillation. *J. Membr. Sci.* **2018,** *565*, 254-265.
463. Tessmer, I.; Kaur, P.; Lin, J.; Wang, H., Investigating bioconjugation by atomic force microscopy. *J. Nanobiotechnol.* **2013,** *11* (1), 25.

464. Sakata, O., Rapid X-ray diffraction method for structural analysis of a nano material on a surface or at an interface and for structural analysis of a solid/liquid interface, and apparatus used for the method. Google Patents: 2006.
465. Xie, M.; Nghiem, L. D.; Price, W. E.; Elimelech, M., Toward resource recovery from wastewater: extraction of phosphorus from digested sludge using a hybrid forward osmosis–membrane distillation process. *Environ. Sci. Technol. Let.* **2014,** *1* (2), 191-195.
466. Zarebska, A.; Nieto, D. R.; Christensen, K. V.; Norddahl, B., Ammonia recovery from agricultural wastes by membrane distillation: fouling characterization and mechanism. *Water Res.* **2014,** *56*, 1-10.
467. Hickenbottom, K. L.; Cath, T. Y., Sustainable operation of membrane distillation for enhancement of mineral recovery from hypersaline solutions. *J. Mem. Sci.* **2014,** *454*, 426-435.
468. Loeb, S. K.; Kim, J.; Jiang, C.; Early, L. S.; Wei, H.; Li, Q.; Kim, J.-H., Nanoparticle Enhanced Interfacial Solar Photothermal Water Disinfection Demonstrated in 3-D Printed Flow-Through Reactors. *Environ. Sci. Technol.* **2019,** *53* (13), 7621-7631.
469. Dudchenko, A. V.; Chen, C.; Cardenas, A.; Rolf, J.; Jassby, D., Frequency-dependent stability of CNT Joule heaters in ionizable media and desalination processes. *Nature Nanotechnol.* **2017,** *12* (6), 557.
470. Gryta, M., Influence of polypropylene membrane surface porosity on the performance of membrane distillation process. *J. Mem. Sci.* **2007,** *287* (1), 67-78.
471. Gao, X.; Ren, H.; Zhou, J.; Du, R.; Yin, C.; Liu, R.; Peng, H.; Tong, L.; Liu, Z.; Zhang, J., Synthesis of hierarchical graphdiyne-based architecture for efficient solar steam generation. *Chem. Mater.* **2017,** *29* (14), 5777-5781.
472. Ma, S.; Qarony, W.; Hossain, M. I.; Yip, C. T.; Tsang, Y. H., Metal-organic framework derived porous carbon of light trapping structures for efficient solar steam generation. *Solar Energy Mater. Solar Cells* **2019,** *196*, 36-42.

Appendices

Curriculum Vitae

Xuanhao (Philip) Wu
Ph.D. candidate
Department of Energy, Environmental and Chemical Engineering
Washington University in St. Louis
One Brookings Drive, Campus Box 1180
Brauer Hall, Room 2029, St. Louis, MO 63130
Email: xwu35@wustl.edu
Tel: 314-250-8558

Education

Ph.D. Environmental & Chemical Engineering (expected in April 2020), Washington University in St. Louis, USA
Advisor: Professor Young-Shin Jun
Dissertation title: Chemistry of Nanoscale Solids and Organic Matter in Sustainable Water Management Systems

B.S. Environmental Science & Engineering (rank 1/50), 2015/06, Fudan University, China

Research Experience

Graduate Researcher at Washington University in St. Louis

1. **Membrane Distillation: Developing Photothermal Membrane Distillation (PMD) using Renewable Solar Energy**

- Developed novel photothermal membranes using polymers/2D materials for solar-driven photothermal membrane distillation (supported by National Science Foundation Environmental Engineering Program: CBET-1604542).

2. **Managed Aquifer Recharge: Iron Oxide Nucleation and Arsenopyrite Mineral Dissolution**

- Investigated heterogeneous iron oxide nucleation using *in situ* grazing incidence small angle X-ray scattering (GISAXS) and grazing incidence wide angle X-ray scattering (GIWAXS).
- Studied dissolved organic matter/abundant oxyanion effects on arsenic mobilization and secondary mineral precipitation from arsenopyrite dissolution (supported by National Science Foundation: EAR-1424927).

3. **Surface Chemistry of Engineered Nanomaterials (ENMs) in Advanced Water Treatment Systems**

- Investigated the co-effects of advanced oxidation processes (UV/H_2O_2 & UV/PS) and dissolved organic matter (DOM) on the surface chemical property changes of engineered nanomaterials (ENMs) such as cerium oxide nanoparticles (CeO_2 NPs) (supported by National Science Foundation: CHE-1214090).

Undergraduate Researcher at Fudan University

4. Microcystins: Growth and Microcystins Production from *Microcystis aeruginosa*

- Investigated the biosynthesis of microcystins with different exogenous amino acids and urea using ^{15}N isotopic tracer technique and LC/MS/MS (supported by Chinese National Science Foundation: 51008083).

Honors & Awards

- 2019, Best Student Presentation Award, Geochemistry Division, 2019 Fall ACS meeting, San Diego
- 2019, Student Travel Award, Geochemistry Division, 2019 Fall ACS meeting, San Diego
- 2019, 1st Place Prize, Fresh Ideas Student Poster Competition, Missouri AWWA conference
- 2019, Graduate Student Award, Environmental Chemistry Division, ACS
- 2018, Selected participant in the 2018 ACS Summer School on Green Chemistry & Sustainable Energy
- 2017, "Certificate of Merit", Environmental Chemistry Division, 2017 Spring ACS meeting, San Francisco
- 2015, Outstanding Graduates of Shanghai (top 2%)
- 2014, Scholarship of Shanghai
- 2013, Arawana Scholarship
- 2012, 2013, 2014, Fudan University Outstanding Student Award
- 2012, National Scholarship of China (top 2%)

Journal Publications

Submitted

15. **Wu, X.**,[†] Cao, S.,[†] Ghim, D., Jiang, Q., Singamaneni, S.,[*] Jun, Y. S.[*] A Thermally Engineered Polydopamine-Bacterial Nanocellulose Bilayer for Photothermal Membrane Distillation*, submitted to Nature Sustainability*. († Equal Contribution)

Published

14. Cao, S., Rathi, P., **Wu, X.**, Ghim, D., Jun, Y. S.,[*] Singamaneni, S.[*] Advances in the Utilization of Cellulose Nanomaterials in Interfacial Evaporators for Desalination*, Advanced Materials, accepted in March 2020.*

13. **Wu, X.**, Burnell, S., Neil, C., Kim, D., Zhang, L., Jung, H., Jun, Y. S.* Effects of Phosphate, Silicate, and Bicarbonate on Arsenopyrite Dissolution and Secondary Mineral Precipitation, ***ACS Earth & Space Chemistry***, **2020**. DOI: 10.1021/acsearthspacechem.9b00273.

12. Cao, S., **Wu, X.**, Zhu, Y., Gupta, R., Tan, A., Wang, Z., Ramani, V., Zhu, W., Wang, X., Jun, Y. S.,* Singamaneni, S.* Polydopamine/Hydroxyapatite Nanowires-based Bilayered Membrane for Solar-driven Membrane Distillation, ***Journal of Materials Chemistry A***, **2020**. DOI: 10.1039/C9TA12703H.

11. **Wu, X.**, Bowers, B., Kim, D., Jun, Y. S.* Dissolved Organic Matter Affects Arsenic Mobility and Iron(III) (hydr)oxides Formation: Implications for Managed Aquifer Recharge, ***Environmental Science & Technology***, **2019**, 53, 24, 14357-14367. DOI: 10.1021/acs.est.9b04873 (highlight in *NSF News* https://www.nsf.gov/discoveries/disc_summ.jsp?cntn_id=299866&org=NSF&from=news)

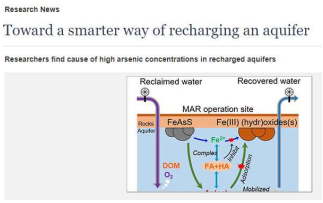

10. Cao, S., Jiang, Q., **Wu, X.**, Ghim, D., Derami, H. G., Chou, P., Jun, Y. S.,* Singamaneni, S.* Advances in Materials for Highly Efficient Photothermal Evaporators, ***Journal of Materials Chemistry A***, **2019,** 7, 24092-24123 (invited). DOI: 10.1039/C9TA06034K.

9. Ray, J. R., **Wu, X.**, Neil, C. W., Jung, H., Li, Z., Jun, Y. S.* Redox Chemistry of CeO_2 Nanoparticles in Aquatic Systems Containing Cr(VI)(aq) and Fe^{2+} Ions, ***Environmental Science: Nano*, 2019**, 6, 2269-2280. DOI: 10.1039/C9EN00201D.

8. Jun, Y. S.,* Ghim, D., **Wu, X.**, Cao, S., Singamaneni, S.* Solar-Enabled Water Treatment in Resource Limited Settings, ***The Journal of the Homeland Defense & Security Information Analysis Center*, 2019,** 6, 2, 21-26 (invited).

7. Jun, Y. S.,* **Wu, X.**, Ghim, D., Jiang, Q., Cao, S., Singamaneni, S.* Photothermal Membrane Water Treatment for Two Worlds, ***Accounts of Chemical Research*, 2019,** 52, 5, 1215-1225 (invited). DOI: 10.1021/acs.accounts.9b00012.

6. Zhang, L., Zhu, Y., **Wu, X.**, Jun, Y. S.* Effects of Sulfate on Biotite Interfacial Reactions under High Temperature and High CO_2 Pressure, ***Physical Chemistry Chemical Physics*, 2019**, 21, 6381-6390. DOI: 10.1039/c8cp07368f.

5. **Wu, X.**, Jiang, Q., Ghim, D., Singamaneni, S.,* Jun, Y. S*. Localized Heating by a Photothermal Polydopamine Coating Facilitates a Novel Membrane Distillation Process, ***Journal of Materials Chemistry A***, **2018**, 18799-18807. DOI: 10.1039/c8ta05738a.

4. **Wu, X.**, Neil, C. W., Kim, D., Jung, H., Jun, Y. S.* Co-effects of UV/H_2O_2 and Natural Organic Matter on the Surface Chemistry of Cerium Oxide Nanoparticles, ***Environmental Science: Nano*, 2018**, 5, 2382-2393. DOI: 10.1039/c8en00435h.

3. **Wu, X.**, Yan, Y., Wang, P., Ni, L., Gao, J., Dai, R.* Effect of urea on growth and microcystins production of *Microcystis aeruginosa*, ***Bioresource Technology*, 2015**, 181, 72-77. Doi:10.1016/j.biortech.2015.01.035.

2. **Wu, X.**, Gao, J., Yan, Y., Zhou, B., Dai, R.* The comparison effects of inorganic nitrogen and organic nitrogen on the growth and microcystin production of *Microcystis aeruginosa*, ***Acta Scientiae Circumstantiae*****, 2015**, 35, 677-683. Doi: 10.13671/j.hjkxxb.2014.0769 (*in Chinese*).

1. Yan, Y., Dai, R.,* Liu, Y.,* Gao, J., **Wu, X.** Comparative effects of inorganic and organic nitrogen on the growth and microcystin production of *Microcystis aeruginosa*, ***World Journal of Microbiology and Biotechnology*****, 2015,** 31, 763-772. Doi: 10.1007/s11274-015-1829-y.

Patents

---

1. Xuanhao Wu, Qisheng Jiang, Srikanth Singamaneni, Young-Shin Jun. "Novel materials and methods for photothermal membrane distillation", US Patent, filed.

Professional Skills

- **Synchrotrons** Grazing incidence small angle X-ray scattering, grazing incidence wide angle X-ray scattering, X-ray absoprtion spectroscopy, wide angle X-ray diffraction
- **Instruments** 3D printed membrane distillation unit design and operation, Raman spectroscopy, Atomic force microscopy, scanning electron microscopy, Fourier transform infrared spectroscope, transmission electron microscopy, ion chromatography, ultraviolet-visible spectroscopy, inductively coupled plasma-mass spectroscopy, inductively coupled plasma-optical emission spectroscopy, X-ray photoelectron spectroscopy, Zetasizer, total organic carbon measurement
- **Programs** MATLAB, Igor Pro (GISAXS), Athena (XAS), Multipak (XPS), Geochemist's Workbench (GWB), CrystalMaker, Nanoscope (AFM)

Conference Presentations and Posters (*Presenter)

---

13. **Xuanhao Wu***, Yongfang Rao, and Young-Shin Jun, Surface Chemistry of Cerium Oxide Nanoparticles in an Engineered UV/Persulfate Process with Dissolved Organic Matter", Special symposium entitled "Basic Research in Colloids, Surfactants & Interfaces, The 258th ACS National Meeting & Exposition, San Diego, California, August 25-29, 2019.

12. **Xuanhao Wu***, Brandon Bowers, Doyoon Kim, Young-Shin Jun, Dissolved organic matter affects arsenopyrite dissolution and secondary iron(III) (hydr)oxides formation, Special symposium entitled "Sorption & Redox at Mineral-Water Interfaces & the Impact on the Biogeochemical Cycling of Trace & Major Elements, The 258th ACS National Meeting & Exposition, San Diego, California, August 25-29, 2019. Received Best Student Presentation Award and Student Travel Award.

11. **Xuanhao Wu**[*], Qisheng Jiang, Deoukchen Ghim, Srikanth Singamaneni, and Young-Shin Jun, Photothermal Membrane Distillation Facilitated by a Mussel-Inspired Polydopamine Coating, Special symposium entitled "Novel Polymeric Materials & Polymer-Based Processes for Energy-Efficient Treatment of Water & Resource Recovery", The 258th ACS National Meeting & Exposition, San Diego, California, August 25-29, 2019.

10. Adrian Martinez[*], **Xuanhao Wu**, and Young-Shin Jun, $CaCO_3$ Fouling on Solar-driven Membrane Distillation Membranes, the 2019 McKelvey School of Engineering Undergraduate Summer Research Symposium, Washington University in St. Louis, MO, 2019.

9. **Xuanhao Wu**[*], Qisheng Jiang, Deoukchen Ghim, Srikanth Singamaneni[*], and Young-Shin Jun[*]. Sustainable Solar-driven Photothermal Membrane Distillation using a Polydopamine Coating, poster, 2019 ACE & AWWA meeting, Denver, Colorado, 2019.

8. **Xuanhao Wu**[*], Qisheng Jiang, Deoukchen Ghim, Srikanth Singamaneni, and Young-Shin Jun. Sustainable Solar-driven Photothermal Membrane Distillation using a Polydopamine Coating, poster, the 2019 Missouri Section of the American Water Works Association (MO-AWWA) and the Missouri Water Environment Association (MWEA) Joint Conference, Osage Beach, Missouri, 2019.

7. **Xuanhao Wu**[*], Qisheng Jiang, Deoukchen Ghim, Srikanth Singamaneni, and Young-Shin Jun. Photothermal Membrane Distillation Facilitated by a Mussel-Inspired Polydopamine Coating, oral, the 24th Mid-American Environmental Engineering Conference (MAEEC), Missouri Science & Technology, Rolla, Missouri, 2018.

6. Brandon Bowers[*], **Xuanhao Wu**, and Young-Shin Jun. Effects of Organic Matter on Arsenic Mobilization from Arsenopyrite Dissolution and Secondary Mineral Precipitation, oral, the 2018 EECE Undergraduate Summer Research Symposium, Washington University in St. Louis, St. Louis, Missouri, 2018.

5. **Xuanhao Wu**[*], Qisheng Jiang, Deoukchen Ghim, Srikanth Singamaneni, Young-Shin Jun. Sustainable Solar-driven Membrane Distillation by Photothermal Active Polydopamine, poster, ACS Summer School on Green Chemistry & Sustainable Energy, Golden, Colorado, 2018.

4. **Xuanhao Wu**[*], Chelsea Neil, Doyoon Kim, Haesung Jung, Young-Shin Jun. Surface property changes of cerium oxide nanoparticles in the presence of UV/H_2O_2 and natural organic matter, oral. Division of Environmental Chemistry: Aquatic Photochemistry. The 255st American Chemical Society National Meeting & Exposition, New Orleans, Louisiana, 2018.

3. **Xuanhao Wu**[*], Samantha Burnell, Chelsea Neil, Doyoon Kim, Haesung Jung, Young-Shin Jun. Effects of oxyanions on arsenic mobilization from arsenopyrite during managed aquifer recharge, oral. Division of Environmental Chemistry: Water Use Optimization: Water Quality, Reuse & Treatment. The 255st American Chemical Society National Meeting & Exposition, New Orleans, Louisiana, 2018.

2. **Xuanhao Wu**[*], Chelsea Neil, Doyoon Kim, Haesung Jung, Young-Shin Jun. Effects of UV/H_2O_2 and natural organic matter on the surface chemistries of cerium oxide nanoparticles, poster, The 2017 Association of Environmental Engineering and Science Professors (AEESP) Conference, Ann Arbor, Michigan, 2017.

1. **Xuanhao Wu**[*], Chelsea Neil, Doyoon Kim, Haesung Jung, Young-Shin Jun. Co-effects of UV/H_2O_2 and natural organic matter on the surface properties and colloidal stability of cerium oxide nanoparticles, oral. Division of Environmental Chemistry: Chemistry & Application of Advanced Oxidation Processes for Water Detoxification, Treatment & Reuse. The 253st American Chemical Society National Meeting & Exposition, San Francisco, California, 2017.

Successful Synchrotron Proposals

Beamlines of Advanced Photon Source (APS) at Argonne National Lab

- Proposal **GUP: 65741**. Investigation of heterogeneous nucleation of mineral foulants on membrane distillation membranes. Beamline: 12-ID-B. **2019-2022**. Technique: *in situ* grazing incidence small angle X-ray scattering (GISAXS) and grazing incidence wide angle X-ray scattering (GIWAXS).
- Proposal **GUP: 53330**. Investigating interfacial energies of heterogeneous iron(III) (hydr)oxide nucleation on earth-abundant mineral surfaces. Beamline: 12-ID-B. **2018-2020**. Technique: *in situ* grazing incidence small angle X-ray scattering (GISAXS) and grazing incidence wide angle X-ray scattering (GIWAXS).
- Proposal **GUP: 52994**. Influence of Reactive Oxygen Species (ROS) on Surface Properties of Cerium Oxide Nanoparticles. Beamline: 11-ID-B, February 15-16, **2017**. Technique: wide angle X-ray diffraction (WAXD).
- Proposal **GUP: 48652**. Influence of Advanced Oxidation Processes on the Fate and Transport of Cerium Oxide Nanoparticles in Engineered Aquatic Environments. Beamline: 13-ID-E, February 8-10, **2017**. Technique: X-ray absorption spectroscopy (XAS).

Teaching Experience

Teaching Assistant

- 2017, EECE 505 Aquatic Chemistry, teaching assistant.
- 2017, EECE 210 Introduction to Environmental Engineering, teaching assistant.
- 2016, EECE 405 Unit Operations Laboratory, teaching assistant.

Undergraduate Student Mentor

5. **Junlong Huang,** Tsinghua University, **2019** fall. Working on project "Effects of Persulfate on Cast Iron Corrosion in Drinking Water Distribution Systems".

4. **Adrian Martinez,** Washington University in St. Louis, **2019** fall. Working on project "$CaCO_3$ Fouling on Solar-driven Membrane Distillation Membranes".
3. **Brandon Bowers,** Missouri Science & Technology, **2018** summer. Worked on project "Effects of Organic Matter on Arsenic Mobilization from Arsenopyrite Dissolution and Secondary Mineral Precipitation".
2. **Daniel Delgado,** San Diego State University, **2017** summer. Worked on project "Effects of Mn(II) concentration on CeO_2 nanoparticle surface reactions in complex natural water systems".
1. **Samantha A Burnell**, Massachusetts Institute of Technology, **2016** summer. Worked on project "Effects of Phosphate, Silicate, and Bicarbonate on Arsenopyrite Dissolution and Secondary Mineral Precipitation".

Outreach Programs and Community Service

- 2015-2019, Moving and Shaking: An Introduction to Environmental Engineering. Education for students in grade 6-8, supported by the St. Louis Area Gifted Resource Council.
- 2015-2017, Hot Topics Workshop on "Sustainable Water" with Middle School Teachers in St. Louis Area. The Institute for School Partnership at Washington University in St. Louis.

Leadership Experience

- 2019, Faculty Search Student Committee, Chair, EECE, WUSTL, St. Louis, USA
- 2013, Academic Minister, Student Union, Fudan University, Shanghai, China
- 2013, President, New Great Wall Club, Fudan University, Shanghai, China